JOHANNES GUTENBERG UNIVERSITÄT MAINZ

Polyoxometalate-derived Composites for Photoelectrochemical Energy Conversion

Dissertation

for the award of the degree

‘‘Doctor of Natural Sciences’’

Doctorate in Chemistry

at the Faculty of Chemistry, Pharmaceutical Sciences, Geography and Geosciences of the Johannes Gutenberg University Mainz

M.Sc. Fan Feng

Born in Xi’an, China

Mainz, 2025

Dean of the Department of Chemistry: Prof. Dr. Eva Rentschler

1st Supervisor: Prof. Dr. Carsten Streb
2nd Supervisor: Prof. Dr. Radim Beránek

Day of the oral examination: 20.03.2025

Statement

The present work ‘‘Polyoxometalate-derived Composites for Photoelectrochemical Energy Conversion’’ was done in the period from March 2021 to July 2022 at the Institute of Inorganic Chemistry I, University of Ulm, and later from August 2022 to March 2025 at the Department of Chemistry, Johannes Gutenberg University Mainz, the working group of Prof. Dr. Carsten Streb.

I hereby declare and confirm that I have done the work independently and have not used any sources than those indicated, and the present work in this dissertation has not been submitted in another doctoral procedure.

Furthermore, I declare that I am familiar with the valid regulations for doctoral studies of the Johannes Gutenberg University Mainz, the doctoral regulations of the Faculty of Natural Sciences for the acquisition of Dr. rer. nat. as well as the statutes of the Johannes Gutenberg University Mainz for ensuring good scientific practice.

Place, Date Mainz, 21.03.2025

Signature Fan Feng

Abstract

To alleviate the global energy crises and environmental problems caused by the conventional fossil fuels, it is important to widespread develop renewable alternative energy schemes (*e.g.* solar- and wind-energies) to meet the growing energy demand of human society. Since the pioneering works on photo-electrocatalysis using TiO_2 reported by Fujishima and Honda, photoelectrochemical (PEC) water splitting is regarded as one of the most promising ways to achieve solar energy conversion and storage into H_2 molecular by splitting water into H_2 and O_2. Compared to the H_2 evolution reaction (HER), the O_2 evolution reaction (OER) is a kinetic bottleneck for overall water splitting, due to the complicated transfer of four electrons and four protons. Moreover, during the water oxidation reaction, some other possible oxidation reactions can occur (*e.g.* degradation of catalysts) in a harsh oxidizing environment. Therefore, one of the most important tasks for solar H_2 production is the development of efficient and stable OER photoanodes for enhancing the solar energy water splitting conversion efficiency.

Bismuth vanadate ($BiVO_4$) is supposed to be one of the most promising photoanodes for solar water splitting due to its suitable bandgap, low valence band position, earth-abundance, stability in aqueous solution and low cost. However, the efficiency of solar energy conversion is still far below the theoretical value due to the sluggish carrier mobility, poor electrical conductivity and slow surface reaction kinetics. Therefore, the rapid progress mainly focuses on the modification of the $BiVO_4$ photoanode materials to improve the PEC performance. One approach to this end is the use of polyoxometalates (POMs) which are a unique class of molecular metal oxide clusters that consist of early transition metals. Benefiting from the unique structure and reactivity, POMs play a key role associated with metal oxide light absorbers materials in photo-electrocatalytic system in terms of both photoanodes and photocathodes.

Based on this background, this thesis summarizes investigations into various $BiVO_4$ photoanode modification strategies for photoelectrochemical water splitting and current progress of POMs-based/derived $BiVO_4$ photoanodes. After an introduction, the main research topics of this thesis are presented in two chapters, which aims at designing new and low-cost POMs-based/derived $BiVO_4$ OER composite materials and innovative methods to promote the OER rate in overall water splitting configurations. For instance, doping with molybdenum or cobalt polyoxometalate (CoPOM = $Na_{10}[Co_4(H_2O)_2(PW_9O_{34})_2]$) in bulk of $BiVO_4$ enhances the electrical conductivity and improves the charge separation efficiency respectively.

Meanwhile, surface modification with CoPOM water oxidation co-catalyst enhances the hole extraction and improves the charge transfer efficiency, particularly significant at very low bias potentials it can partially compensate the detrimental effects of the electron polaronic states from doping. Besides, several innovative methods are also developed for energy electrode materials fabrication, such as 'Double-Use' strategy for CoPOM used both as a bulk doping agent as well as a surface-deposited water oxidation co-catalyst to develop high-performance $BiVO_4$ photoanodes materials.

Apart from the aboved material design, a variety of characterization techniques such as UV-Vis absorption spectra, X-ray diffraction (XRD), X-ray photoelectron spectroscopy (XPS), scanning electron microscopy (SEM), and high-resolution transmission electron microscopy (HR-TEM) were employed to acquire sufficient information on the optical properties, elemental composition, crystal structures and morphology for all materials before and after reaction involved in the thesis. Besides, PEC performances are conducted by potentiostat in a typical 3-electrode system under a Xe lamp equipped with an AM 1.5G filter and O_2 production is directly recorded by the FireSting optical fiber O_2 sensor for the evaluation of OER performance. Parts of the corresponding studies have already been published in academic journals.

Kurzzusammenfassung

Um die globale Energiekrise und die Umweltprobleme zu lindern, die durch konventionelle fossile Brennstoffe verursacht werden, ist es wichtig, erneuerbare alternative Energiesysteme (z. B. Solar- und Windenergie) weiter zu entwickeln, um den wachsenden Energiebedarf der Menschheit zu decken. Seit den Pionierarbeiten zur Photoelektrokatalyse mit TiO_2 von Fujishima und Honda gilt die photoelektrochemische (PEC) Wasserspaltung als eine der vielversprechendsten Möglichkeiten, Sonnenenergie zu speichern, indem Wasser in H_2 und O_2 gespalten wird. Im Vergleich zur H_2-Entwicklungsreaktion (HER) ist die O_2-Entwicklungsreaktion (OER) aufgrund der komplizierten Übertragung von vier Elektronen und vier Protonen ein kinetischer Engpass für die gesamte Wasserspaltung. Darüber hinaus können während der Wasseroxidationsreaktion in einer hoch oxidierenden Umgebung einige andere mögliche Oxidationsreaktionen auftreten (z. B. Zersetzung der Katalysatoren). Daher ist eine der wichtigsten Aufgaben für die solare H_2-Produktion die Entwicklung effizienter und stabiler OER-Photoanoden zur Verbesserung der Umwandlungseffizienz der lichtgetriebenen Wasserspaltung.

Bismutvanadat ($BiVO_4$) gilt aufgrund seiner geeigneten Bandlücke, seiner niedrigen Valenzbandposition, seines Vorkommens auf der Erde, seiner Stabilität in wässriger Lösung und seiner geringen Kosten als eine der vielversprechendsten Photoanoden für die solare Wasserspaltung. Aufgrund der geringen Ladungsträgerbeweglichkeit, der schlechten elektrischen Leitfähigkeit und der langsamen Oberflächenreaktionskinetik liegt die Effizienz der Solarenergieumwandlung jedoch noch weit unter dem theoretischen Wert. Daher konzentriert sich die Forschung derzeit auf die Modifizierung der $BiVO_4$-Photoanodenmaterialien zur Verbesserung der PEC-Leistung. Ein Ansatz ist die Verwendung von Polyoxometallaten (POMs), einer einzigartigen Klasse molekularer Metalloxidcluster, die aus frühen Übergangsmetallen bestehen. Aufgrund ihrer einzigartigen Struktur und Reaktivität spielen POMs eine Schlüsselrolle im Zusammenhang mit Metalloxid-Lichtabsorbermaterialien in photoelektrokatalytischen Systemen sowohl in Bezug auf Photoanoden als auch Photokathoden.

Vor diesem Hintergrund fasst diese Arbeit Untersuchungen zu verschiedenen Modifizierungsstrategien für $BiVO_4$-Photoanoden zur photoelektrochemischen Wasserspaltung und den aktuellen Fortschritt bei $BiVO_4$-Photoanoden auf POM-Basis/abgeleiteter Basis zusammen. Nach einer Einführung werden die wichtigsten

Forschungsthemen dieser Arbeit in zwei Kapiteln vorgestellt, die auf die Entwicklung neuer und kostengünstiger $BiVO_4$-OER-Verbundwerkstoffe auf POM-Basis und innovativer Methoden zur Verbesserung der OER-Rate in Wasserspaltungskonfigurationen abzielen. So erhöht beispielsweise die Dotierung von $BiVO_4$ mit Molybdän- oder Kobaltpolyoxometallat (CoPOM = $Na_{10}[Co_4(H_2O)_2(PW_9O_{34})_2]$) die elektrische Leitfähigkeit bzw. die Ladungstrennungseffizienz. Gleichzeitig verbessert die Oberflächenmodifizierung mit dem CoPOM-Wasseroxidations-Kokatalysator die Lochextraktion und die Ladungsübertragungseffizienz, was insbesondere bei sehr niedrigen Überspannungspotentialen von Bedeutung ist, da es die nachteiligen Auswirkungen der Elektronenpolaronzustände durch die Dotierung teilweise kompensieren kann. Darüber hinaus werden auch mehrere innovative Methoden zur Herstellung von Elektrodenmaterialien entwickelt, wie etwa die „Double-Use“-Strategie für CoPOM, das sowohl als Massendotierungsmittel als auch als oberflächenabgelagerter Cokatalysator für die Wasseroxidation verwendet wird, um hochleistungsfähige $BiVO_4$-Photoanodenmaterialien zu entwickeln.

Neben dem oben genannten Materialdesign wurden verschiedene Charakterisierungstechniken wie UV-Vis-Absorptionsspektren, Röntgenbeugung (XRD), Röntgen-Photoelektronenspektroskopie (XPS), Rasterelektronenmikroskopie (SEM) und hochauflösende Transmissionselektronenmikroskopie (HR-TEM) eingesetzt, um ausreichende Informationen über die optischen Eigenschaften, die Elementzusammensetzung, die Kristallstrukturen und die Morphologie aller Materialien vor und nach der Reaktion zu erhalten, die in der Arbeit verwendet werden. Darüber hinaus werden PEC-Leistungen mit einem Potentiostat in einem typischen 3-Elektroden-System unter einer Xe-Lampe mit einem AM 1,5G-Filter durchgeführt, und die O_2-Produktion wird zur Bewertung der OER-Leistung direkt vom FireSting-Glasfaser-O_2-Sensor aufgezeichnet. Teile der entsprechenden Studien wurden bereits in wissenschaftlichen Zeitschriften veröffentlicht.

Table of Contents

List of Abbreviations

Abbreviations	**Full statement**
PEC	Photoelectrochemical
NRR	Nitrogen reduction reaction
NO_3RR	Nitrate reduction reaction
OER	Oxygen evolution reaction
HER	Hydrogen evolution reaction
STH	Solar-to-hydrogen
LSV	Linear sweep voltammetry
$*E_{Fn}$	*Quasi*-Fermi level of electrons
EIS	Electrochemical impedance spectroscopy
CA	Chronoamperometry
FE	Faradaic efficiency
SHE	Standard hydrogen electrode
RHE	Reversible hydrogen electrode
TWh	Terawatt hours
OCP	Open circuit (photo)potential
ABPE	Applied bias photoconversion efficiency
IPCE	Incident photon-to-current conversion efficiency
BS	Backside
FS	Frontside
η_{sep}	Photocharge separation efficiency
η_{tr}	Photohole transfer efficiency
LHE	Light harvesting efficiency
J_{max}/J_{abs}	Maximum achievable photocurrents/Complete conversion of absorbed photons to photocurrent
R_s	Uncompensated series resistance
R_{ct}	Charge transport and interfacial charge transfer resistance
e.g.	For example
et al.	And others
vs.	Versus
wt.%	Weight percent
POM	Polyoxometalate

$Co_4POM/CoPOM$	$[Co_4(H_2O)_2(PW_9O_{34})_2]^{10-}$
WOC	Water oxidation catalyst
SCL	Semiconductor–liquid junction
PL	Photoluminescence
FTO	Fluorine-doped tin oxide
PEI	Polyethyleneimine
XRD	X-ray diffraction
FT-IR	Fourier transform infrared spectroscopy
XPS	X-ray photoelectron spectroscopy
UV-Vis	Ultraviolet-visible spectroscopy
SEM	Scanning electron microscopy
FESEM	Field emission scanning electron microscopy
TEM	Transmission electron microscopy
HRTEM	High-resolution transmission electron microscopy
EDX	Energy-dispersive X-ray spectroscopy
ICP-AES	Inductively coupled plasma atomic emission spectrometry
CB	Conduction band
VB	Valence band
E_{app}	Applied bias potential
E_g	Bandgap
V_{ph}	Photovoltage
CN_x	Carbon nitride
$BiVO_4$	Bismuth vanadate
J-V	(Photo)Current density-potential
A	Surface area of the working electrode
rps	Revolutions per second
mM	Millimol per Liter
mA/cm^2	Milliampere per square centimeter
Q	Quantity of applied electricity
F	Faraday constant
λ	Irradiation wavelength
P	Light power density
$^oC/min$	Degree celsius per minute
kJ/mol	Kilojoule per mol

1. Introduction

The total world energy consumption in 2022 was 1.8×10^5 Terawatt hours (TWh), rising to 2.4×10^5 TWh in 2040, an averaging increase of 1% to 2% per year.[1,2] Fossil fuels currently supply us with 85% of our energy, with carbon dioxide (CO_2) emissions in the atmosphere rising from 278 ppm at the beginning of the industrial revolution to > 400 ppm today.[3] As the global industries are under intense pressure from energy scarcity and fossil fuel depletion, international energy deployment has set a goal of near net-zero emissions by 2050.[4] It is urgently needed to develop eco-friendly, clean, and green energy to deal with the energy crisis and environmental issues for modern society, which include solar, wind, hydropower, geothermal and biomass energy.[4–8] Many countries are taking action to produce renewable energy sources to reduce carbon emissions. For example, the European Union (EU) solar generation capacity keeps increasing and reached, according to SolarPower Europe, an estimated 259.99 GW in 2023.[9]

Although fossil fuels will remain for decades, a path to zero emissions is envisioned in Figure 1.[3] An increasing amount of clean renewable energy (such as solar- or wind-energy) is being converted into electricity and stored in batteries for industrial production and household applications such as lighting and power electric vehicles. Transmission and distribution of electricity is becoming more efficient thanks to breakthroughs in wide bandgap semiconductors and dielectric materials. As the cost of clean energy continues to plunge, new catalysts and photoelectrochemical devices will enable us to economically achieve electrocatalytic high-values chemical production, such as hydrogen (H_2) production by splitting water,[10–13] carbon monoxide (CO), methane, ethylene et al. by carbon dioxide reduction reaction (CO_2RR),[14,15] ammonia (NH_3) production by nitrogen reduction reaction (NRR)[16,17] or nitrate reduction reaction (NO_3RR) etc.[18,19] Moreover, other novel carbon-capture materials will decrease CO_2 from the industry generation, and ultimately the atmosphere. After recycling as much of the captured carbon as possible, advances in materials science will allow us to permanently sequester the rest of the carbon.[3]

As nature accomplishes by photosynthesis, harvesting sunlight into chemical bonds directly is a highly promising approach to lower the carbon footprint.[20] One example is using solar energy to split water into hydrogen and oxygen by semiconductors, from intermittent solar energy into an inherently more storable energy of chemical bonds,[21] where H_2 could subsequently be stored and transported to other energy conversion systems.[20] For example, combusting of H_2 produces water as the only harmless product with the help of oxygen (O_2),

releasing the stored energy. This can be able to accomplish an attractive carbon-free cycle between H_2 production and combustion. Since Fujishima and Honda's electrochemical photolysis of water by TiO_2,[22] photoelectrochemical (PEC) water splitting has been proved to be an elegant and environmentally benign pathway to produce H_2.

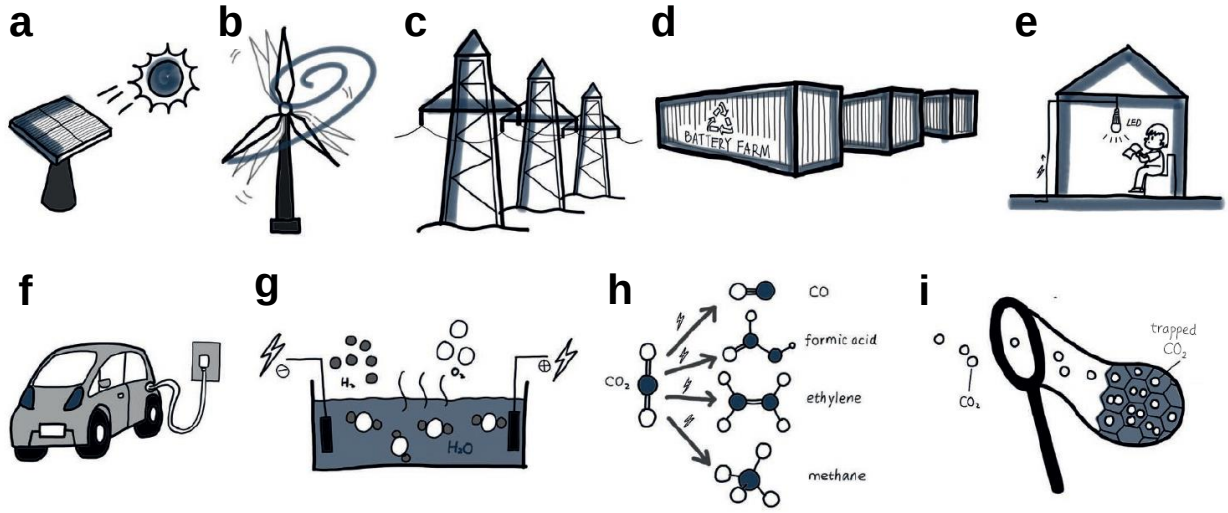

Figure 1: Renewable energy future. (a–i) advances in materials science and engineering are increasing the efficiency of electricity generation from clean renewable energy sources — for instance, (a) solar panels and (b) wind turbines— as well as electricity (c) distribution and (d) storage. Improved energy management in (e) buildings and (f) widespread diffusion of electric vehicles are decreasing our carbon footprint. Better catalysts and photoelectrochemical devices allow a more efficient generation of (g) hydrogen and oxygen, and (h) CO_2 conversion to fuels and chemicals. (i) Carbon-capture materials will decrease the amount of CO_2 released in the atmosphere.[3] Reprinted with permission from (*Nature Materials, 2017, 16, 16-22*). Copyright 2017, Springer Nature.

Overall splitting water into H_2 and O_2 depicted in the following two half-reactions under alkaline conditions, which are hydrogen evolution reaction (HER) and oxygen evolution reaction (OER).[23,24]

Alkaline HER:	$2H_2O + 2e^- \rightarrow H_2 + 2OH^-$	Reaction 1
Alkaline OER:	$4OH^- \rightarrow O_2 + 2H_2O + 4e^-$	Reaction 2
Overall reaction:	$2H_2O \rightarrow 2H_2 + O_2$, $\Delta G^\circ = 238$ kJ mol^{-1}	Reaction 3

Compared to the HER, which is a proton-coupled two-electron process, the OER is a typical kinetic bottleneck of overall water splitting since the mechanism of oxygen generation is much more complex, involving concerted transfer of four electrons and four protons. Therefore, one of the most important tasks for solar hydrogen production is the development of efficient and stable OER photoanodes for promoting the oxygen evolution reactivity and enhancing the solar energy conversion efficiency of PEC water splitting.[25]

Moreover, polyoxometalates (POMs) are a unique type of molecular metal oxide clusters that consist of early transition metals (e.g., Mo^{6+}, W^{6+}, V^{5+}) with high oxidation valences, which represent a tremendous range of crystalline inorganic clusters with an unmatched range of physical and chemical properties.[26,27] With continuous in-depth study, POMs is of great significance associated with conductive metal oxide materials in the various (photo)electrocatalytic systems in terms of (photo)anodes and (photo)cathodes.[28,29]

Based on this background, the work presented in this thesis deals with the design of innovative POMs-based/derived OER photoelectrodes for photoelectrochemical (photo-electrocatalytic) water splitting.

1.1. Photoelectrochemical (PEC) water splitting

1.1.1. Mechanism of PEC water splitting

Figure 2a shows a PEC cell in a 3-electrode system with an n-type semiconductor photoanode as working electrode, a metallic cathode as counter electrode and a reference electrode under an aqueous electrolyte. Taking the n-type semiconductor photoanode as an example, as shown in Figure 2b, when the photoanode film absorbs photons with energy equal to or greater than the bandgap energy (E_g) of the semiconductor, electrons are excited to the conduction band (CB) (photogenerated electrons), while leaving holes in the valence band (VB) (photogenerated holes). Because of band bending occurring at the semiconductor||electrolyte interface, holes migrate to the surface of photoanode and oxidize water to generate oxygen (Reaction 2) and electrons move to the surface of counter electrode through the external circuit, driven by an applied bias potential (E_{app}), and then reduce water to generate hydrogen (Reaction 1). This process leads to the overall water splitting reaction and produces hydrogen from water using solar light.[20,23,30,31]

Overall, there are three basic steps, i.e., the light absorption and charge separation, the charge transport from the bulk to the surface, and the surface reaction to evolve oxygen occurring at the surface of the photoanode. The objective of the PEC device is to produce the largest photocurrent (J_{ph}) with a minimum amount of applied bias. This could be achieved by maximizing light absorption (J_{abs}) by using a semiconductor with an appropriate E_g and minimizing the loss of charges due to bulk recombination (J_{br}) and surface recombination (J_{sr}) by proper modifications of the semiconductor.[23]

There is the experimental method to quantify J_{abs}, J_{ph}, J_{br} and J_{sr}, which provides an important basis to understand fundamental processes occurring on the photoelectrode.

Figure 2b shows the transfer and loss processes of photogenerated charges on a photoanode. The light absorption by a photocatalyst generates photocurrent (J_{abs}) that undergoes two major losses through bulk and surface recombination. Hence, the measured photocurrent by water oxidation (J_{H_2O}) is expressed by[23]

$$J_{H_2O} = J_{abs} \times \eta_{bulk} \times \eta_{surf} \qquad Equation\ 1$$

where η denotes the charge separation efficiency in the bulk of semiconductor (η_{bulk}) or on the surface (η_{surf}).

The photogenerated electron-hole recombination at the semiconductor||electrolyte interface can be neglected when the system is introduced readily oxidizable reducing agent such as H_2O_2 and Na_2SO_3.[23]

Water oxidation: $2H_2O + 4h^+ \rightarrow O_2 + 4H^+$, $E^\circ = 1.23$ V *vs.* RHE Reaction 4

H_2O_2 oxidation: $H_2O_2 + 2h^+ \rightarrow O_2 + 2H^+$, $E^\circ = 0.68$ V *vs.* RHE Reaction 5

Sulfite oxidation: $SO_3^{2-} + h^+ \rightarrow SO_3^-$, $E^\circ = 0.73$ V *vs.* RHE Reaction 6

Thus, hole transfer toward the sacrificial reagents is kinetically favorable at the semiconductor||electrolyte interface, which means that almost 100% photogenerated holes can be injected to their oxidation reaction ($\eta_{surf} = 100\%$). The charge bulk separation efficiency (η_{bulk}) is estimated by the equation:[23]

$$\eta_{bulk}(\%) = \frac{J_{Na_2SO_3}}{J_{abs}} \qquad Equation\ 2$$

where J_{abs} is the unit-converted photocurrent density obtained by integrating the UV–vis absorptance spectrum over the AM 1.5G solar spectrum according to the following formula:[32]

$$J_{abs} = \int N_{ph}(\lambda) \times LHE(\lambda) \times ed\lambda \qquad Equation\ 3$$

Where, $N_{ph}(\lambda)$ is the photon flux (unit: mW cm^{-2} nm^{-1}) and e is the electron charge (1.602×10^{-19} C). LHE is the light harvesting efficiency (defined as the ratio of absorbed light to incident light) is calculated from the UV-vis absorption spectrum according to the following formula:[33]

$$LHE = 1 - 10^{-A(\lambda)} \qquad Equation\ 4$$

where $A(\lambda)$ is the absorbance of the sample at wavelength λ.

The hole surface transfer efficiency (η_{surf}) was determined using the equation:[34]

$$\eta_{surf}(\%) = \frac{J_{H_2O}}{J_{Na_2SO_3}} \qquad Equation\ 5$$

where J_{H_2O} and $J_{Na_2SO_3}$ are the photocurrents measured in the absence and presence of an additional hole scavenger (Na_2SO_3).

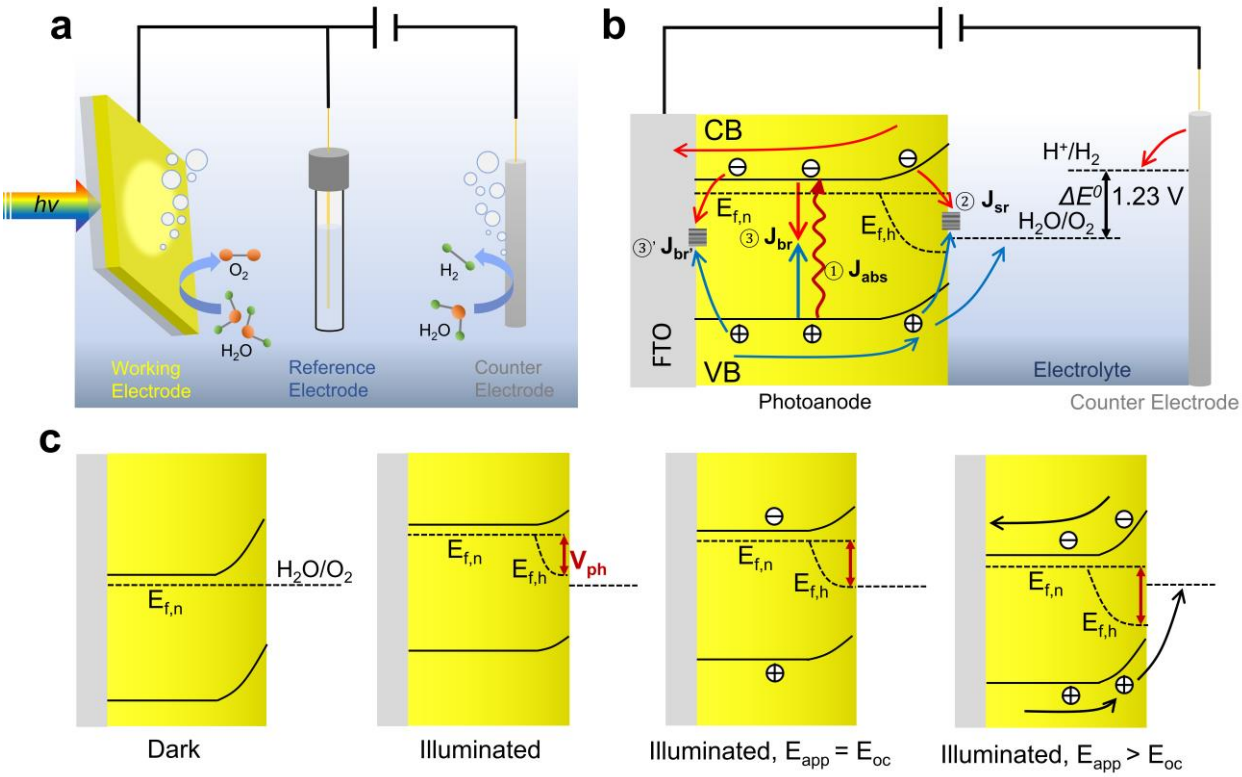

Figure 2: (a) Photoelectrochemical cell in three-electrode configuration. (b) Working principle showing charge transfer and loss processes (where, J_{abs} – current with maximum light absorption, J_{br} – bulk recombination, J_{sr} – surface recombination, $J_{br'}$ – interfacial recombination). (c) Formation of semiconductor||electrolyte junction for a photoanode in direct contact of electrolyte (redox was set for H_2O/O_2, 1.23 V *vs.* RHE): (i) Equilibrium state of Fermi level of n-type semiconductor ($E_{f,n}$) without illumination or bias; (ii) Illumination and formation of quasi-Fermi level ($E_{f,h}$). The gap between $E_{f,n}$ and $E_{f,h}$ is the photovoltage (V_{ph}); (iii) With applied bias (E_{app}) of the same as the potential needed for initial charge transfer (onset potential, E_{oc}); (iv) In the case of $E_{app} > E_{oc}$.

The formation of a semiconductor||electrolyte junction, also well known as a semiconductor–liquid (SCL) junction, is the key phenomenon of a PEC cell composed of photoelectrodes. As depicted in Figure 2c, illumination provides a photovoltage ($V_{ph} = E_{f,n} - E_{f,h}$) from the generation of charge carriers by the photoexcitation. Often, V_{ph} alone is not large enough to drive the charge transfer, and then applied bias (E_{app}) adds up and provides enough driving force, when E_{app} is larger than the onset potential (E_{oc}).[23]

1.1.2. Photoelectrode requirements

Theoretically, a semiconductor can split water if its E_g is greater than 1.23 eV (water dissociation energy) and its CB and VB edge energy levels are more negative and more positive

than the water reduction (0.0 V *vs.* RHE) and oxidation (1.23 V *vs*. RHE) potentials, respectively.[30] In reality, thermodynamic losses of 0.3 – 0.4 eV and the existence of an overpotential to ensure sufficiently fast reaction kinetics (0.4 – 0.6 eV) must also be considered. As a result, the band gap should be at least 1.9 eV, which corresponds to the absorption onset at 650 nm. Below 400 nm the intensity of sunlight drops rapidly, imposing an upper limit of 3.1 eV on the bandgap. Therefore, the optimum value of the bandgap should be somewhere between 1.9 and 3.1 eV, which is within the visible range of the solar spectrum.[30,35]

The E_g and the band edge of VB and CB only determine whether the semiconductor can be able to perform photoelectrochemical water splitting from a thermodynamic perspective. In addition, the ideal photoelectrode fulfills several tasks at once: good light absorption, efficient charge separation and transport, low overpotentials for H_2 or O_2 evolution at its surface. Moreover, the photoelectrode must stand the tests of harsh environmental conditions such as water, salts, and strong sunlight and have the potential to be made at low cost.[30] To date, no earth-abundant material fulfills all these requirements. One solution to this is to use two semiconductors for HER and OER, respectively. Water reduction (Reaction 1) occurs on photocathodes while water oxidation (Reaction 2) on photoanodes. This tandem configuration not only takes sufficient use of the incident sunlight but also combines photovoltage generated from two electrodes.[20,36] Compared to HER, OER half-reaction is regarded as the bottleneck for water splitting because the generation of one oxygen molecule involves four electrons, determining the reaction rate.[23,25] Therefore, the development of efficient and stable OER photoanodes plays a critical role to enhance the solar energy conversion efficiency of PEC water splitting.

1.2. $BiVO_4$-based photoanodes for PEC water splitting

1.2.1. $BiVO_4$ as a photoanode material

To date, numerous n-type porous semiconductors have been explored as photoanodes for PEC water oxidation, including TiO_2,[37–39] Fe_2O_3,[20,40] WO_3,[41,42] $BiVO_4$,[23,31,43,44] Ta_3N_5,[45,46] Bi_2WO_6,[47] etc. Among these semiconductors, Bi-based mixed-oxide semiconductors have become the hot research materials because of their special band structures. The valence band (VB) potential is shifted negatively to decrease the bandgap when hybrid orbitals of O-2p and Bi-6s are formed due to repulsion of the two orbitals. As a sample of $BiVO_4$ in Figure 3a, CB is made of V 3d, while VB is composed of hybrid orbitals of O-2p and Bi-6s, reducing the bandgap value. However, in conventional simple oxide semiconductors,

the valence band primarily consists of O-2p orbitals when the metal d orbital is unoccupied, which results in a need for an external bias for the photoelectrode as the conduction band shifts positively (as samples of TiO_2 and WO_3 in Figure 3a).[30]

Among Bi-based mixed-oxide semiconductors, bismuth vanadate ($BiVO_4$) stands out for its multifold features such as earth-abundance, low valence band position, appropriate bandgap, and high stability in aqueous solution.[48–50] Monoclinic scheelite $BiVO_4$ has a strong yellow color and is often used as a pigment for strong reflection.[51] As shown in Figure 3b, the scheelite structure contains a V ion coordinated by four O atoms in a tetrahedral site and a Bi ion coordinated by eight O atoms in a dodecahedron polymorphs, which has a high asymmetry of crystal structure with different Bi–O and V–O distances. Thus, $BiVO_4$ also has a very high anisotropic electronic structure (polarized) owing to the great degree of asymmetry of VO_4 and BiO_8.[23,31] $BiVO_4$ possesses a bandgap of around 2.4 eV, corresponds to 516 nm wavelength of light, absorbing up to ~ 30% of the solar radiation, resulting in a theoretical photocurrent density of 7.5 mA cm^{-2} corresponding to the solar-to-hydrogen (STH) efficiency of 9.2%.[31,52,53]

As an n-type photocatalyst, the efficient hole transfer plays a key role for photoanodic water oxidation. Similar to the case of Fe_2O_3,[20,54] the charge carrier transfer in $BiVO_4$ is governed by a polaron hopping conduction mechanism occurring rapidly at a time scale of ≈ ps,[55] in which a detailed study shows that electrons and holes are heavily bound to those intragap polaron levels with characteristic potentials located ≈0.88 eV below the conduction band minimum (CBM, edge of CB) and ≈0.11 eV above the valence band maximum (VBM, edge of VB). They can effectively trap electrons and holes, limit their mobility and suggest that electron–hole recombination through polaronic states could hamper the evolution of the water splitting reaction.[54] This accounts for the relatively sluggish electron mobility of $BiVO_4$ of 0.02–0.044 $cm^2\ V^{-1}\ s^{-1}$ (polycrystalline) to ≈12 $cm^2\ V^{-1}\ s^{-1}$ (single crystalline), which is significantly lower than those of WO_3 (10 $cm^2\ V^{-1}\ s^{-1}$). Its hole mobility (≈2 $cm^2\ V^{-1}\ s^{-1}$) is higher than that of Fe_2O_3 (0.0001 $cm^2\ V^{-1}\ s^{-1}$).[23]

Despite the low mobility, high quantum efficiencies can nevertheless be achieved in $BiVO_4$ due to the long lifetime of the photogenerated charge carriers (~40 ns), which leads to relatively long carrier diffusion lengths defined as the average distance that an excited carrier will travel before recombining, as shown in Figure 3c.[56] The minority carrier diffusion length, L_D, or the carrier lifetime, τ_R, often express the susceptibility to recombination. They are related through[30]

$$L_D \simeq \sqrt{D\tau_R} \qquad Equation\ 6$$

where the diffusivity of the free carriers, D, is related to their mobility, μ, via the Nernst–Einstein equation:[30]

$$D = \frac{kT\mu}{e} \qquad Equation\ 7$$

Where k is the Boltzmann constant, T is the temperature, and e is the charge of an electron. Values of L_D range from several nanometers to several hundred nanometers in some oxides. Table 1 summarizes the carrier diffusion length, lifetimes and mobilities of promising photoelectrode materials. The hole diffusion length (L_D) of $BiVO_4$ was calculated as 70 nm, which is relatively longer than that of Fe_2O_3 (2 – 4 nm) but shorter than that of WO_3 (150 – 500 nm).[56]

Table 1: Comparison of carrier mobility, lifetime, and diffusion length of several promising metal oxides.[56]

Photoelectrode materials	Carrier mobility μ ($cm^2\ V^{-1}\ s^{-1}$)	Carrier lifetime τ_R	Carrier diffusion length L_D (nm)
Fe_2O_3	0.5	3 ps	2 – 4
WO_3	10	1 – 9 ns	150 – 500
$BiVO_4$	0.044	40 ns	70

$BiVO_4$ is inherently stable without itself getting oxidized during water oxidation. However, $BiVO_4$ is generally not highly stable in electrolytes, especially in phosphate (PO_4^{3-}, HPO_4^{2-}, and $H_2PO_4^-$), and tends to be more stable in bicarbonate (HCO_3^{2-}) and especially borate (BO_3^{2-}).[23] The Pourbaix diagram for $BiVO_4$ was recently reported by Toma et al. As shown in Figure 3d, $BiVO_4$ is stable in a large region with pH values from 1 to 11 and at the electrochemical potentials within the water stability region. Unfortunately, $BiVO_4$ is no longer thermodynamically stable at potentials close to the oxygen evolution potential, whose constituent is expected to dissolve as VO_4^- ions and Bi oxyhydroxides.[57] From a thermodynamic perspective, it is expected that the $BiVO_4$ would self-passivate via formation of a chemically stable bismuth oxide at its surface. Sayama et al reported that the $BiVO_4$ dissolved V atoms from the surface during the photoreaction and formatted a thin Bi-rich layer (BiO_x layer), which may help prevent further erosion of $BiVO_4$.[58]

Therefore, a rapid development is obvious that $BiVO_4$ has become one of the most promising materials for a metal oxide–based photoanode in the field of PEC water splitting.

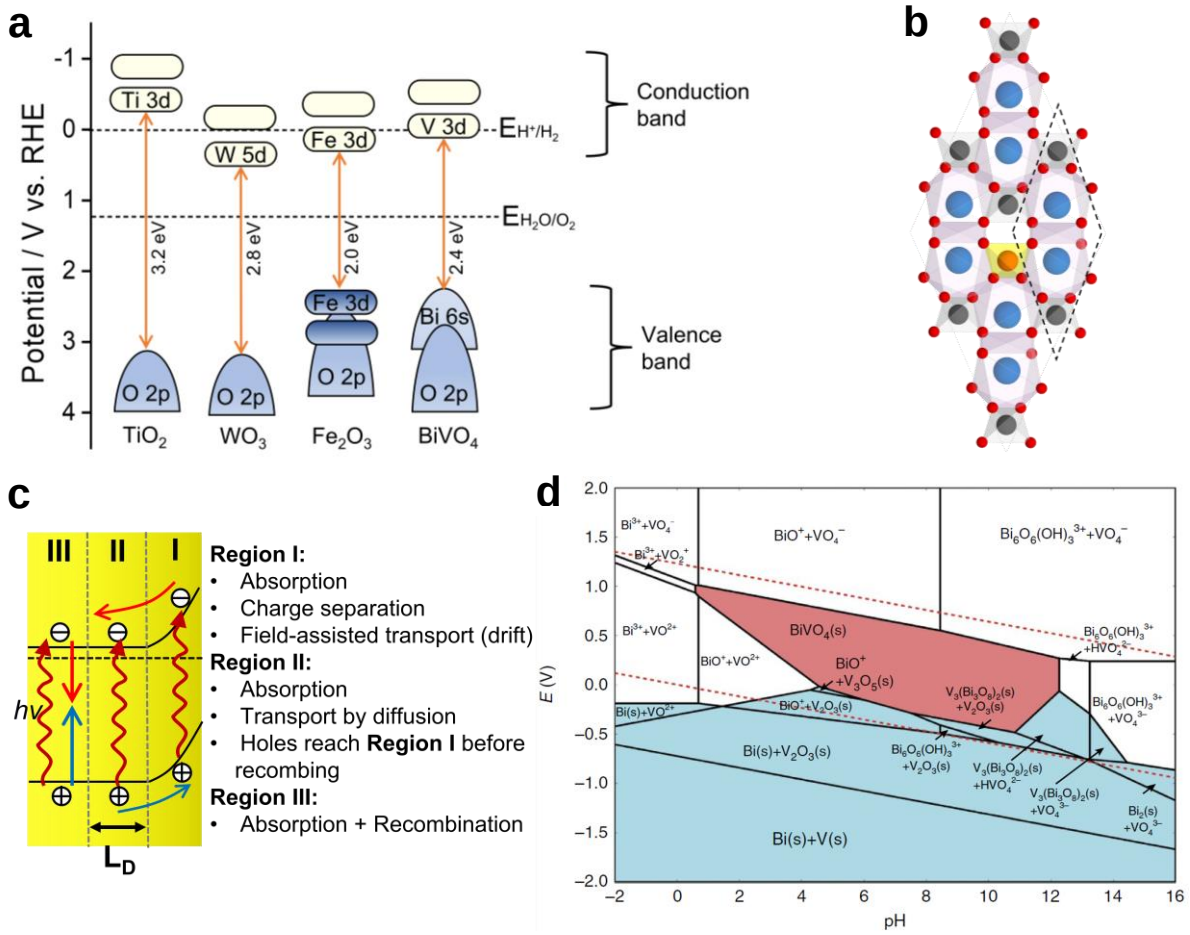

Figure 3: (a) Band structure of TiO_2, WO_3, Fe_2O_3 and $BiVO_4$. (b) Crystal structure of monoclinic scheelite Mo-doped $BiVO_4$ (Red balls: O; dark green balls: V; bule balls: Bi; orange ball: Mo). (c) Absorption regions in a semiconducting photoanode. (d) Pourbaix diagram of the 50:50 Bi:V system in an aqueous solution, assuming Bi and V concentrations of 10^{-5} mol kg^{-1}. Upper red dashed line: potential for OER; lower red dashed line: potential for HER. Cyan regions: stable solid compounds; pink region: $BiVO_4$ (s); white regions: ions dissolved in aqueous solution.[57] Reproduced with permission (*Nat. Commun., 2016, 7, 12012*). Copyright 2016, Springer Nature.

However, up to now, the STH efficiency for $BiVO_4$ photoanode is still far below its theoretical efficiency. This discrepancy in performance arises due to the rapid recombination of photogenerated charge carriers at $BiVO_4$ surface (J_{sr}) and bulk (J_{br}) as well as $BiVO_4$/substrate interface ($J_{br'}$) (Figure 2b). First, charge recombination at $BiVO_4$ surface readily happens at surface trapping states (defect states), trapping free electrons from the bulk due to -OH surface termination from the water dissociatively adsorbed at its surface.[30] This leads to poor surface reaction kinetics and thereby the low onset potential in $BiVO_4$ (typically ≈ 0.6 V vs. RHE).[59] Second, the sluggish carrier mobility (high resistivity) confirms that the bulk electronic conductivity in $BiVO_4$ is the main limiting factor.[56,60] Therefore, photogenerated electrons and holes recombine before they reach the substrate or the surface to

decrease the charge bulk separation efficiency. Third, the charge recombination at the $BiVO_4$/substrate occurs due to interfacial defect states as a result of lattice mismatching between $BiVO_4$ and substrates.[61] The above aspects, involving surface, bulk, and interface properties directly impact the PEC performance of $BiVO_4$ photoanodes.

To address the above-mentioned problems in $BiVO_4$ photoelectrodes, and to increase its overall PEC performance, commonly used methods include: (1) surface modification (surface state passivation and loading of co-catalysts, etc.); (2) bulk modification (element doping, construction of heterojunctions and nanostructure design, etc.); and (3) optimization of the interface between $BiVO_4$ and the substrate.

1.2.2. Surface modification strategies

Compared with the rapid generation of photogenerated electron-hole pairs in the semiconductor, the poor surface charge transfer at the semiconductor||electrolyte interface usually progress on a considerably longer scale (from nanoseconds to microseconds).[62] The severe surface charge recombination and slow surface reaction kinetics greatly restricts the PEC performance of $BiVO_4$. The cocatalysts deposition on $BiVO_4$ photoanodes has been extensively studied as an effective strategy to promote charge separation, suppress surface charge carrier recombination, reduce the overpotential and accelerate the surface water oxidation kinetics of $BiVO_4$.[63,64] In this section, we focus on the surface functionalization of $BiVO_4$ via different surface-deposited materials as cocatalysts or passivation layer.

IrO_x and RuO_x are well-known electrochemical oxygen evolution catalysts, but their efficiency as cocatalysts on $BiVO_4$ is very low due to the relative poor capability of the hole injection into the OER of water, compared with cobalt (oxy)hydroxide phosphate (Co–Pi) or FeOOH.[65,66] Co–Pi,[67–71] CoO_x,[72,73] $FeCoO_x$,[74] CoOOH[75,76] etc cobalt-based co-catalysts are widely reported. Bi group demonstrated that the plasma-exfoliation of CoOOH nanolayers ($\approx$8 nm) into an ultrathin structure ($\approx$2 nm) could significantly improve the PEC activities of $BiVO_4$ photoanodes due to the enhanced charge separation and increased surface active sites. [76] Co–Pi was first reported by Kanan and Nocera,[77] and later Co–Pi was introduced onto $BiVO_4$ by electrodeposition or photo-assisted electrodeposition.[71,78] The Gamelin group reported quantitative analysis of the charge transfer efficiency owing to cocatalysts, demonstrating that Co–Pi modification on W:$BiVO_4$ increased the photocurrents, yielded a cathodic onset potential shift of $\sim$0.44 V (Figure 4a), and achieved a near-complete suppression of surface recombination in PEC water splitting (energy diagram in Figure 4b).[78] A detailed study by the

Durrant group reported that the kinetics of hole transfer from the $BiVO_4$ to the Co–Pi layer are more sluggish than the direct water oxidation from $BiVO_4$. The performance enhanced by Co–Pi deposition due its ability to suppress electron/hole recombination within the $BiVO_4$ photoanode.[79] This was further proven by the Krol group by using intensity modulated photocurrent spectroscopy (IMPS), as shown in Figure 4c to determine that the main role of CoPi is to suppress surface charge carrier recombination as it passivates the surface states of $BiVO_4$.[80] However, the long-term stability remains an issue for Co–Pi cocatalyst due to the dissolution of Co–Pi in a phosphate buffer solution.[81] Co-borate (CoBi) onto $BiVO_4$ photoanode also has the same problem of stability, although the onset potential is negatively shifted and the photocurrent are significantly improved.[82] An iron-cobalt oxide ($FeCoO_x$) as an efficient co-catalyst was beneficial to achieve a significantly higher stability of over 10 h than that by CoO_x, as shown in Figure 4d.[74]

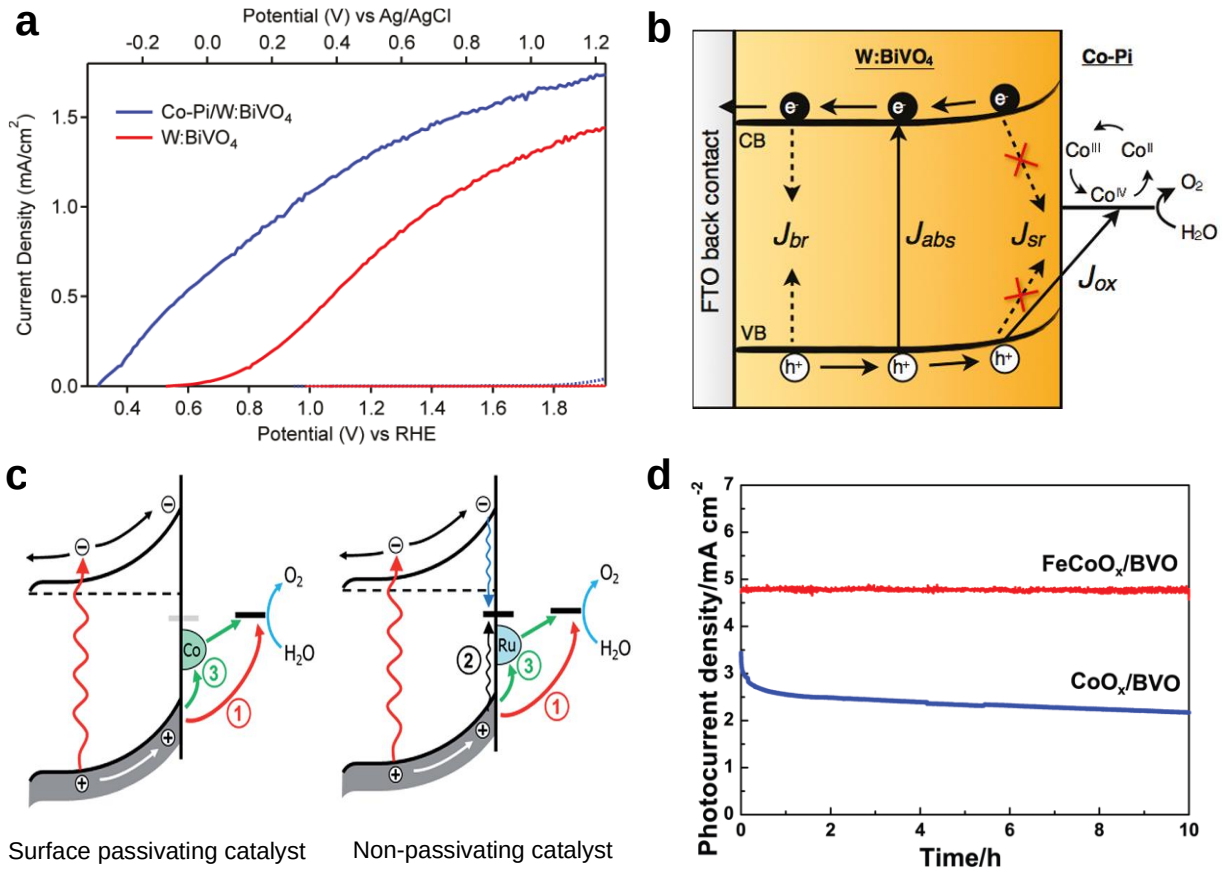

Figure 4: (a) Photocurrent density vs. applied potential (J-V) curves, and (b) energy diagram showing the kinetic processes for Co-Pi/W:$BiVO_4$ photoanodes.[78] Reprinted with permission from (*J. Am. Chem. Soc., 2011, 133, 18370–18377*). Copyright 2011, American Chemical Society. (c) Simplified model of the elementary processes in a $BiVO_4$ photoanode.[80] Reprinted with permission from (*Chem. Sci., 2017, 8, 3712–3719*). Copyright 2017, the Royal Society of Chemistry. (d) Stability curves of the $FeCoO_x/BiVO_4$ and $CoO_x/BiVO_4$ photoanodes at 1.23 V vs. RHE.[74] Reprinted with permission from (*Adv. Funct. Mater., 2018, 28, 1802685*). Copyright 2018, Wiley-VCH GmbH.

In addition to cobalt-based co-catalysts, there are also other co-catalysts widely used in PEC water splitting, such as transition metal hydroxyl oxides. FeOOH[83] and plasma etched-NiOOH,[84] respectively, on the $BiVO_4$ surface as an oxygen evolution catalyst significantly improved photocurrent and long-term photostability for solar water splitting. The dual-layer NiOOH/FeOOH for nanoporous $BiVO_4$ photoanodes also maintain an excellent long-term stability of 48 h, as shown in Figure 5a and 5b. The resulting $BiVO_4$/FeOOH/NiOOH photoanode achieves a photocurrent density of 2.73 mA cm^{-2} at a potential as low as 0.6 V vs. RHE. An electron-hole separation efficiency of 0.90 at 1.23 V vs. RHE can be achieved. It turned out that FeOOH had a good interaction with $BiVO_4$, while NiOOH had better water oxidation kinetics, thus, their combination provided synergistic effects of both activity and stability.[85]

Transition metal oxides or sulfides have been reported in $BiVO_4$ photoanodes system. The Bi group reported that N- incorporation $NiFeO_x$ catalysts significantly enhanced the oxygen evolution activity and stability of $BiVO_4$ photoanodes. The excellent PEC performance can be attributed to the relatively low electronegativity of N atoms incorporated into the $NiFeO_x$ catalysts to partial substitute O sites, which promotes electron enrichment at the Fe and Ni sites. Furthermore, the electron-enriched Ni sites would donate electrons to V sites of $BiVO_4$ for restraining V^{5+} dissolution and improving the PEC stability, while the Fe sites could effectively attract holes for promoting the oxygen-evolution activity.[86] The Huang group reported a vanadium oxide (VO_x) OEC with enriched oxygen vacancies on $BiVO_4$ photoanodes obtained by a simple photo-assisted electrodeposition process, which exhibits an excellent photocurrent density of 6.29 mA cm^{-2} at 1.23 V vs. RHE under AM 1.5 G illumination (Figure 5c) and achieves a high charge surface separation efficiency of 96% at 1.23 V vs. RHE. Specifically, the photogenerated holes are transferred to the surfaces of the $BiVO_4$ particles to oxidize V^{4+} ions in the VF_4 aqueous solution for generating oxygen vacancies in VO_x. The presence of oxygen vacancies in VO_x that forms undercoordinated sites could strengthen the adsorption of water molecules onto the active sites and promote charge transfer during the oxygen evolution reaction.[87] The Zhou group reported that a cobalt/nickel- based sulfide ($NiCo_2S_4$) cocatalyst on $BiVO_4$ photoanode increased photocurrent density and caused negative shift of onset potential, achieving a surface hole injection yield of nearly 99%. The kinetic data based on IMPS show that $NiCo_2S_4$ decreases surface charge recombination rate, which reveals that $NiCo_2S_4$ serves as a passivation layer to suppress recombination at surface states and consequently enhance surface water oxidation kinetics (Figure 5d).[88] However, it

is known that transition metal sulfides are thermodynamically unstable under OER conditions, which tend to be oxidized to their corresponding metal oxides/(oxy)hydroxides, especially in the strong alkaline environment, but still be activated in OER reaction.[89] Other surface state passivation species of $BiVO_4$ includes NiO_x,[90] Al_2O_3,[91] TiO_2[92] etc.

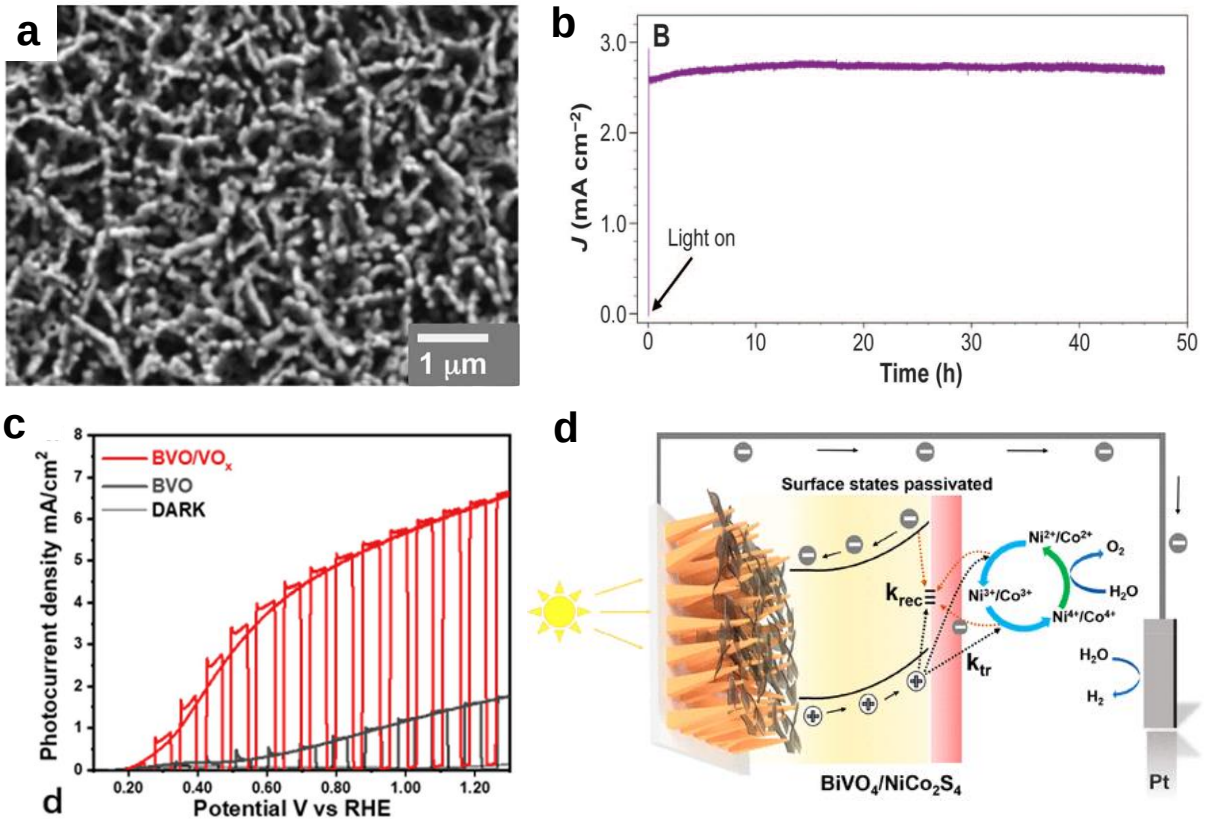

Figure 5: (a) SEM images of nanoporous $BiVO_4$, and (b) J-t curve for $BiVO_4$/FeOOH/NiOOH photoanode measured at 0.6 V vs. counter electrode.[85] Reprinted with permission from (*Science, 2014, 343, 990-994*). Copyright 2014, Science. (c) J-V curves of the $BiVO_4$ and $BiVO_4/VO_x$ photoanodes.[87] Reprinted with permission from (*Angew. Chem., 2023, 135, e202217346*). Copyright 2023, Wiley-VCH GmbH. (d) Possible surface water oxidation kinetics mechanism of $BiVO_4/NiCo_2S_4$.[88] Reprinted with permission from (*ACS Appl. Energy Mater., 2020, 3, 9089−9097*). Copyright 2020, American Chemical Society.

1.2.3. Bulk modification strategies

As a n-type semiconductor, a good hole conductivity of $BiVO_4$ is critical for the hole transfer during photoanodic water oxidation.[59,67,69,70] The extremely slow hole mobility (~2 $cm^2\ V^{-1}\ s^{-1}$) and extremely sluggish electron mobility (0.02–0.044 $cm^2\ V^{-1}\ s^{-1}$) will lead to serious photogenerated carrier bulk recombination in the $BiVO_4$, severely limiting the PEC performance.[23,56] Therefore, the bulk modification strategies, including morphology, doping,

defect engineering and heterojunction, are of great significance for enhanced PEC water splitting.[23,31]

Morphology engineering plays a vital role in increasing the efficiency of PEC. Nanostructured $BiVO_4$ films, such as nano shuttle,[93] nanotubes,[94] nanorods,[95] nanoflake,[96] and nanoworm,[97] assist the carrier diffusion length (shortening the distance for the carriers to travel to reach the surface of $BiVO_4$) and have an optical effect (increased light absorption efficiency) and high active surface area, effectively boosting the PEC performance. The ground-breaking work by the Zhou group designed 3D inverse opal type architecture of Mo:$BiVO_4$ onto FTO substrate (Figure 6a) via template-assisted filtration method, showing 1.5-fold increment in the photocurrent density (Figure 6b). The superior enhancement of the PEC performance was attributed to the surface morphology engineering in the form of an inverse opal architecture that facilitates the interconnected and well-directed paths for charge transport through photoanode.[98] The Lee group demonstrated a 3D periodic, micropillar-structured FTO (FTO-MP) deposited with $BiVO_4$ in Figure 6c, and exhibited excellent photocurrent densities of 2.97 mA cm^{-2} at 1.23 V vs. RHE (Figure 6d), which are significantly enhanced than that of flat $BiVO_4$. The main reason for this enhanced PEC performance is the increased light absorption efficiency by light scattering of the 3D periodic structure and enlarged surface area.[99] However, it can not always have positive effects on charge separation and transport by increasing surface area as it can result in the increase in surface states, defect sites and grain boundaries while decreasing crystallinity.[59] Therefore, the morphologies and surface areas of a photoelectrode should be finely optimized to the overall positive effect.

Doping engineering is an effective strategy to increase the n-type conductivity and charge separation/transfer efficiencies of $BiVO_4$ due to poor electron transfer.[23] The Selli group reported that Mo doping enhanced the bulk electron conductivity of $BiVO_4$ and the passivation of its trap surface states.[100] The Andreu group reported that W-doped $BiVO_4$ shows the a higher donor density and a higher concentration of surface states that can act as reaction sites, thus leading to improvements of both conductivity and surface catalytic activity.[101] The Xv group reported that cobalt ion-doped $BiVO_4$ photoanode exhibited an improved PEC performance due to a part of Co ions being incorporated into the $BiVO_4$ lattice, enhancing electronic conductivity, whereby excess Co ions formed a Co_3O_4 co-catalyst on the surface (Figure 7a).[102] The Lee group tried the doping of Mo, W, Ti, Cr, Fe, Zn, Nb, Ru, Pt, Sn, Ce, and Ta into the V sites of $BiVO_4$, and observed a drastic improvement in the visible-light-induced water oxidation activity only with W or Mo doping, while Mo doping showed a

more pronounced promoting effect than that of W doping (Figure 7b). Electrochemical impedance spectroscopy (EIS) and Mott–Schottky (MS) analysis indicated a reduced charge-transfer resistance and a higher carrier concentration for W- or Mo-doped $BiVO_4$ relative to undoped $BiVO_4$. Electronic structure calculations revealed that both W and Mo act as shallow donors, with Mo forming a hybrid band with V, resulting in a density of states (DOS) twice as high as that of W (Figure 7c). The effective hybridization of $Mo^{6+} \leftrightarrow V^{5+}$ reflects the higher donor capacity of Mo compared to W.[103]

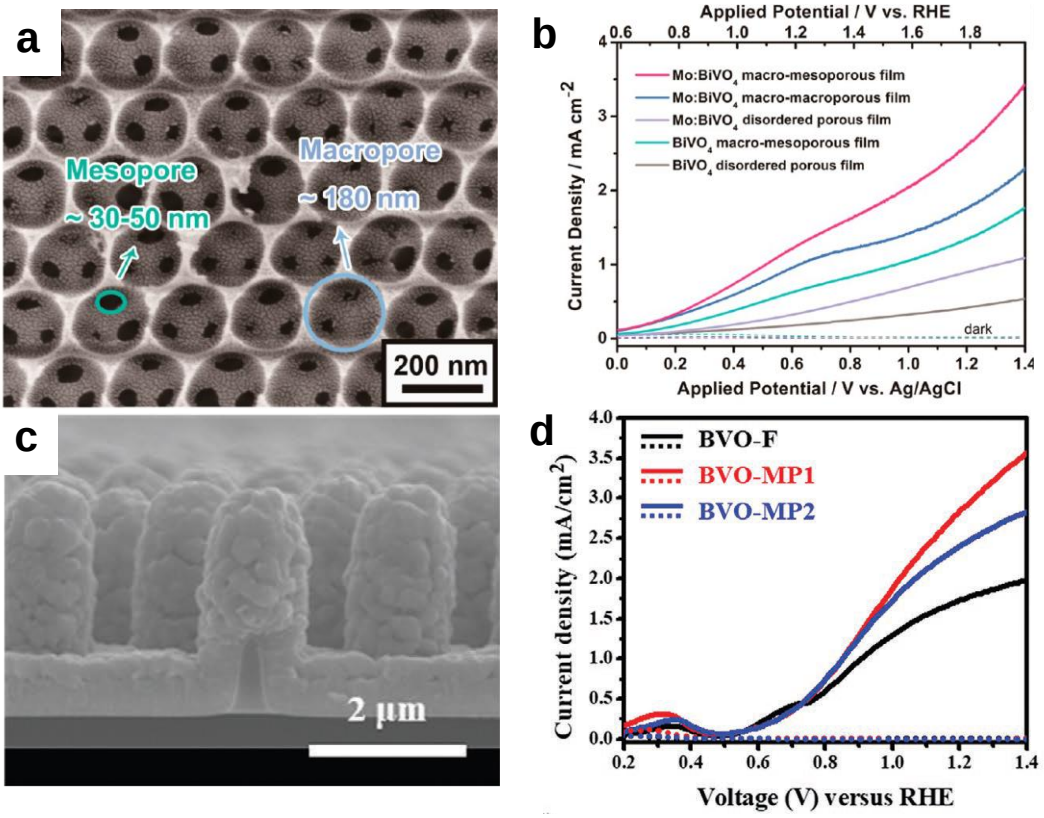

Figure 6: (a) SEM image of macroporous Mo:$BiVO_4$ onto 3D inverse opal structure, and (b) J–V curves of different photoelectrodes in sodium sulfate electrolyte.[98] Reproduced with permission from (*ACS Nano, 2014, 8,7088–7098*). Copyright 2014, American Chemical Society. (c) SEM images of BVO-MP1 (micropillar-patterned $BiVO_4$: height of 1.9 μm, diameter of 500 nm, and period of 2.0 μm), and (d) J–V measurements BVO-F (flat $BiVO_4$), BVO-MP1, and BVO-MP2 (micropillar-patterned $BiVO_4$: height of 1.9 μm, diameter of 500 nm, and period of 4.0 μm) conducted in a 0.5 m phosphate buffer solution (pH 7.1) under AM 1.5G illumination (dashed line is under dark condition).[99] Reproduced with permission from (*Small, 2021, 17, 2006558*). Copyright 2021, Wiley-VCH GmbH.

Multiple transition metal ions doping in $BiVO_4$ is also an effective process to improve conductivity of $BiVO_4$ and promote PEC performance. The Mullins group developed the Mo and W co-doped $BiVO_4$ nanoflake array films to increase conductivity of $BiVO_4$ or to slightly enhance water oxidation kinetics.[96] The Huang group fabricated Mo and Co co-doped $BiVO_4$

films (Mo:$BiVO_4$/Co:$BiVO_4$) by depositing Co:$BiVO_4$ layer on the top of Mo:$BiVO_4$ layer, and demonstrated the enhanced PEC performances. Co:$BiVO_4$ layers were found to be important for the enhanced charge separation efficiencies, which can not only act as reactive sites for water oxidation to promote the interfacial charge separation (surface exposed Co^{2+} ions), but also be able to tune the built in electric fields due to shifting in Fermi energy levels via doping and optimize the charge transfer in Co:$BiVO_4$ layers to improve the bulk charge separation (Co^{2+}doping inside) in Mo:$BiVO_4$/Co:$BiVO_4$ photoanodes.[104] Specially, the Krol group introduced a gradient-doped W:$BiVO_4$ film, creating a distributed n^+–n homojunction for enhancing charge separation throughout the bulk of the material. By combining cobalt phosphate water-oxidation catalyst, the AM 1.5 photocurrent improves to ~3.6 $mAcm^{-2}$ at 1.23V vs. RHE, representing a ~60% improvement over the same electrode with a homogeneous W-dopant concentration.[105]

In addition, non-metal elements doping has also been widely reported. The Abdi group incorporated sulfur in $BiVO_4$ thin films, which decreases the bandgap of ∼0.3 eV by the upward shifting of the valence band maximum (VBM), increasing the theoretical maximum STH efficiency from 9 to 12%. Time-resolved microwave conductivity measurements reveal a ∼3 times higher charge carrier mobility compared to unmodified $BiVO_4$, resulting in a ∼70% increase in the carrier diffusion length (Figure 7d).[106] The Lee group investigated phosphate doping into $BiVO_4$, replacing some of the VO_4^{3-} oxoanions with PO_4^{3-} oxoanions, and the best photocurrent density of 0.5% PO_4-doped $BiVO_4$ is about 30 times higher than that of pristine $BiVO_4$, which revealed that PO_4^{3-} oxoanion doping lowered the charge transfer resistance and increased charge carriers of $BiVO_4$.[107]

Another powerful doping strategy into $BiVO_4$ lattice is to create oxygen vacancies by electrochemical reduction,[108] hydrogen gas treatment,[109] photocharging,[110] and N_2 treatment.[111] The Wang group demonstrate that the cocatalyst-free $BiVO_4$ photoanode exhibited a record photocurrent of 4.60 mA cm^{-2} at 1.23 V vs. RHE with an outstanding onset potential of 0.23 V *vs.* RHE. The increased oxygen vacancies and the passivated surface states at the $BiVO_4$/electrolyte interface as a result of potentiostatic photopolarization are suggested to boost the charge transport and reduce the surface recombination, further inhibiting photo-corrosion.[108] The Choi group show that annealing nanoporous $BiVO_4$ under nitrogen flow can result in nitrogen doping and generation of oxygen vacancies, which not only effectively reduces the bandgap by ~0.2 eV but also increases the majority carrier density and mobility, enhancing electron–hole separation.[111]

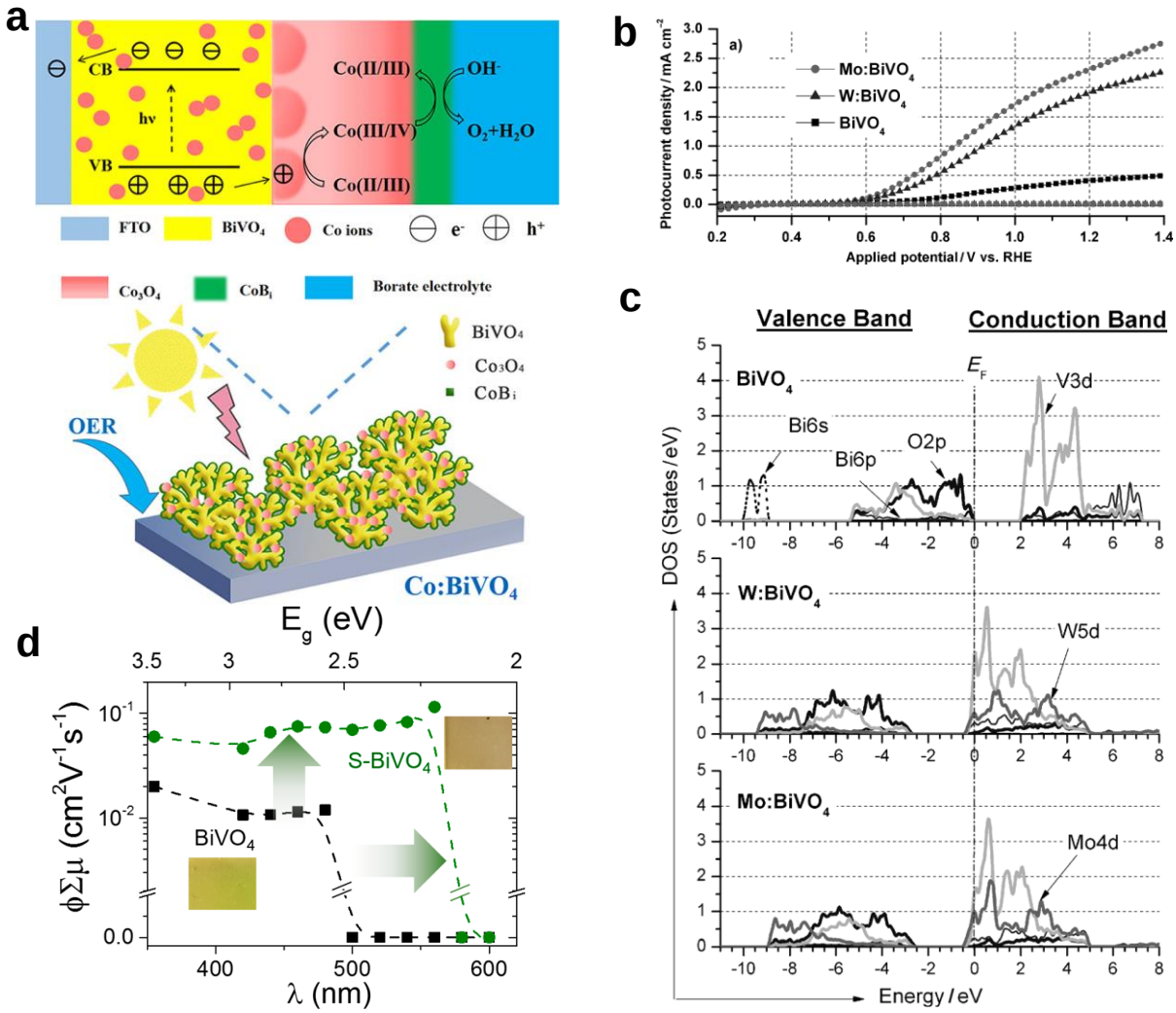

Figure 7: (a) Schematic diagram of the mechanism for Co doping improving the PEC water oxidation of $BiVO_4$.[102] Reproduced with permission from (*ACS Appl. Energy Mater. 2022, 5, 6313−6323*). Copyright 2022, American Chemical Society. (b) J–V curves, and (c) DOS plots of pure $BiVO_4$ and W- or Mo-doped $BiVO_4$.[103] Reproduced with permission from (*ChemSusChem, 2012, 5, 1926– 1934*). Copyright 2012, Wiley-VCH GmbH. (d) Photoconductivity action spectroscopy (PCAS), i.e., charge carrier mobility ($\phi\Sigma\mu max$) vs. wavelength, of $BiVO_4$ and S-treated $BiVO_4$ films.[106] Reproduced with permission from (*Chem. Mater., 2018, 30, 8630−8638*). Copyright 2018, American Chemical Society.

Constructing a heterostructure with two or more semiconductors via surface/interface engineering has been considered as an effective way for efficient charge separation/transfer efficiency to improve the PEC performance of a photoelectrode. There exist two kinds of heterojunctions: staggered junction and Z-scheme junction (Figure 8). In a typical staggered band alignment (Figure 8a), both CB and VB positions of semiconductor 2 (sem 2) are slightly higher than that of semiconductor 1 (sem 1). After band bending, a built-in field is formed that drives the photogenerated electrons from sem 2 to sem 1, and photogenerated holes from sem

1 to sem 2, leading to a spatial separation of the electrons and holes on two sides of heterojunction. For Z-scheme heterojunction (Figure 8b), the CB position of sem 1 is close to the VB position of sem 2, resulting in the interfacial recombination between photogenerated electrons from sem 1 and holes from sem 2. Such recombination enables forward current flow and the photovoltage is the sum of the photovoltage of sem 1 and sem 2.[20]

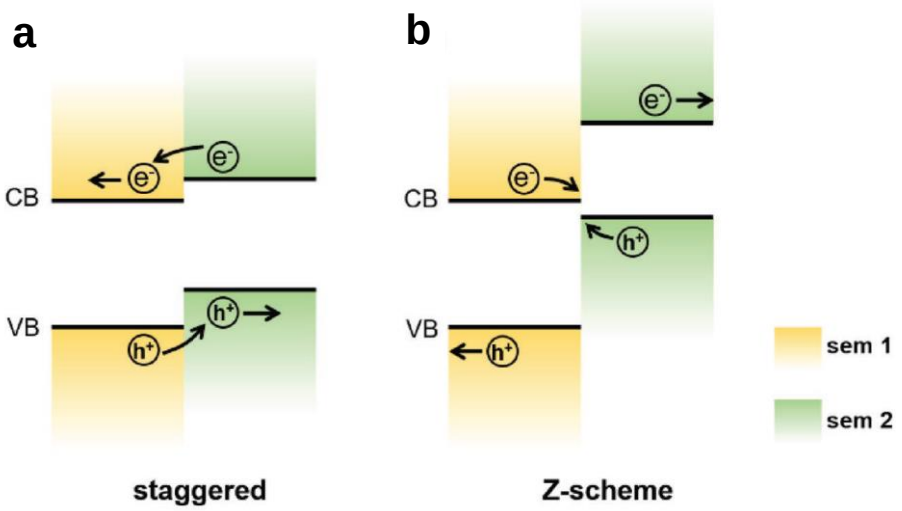

Figure 8: Band structure of two kinds of heterojunction. (a) Staggered junction. (b) Z-scheme junction.[20] Reproduced with permission from (*Adv. Mater. 2018, 30, 1707502*). Copyright 2018, Wiley-VCH GmbH.

The Fu group prepared a ternary $WO_3/BiVO_4/NiOOH$ photoanode with a photoresponse of 3.00 mA cm^{-2} at 1.23 V *vs.* RHE, which is 7 times higher than that of pure $BiVO_4$. The photogenerated carriers' transport is efficiently driven by the well-matched $WO_3/BiVO_4$ staggered heterojunction, as shown in Figure 9a, where the holes can move from the valence band of WO_3 (2.76 eV) to that of $BiVO_4$ (2.52 eV), while electrons can move from the conduction band of $BiVO_4$ (0.05 eV) to that of WO_3 (0.16 eV). NiOOH, as a water oxidation cocatalyst, accelerates the water oxidation kinetics.[112] The Hwang group demonstrated that the PEC performance of $BiVO_4$ can be improved by combining it with the more negative CB potential of n-Si. As shown in Figure 9b, it suggests that the photogenerated holes in Si and electrons in $BiVO_4$ are recombined and holes in $BiVO_4$ are used for oxygen evolution, while electrons in the Si layer are transferred to the counter electrode for hydrogen evolution (Z-scheme heterojunction). The TiO_2 layer protects Si from oxidation and aids in charge recombination between Si and $BiVO_4$.[113]

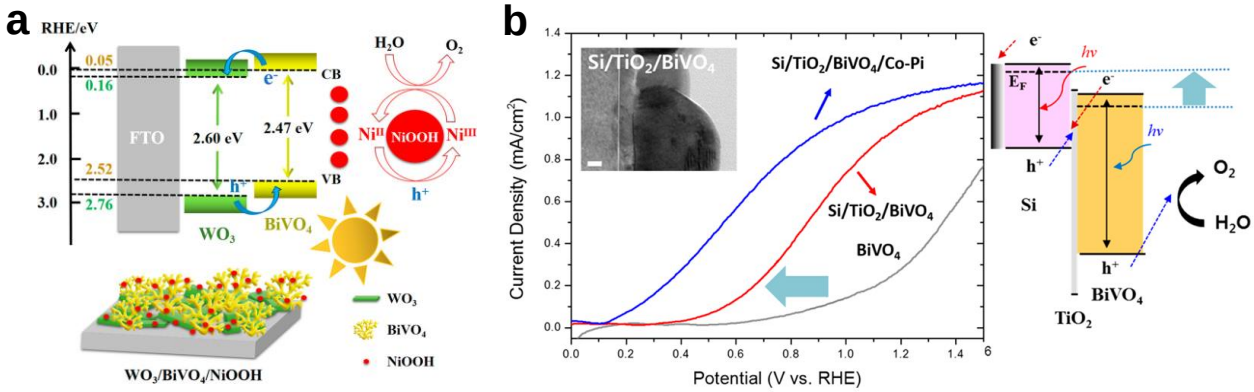

Figure 9: (a) Mechanism diagram of WO_3 and NiOOH co-modification to enhance the PEC activity of $BiVO_4$ photoanode.[112] Reproduced with permission from (*ACS Appl. Energy Mater. 2022, 5, 11402−11412*). Copyright 2022, American Chemical Society. (b) J-V curves and diagram of charge flows with $Si/TiO_2/BiVO_4$ Photoanode.[113] Reproduced with permission from (*ACS Appl. Mater. Interfaces 2015, 7, 5788−5796*). Copyright 2015, American Chemical Society.

1.2.4. Interface between $BiVO_4$ and the substrate modification strategies

In addition to surface modification and bulk promotion, the interface between $BiVO_4$ and the substrates (FTO glasses or other loaded support materials) is a challenge for photocarriers to be collected to the external circuit.[20] Inserting metal oxides between the substrate and $BiVO_4$ is an effective way to reduce the lattice mismatch and passivate defect trapping states for improving the photoactivity of $BiVO_4$. The Lee group investigated the epitaxial growth of $BiVO_4$ utilizing a thin γ-WO_3 template layer deposited on a $SrTiO_3$ (001) substrate covered by a $SrRuO_3$ (SRO) at the bottom. They found that the photocurrent density of template-assisted $BiVO_4$ is approximately 10 times greater than that of pristine $BiVO_4$. The template layer helps minimize the lattice mismatch between $BiVO_4$ and SRO, facilitates the migration of photogenerated electrons from $BiVO_4$ to the SRO bottom layer, and also acts as a hole-blocking layer (Figure 10a and 10b).[61] The Shin group demonstrated that a SnO_2 buffer layer as hole blocking layer has been introduced at the interfaces between $BiVO_4$ and FTO substrate (Figure 10c). The defect trapping states (DTS*) located at the FTO/$BiVO_4$ interface are fully passivated. Furthermore, the SnO_2 buffer layer induces a favorable band bending in the $BiVO_4$ layer, which leads to efficient electron transport towards the FTO through the SnO_2 layer and effectively prohibits charge recombination.[114]

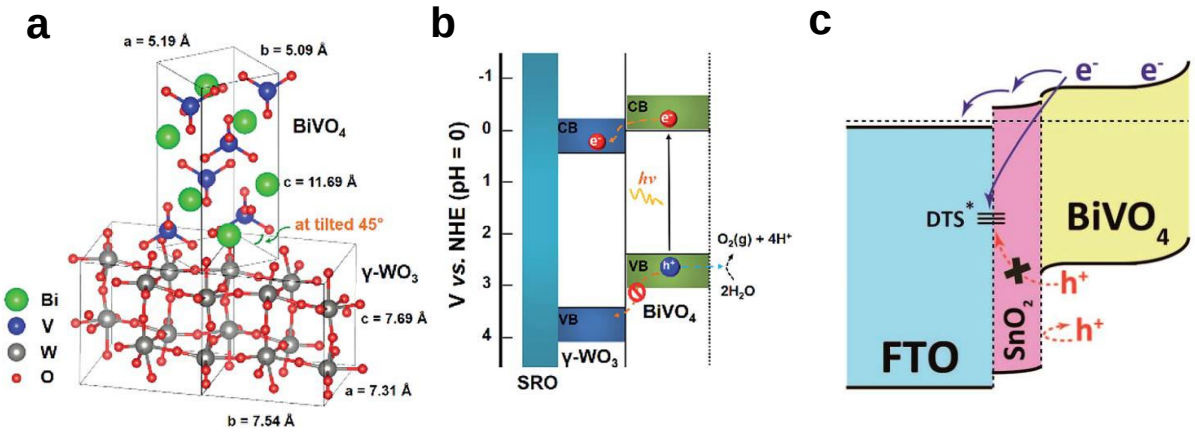

Figure 10: Schematic of the (a) structural model for $BiVO_4$ deposited on the g-WO_3 template layer, (b) energy-band diagram of the $BiVO_4$/g-WO_3 photoanode.[61] Reproduced with permission from (*J. Mater. Chem. A, 2017, 5, 18831–18838*). Copyright 2017, the Royal Society of Chemistry. (c) The schematic illustration of the SnO_2 as a hole blocking layer under the $BiVO_4$.[114] Reproduced with permission from (*J. Mater. Chem. A, 2017, 5, 6905–6913*). Copyright 2017, the Royal Society of Chemistry.

1.3. Polyoxometalates (POMs)-based/derived composites for PEC water splitting

1.3.1. Fundamentals of POMs

POMs are a large class of polynuclear metal–oxo clusters that consist of early transition metals (e.g., Mo^{6+}, W^{6+}, V^{5+}) with high oxidation states.[115] The starting metal salts (e.g., MoO_4^{2-}, WO_4^{2-}, VO_3^-) could transform into the $[MO_y]$ polyhedral units with y = 4 – 7 during the reaction, where M represents an metal ion defined as *addenda* atom.[115,116] POMs are typically constructed by linking $[MO_y]$ polyhedral units through self-assembly process in aqueous or organic solutions, which could assembly through different linkage approaches, such as bridged by one oxo-group (corner-shared), two oxo groups (edge-shared) or three oxo groups (face-sharing, which is rarely observed) to construct tremendous nanoclusters with different structures and compositions.[26,116,117] The *addenda* atom can also be substituted by other metal elements to generate functionalized POM materials. Moreover, the negative charge of POMs will be balanced by various countercations, which control the cluster solubility.[118]

A large number of structure types of POMs can be broadly classified into three categories (see Figure 11):[118–120] (i) **Isopolyoxometalates** are molecular metal oxide anions including single species of *addenda* atom and oxygen without any heteroatom, see Figure 11a and 11b, resulting in the general formula of $[M_xO_y]^{n-}$. Though isopolyoxometalates are less stable than their heteropolyoxometalate counterparts, they also have interesting physical

properties, such as high charges and strongly basic oxygen surfaces, which make them as attractive building blocks for applications. (ii) **Heteropolyoxometalates** are metal oxide frameworks containing one or more heteroatoms, and two fundamental heteropolyoxometalates shown in Figure 11c and 11d (Keggin-type $[XM_{12}O_{40}]^{n-}$and Wells-Dawson-type $[X_2M_{18}O_{62}]^{n-}$), described by the formula $[X_zM_xO_y]^{n-}$ with $z \leq x$ for heteroatom X, such as transition metals V, Cr, Mn, Fe, Co, or nonmetals Si, P, S, As, I.[119] Heteroatoms X can act either as a template in the self-assembly process stabilizing the cluster (e.g. Keggin anion $[SiW_{12}O_{40}]^{4-}$) or as a linker between polyoxometalate units to form into supramolecular POM-based structures (e.g. $[Co_4(H_2O)_2(PW_9O_{34})_2]^{10-}$).[121] In addition, a well-established procedure to incorporate heterometals into POMs is using lacunary clusters, see Figure 11e as one example. (iii) **Mo-blues/Mo-browns** are highly reduced polyoxometalate clusters based Mo, which often form high nuclearity ring- or ball-shaped cluster topologies, see Figure 11f. The $\{Mo_{132}\}$ spherical ball-like cluster and $\{Mo_{154}\}$ ring-shaped cluster have been structurally discovered and characterized by A. Müller.[122,123]

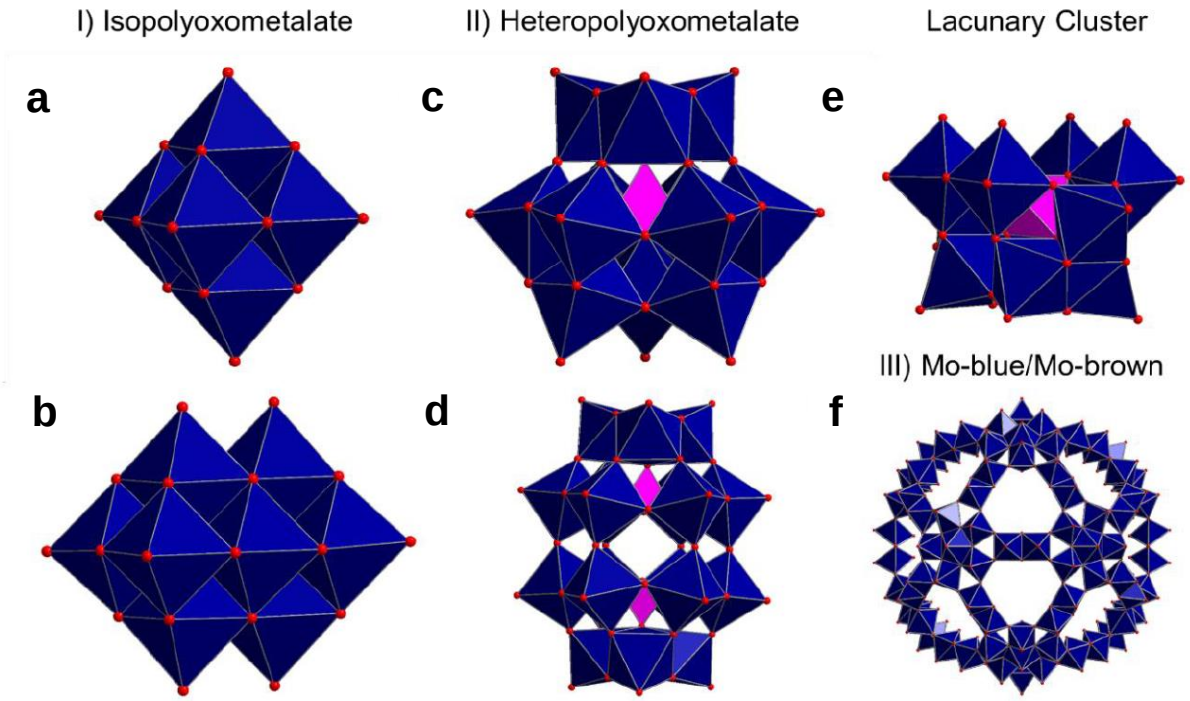

Figure 11: Common polyoxometalate frameworks illustrated in polyhedral presentation. **a**) Isopolyoxometalate Lindqvist-type hexametalate $[M_6O_{19}]^{n-}$. **b**) Isopolyoxometalate decametalate $[M_{10}O_{28}]^{n-}$. **c**) Heteropolyoxometalate Keggin-type $[XM_{12}O_{40}]^{n-}$. **d**) Heteropolyoxometalate Wells-Dawson-type $[X_2M_{18}O_{62}]^{n-}$. **e**) Lacunary heteropolyoxometalate Keggin-type $[XM_{10}O_{36}]^{n-}$. **f**) Supramolecular spherical Molybdenum $\{\mathbf{Mo_{132}}\}$ cluster. Colour scheme: dark blue: polyhedral $[MO_6]$; purple: tetrahedral $[XO_4]$; red: O.[120] Reprinted with permission from (*S. Repp. Self-assembly and Supramolecular Functionalization of Hybrid Organic-inorganic Molecular Vanadium Oxides. 2023, Universität Ulm*). Copyright 2023, Universität Ulm.

1.3.2. POMs-based/derived photoelectrodes

Owing to the variety of advantages, such as redox activity, solubility, unique electronic properties, compositional flexibility, thermal-/chemical stability can be adjusted by changing constituent elements, organic bridging components and structural dimensions (e.g. POM-based chains, layers and frameworks).[115,124] POMs have become potential materials for broad research fields, especially in catalysis.[125–127] Up to now, many POM-based compounds (see Figure 12) involving POM clusters,[128,129] POM molecule encapsulated into metal-organic frameworks (POM@MOFs),[118,130,131] POM-based metal organic frameworks (POMOFs)[124] and POM molecule deposited onto conductive substrates (POM@Substrates)[132,133] have been explored extensively in photo/electrocatalytic.[127] Benefiting from the fast (multi-)electron and proton transfer abilities, researchers often associate POMs with semiconductor materials such as TiO_2,[134] WO_3,[135] Fe_2O_3,[136] Cu_2O[137] in terms of both photoanodes and photocathodes in photo-electrocatalytic system.

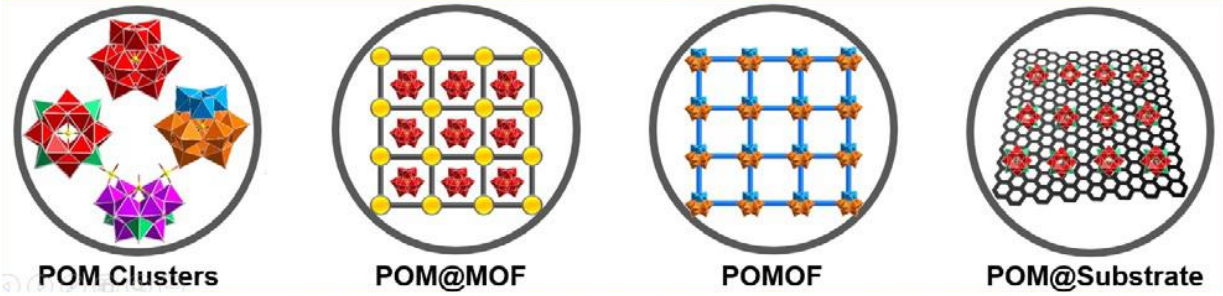

Figure 12: POM-based compounds.[127] Reprinted with permission from (*Angew. Chem. Int. Ed., 2020, 59, 20779–20793*). Copyright 2020, Wiley-VCH GmbH.

POMs in Photocathodes: The Guo group reported that the POM ($[PW_{10}Mo_2O_{40}]^{5-}$) anions were adsorbed on Cu_2O crystal faces by electrostatic attractive interaction to achieve the POM/Cu_2O photocathodes. The Cu_2O/POM composite films exhibit significant photovoltaic enhancement because the POM could act as electron-acceptor to retard the electron–hole recombination and facilitate the photoexcited electron transfer.[137] The Li group reported a POM ($Ag_6[P_2W_{18}O_{62}]$) -modified $CuBi_2O_4$/Mg-$CuBi_2O_4$ homojunction photocathode to improve both the bulk and interfacial charge carrier transport, while the built-in electric field from $CuBi_2O_4$/Mg-$CuBi_2O_4$ homojunction promotes the migration of photo-excited carries and the reduced POM co-catalyst was used as a proton sponge to accelerate surface reaction kinetics and suppress carrier recombination (Figure 13a).[138]

POMs in Photoanodes: The Ryu group reported that an organic/inorganic hybrid WO_3/PPy:Ru_4POM (PPy: polypyrrole; Ru_4POM: $[Ru_4O_4(OH)_2(H_2O)_4(\gamma\text{-}SiW_{10}O_{36})_2]^{10-}$) photoanodes prepared by the electro-polymerization, where the deposition of the PPy:Ru_4POM layer is contributed to a remarkably improved photoelectrochemical performance due to the formation of a WO_3/PPy p−n heterojunction and the incorporation of Ru_4POM WOCs, and enhanced photostability due to the suppression of the formation of hydrogen peroxide.[139] The Lian group constructed a TiO_2−Co_9POM $\{Na_8K_8[Co_9(H_2O)_6(OH)_3(HPO_4)_2(PW_9O_{34})_3]\}$ photoanode by first anchoring the cationic 3-aminopropyltrimethoxysilane (APS) ligand on a metal oxide light absorber. Results indicate that surface-bound Co_9POM retains its structural integrity throughout all photoelectrochemical water oxidation studies and Co_9POM serves as an efficient WOC, extracting photogenerated holes from TiO_2 on the picosecond time scale.[140] The Ryu group successfully build a photoanode by depositing a thin film of diverse cationic polyelectrolytes and anionic $[Co_4(H_2O)_2(PW_9O_{34})_2]^{10-}$ POM-WOCs on the surface of various photoelectrode materials (e.g. Fe_2O_3, $BiVO_4$ and TiO_2) using the layer-by-layer (LbL) assembly technique (Figure 13b). This proof of concept showed that the performance of these photoanodes was significantly improved in terms of stability as well as photocatalytic properties.[136] The Rau group reported that a cationic polymer linker polyethyleneimine (PEI) for immobilization of the anionic co-catalysis CoPOM onto the negatively charged surface of carbon nitrides (CN_x) improved efficiency of the transfer of photogenerated holes to water molecules and to enhanced photo-electrocatalytic oxygen evolution, as shown in Figure 13c.[141]

Although cationic polymer linkers for stabilization of anionic POMs have been reported, POMs are not always stable as a molecular catalyst, depending on specific experimental conditions (e.g., pH and composition of electrolyte, catalyst concentration, applied electrode potential). For example, cobalt-based polyoxometalates $[Co_4(H_2O)_2(PW_9O_{34})_2]^{10-}$ (CoPOM) has been reported to be an efficient homogeneous water oxidation catalyst,[128,129,142] but this CoPOM as a pre-catalyst can also undergo conversion to cobalt oxide,[143,144] cobalt hydroxide,[145] cobalt phosphate[146] etc. accounts for the major part of activity in water oxidation. The Ding group reported a Co_8POM ($[(A\text{-}\alpha\text{-}SiW_9O_{34})_2Co_8(OH)_6(H_2O)_2(CO_3)_3]^{16-}$) modified Fe_2O_3 photoanodes prepared by a simple photo-deposition method, where an ultrathin CoO_x overlayer derived from Co_8POM is confirmed as the true active species on the hematite nanorod to improve the photoresponse and reduces the water oxidation overpotential (Figure 13d).[147] The Lin group reported that an ultrathin nanofilm FeO_x cocatalyst decomposed from eleven iron-containing polyoxometalate $Na_{27}[Fe_{11}(H_2O)_{14}(OH)_2(W_3O_{10})_2(\alpha\text{-}SbW_9O_{33})_6]$

(Fe_{11}POM) on the decisive (110) facet of $BiVO_4$ significantly enhanced photocatalytic water oxidation performance compared to pure $BiVO_4$, which could effectively capture the photogenerated holes and suppress the recombination of electron–hole pairs through fast interfacial hole transfer process.[148] In conclusion, the related post-catalyst derived from the degradation of POMs are still activated for the reaction activity in catalysis system.

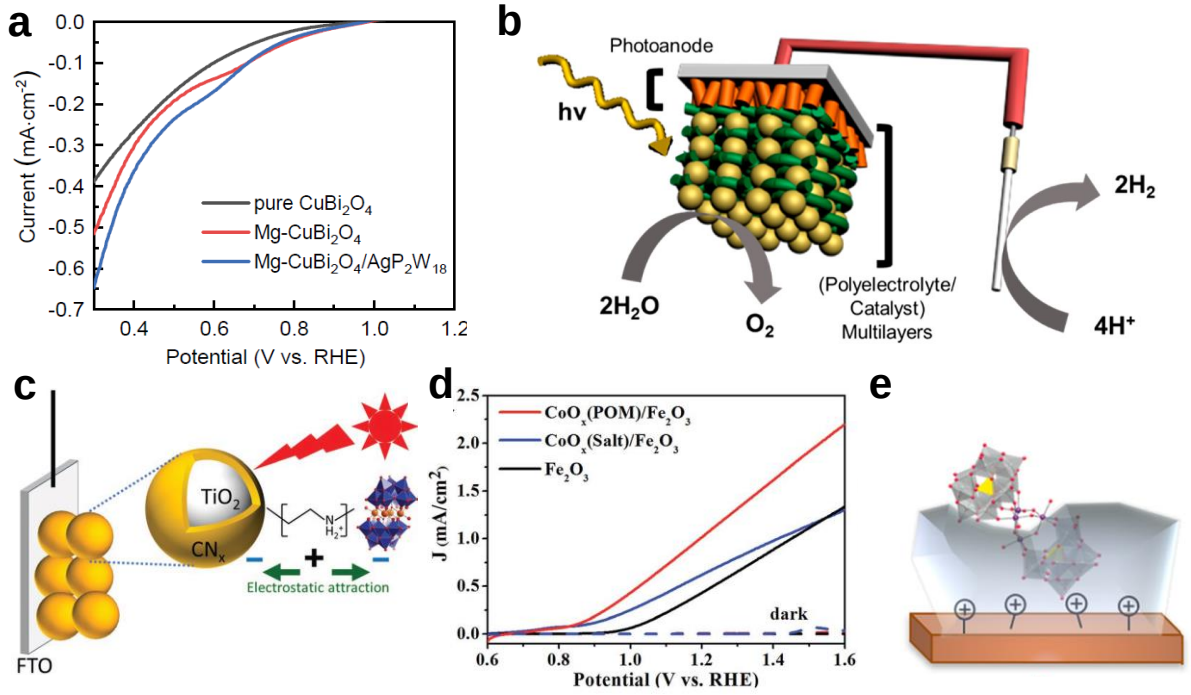

Figure 13: (a) Current–potential of $CuBi_2O_4$ photocathode with homojunction and AgP_2W_{18} surface modification.[138] Reprinted with permission from (*Acta Phys. -Chim. Sin. 2024, 40 (2), 2304006*). Copyright 2024, Editorial office of Acta Physico-Chimica Sinica. (b) Experimental setup for the photoelectrochemical performance of LbL-modified photoanodes.[136] Reprinted with permission from (*ACS Appl. Mater. Interfaces 2017, 9, 40151−40161*). Copyright 2017, American Chemical Society. (c) The fabrication of the CN_x/TiO_2 hybrid photoanode with an anionic molecular CoPOM cocatalyst immobilized via electrostatic attraction on the negatively charged CNx surface using a positively charged cationic polyethyleneimine (PEI) linking agent.[141] Reprinted with permission from (*Adv. Sustainable Syst., 2022, 6, 2100473*). Copyright 2022, Wiley-VCH GmbH. (d) LSV of CoO_x(POM)/Fe_2O_3, CoO_x(salt)/ Fe_2O_3, and Fe_2O_3 photoanodes under AM 1.5G irradiation in 80 mM borate buffer (pH 9).[147] Reprinted with permission from (*J. Mater. Chem. A, 2019, 7, 6294–6303*). Copyright 2019, the Royal Society of Chemistry. (e) Schematic illustrations of photoanodes with Al_2O_3 ALD protection.[149] Reprinted with permission from (*ACS Appl. Mater. Interfaces 2017, 9, 35048−35056*). Copyright 2017, American Chemical Society.

On the other hand, to avoid the degradation of POMs supported on photoelectrode surfaces under applied potential, the Hill group reported that a 4 nm thick Al_2O_3 layer applied by the atomic layer deposition (ALD) aids immobilization and greatly stabilizes $[\{Ru^{IV}_4(OH)_2(H_2O)_4\}(\gamma\text{-}SiW_{10}O_{34})_2]^{10-}$ (Ru_4Si_2) on hematite surfaces, as shown in Figure 13e.

Results indicate that Ru_4Si_2 remains intact with Al_2O_3 ALD protection, which provides optimal performance with nearly 100% faradaic efficiency for oxygen generation under visible-light illumination.[149] Furthermore, POMs also can be as a pre-catalyst by annealing to active the catalytic reaction. The Ryu group annealed soluble POM $[Co_4(H_2O)_2(PW_9O_{34})_2]^{10-}$ molecules at high temperatures in air led to the formation of insoluble amorphous $CoWO_4$ nanoparticles on the surface of Fe_2O_3, which exhibited excellent catalytic activity. Its outstanding performance resulted from the generation of large amounts of oxygen vacancies upon annealing, leading to the optimum distance between the nearest Co ions for the Langmuir-Hinshelwood (LH) mechanism.[150]

1.3.3. POMs-based/derived $BiVO_4$ photoanodes

POMs are an outstanding class of electron acceptors/donators as WOCs, which can capture and transport photo-generated electrons or holes to reduce the fast carrier recombination.[127] The Xu group reported a Co-based POM ($Ag_{10}[Co_4(H_2O)_2(PW_9O_{34})_2]$) serving as a hole extraction layer on the surface of $BiVO_4$ photoanode for boosting PEC activity by promoting hole extraction and transfer.[151] As shown in Figure 14a, the Ryu group exhibited a superior PEC performance for $BiVO_4$ photoanodes with catalytic multilayers (CMs), where cationic polyelectrolytes and anionic $Na_{10}[Co_4(H_2O)_2(VW_9O_{34})_2]$ WOCs were assembled in a desired amount. EIS analysis combined with various PEC characterization methods showed that the CMs improved water oxidation kinetics at the electrode/electrolyte interface via the deposition of efficient POM WOCs and the kinetics of photogenerated carrier separation/transport within bulk $BiVO_4$ by passivating surface recombination centers (Figure 14b).[152] The Ding group reported a Ni_3POM ($K_6Na[Ni_3(H_2O)_3PW_{10}O_{39}H_2O]\cdot 12H_2O$) as a novel molecular cocatalyst incorporated into a typical FeOOH/$BiVO_4$ composite photoanode through a simple impregnation method for boosting PEC performance (Figure 14c). Notably, the introduction of Ni_3POM accelerates the separation and transfer of carriers and surface reaction kinetics, simultaneously improving the PEC stability.[153] The Fan group investigated the $Na_{10}[Co_4(H_2O)_2(PW_9O_{34})_2]$ (CoPOM) cocatalyst locating at N-doped carbon (N/C) to specially boost the charge transfer efficiency and achieve lower onset potential of $BiVO_4$ photoanodes for PEC water oxidation (Figure 14d), which showed a good stability and well maintained the original structure and morphology of $BiVO_4$-N/C-CoPOM.[154] In addition, the Ryu group fabricated an efficient and stable bias-free PEC cell composed of dual photoelectrodes—deposition of the respective CMs on a Cu_2O photocathode and a $BiVO_4$

photoanode—for overall water splitting using LbL assembly (Figure 14e and 14f). Detailed PEC analysis revealed that the CMs not only facilitated catalytic activity and charge transport to the photoelectrode/electrolyte interface, but also suppressed the deactivation of photoelectrodes, especially for an unstable Cu_2O photocathode, by the formation of a protective coating layer.[155]

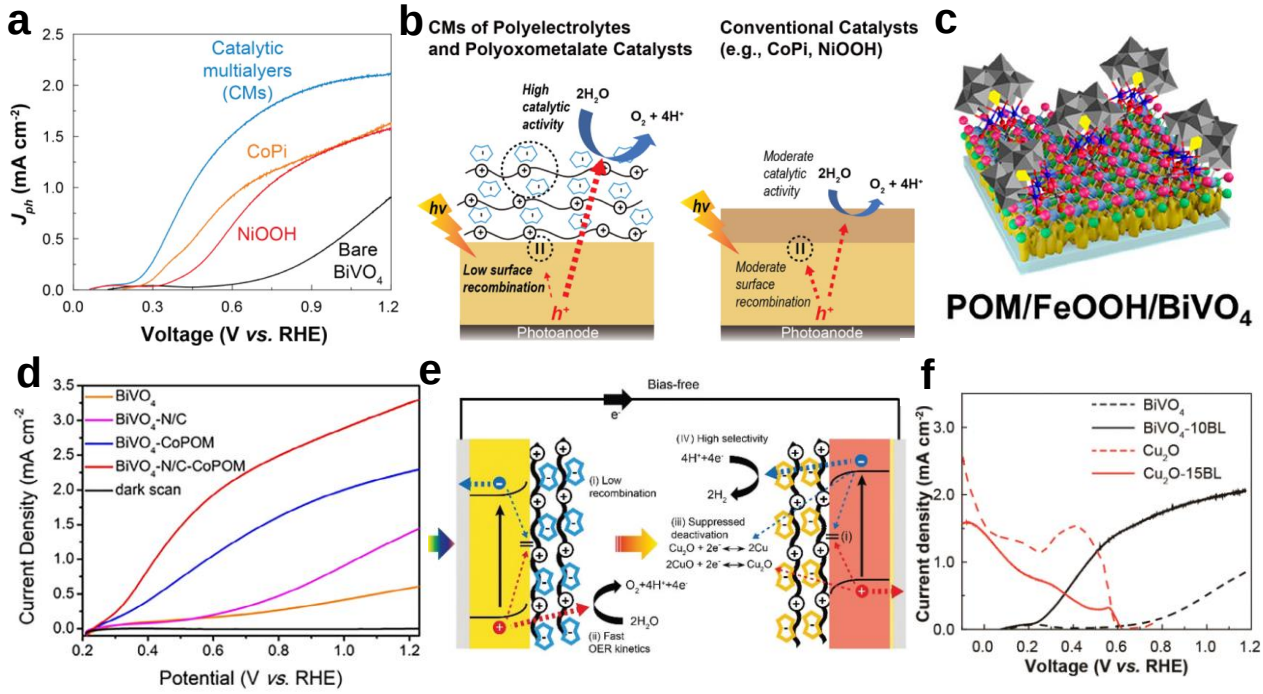

Figure 14: (a) J-V curves and (b) schematic illustration for the preparation of the $BiVO_4$ photoanodes modified with molecular CMs.[152] Reproduced with permission from (*ACS Appl. Mater. Interfaces 2019, 11, 7990−7999*). Copyright 2019, American Chemical Society. (c) Schematic diagram for Ni_3POM/FeOOH/$BiVO_4$ photoanode.[153] Reproduced with permission from (*ACS Sustainable Chem. Eng., 2023, 11, 7367−7377*). Copyright 2023, American Chemical Society. (d) LSV curves of $BiVO_4$, $BiVO_4$-N/C, $BiVO_4$-CoPOM and $BiVO_4$-N/C-CoPOM under AM 1.5G illumination.[154] Reproduced with permission from (*Chem. Eng. J., 2020, 392,123744*). Copyright 2020, Elsevier Ltd. (e) Schematic illustrations and (f) J-V curves a bias-free PEC cell composed of a Cu_2O photocathode with HER CMs (cationic polyethyleneimine and NiPOM $[Ni_4(H_2O)_2(PW_9O_{34})_2]^{10-}$) and a $BiVO_4$ photoanode with OER CMs (cationic polyethyleneimine and CoPOM $[Co_4(H_2O)_2(VW_9O_{34})_2]^{10-}$).[155] Reproduced with permission from (*Green Chem., 2018, 20, 3732–3742*). Copyright 2018, the Royal Society of Chemistry.

As mentioned above, POMs are not always stable as a molecular catalyst. Although post-catalyst derived from the degradation of POMs accounts for the reaction activity in catalysis system, scientists are still exploring more methods to improve the stability of molecular POMs. One effective method is incorporating POMs into metal−organic frameworks (MOFs) containing active catalytic sites, which is attributed to MOFs feature organic ligands porous network, and electron-rich centers of POMs that can modulate the chemical bonds

between the metal ions and organic linkers of MOFs. The Wang group constructed a $BiVO_4$ photoanode by securely encapsulated the electron-rich $K_6Na[Ni_3(H_2O)_3PW_{10}O_{39}H_2O]\cdot 12H_2O$ (NiPOM) into metal−organic framework MIL-101(Cr), which effectively preserves the catalytic activity of the NiPOM while providing adequate space for catalytic reactions. The improved catalytic performance can be attributed to NiPOM serving as the primary active species, accelerating surface catalytic reactions, providing electrons from its Ni sites to the V sites on the $BiVO_4$ surface, effectively suppressing V^{5+} dissolution, and enhancing the oxidative stability of PEC water splitting.[156] Furthermore, the Liu group reported a modified-$BiVO_4$ photoanode through the coupling of $H_3O_{40}PW_{12}\cdot xH_2O$ (PWO) with CoOOH, demonstrating that the decoration of PWO serves as an intermediate layer to promote the transport of holes from $BiVO_4$ to CoOOH, while the deposition of CoOOH acts as a protective layer as well as cocatalyst to reduce the photo-corrosion and improve the PEC activities of $BiVO_4$.[157]

Notably, POMs could be a potential PEC co-catalyst candidate with excellent photoactivity directly applied in $BiVO_4$ PEC systems. To the best of our knowledge, a photoelectrode fabricated by combining $BiVO_4$ and POMs for OER is normally with linkers or binders or intermediate layers. However, in our case, we choose direct deposition of CoPOM ($Na_{10}[Co_4(H_2O)_2(PW_9O_{34})_2]$) as an example from the POMs family without any linkers or binders on the surface of Mo-doping mesoporous $BiVO_4$. Meanwhile, the addition of the polyethyleneimine (PEI) as a cationic polymer linker was compared with the photoelectrode without PEI linker, which results had no beneficial effect on the performance of the photoanodes with PEI linker for our Mo-doped $BiVO_4$ photoanodes. Furthermore, we proved the contributions of the Mo-doping and modification with CoPOM to the performance enhancement. In addition, we provide several unprecedented insights into the effects of both Mo-doping (*e.g.,* Mo-induced limitation of photovoltage) and CoPOM modification (*e.g.,* compositional changes under operating conditions and significant electrolyte effects). See corresponding details in the next chapter 3.1.

POMs can be considered as molecular analogues of solid-state metal oxide semiconductors. They have similar chemical composition and electronic property.[158] It is recognized that the highest occupied molecular orbital (HOMO) and lowest unoccupied molecular orbital (LUMO) in POMs are similar to the valence band (VB) and conduction band (CB) in semiconductors. When exposed to ultraviolet light, there is an electron transition in POMs from HOMO to LUMO (O→M charge transfer). Thus, electrons which are promoted to

empty metal d-orbitals can be described as photo-generated electrons, and the vacant oxygen 2p-orbitals can be considered as photo-generated holes.[159,160] The quasi-semiconductor characteristics of POMs make them important for photocatalytic systems. For example, the Xu group doped Keggin-type POMs such as $H_3[PW_{12}O_{40}]$ (PW_{12}) and $K_6[CoW_{12}O_{40}]$ (CoW_{12}) into $BiVO_4$ to improve photo-electrocatalytic water oxidation performance of $BiVO_4$, as shown in Figure 15a, which attributes to energy band matching between $BiVO_4$ and POMs to drive migrating of photogenic electrons from $BiVO_4$ to POMs.[161] The Zheng group synthesized an amino-modified Ti_5 clusters (NH_2-TOCs) on $BiVO_4$ that exhibited high performance on PEC water splitting by as-formed NH_2-TOCs/$BiVO_4$ heterojunction, which was ascribed to strong M-O-Ti (M=Bi, V) bonding at the interface.[162] The Lee group proposed incorporating POM ($[Co_4(H_2O)_2(PW_9O_{34})_2]^{10-}$) within a polypyrrole (PPy) network coated on $BiVO_4$ to boost light absorption and charge separation through the heterojunction between $BiVO_4$ and PPy, and found that the use of POM plays a crucial role in reducing the charge recombination at the interface, achieving high hole transfer efficiency (Figure 15b).[163] Xu group reported a dual modification of $BiVO_4$ photoanodes utilising the POM $H_3PW_{12}O_{40}$ (PW_{12}), as electron acceptor to suppress electron-hole recombination, and nickel (II) phthalocyanine tetrasulfonic acid (NiTsPc), acting as hole extractor. Besides, the energy band matching is beneficial to driving charge carrier transfer, the photoelectron to transfer from $BiVO_4$ to PW_{12} and the hole from $BiVO_4$ to NiTsPc for the improved photoactivity of $BiVO_4$ (Figure 15c).[164]

To date, using POMs as a doping agent has been reported in various fields, including gas sensing application,[165] dye-sensitized[166] or perovskite solar cells,[167] biothiol detection[168] and photocatalytic[169,170]. Due to the abundancy of transition metals involved in typical POMs, they also hold potential as doping agents in PEC water splitting systems. However, as mentioned-above, the reported POMs-doped into $BiVO_4$ are attributed to energy band matching between $BiVO_4$ and POMs. Hence, it has great significance to explore POMs with abundant transition metal elements as a doping agent to add in the precursor solution for the synthesis of $BiVO_4$ photoanodes in PEC system, manipulating the electronic structure of $BiVO_4$ film photoanodes. In our case, we used a 'Double-Use' strategy for the development of high-performance $BiVO_4$ photoanodes for solar water splitting, where CoPOM ($Na_{10}[Co_4(H_2O)_2(PW_9O_{34})_2]$) was simultaneously used both as a bulk doping agent as well as a surface-deposited water oxidation co-catalyst. Most importantly, the combination of both modification routes resulted in significantly increased photoresponse and faster O_2 production compared with pristine $BiVO_4$, and discussed in detail the mechanistic aspects of the improved

activity and stability related to the ratio of W/Co on the surface of photoanode, which are of great importance for the further design and development of efficient energy materials. See corresponding details in the next chapter 3.2.

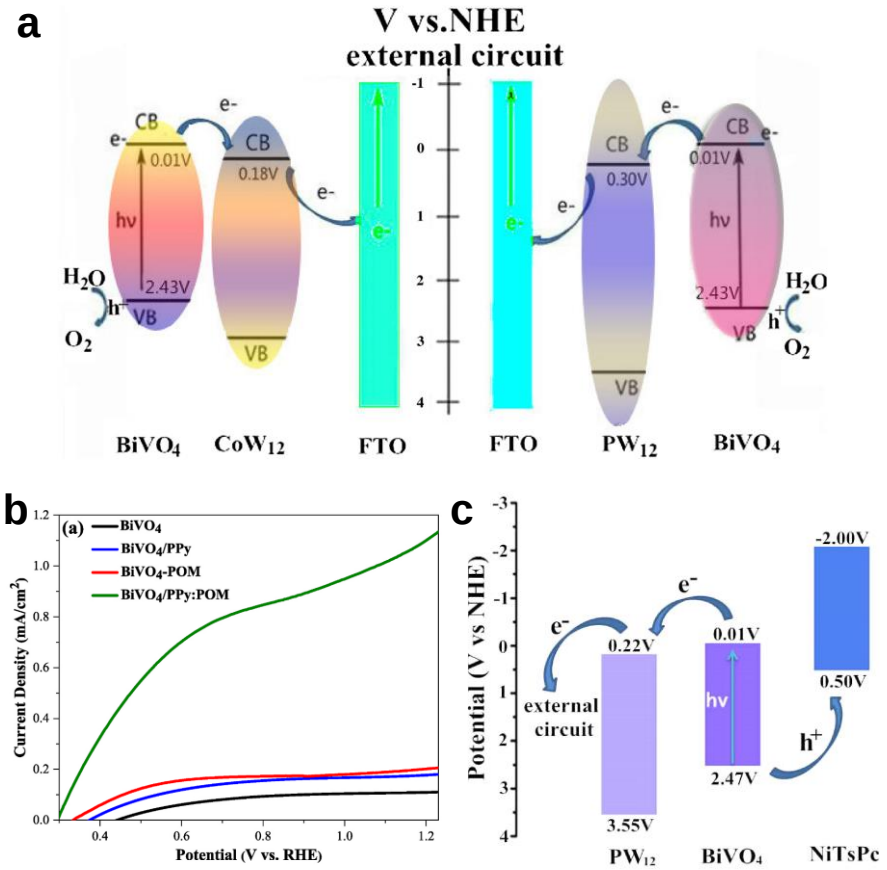

Figure 15: (a) Schematic illustration of charge transfer processes for $BiVO_4/CoW_{12}$ and $BiVO_4/PW_{12}$ electrodes.[161] Reproduced with permission from (*Appl. Cata. A: General, 2017, 536, 67–74*). Copyright 2017, Elsevier Ltd. (b) LSV curves of $BiVO_4$, $BiVO_4$-POM, $BiVO_4$/PPy and $BiVO_4$/PPy:POM photoanodes.[163] Reproduced with permission from (*Mater. Chem. Phys., 2023, 309, 128430*). Copyright 2023, Elsevier Ltd. (c) The schematic illustration of charge transfer processes for $BiVO_4/PW_{12}$/NiTsPc photoanode.[164] Reproduced with permission from (*ChemElectroChem, 2018, 5, 2534–2541*). Copyright 2018, Wiley-VCH Verlag GmbH & Co. KGaA, Weinheim.

2. Objectives

As mentioned above, POMs, as a vast class of green, cheap and stable early transition metal-oxygen clusters, offer multiple advantages, including redox activity, solubility, unique electronic properties, compositional flexibility, and the ability to mediate fast electron and proton transfer. These qualities make them an attractive class of molecular catalysts, pre-catalysts, and redox mediators for photo- and electrocatalytic systems. Monoclinic $BiVO_4$ has become one of the most promising photoanode materials in the field of photoelectrochemical water splitting for its multifold features such as earth-abundance, suitable bandgap, low valence band position and high stability in aqueous solution and low-cost. In this context, POMs serve not only as metal doping precursors for bulk modification but also as cocatalysts or pre-catalysts for surface modification, leading to enhanced photo-electrocatalytic activity in nanoporous $BiVO_4$ photoanodes.

The main objective of this thesis is to develop effective and stable $BiVO_4$ photoanodes for photoelectrochemical water splitting (driven by solar light). The effort to achieve this goal can be categorized into two parts.

- Design and fabrication of nanoporous $BiVO_4$ thin films through doping and cocatalyst modification, along with the evaluation of their photo-electrocatalytic performance.
- Mechanistic analysis to demonstrate the contributions of doping and cocatalyst modification.

The first objective of this thesis is to synthesize a thin-film photoelectrode based on nanoporous $BiVO_4$ that exhibits not only good light absorption but also efficient charge separation and transport. The introduction of F-108 as a structural agent during synthesis induces a three-dimensional nanoporous structure with worm-like nanoparticles ranging in size from tens of nanometers. The thickness of the thin film is adjusted by varying the number of spin-coating cycles of the precursor solution to achieve optimal light absorption. Concurrently, the doping concentration is fine-tuned by adding different amounts of the doping agent to the precursor solution, while CoPOM cocatalyst is incorporated into the photoanodes by immersion in a CoPOM aqueous solution to enhance charge separation and transport. The photo-electrocatalytic activities of the resulting photoanodes will be tested by potentiostat in borate buffer under AM 1.5G illumination (1 sun) from the backside (through the FTO glass),

using a standard three-electrode configuration. O_2 production is directly recorded by the FireSting optical fiber O_2 sensor for the evaluation of OER performance.

The second objective of this research is to analyze the contributions of doping (Mo-doping and CoPOM-doping) and CoPOM cocatalysts modifications throughout the catalytic process. This involves a comprehensive investigation of the open-circuit photopotential (OCP), applied bias photoconversion efficiency (ABPE), incident photon-to-current conversion efficiency (IPCE), charge separation efficiency (η_{sep}), the hole transfer efficiency (η_{tr}), electrochemical impedance spectroscopy (EIS), stability, and photo-electrocatalytic performance both before and after catalysis. Such analyses elucidate the roles of CoPOM-based water oxidation catalysts and the doping agent within the CoPOM-derived $BiVO_4$ system, providing valuable guidance for the future synthesis of photoelectrodes.

3. Result and discussion

Parts of this thesis have been published in peer-reviewed scientific journals. With permissions from corresponding journals, reprints of these publications are presented in chapter 3.1-3.3 followed by corresponding supporting information in chapter 6.1-6.3, where the contributions of individual authors for each publication are given.

In chapter 3.1, titled ‘‘High-Performance $BiVO_4$ Photoanodes: Elucidating the Combined Effects of Mo-doping and Modification with Cobalt Polyoxometalate’’, bulk doping of $BiVO_4$ with molybdenum combined with surface modification with a cobalt polyoxometalate water oxidation catalyst (CoPOM) was successfully synthesized on $BiVO_4$ photoanodes. The best-performing Mo-$BiVO_4$/CoPOM photoanode exhibits a photocurrent density of 4.32 mA cm^{-2} at 1.23 V *vs.* RHE under AM 1.5G (1 sun) illumination and an ABPE of ~0.73%, which is an improvement by the factor of ~24 with respect to pristine $BiVO_4$. Mechanistic analyses are used to prove the contributions of Mo-doping and CoPOM modification. Mo-doping is shown to result in enhanced electronic conductivity and passivation of surface states, whereby these beneficial effects are operative only at relatively high applied bias potentials (> 0.9 V vs. RHE), and at lower bias potentials (< 0.7 V vs. RHE) they are counterbalanced by strongly detrimental effects related to increased concentration of electron polaronic states induced by the Mo-doping. CoPOM deposition is related to the enhancement of water oxidation catalysis. The molecular CoPOM acts as a pre-catalyst and undergoes (partial) conversion to cobalt oxide under the PEC operating conditions. The study demonstrates CoPOM-derived catalysts as effective water oxidation catalysts at $BiVO_4$ photoanodes and suggests that further progress in $BiVO_4$ photoanode development depends on alternative strategies for conductivity enhancement to avoid detrimental polaronic effects associated with the conventional bulk doping of $BiVO_4$.

In chapter 3.2, titled ‘‘"Double-Use" Strategy for Improving the Photoelectrochemical Performance of $BiVO_4$ Photoanodes using a Cobalt-Functionalized Polyoxotungstate’’, a molecular cobalt-phosphotungstate (CoPOM = $Na_{10}[Co_4(H_2O)_2(PW_9O_{34})_2]$) is used both as a bulk doping agent as well as a surface-deposited water oxidation co-catalyst. The use of CoPOM for bulk doping of $BiVO_4$ is shown to enhance the electrical conductivity and improve the charge separation efficiency, resulting in the enhancement of the maximum applied-bias photoconversion efficiency (ABPE) by a factor of ~18 to 0.54% at 0.87 V *vs*. RHE, as compared to pristine $BiVO_4$ (0.03% at 1.04 V *vs*. RHE). The ratio of W/Co on the surface of

photoanode is related to the activity and stability. In addition, modification of CoPOM-doped $BiVO_4$ with CoPOM as a surface co-catalyst enhances the hole extraction and improves the water oxidation kinetics, resulting in the overall enhancement of the ABPE to 0.79% (at 0.82 V *vs*. RHE), *i.e*. by a factor of ~26 with respect to pristine $BiVO_4$. This study establishes the 'Double-Use' strategy involving CoPOMs as an effective, straightforward and easily scalable approach for the development of high-quality photoanodes for solar water splitting, and highlights the future potential of utilizing well-designed polyoxometalates as precursors for the synthesis of energy materials.

In chapter 3.3, titled ''Atomically Engineered Defect-Rich Palladium Metallene for High-Performance Alkaline Oxygen Reduction Electrocatalysis'', it is reported how targeted introduction of defect sites in a 2D palladium metallene nanostructure results in a highly active catalyst for the alkaline oxygen reduction reaction (ORR). A defect-rich WO_x and MoO_x modified Pd metallene (denoted: D-Pd M) is synthesized by a facile and scalable approach. Detailed structural analyses reveal the presence of three distinct atomic-level defects, that are pores, concave surfaces, and surface-anchored individual WO_x and MoO_x sites. Mechanistic studies reveal that these defects result in excellent catalytic ORR activity, half-wave potential 0.93 V *vs.* RHE, mass activity 1.3 A mg Pd^{-1} at 0.9 V *vs.* RHE. The practical usage of the compound is demonstrated by integration into a custom-built Zn-air battery. At low D-Pd M loading (26 μg Pd cm^{-2}), the system achieves high specific capacity and shows excellent discharge potential stability. This study therefore provides a blueprint for the molecular design of defect sites in 2D metallene nanostructures for advanced energy technology applications.

3.1 (FF-1) High-Performance $BiVO_4$ Photoanodes: Elucidating the Combined Effects of Mo-Doping and Modification with Cobalt Polyoxometalate

Fan Feng, Dariusz Mitoraj, Ruihao Gong, Dandan Gao, Mohamed M. Elnagar, Rongji Liu, Radim Beranek*, Carsten Streb*

* Corresponding authors

Published in Material Advances, **2024**.

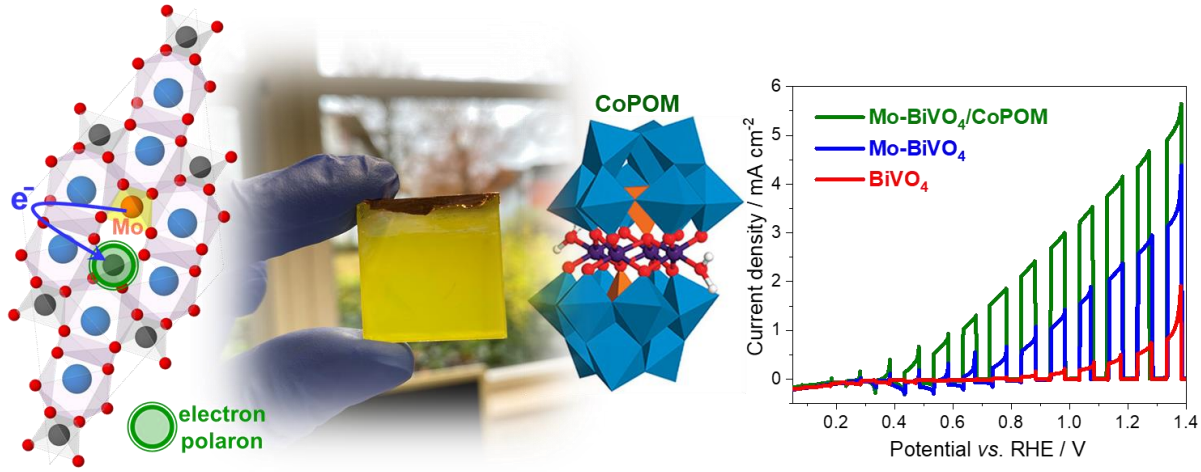

This publication reports on the synthesis and characterization of bulk doping of $BiVO_4$ with molybdenum combined with surface modification with a cobalt polyoxometalate water oxidation catalyst (CoPOM = $Na_{10}[Co_4(H_2O)_2(PW_9O_{34})_2]$). The optimized Mo-$BiVO_4$/CoPOM photoanode exhibits a photocurrent density of 4.32 mA cm^{-2} at 1.23 V vs. RHE under AM 1.5G (1 sun) illumination and an applied-bias photoconversion efficiency (ABPE) of ~0.73%. Mechanistic analyses demonstrate that Mo doping enhances electronic conductivity and passivates surface states at relatively high applied bias potentials, while molecular CoPOM serves as a pre-catalyst to improve water oxidation.

Supporting Information can be found in chapter 6.1.

Author contributions:

Fan Feng:	Conceiving the idea for the project, fabrication of all electrodes and characterizations, photoelectrochemical and photophysical studies, data analyses and writing and revision of the manuscript.
Dariusz Mitoraj:	Supporting the experimental design and photoelectrochemical investigations and structuring the article.
Ruihao Gong:	Supporting the photoelectrochemical performance.
Dandan Gao:	Supporting the synthesis and purification of CoPOM.
Mohamed M. Elnagar:	SEM and EDX investigations.
Rongji Liu:	Data analyses.
Radim Beranek:	Conceiving the research and finalizing the article.
Carsten Streb:	Conceiving the research and finalizing the article.

Materials Advances

ROYAL SOCIETY OF CHEMISTRY

PAPER

View Article Online
View Journal | View Issue

Cite this: *Mater. Adv.*, 2024, **5**, 4932

High-performance $BiVO_4$ photoanodes: elucidating the combined effects of Mo-doping and modification with cobalt polyoxometalate†

Fan Feng,[a] Dariusz Mitoraj,[b] Ruihao Gong,[c] Dandan Gao,[a] Mohamed M. Elnagar,[b] Rongji Liu,[a] Radim Beranek *[b] and Carsten Streb *[a]

Received 30th January 2024,
Accepted 26th April 2024

DOI: 10.1039/d4ma00089g

rsc.li/materials-advances

Bulk doping of $BiVO_4$ with molybdenum combined with surface modification with a cobalt polyoxometalate water oxidation catalyst (CoPOM = $Na_{10}[Co_4(H_2O)_2(PW_9O_{34})_2]$) is reported. The best-performing Mo–$BiVO_4$/CoPOM photoanode exhibits a photocurrent density of 4.32 mA cm^{-2} at 1.23 V *vs.* RHE under AM 1.5G (1 sun) illumination and an applied-bias photoconversion efficiency (ABPE) of ~0.73%, which is an improvement by a factor of ~24 with respect to pristine $BiVO_4$. Mechanistic analyses are used to prove the contributions of Mo-doping and CoPOM modification. Mo-doping is shown to result in enhanced electronic conductivity and passivation of surface states, whereby these beneficial effects are operative only at relatively high applied bias potentials (>0.9 V *vs.* RHE), and at lower bias potentials (<0.7 V *vs.* RHE) they are counterbalanced by strongly detrimental effects related to increased concentration of electron polaronic states induced by the Mo-doping. CoPOM deposition is related to the enhancement of water oxidation catalysis. The molecular CoPOM acts as a pre-catalyst and undergoes (partial) conversion to cobalt oxide under the PEC operating conditions. The study demonstrates CoPOM-derived catalysts as effective water oxidation catalysts at $BiVO_4$ photoanodes and suggests that further progress in $BiVO_4$ photoanode development depends on alternative strategies for conductivity enhancement to avoid detrimental polaronic effects associated with the conventional bulk doping of $BiVO_4$.

1. Introduction

Hydrogen generation *via* photoelectrochemical (PEC) water splitting represents one of the promising strategies to secure the future supply of free (low-entropy) energy in an environmentally sustainable manner.[1–4] Compared to the hydrogen evolution reaction (HER), which is a proton-coupled two-electron process, the oxygen evolution reaction (OER) is a typical kinetic bottleneck of PEC devices since the mechanism of oxygen generation is much more complex, involving concerted transfer of four electrons and four protons.[5,6] Accordingly, the development of efficient, stable and low-cost photoanodes for water oxidation is of paramount importance for the realization of economically viable PEC water splitting devices.[7] Some of the most intensely investigated photoanodes are based on passivated high-quality semiconductors (*e.g.*, Si or III–V compounds),[8–10] hybrid inorganic–organic architectures,[11–14] or on low-cost metal oxides, such as Fe_2O_3,[15,16] $CuWO_4$[17,18] or $BiVO_4$.[3,19–27] In particular, $BiVO_4$ is an attractive material owing to its bandgap energy of ~2.4 to 2.6 eV, which translates to the maximum theoretically achievable photocurrents of 6.4–8.9 mA cm^{-2} and the solar-to-hydrogen (STH) efficiencies of 8–11% under AM 1.5G (1 sun) illumination. However, the PEC performance of pristine $BiVO_4$ photoanodes is typically far below the theoretical limit, both in terms of maximum photocurrents and achievable photovoltages, the latter manifested by rather positive photocurrent onset potentials (with respect to the reversible hydrogen electrode, RHE) and generally poor fill-factors of the photocurrent density–potential (*J–V*) curves. The reasons for this suboptimal performance have been identified as (i) poor bulk electronic conductivity of $BiVO_4$ and the presence of surface intragap states, both of which result in severe electron–hole recombination,[21,28,29] and (ii) ineffective hole extraction and slow rate of water oxidation at pristine $BiVO_4$ surfaces.[3,20,22] Concerning the former, significant improvements in performance have

[a] *Department of Chemistry, Johannes Gutenberg University Mainz, Duesbergweg 10-14, 55128 Mainz, Germany. E-mail: carsten.streb@uni-mainz.de*
[b] *Institute of Electrochemistry, Ulm University, Albert-Einstein-Allee 47, 89081 Ulm, Germany. E-mail: radim.beranek@uni-ulm.de*
[c] *Institute of Inorganic Chemistry I, Ulm University, Albert-Einstein-Allee 11, 89081 Ulm, Germany*

† Electronic supplementary information (ESI) available. See DOI: **https://doi.org/10.1039/d4ma00089g**

been demonstrated, for example, by doping $BiVO_4$ with molybdenum,[30–34] whereby the beneficial effect of Mo doping has been ascribed to increased electronic conductivity and/or passivation of surface recombination centers.[28,35–37] In addition, further improvements have been reported after modification of $BiVO_4$ with various additional hole extractors and/or OER catalysts, such as rhodium oxide,[30] vanadium oxide,[38] iron oxyhydroxide,[31] nickel hydroxide,[39] cobalt oxide,[33,40,41] cobalt hexacyanoferrate,[42] iron/nickel oxide,[3,20,37,43,44] or cobalt/nickel sulfide,[45] whereby the question of whether the improvement should be ascribed to enhanced water oxidation kinetics or to other factors (*e.g.*, enhanced charge extraction or passivation of surface recombination centers) is still a source of intense debate and seems to depend on specific catalysts and photoanode architectures.[42,46–50]

Well-defined polyoxometalates (POMs) – molecular metal oxide clusters – comprising redox-active transition metals, *e.g.* Co or Mn, are known to be effective catalysts in various (photo)electrocatalytic systems.[51–54] A prototypical example is the complex CoPOM ($Na_{10}[Co_4(H_2O)_2(PW_9O_{34})_2]$) with a Co_4O_4 core stabilized by oxidatively resistant polytungstate ligands.[54] Notably, this CoPOM has been reported to be an efficient *homogeneous* water oxidation catalyst,[54–56] though there is also some evidence that – depending on specific experimental conditions (*e.g.*, pH and composition of the electrolyte, catalyst concentration, applied electrode potential) – this CoPOM can also undergo conversion to cobalt oxide, and thus behave rather as a pre-catalyst for the formation of a heterogeneous water oxidation catalyst (CoO_x) which then often accounts for the major part of activity in water oxidation.[57,58] Very recently, there have been several reports of successful immobilization of CoPOM onto various photoanodes (*e.g.*, TiO_2, Fe_2O_3, $BiVO_4$,[59] or TiO_2/carbon nitride hybrids[60]), typically using diverse cationic polyelectrolytes (*e.g.*, polyethyleneimine) or N-doped carbon[61] as an interlayer or linker. However, the scope of CoPOM-modified photoanodes investigated so far is rather limited, and our knowledge of the factors governing the PEC performance of CoPOM-containing photoelectrochemical architectures is still underdeveloped, which makes the rational design of high-performance Co-POM-based photoanodes very challenging.

In the present work, we report significant improvements of the PEC performance of mesoporous $BiVO_4$ photoanodes using a combined strategy of Mo-doping and direct deposition of CoPOM *via* a simple impregnation protocol without any linkers or binders. The best-performing optimized Mo–$BiVO_4$/CoPOM photoanode exhibits a photocurrent density of 4.32 mA cm^{-2} at 1.23 V *vs.* RHE under AM 1.5G (1 sun) irradiation and an applied-bias photoconversion efficiency (ABPE) of ~0.73%, which is an improvement by a factor of 24 and 2.5 compared to pristine $BiVO_4$ (~0.03%) and Mo–$BiVO_4$ (~0.29%), respectively. Furthermore, we disentangle the respective contributions of the Mo-doping and modification with CoPOM to the performance enhancement and show compelling evidence that the beneficial role of CoPOM is related to enhanced kinetics of water oxidation. Finally, we provide several unprecedented insights into the effects of both Mo-doping (*e.g.*, Mo-induced limitation of photovoltage) and CoPOM modification (*e.g.*, compositional changes under operating conditions and significant electrolyte effects), which are of great importance for the further design and development of efficient photoanodes for water splitting.

2. Results and discussion

The detailed descriptions for the fabrication of $BiVO_4$ and Mo–$BiVO_4$/CoPOM films are given in the ESI.† The fabrication protocols (including doping concentration and co-catalyst loading) were optimized by screening for the highest photoelectrocatalytic activity in each case. In short, the $BiVO_4$ and Mo–$BiVO_4$ films were prepared *via* spin coating onto FTO glass substrates, followed by drying and calcination. The CoPOM complex was synthesized according to a previously reported method,[54] and deposited *via* impregnation to obtain Mo–$BiVO_4$/CoPOM photoelectrodes. The X-ray diffraction (XRD) patterns of all $BiVO_4$-based photoanodes exhibit the typical diffraction peaks of monoclinic scheelite $BiVO_4$ (Fig. S1a, ESI†), indicating that the crystal structure of $BiVO_4$ is not significantly altered upon Mo-doping or deposition of CoPOM. No shifts of diffraction peaks or new reflexes related to molybdenum oxide were detected, which suggests that Mo is present in low amounts as a homogenously distributed dopant without affecting the structure of $BiVO_4$. As expected, as the amount of deposited CoPOM was very low, it could be detected neither in XRD nor by using Fourier-transform infrared (FT-IR) spectroscopy (Fig. S1b, ESI†). However, the presence of CoPOM in Mo–$BiVO_4$/CoPOM was verified by transmission electron microscopy, energy dispersive X-ray spectroscopy (EDX) and X-ray photoelectron spectroscopy (XPS) (see below).

The morphology and film thickness of as-prepared $BiVO_4$, Mo–$BiVO_4$ and Mo–$BiVO_4$/CoPOM photoanodes were investigated by field emission scanning electron microscopy (FESEM). As shown in Fig. 1a, all of the films are composed of uniform and homogeneous worm-like nanoparticles with an average diameter of ~100 to 200 nm, forming a three-dimensional mesoporous structure with pore sizes in the range of tens of nanometers. The introduction of F-108 as a structural agent during the synthesis is responsible for inducing this porous architecture,[62] which serves as the foundation for all subsequent surface-modified photoanodes. Notably, both Mo doping shown in Fig. 1b and surface modification with CoPOM shown in Fig. 1c have no appreciable effect on the morphology of $BiVO_4$, retaining the typical porous structure. Fig. S2a–c (ESI†) shows the cross-section SEM images of all three photoanodes, showing that the material layers have a comparable thickness of 600 ± 20 nm. Since the structure of the Mo–$BiVO_4$ material is porous and the CoPOM was deposited *via* the impregnation method, a homogenous distribution of the co-catalyst throughout the porous layer is expected. To investigate the distribution of CoPOM, EDX elemental mapping was carried out. Both in the cross-section and the surface of Mo–$BiVO_4$/CoPOM, the

View Article Online
Materials Advances Paper

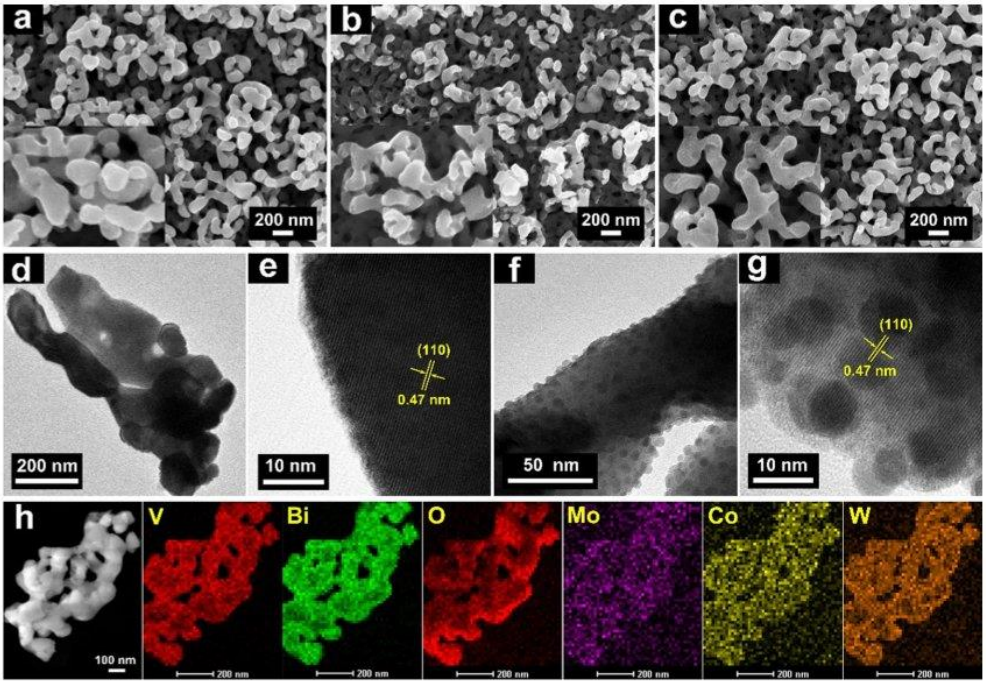

Fig. 1 FESEM images of (a) $BiVO_4$, (b) Mo–$BiVO_4$ and (c) Mo–$BiVO_4$/CoPOM. High-resolution TEM images of Mo–$BiVO_4$ (d) and (e) and Mo–$BiVO_4$/CoPOM (f) and (g). (h) EDX elemental mappings of Mo–$BiVO_4$/CoPOM. The lattice spacing of 0.47 nm is characteristic of the (110) planes of $BiVO_4$ (JCPDS card number 14-0688).[63]

elements Mo, Bi, V and O (representing Mo–$BiVO_4$) and Co, W (representing CoPOM) have been detected. These EDX mapping results demonstrate a very dense and uniform distribution of CoPOM within the mesoporous Mo–$BiVO_4$ structure (Fig. S2d and e, ESI†). A closer look with the help of high-resolution transmission electron microscopy (HRTEM) revealed that Mo–$BiVO_4$/CoPOM contains uniformly distributed amorphous nanospheres with a diameter of less than 10 nm (Fig. 1f and g). Since these nanospheres are completely absent in the (CoPOM-free) Mo–$BiVO_4$ photoanode (Fig. 1d and e), we assume the nanospheres to be CoPOM nanoparticles. These CoPOM nanospheres are closely spaced and homogeneously distributed on the surface of the Mo–$BiVO_4$ porous support (Fig. 1f and g). Furthermore, Fig. 1h shows the scanning transmission electron microscopy (STEM) image of Mo–$BiVO_4$/CoPOM with EDX mapping images of Bi, V, O, Mo, Co, and W, which again confirms the uniform distribution of the Mo dopant and of the CoPOM co-catalyst.

In order to further verify the presence of CoPOM in the Mo–$BiVO_4$/CoPOM and to investigate the surface chemical composition of the photoelectrode material, XPS analysis was carried out at $BiVO_4$, Mo–$BiVO_4$ and Mo–$BiVO_4$/CoPOM electrodes. As shown in Fig. S3a (ESI†), all expected signals of Mo, Bi, V, O, Na, Co and W elements are observed in the XP survey spectrum of Mo–$BiVO_4$/CoPOM, which indicates the successful preparation of the composite material. Two typical spin–orbit coupling peaks of Bi (at 164.3 eV and 159.1 eV for Bi $4f_{5/2}$ and Bi $4f_{7/2}$, respectively) are assigned to Bi^{3+} in $BiVO_4$ (Fig. 2a and Fig. S3b, ESI†).[64,65] The O 1s XP spectrum (Fig. 2b) can be fitted to two peaks located at 529.8 eV and 530.7 eV, which are assigned to the lattice oxygen in $BiVO_4$ and surface hydroxyl oxygen, respectively.[61,66] The vanadium signals (Fig. 2b and Fig. S3c, ESI†) can be fitted into two spin–orbit coupling peaks located at 524.0 eV (V $2p_{1/2}$) and 516.6 eV (V $2p_{3/2}$), which are characteristic of V^{5+} species in $BiVO_4$.[67–69] As shown in Fig. S3d (ESI†), the binding energies of the Mo $3d_{3/2}$ (235.1 eV) and Mo $3d_{5/2}$ (232.0 eV) peaks indicate that the molybdenum dopant is in the oxidation state of +VI.[61,65,70] The high-resolution XP spectrum of Co 2p (Fig. 2c) shows two core-level spin–orbit coupling peaks located at 797.1 (Co $2p_{1/2}$) and 781.2 eV (Co $2p_{3/2}$) with typical satellite peaks at 805.4 and 785.7 eV, indicating the presence of Co^{2+}.[70–72] In Fig. 2d, the two spin–orbit splitting peaks at 37.6 eV and 35.4 eV attributed to W $4f_{5/2}$ and W $4f_{7/2}$ confirm the presence of W^{6+}.[73] Importantly, the Co 2p and W 4f XPS signals of authentic CoPOM powder (Fig. S4, ESI†) are nearly identical to the corresponding XPS signals of the CoPOM in the electrode, which further corroborates the successful loading of CoPOM clusters into the porous structure of the Mo–$BiVO_4$/CoPOM photoelectrode.

The UV-vis electronic absorption spectra of $BiVO_4$, Mo–$BiVO_4$ and Mo–$BiVO_4$/CoPOM samples displayed in the ESI,† Fig. S5a and b (ESI†) show that all samples exhibit comparable

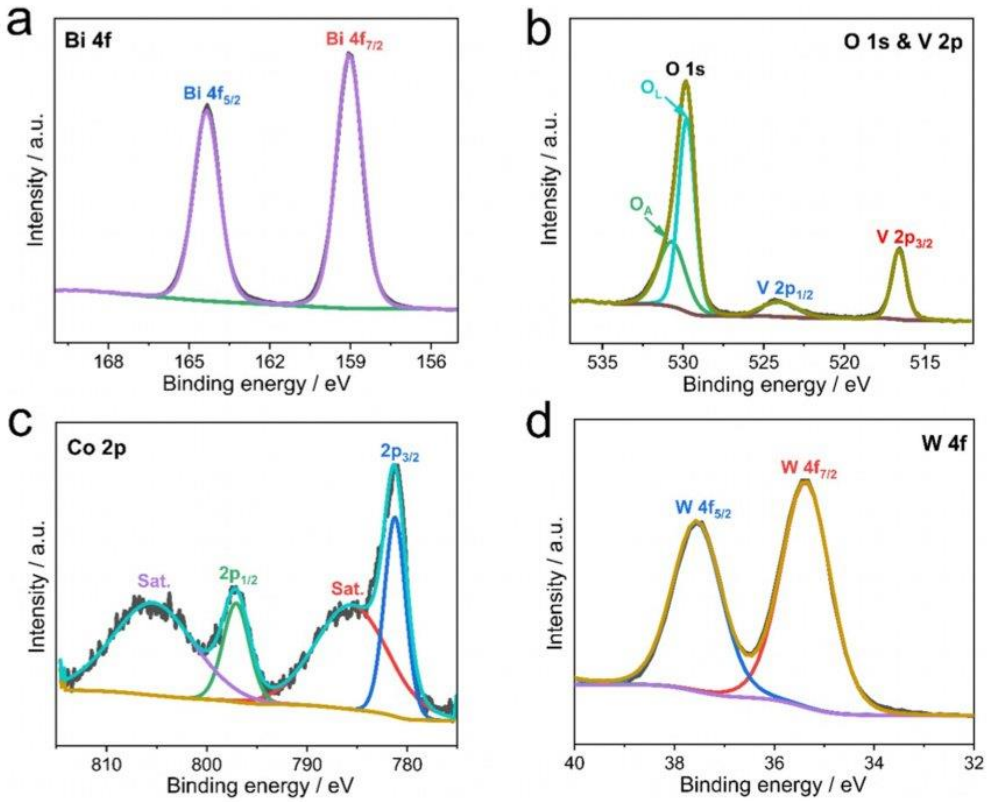

Fig. 2 XP spectra of the Mo–$BiVO_4$/CoPOM photoanode: (a) Bi 4f, (b) O 1s and V 2p, (c) Co 2p and (d) W 4f.

light absorption onsets at ~515 nm. In this context, we note that in the literature there are conflicting reports about whether $BiVO_4$ is a direct[74] or indirect[75] bandgap semiconductor. The bandgap energies of all photoelectrodes were estimated to be ~2.56 eV and ~2.50 eV for direct and indirect optical transition, respectively, using the Tauc formalism (Fig. S5c and d, ESI†). Importantly, these results reveal that the effects of Mo-doping and CoPOM deposition on the electronic absorption properties of $BiVO_4$ photoanodes are negligible, without any changes of the fundamental absorption edge, nor any significant parasitic light absorption by the CoPOM catalyst.

To investigate the combined effects of Mo-doping and modification by CoPOM on PEC performance of $BiVO_4$ photoanodes, the photocurrent density–potential (*J–V*) curves of $BiVO_4$, Mo–$BiVO_4$ and Mo–$BiVO_4$/CoPOM photoanodes were measured under intermittent AM 1.5G irradiation (1 sun) using a three-electrode setup in a 0.5 M sodium borate buffer electrolyte at pH 9.0 (Fig. 3a). The PEC performance of the photoanodes was optimized for (i) Mo doping concentration of $BiVO_4$, (ii) calcination temperature of Mo–$BiVO_4$, (iii) loading of the CoPOM in Mo–$BiVO_4$ and (iv) various pH values of borate electrolyte (the results of optimization protocols are summarized in the ESI,† Fig. S6). The content of Mo, Co and W elements in the Mo–$BiVO_4$/CoPOM photoanode optimized for the highest PEC efficiency was 0.79 at%, 0.95 at% and 1.92 at%, respectively, as estimated by the SEM-EDX analysis (Table S1, ESI†), which is also in line with the elemental analysis based on XPS results (Table S2, ESI†). The optimum calcination temperature was 450 °C and the optimal PEC performance was achieved in a borate buffer at pH 9.0.

Fig. 3a shows the *J–V* curves of various optimized photoanode architectures under back-side illumination (from the FTO-glass side). The $BiVO_4$ and Mo-doped $BiVO_4$ photoanodes reach a photocurrent density of 0.65 mA cm^{-2} and 2.53 mA cm^{-2} at 1.23 V *vs.* RHE, respectively. After the modification by CoPOM, the highest photocurrent density of Mo–$BiVO_4$/CoPOM increases up to 4.32 mA cm^{-2} at 1.23 V *vs.* RHE, which is an enhancement by the factor of 6.6, and 1.7 with respect to $BiVO_4$, and Mo–$BiVO_4$, respectively. Importantly, both Mo–$BiVO_4$ and Mo–$BiVO_4$/CoPOM photoanodes exhibit a remarkable cathodic shift of the photocurrent onset potential by ~0.5 V as compared to the pristine $BiVO_4$ photoanode, whereby the modification with CoPOM significantly increases photocurrents even at very low bias potentials, improving thus the fill-factor of the *J–V* curve. In other words, the combination of Mo-doping and CoPOM modifications results in a substantial increase of the photovoltage available for driving the water splitting reaction. In order to further disentangle the effects of Mo-doping and

View Article Online
Materials Advances Paper

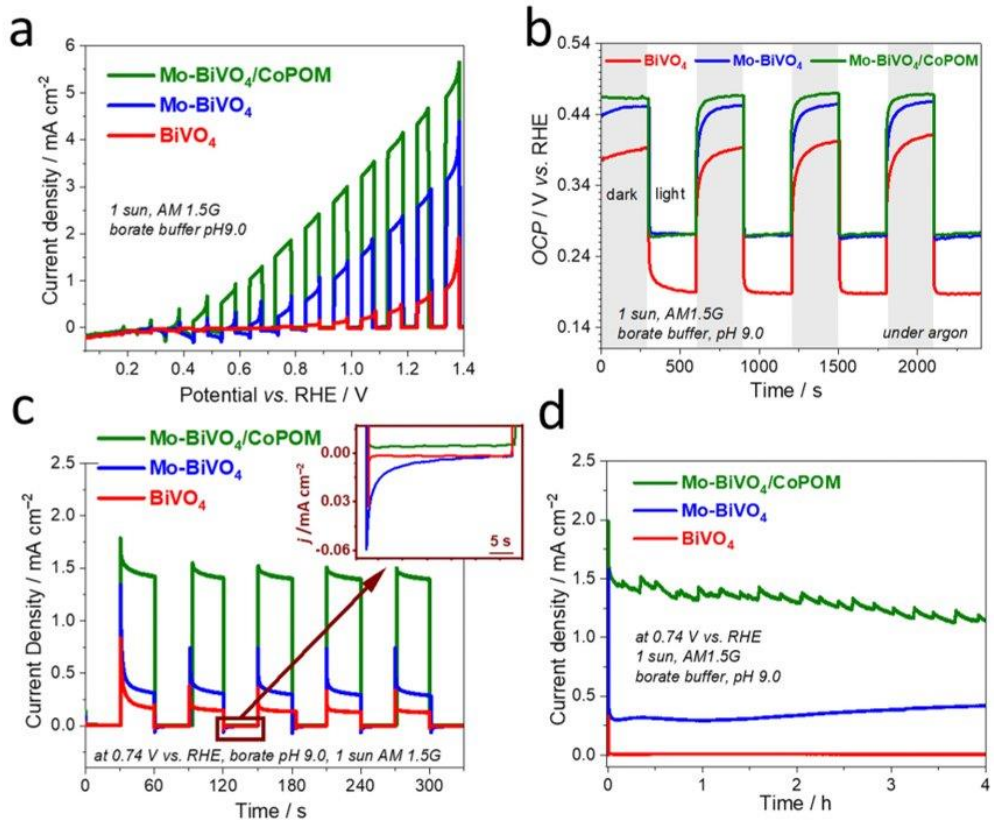

Fig. 3 (a) Linear-sweep voltammetry (LSV) curves recorded under intermittent AM 1.5G illumination in borate buffer (0.5 M, pH 9.0) at a cathodic sweep of 10 mV s^{-1}, (b) open-circuit potential (OCP) transients recorded under interrupted AM 1.5G (1 sun) illumination in 0.5 M borate buffer under an argon atmosphere (to prevent electron transfer to O_2), (c) photocurrent transients under AM 1.5G illumination, (d) stability chronoamperometric tests measured in borate buffer (0.5 M, pH 9.0) under AM 1.5G illumination (1 sun) at 0.74 V *vs.* RHE for all three photoanodes. All photocurrent measurements were carried out at least in triplicate, and representative average data are shown.

Co-POM modification, we also directly compared the *J–V* curves of Mo-free (undoped) $BiVO_4$/CoPOM with Mo–$BiVO_4$/CoPOM (Fig. S7, ESI†). Interestingly, the Mo–$BiVO_4$/CoPOM shows much higher photocurrents at relatively higher applied potentials (> 0.9 V *vs.* RHE), but at very low bias potentials (< 0.7 V *vs.* RHE) the situation is reversed and the Mo-free $BiVO_4$/CoPOM electrode yields even slightly higher photocurrents than the Mo–$BiVO_4$/CoPOM photoanode. These observations imply that (i) the combination of Mo-doping and Co-POM deposition significantly improves the photocurrent response in the whole potential range with respect to pristine $BiVO_4$, (ii) the enhancement due to the deposition of CoPOM is particularly pronounced at low bias potentials, *i.e.*, the beneficial negative shift of the photocurrent onset potential and improved fill-factor is mainly due to the CoPOM deposition, and (iii) at very low bias potentials the Mo-doping might even partially counteract the positive effects induced by the CoPOM deposition. The observation that the Mo-doping might be detrimental at relatively low bias potentials prompted us to measure the open-circuit photopotential (OCP) of all photoanodes (Fig. 3b). Under illumination, the observed OCP should correspond to the quasi-Fermi level of electrons $^*E_{Fn}$ (*i.e.*, the electrochemical potential of electrons) in the illuminated semiconductor, which in turn is directly related to the photocurrent onset potential (and the fill-factor at low bias potentials), and thus to the maximum achievable photovoltage of the water-splitting system. Indeed, the OCP results clearly show that for both Mo–$BiVO_4$ and Mo–$BiVO_4$/CoPOM the Mo-doping leads to a positive shift (by ~90 mV) of the maximum achievable quasi-Fermi level of electrons as compared to pristine $BiVO_4$. It should be noted that this observation is in stark contrast to the data for Mo-doped $BiVO_4$ (with similar doping concentration) reported by Ye *et al.*[34] who observed a slight negative shift of the OCP after Mo-doping. However, our observation of a positive shift of the OCP after the Mo-doping is completely in line with the observed decrease of photocurrent at low bias potentials induced by the Mo-doping (Fig. S7, ESI†), and suggests that the Mo-doping does not have only beneficial effects, such as the

enhancement of photocurrents at relatively high bias potentials, but also induces effects that are detrimental to the PEC performance.

Our experimental proof that the maximum achievable quasi-Fermi level of electrons is less negative after Mo-doping is significant and deserves a more detailed discussion. In this context, we point out that it is well-established that the maximum achievable photovoltage in metal oxide photoanodes is typically limited by the presence of intragap electron polaronic states formed upon self-trapping of excess electrons at reduced ionic sites (*e.g.*, Fe^{2+} in hematite Fe_2O_3, or V^{4+} in $BiVO_4$) in the lattice, accompanied by the displacement of surrounding atoms *via* electron–phonon interactions, forming thus a quasi-particle called polaron.[76,77] As the electron polaron level is typically significantly below the conduction band edge, it effectively traps electrons, limits their mobility, acts as a recombination center, and therefore establishes an inherent limitation of the maximum achievable quasi-Fermi level of electrons and photovoltage. For both pristine and doped $BiVO_4$, it is reported that the excess electrons are localized in hybridized vanadium $3d_{z^2}$ orbitals,[78,79] which is accompanied by elongation of the V–O bond by ~0.1 Å and formation of small polarons located *ca.* 0.88 eV below the conduction band edge.[80] Doping by molybdenum substitutes V^{5+} with ionized Mo^{6+} dopants, whereby the excess electron is readily localized at V^{4+} polaronic states.[78] The detrimental polaronic effects can be then (at least partially) avoided by applying a sufficient external electric bias, which, however, compromises the overall photoconversion efficiency. To summarize, the conductivity enhancement upon Mo-doping, which is apparent from enhanced photocurrents at higher bias potentials, is mainly due to the increased electron concentration, whereby the electron mobility is apparently not improved.[81] However, at low bias potentials the beneficial effect of the Mo-doping is counterbalanced by enhanced recombination due to the presence of deep electron polaron states,[78] which makes itself apparent by decreased photocurrents at low bias potentials and by a less negative OCP (*i.e.*, less negative quasi-Fermi level of electrons) under irradiation.

In order to assess the dynamics of photogenerated charge carriers, transient photocurrent measurements of pristine $BiVO_4$, Mo–$BiVO_4$ and Mo–$BiVO_4$/CoPOM photoanodes were carried out at a moderate bias potential of +0.74 V *vs.* RHE under chopped AM 1.5G (1 sun) illumination (Fig. 3c). On the timescale of this experiment (~minutes), the photocurrent response indicates an excellent short-term stability. Evidently, for both CoPOM-free photoanodes (red and blue line), the photocurrent spikes after switching on the light and negative current overshoots after switching off the light (see inset in Fig. 3c) are significantly more pronounced, demonstrating that in the absence of a water oxidation catalyst the charge carriers are prone to intense surface recombination.[82] In other words, in the absence of the CoPOM co-catalyst, the photogenerated holes do not react fast enough with water but accumulate in the surface layer of $BiVO_4$ or Mo–$BiVO_4$, thus enhancing the probability of recombination with electrons. The intense recombination of surface-accumulated holes and electrons leads to a rapid decrease of the photocurrent immediately after switching on the light, and continues even after the light is switched off, as is apparent from the negative current overshoot after switching off the light. In contrast, the current spikes are less pronounced, and the overshoots are nearly absent at the Mo–$BiVO_4$/CoPOM photoanode, which clearly demonstrates that the CoPOM co-catalyst efficiently extracts the holes photogenerated in the Mo–$BiVO_4$ layer and channels them to water molecules in the electrolyte solution. This explains the significant photocurrent enhancement upon the deposition of CoPOM shown in Fig. 3a and c. In this context, we also note that the addition of polyethyleneimine (PEI) as a cationic linker has no effect on the performance of the photoanodes (Fig. S8, ESI†), which highlights the intrinsically good electronic communication between the CoPOM and $BiVO_4$.

The long-term stability of the photoanode and its PEC performance is an important issue not only with respect to possible applications, but in our case also with respect to fundamental questions regarding the stability and/or compositional changes of the used CoPOM polyoxometalate catalyst under PEC operational conditions. As illustrated in Fig. 3d, the photocurrent generated by the investigated photoanodes was measured at a constant potential of +0.74 V *vs.* RHE for four hours under simulated AM 1.5G (1 sun) illumination, and only a very slight (by ~15%), yet continuous, decline of photocurrent density was observed for the optimized Mo–$BiVO_4$/CoPOM electrode. The small perturbations of the photocurrent are likely related to the release of oxygen bubbles from the electrode surface, which can be observed by the naked eye (see Video in the ESI†). The XRD patterns of all samples recorded after the PEC experiment show the typical diffraction peaks of monoclinic scheelite $BiVO_4$, indicating that the $BiVO_4$-based light absorber did not undergo any structural changes under the operating conditions (Fig. S9, ESI†), compared with Fig. S1a, ESI†). However, a question arises regarding the stability of the CoPOM co-catalyst under PEC operation since it has been reported that this polyoxometalate can – depending on experimental conditions – undergo conversion to cobalt oxide (CoO_x) which then often plays a chief role in water oxidation catalysis.[57,58] In order to shed light on the fate of CoPOM in our photoanodes during operation, we analyzed in detail both the composition of the Mo–$BiVO_4$/CoPOM photoanode after the PEC operation and the elemental composition of the electrolyte before and after the PEC experiments. First of all, we note that the small nanospheres attributed to CoPOM that could be seen before the PEC operation (Fig. 1f and g), were not observed anymore by HRTEM after the PEC operation (Fig. S10, ESI†), which indicates that the CoPOM cocatalyst has undergone (at least partially) morphological changes. Notably, the XPS analysis revealed that the signals related to the presence of W and Co are significantly weaker after the PEC operation (Fig. S11a, ESI†), whereby the XPS signature of Co is still well-detectable in the high-resolution XP spectrum and is very similar to the situation before the PEC operation (Fig. S11b, ESI†), compared with Fig. 2c). Notably, the surface

content of both Co and W derived from the XPS analysis is significantly decreased and the W/Co atomic ratio increased after the PEC operation (Table S3, ESI†). However, EDX analyses performed both from the top-view (Table S4, ESI†) and from the cross-sectional view (Table S5, ESI†) clearly show that both W and Co are still present in the photoelectrode in significant amounts, albeit with a significantly higher W/Co ratio than before the PEC operation. In this context, it should be noted that quantitative EDX analysis is rather challenging in this case due to the overlap between the Si–K (from the underlying glass) and W–M lines and since the content of Co and W is very low. Yet, the above differences in the composition before and after the PEC operation, in particular the changing ratio of W/Co, indicate that at least a partial dissolution of CoPOM and/or conversion of CoPOM to cobalt and tungsten oxides can occur during the PEC operation. Interestingly, an analysis of the composition of the electrolyte solution before and after the PEC operation using inductively coupled plasma atomic emission spectrometry (ICP-AES) did not detect any Co, and the concentration of W also did not increase (Table S6, ESI†). While we cannot completely rule out the dissolution of CoPOM as the dissolved amount of Co and W might be below the detection limit of ICP-OES, our results indicate that a complete dissolution of CoPOM is not an issue. All the above observations suggest that, though the CoPOM catalyst does not dissolve in the electrolyte solution, it does undergo, at least partially, conversion to cobalt oxide, as previously reported for borate electrolytes by Finke *et al.*[57] In other words, under our PEC operating conditions, the CoPOM co-catalyst should be rather conceived as a pre-catalyst, whereby a substantial part of water oxidation catalysis might be performed by cobalt oxide-based catalyst derived from CoPOM under operating conditions, as suggested by Finke *et al.* for CoPOM behavior in electrocatalysis.[57] However, in this context, it should be also noted that the activity and stability of various cobalt oxide-based water oxidation catalysts can strongly depend on their precursor and operating conditions, as minute changes in composition can often exert strong effects on catalysis. For comparison, we have therefore also tested the performance of our Mo–$BiVO_4$ photoanode after modification with a CoPi co-catalyst (*i.e.*, cobalt oxy-hydroxide formed upon photodeposition in Co^{2+} containing phosphate buffer) and with a $CoO(OH)_x$ co-catalyst (*i.e.*, cobalt oxy-hydroxide deposited *via* a two-step impregnation process).[11] These two photoanodes reached slightly lower (by 9% and 33%, respectively) photocurrents than the Mo–$BiVO_4$/CoPOM photoanode (Fig. S12, ESI†), which confirms that the "pre-history" of the catalyst can make a difference to its activity in photoanodes, and that the CoPOM-derived water oxidation catalyst exhibits optimal performance.

Furthermore, it is well established that the activity and stability of Co-based electrocatalysts can depend strongly on the electrolyte composition,[83] and our group previously observed strong electrolyte effects on the stability of $CoO(OH)_x$ water oxidation co-catalysts in hybrid photoanodes.[11] Therefore, we carried out a comparative analysis of the PEC operational stability of our photoanodes in borate and phosphate electrolytes. Specifically, we measured the linear sweep voltammetry under chopped illumination in the borate and the phosphate electrolyte at pH 9.0, and then repeated the measurement six times. In the borate buffer electrolyte at pH 9.0 (Fig. S13a–c, ESI†), the photocurrents for $BiVO_4$, Mo–$BiVO_4$ and Mo–$BiVO_4$/CoPOM photoanodes remained completely stable over all six cycles. In contrast, in the phosphate electrolyte at pH 9.0 (Fig. S13d–f, ESI†), Mo–$BiVO_4$/CoPOM exhibits a gradual decrease of photocurrents. The much higher operational stability of Mo–$BiVO_4$/CoPOM photoanodes in a borate electrolyte is also clearly apparent from the long-term (4 hours) chronoamperometric measurements at +0.74 V *vs.* RHE under 1 sun irradiation (Fig. S14, ESI†). In this context, two points are noteworthy. First, the clearly detrimental effect of phosphate anions on the PEC performance stability of Mo–$BiVO_4$/CoPOM is not simply related to the fact that the phosphate electrolyte is operated at pH 9.0 (*i.e.*, beyond its ideal buffering pH range around pH ~7), whereas the borate electrolyte operates at its optimal buffering capacity (pH ~9), since comparative experiments performed at pH 7.0 also revealed that the photocurrents at Mo–$BiVO_4$/CoPOM were more stable in the borate electrolyte than in the phosphate electrolyte (Fig. S15, ESI†). Second, similar to the case of the borate electrolyte, no cobalt could be detected in the phosphate electrolyte after PEC operation (Table S6, ESI†), suggesting that the dissolution of the co-catalyst is not the major reason for lower photoanode stability in phosphate electrolytes. We, therefore, conclude that the PEC operational stability of our photoanodes is related to the presence of specific electrolyte anions, whereby borate electrolytes are more beneficial as compared to phosphate electrolytes. Drawing on our previous discussion,[11] we assume that the Co(III/IV) ions, which are formed *in situ* during the water oxidation catalytic cycle and which represent, in terms of the HSAB theory, hard acid species, can interact more strongly with phosphate ions, which are much harder bases than the relatively large borate anions (present mainly as tetraborates). We speculate that the relatively stronger interaction of cobalt ions with phosphate anions can induce, during the PEC operation, changes in the interaction between the $BiVO_4$ light absorber and the co-catalyst, which eventually results in a lower observed stability of PEC performance in phosphate-containing electrolytes.

From a practical point of view, the applied bias photoconversion efficiency (ABPE) is the most important and informative performance metric for water splitting photoanodes. As presented in Fig. 4a, the maximum ABPE of 0.73% was determined for the Mo–$BiVO_4$/CoPOM photoanode at a potential of +0.86 V *vs.* RHE, which is an enhancement by a factor of 24 and 2.5 compared to pristine $BiVO_4$ (~0.03% at +1.07 V *vs.* RHE) and Mo–$BiVO_4$ (~0.29% at +0.98 V *vs.* RHE), respectively. (For a comparison of the PEC performance of our Mo–$BiVO_4$/CoPOM photoanodes with other $BiVO_4$-based photoanodes reported in the literature, see Table S7 (ESI†).) Apart from the significant increase of the photoconversion efficiency upon the combined effect of doping with Mo and modification with CoPOM, the

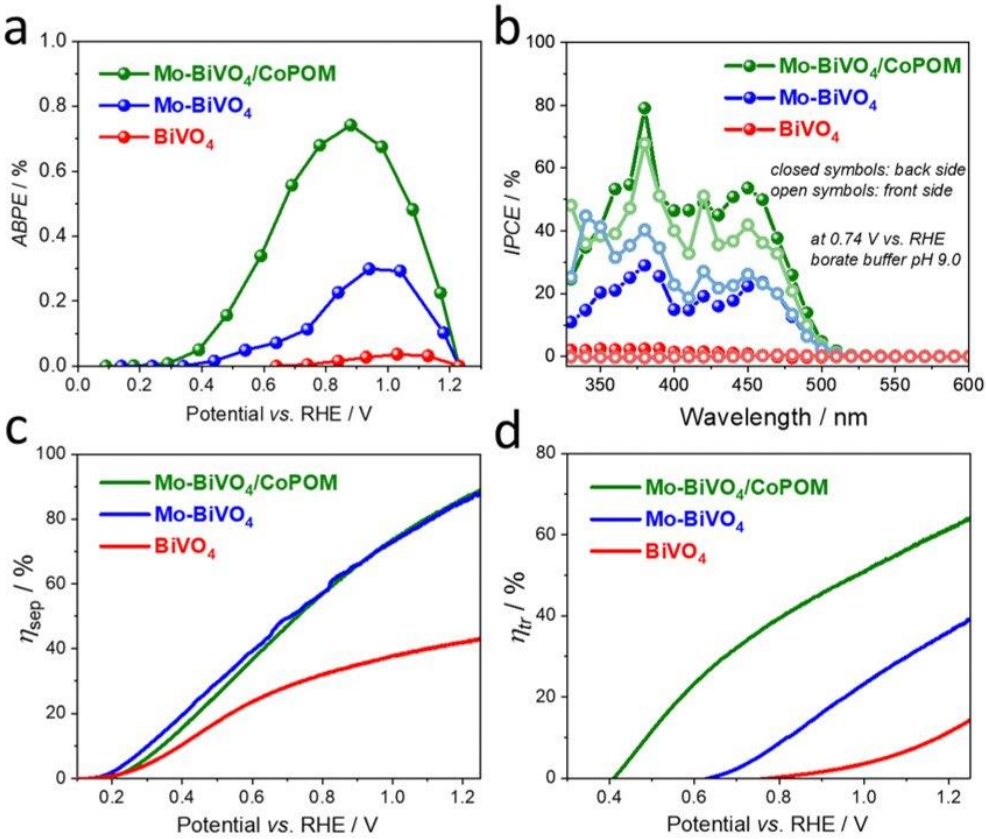

Fig. 4 (a) Applied bias photoconversion efficiency (ABPE). (b) IPCE spectra measured under intermittent monochromatic irradiation at 0.74 V *vs.* RHE. (c) Charge separation efficiency (η_{sep}) and (d) charge transfer efficiency (η_{tr}) for $BiVO_4$, Mo–$BiVO_4$ and Mo–$BiVO_4$/CoPOM photoanodes as a function of applied bias.

fact that the maximum power point is shifted to more negative bias potentials is particularly important in view of more feasible integration with photocathodes for hydrogen evolution in tandem solar-driven water splitting systems.

In order to obtain further insight into the PEC operation of our photoanodes, the wavelength-resolved incident photon-to-current conversion efficiency (IPCE) was measured at +0.74 V *vs.* RHE under illumination from the backside (BS, *i.e.* from the substrate side) and frontside (FS, *i.e.* from the electrolyte side) (Fig. 4b). The photoaction spectra show an onset at *ca.* 510 nm, which is in line with the electronic absorption properties of the photoanodes (compare with Fig. S5, ESI†). The IPCE values are, independently of the illumination side, the highest for the Mo–$BiVO_4$/CoPOM photoanode, followed by Mo–$BiVO_4$ and pure $BiVO_4$ over the whole wavelength range, which is in line with the photocurrent performance under polychromatic light at the same bias, as shown in Fig. S16 in the ESI† (see also Fig. 3c). From the mechanistic point of view, it is often worth looking at the difference in IPCE values under the FS and BS illumination for a given photoelectrode. The most notable difference is in the behavior of the Mo-free pristine $BiVO_4$ photoanode as compared to Mo–$BiVO_4$ and Mo–$BiVO_4$/CoPOM photoanodes. While the latter two photoanodes show a very small difference in IPCE values recorded under the FS and BS illumination, the Mo-free pristine $BiVO_4$ photoanode exhibits much larger (by the factor of ~10) IPCE values under the BS illumination than under the FS illumination (for a detailed view see the ESI,† Fig. S17). This is exactly what one expects for a porous photoanode in which the photocurrent is mainly limited by the transport of electrons through the porous network, *i.e.* by the electronic conductivity of $BiVO_4$. Under the FS illumination, most of the photogenerated electron–hole pairs are generated close to the film/electrolyte interface, and while the holes can readily react with water within the pores of the electrode, the electrons have to travel through the porous electrode to the underlying FTO back contact. Since under the BS illumination the electron–hole pairs are generated much closer to the FTO/film interface, the photogenerated electrons have a much shorter pathway to reach the FTO, resulting in significantly higher IPCE values under the BS illumination. Interestingly, the pristine $BiVO_4$ photoanode even exhibits a wavelength-dependent switching (at ~460 nm) of the sign of the photocurrent from anodic to

cathodic under the BS illumination and from cathodic to anodic under the FS illumination. This behavior can be again rationalized by the dominant effect of the poor electron transport properties of pristine $BiVO_4$ on the photocurrent response, which, in combination with the different penetration depths of short (below 460 nm) and long (above 460 nm) wavelengths of light and with the generally higher intensity of the visible light as compared to UV light in our setup, can even result in the reversal of the photocurrent sign. In this context, we note that while the potential-dependent photocurrent switching has been reported for $BiVO_4$ photoelectrodes,[84] the fact that at a specific bias potential (in our case a rather moderate bias potential of +0.74 V *vs.* RHE) the photocurrent switching at $BiVO_4$ can be controlled even by the light wavelength and by the illumination side has not been reported before, and would deserve further investigation given the importance of such phenomena for the development of photoelectrochemical optoelectronic switches.[85–89] In contrast to the behavior of the pristine $BiVO_4$ photoanode that is dominated by its low electronic conductivity, the very small difference in IPCE values under the FS and BS illumination observed for both Mo-doped samples Mo–$BiVO_4$ and Mo–$BiVO_4$/CoPOM (Fig. 4b) nicely illustrate that the beneficial effect of Mo-doping consists mainly in improving the electronic conductivity of Mo–$BiVO_4$ by increasing the electron concentration, as discussed in detail above.

Further valuable insights into the effects of Mo-doping and the role of the CoPOM co-catalyst on the PEC performance can be gained by determining the charge separation efficiency (η_{sep}) and the hole transfer efficiency (η_{tr}) as a function of applied potential (Fig. 4c and d), employing the methodology developed by Dotan *et al.* and Hamann *et al.* (for details see the ESI†).[17,90] Firstly, by integrating the electronic absorption spectra (Fig. S5b, ESI†) over the reference AM1.5G photon flux spectra, the maximum theoretically achievable photocurrents J_{max} were calculated to be 7.37 mA cm^{-2}, 7.36 mA cm^{-2} and 7.34 mA cm^{-2} for $BiVO_4$, Mo–$BiVO_4$ and Mo–$BiVO_4$/CoPOM, respectively. The photocurrent density of both Mo–$BiVO_4$ and Mo–$BiVO_4$/CoPOM photoanodes in the presence of Na_2SO_3 acting as a readily oxidizable reducing agent (*i.e.*, sacrificial hole scavenger) is significantly higher than that of pristine $BiVO_4$ and reaches 6.5 mA cm^{-2} as compared to 3.2 mA cm^{-2} at 1.23 V *vs.* RHE, respectively (Fig. S18, ESI†). Based on the above results, the charge separation efficiency η_{sep} is calculated and plotted in Fig. 4c. Notably, η_{sep} for Mo–$BiVO_4$ and Mo–$BiVO_4$/CoPOM is significantly higher than for pristine $BiVO_4$ in a wide potential range, whereby the enhancement is increasingly pronounced at more positive bias potentials. This behavior is in line with our finding that the beneficial effects of the improvement of electronic conductivity upon Mo-doping are more pronounced at positive bias potentials, whereby at very low bias potentials the positive effects are traded off against the detrimental effects of Mo-doping associated with increased concentration of intragap electron polaronic states. Interestingly, at higher bias potentials (>0.7 V *vs.* RHE), the Mo-doped Mo–$BiVO_4$ exhibits also an improved interfacial hole transfer efficiency η_{tr} with respect to pristine $BiVO_4$ (Fig. 4d). This positive effect of Mo-doping on η_{tr} can be interpreted as partial mitigation of excessive hole accumulation in the surface states, as reported recently by Selli *et al.*[28] After the deposition of CoPOM, the hole transfer efficiency η_{tr} (Fig. 4d) is greatly enhanced over the entire potential range and shifted to more cathodic potentials. For example, at 1.23 V *vs.* RHE, the η_{tr} increases from 13.1% for $BiVO_4$ to 37.8% after Mo-doping (Mo–$BiVO_4$) up to 63.0% for Mo–$BiVO_4$/CoPOM photoanode. Importantly, the charge separation efficiencies (η_{sep}) for Mo–$BiVO_4$/CoPOM and Mo–$BiVO_4$ are nearly identical in the whole potential range (Fig. 4c), which clearly indicates that the beneficial effect of CoPOM deposition consists chiefly in enhancing the catalysis of water oxidation. This is a significant result since the effect of co-catalysts on photocurrent enhancement at $BiVO_4$ photoanodes is a much-debated issue and, apart from enhancing the catalysis of water oxidation, other effects of various co-catalysts (*e.g.*, improved charge extraction or passivation of surface states) are often reported to be responsible for photocurrent enhancement in the literature reports.[42,46–50] Our results unambiguously demonstrate that in our photoanodes the beneficial effect of CoPOM deposition consists mainly in enhancing the rate of water oxidation by photogenerated holes.

Furthermore, the combined beneficial effects of Mo-doping and modification with CoPOM make themselves also clearly apparent in the results of the electrochemical impedance spectroscopy (EIS) analysis performed under irradiation (for details see the ESI,† Fig. S19). For the sake of simplicity, we used a Randles-type equivalent circuit model, where R_s represents the uncompensated series resistance, and R_{ct} in our case represents the combined charge transport and interfacial charge transfer resistance.[29] The fitted values of R_s and R_{ct} are shown in the ESI,† Table S8. The similar R_s values of three films indicate that the effect of doping and modification on the series resistance is negligible,[29] while the values of R_{ct} of Mo–$BiVO_4$ ($\sim$385 Ω) and Mo–$BiVO_4$/CoPOM ($\sim$113 Ω) decrease significantly as compared to pristine $BiVO_4$ ($\sim$2620 Ω), indicating that Mo-doping and CoPOM modification greatly enhance both charge transport (*i.e.*, conductivity) and the charge transfer, resulting in enhanced photocurrent density.[62,63]

Finally, in order to provide direct evidence for dioxygen evolution at our photoanodes, we performed photoelectrocatalytic OER measurements (Fig. 5a) in a borate solution (pH 9.0) at 0.74 V *vs.* RHE under AM 1.5G (1 sun) illumination. As expected, the Mo–$BiVO_4$/CoPOM photoanode exhibits an excellent oxygen evolution rate with an average faradaic efficiency of oxygen evolution of 102.1% ± 6.2% (calculated from three measurements; the error is taken as $\pm 1\sigma$, σ = standard deviation), which demonstrates that the conversion of H_2O to O_2 by photogenerated holes is practically quantitative and no side reactions (*e.g.*, photocorrosion or H_2O_2 evolution) occur. Similar results were obtained for Mo–$BiVO_4$ (100.0% ± 12.0%), whereby at pristine $BiVO_4$ the faradaic efficiency was slightly lower (90.3% ± 8.3%), suggesting a minor role of side reactions, possibly related to the photocorrosion.[91] These results suggest that Mo-doping has also a beneficial effect on the stability of the photoanodes under the PEC operation, which

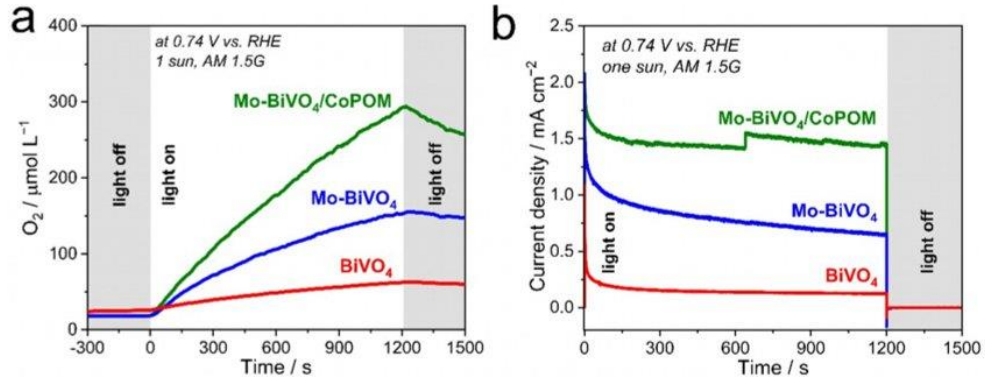

Fig. 5 (a) Dioxygen evolution and (b) corresponding photocurrent transients recorded under AM 1.5G one sun illumination at 0.74 V *vs.* RHE in a borate electrolyte (0.5 M, pH 9.0). All measurements were carried out at least in triplicate, and representative average data are shown.

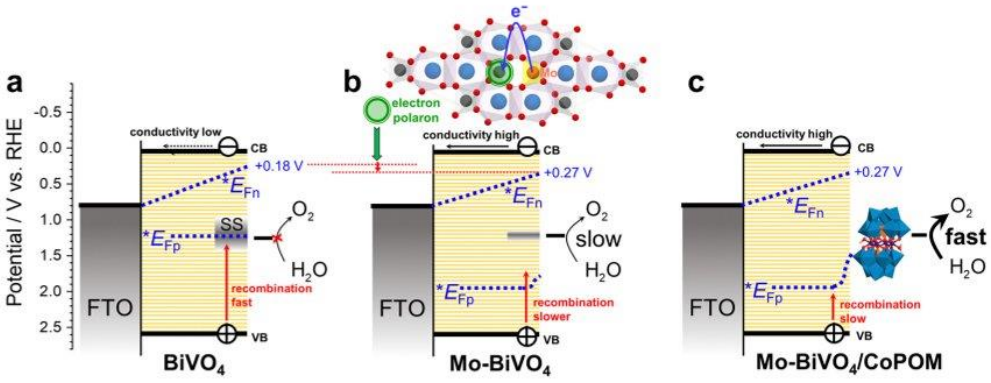

Fig. 6 A simplified scheme for (a) $BiVO_4$, (b) Mo–$BiVO_4$ and (c) Mo–$BiVO_4$/CoPOM at a moderate electrode bias of 0.74 V *vs.* RHE. Note that the band bending is assumed to be negligible due to the mesoporous nature of the $BiVO_4$ film. CB and VB stand for the conduction band edge and valence band edge, respectively; $^*E_{Fn}$ and $^*E_{Fp}$ stand for the quasi-Fermi level of electrons and holes in the mesoporous film, respectively.

again might be related to the decreased charge accumulation in the surface states,[28] since excessive hole accumulation in the surface states can be expected to render the dissolution of $BiVO_4$ more facile.

The key factors influencing the PEC performance of all electrodes at a moderate electrode bias of 0.74 V *vs.* RHE are summarized in Fig. 6. In pristine $BiVO_4$ (Fig. 6a) the photocurrents are negligible (*cf.* Fig. 3) due to intense surface recombination in the surface states (SS) and the very low conductivity of the $BiVO_4$ film. The Mo-doping in Mo–$BiVO_4$ (Fig. 6b) enhances the conductivity and passivates partially the surface states, resulting in a moderate photocurrent response (Fig. 3) due to the slow kinetics of water oxidation and the detrimental effect of electron polaronic states on the quasi-Fermi level of electrons ($^*E_{Fn}$). The deposition of the CoPOM catalyst (Fig. 6c) results in highly enhanced photocurrents (Fig. 3) due to significantly increased kinetics of water oxidation; however, the negative effects (shift of $^*E_{Fn}$) associated with the presence of Mo-induced polaronic states still persist, and represent an inherent limitation for the maximum achievable photovoltage in Mo-doped $BiVO_4$.

3. Conclusions

This study reports a facile two-in-one strategy to enhance the performance of $BiVO_4$ photoanodes for water oxidation by combining the bulk doping of $BiVO_4$ with molybdenum and its surface modification with a well-defined molecular cobalt polyoxometalate (CoPOM = $Na_{10}[Co_4(H_2O)_2(PW_9O_{34})_2]$). The resulting modified photoanodes show significantly improved photocurrent densities compared to non-modified references. Mechanistic investigations elucidate the contributions of the Mo-doping and modification with CoPOM to the performance enhancement for water oxidation. Mo-doping leads to enhanced electronic conductivity and passivation of surface states. The deposition of CoPOM enhances photocurrents across the whole potential range, which results in enhanced

water oxidation catalysis. Experimental evidence shows that under the PEC operating conditions the molecular CoPOM is, at least partially, disintegrated and converted to cobalt oxide, and is therefore considered as a pre-catalyst. In summary, this work establishes CoPOM-derived catalysts as effective water oxidation catalysts at $BiVO_4$ photoanodes, provides new insights into the combined effects of Mo-doping and modification with molecular cobalt polyoxometalates on the PEC performance of $BiVO_4$, and suggests that further progress in the development of $BiVO_4$ photoanodes depends critically on devising alternative doping strategies to overcome the negative polaronic effects associated with bulk doping of $BiVO_4$, since these detrimental effects set fundamental limits for the maximum achievable photovoltage and thus compromise the overall photoconversion efficiency.

Data availability

All datasets related to this work are available from the repository: 10.5281/zenodo.10401296.

Author contributions

C. S. and R. B. conceptualized and supervised the study and acquired funding. F. F., D. M., R. G., D. G., M. M. E. and R. L. performed investigations, acquired and analyzed data. All co-authors wrote and reviewed the manuscript.

Conflicts of interest

There are no conflicts to declare.

Acknowledgements

The authors gratefully acknowledge financial support from the Deutsche Forschungsgemeinschaft DFG (TRR 234 "CataLight", projects A4/B3/B6/C4, project no. 364549901, and project no. BE 5102/5-1). F. F. gratefully acknowledges the China Scholarship Council CSC for a PhD fellowship. R. B. and D. M. acknowledge funding from the European Union's Horizon Europe programme for research and innovation under grant agreement No. 101122061 (SUNGATE). D. G. acknowledges Deutsche Forschungsgemeinschaft (DFG) for a Walter Benjamin Fellowship (project no. 510966757). C. S. and D. G. acknowledge funding from the Top Level Research Area SusInnoScience of the federal state of Rheinland-Pfalz. The authors thank Joachim Bansmann (XPS analysis), Manuel Mundszinger (EDX analysis), and Changbin Im (TOC image) for their help.

References

1 S. Chu, Y. Cui and N. Liu, *Nat. Mater.*, 2017, **16**, 16–22.
2 I. Roger, M. A. Shipman and M. D. Symes, *Nat. Rev. Chem.*, 2017, **1**, 0003.
3 Z. Zhang, X. Huang, B. Zhang and Y. Bi, *Energy Environ. Sci.*, 2022, **15**, 2867–2873.
4 M. E. Ivanova, R. Peters, M. Müller, S. Haas, M. F. Seidler, G. Mutschke, K. Eckert, P. Röse, S. Calnan, R. Bagacki, R. Schlatmann, C. Grosselindemann, L.-A. Schäfer, N. H. Menzler, A. Weber, R. van de Krol, F. Liang, F. F. Abdi, S. Brendelberger, N. Neumann, J. Grobbel, M. Roeb, C. Sattler, I. Duran, B. Dietrich, M. E. C. Hofberger, L. Stoppel, N. Uhlenbruck, T. Wetzel, D. Rauner, A. Hecimovic, U. Fantz, N. Kulyk, J. Harting and O. Guillon, *Angew. Chem., Int. Ed.*, 2023, **62**, e202218850.
5 H. Dau, C. Limberg, T. Reier, M. Risch, S. Roggan and P. Strasser, *ChemCatChem*, 2010, **2**, 724–761.
6 J. Song, C. Wei, Z.-F. Huang, C. Liu, L. Zeng, X. Wang and Z. J. Xu, *Chem. Soc. Rev.*, 2020, **49**, 2196–2214.
7 J. Seo, H. Nishiyama, T. Yamada and K. Domen, *Angew. Chem., Int. Ed.*, 2018, **57**, 8396–8415.
8 A. G. Scheuermann, J. D. Prange, M. Gunji, C. E. D. Chidsey and P. C. McIntyre, *Energy Environ. Sci.*, 2013, **6**, 2487–2496.
9 S. Hu, M. R. Shaner, J. A. Beardslee, M. Lichterman, B. S. Brunschwig and N. S. Lewis, *Science*, 2014, **344**, 1005–1009.
10 I. A. Digdaya, G. W. P. Adhyaksa, B. J. Trześniewski, E. C. Garnett and W. A. Smith, *Nat. Commun.*, 2017, **8**, 15968.
11 L. Wang, D. Mitoraj, S. Turner, O. V. Khavryuchenko, T. Jacob, R. K. Hocking and R. Beranek, *ACS Catal.*, 2017, **7**, 4759–4767.
12 P. Longchin, D. Mitoraj, O. M. Reyes, C. Adler, N. Wetchakun and R. Beranek, *J. Phys. Energy*, 2020, **2**, 044001.
13 R. Gong, D. Mitoraj, R. Leiter, M. Mundszinger, A. K. Mengele, I. Krivtsov, J. Biskupek, U. Kaiser, R. Beranek and S. Rau, *Front. Chem.*, 2021, **9**, 709903.
14 J. T. Kirner and R. G. Finke, *J. Mater. Chem. A*, 2017, **5**, 19560–19592.
15 L. M. Peter, K. G. U. Wijayantha and A. A. Tahir, *Faraday Discuss.*, 2012, **155**, 309–322.
16 J. Park, J. Kang, S. Chaule and J.-H. Jang, *J. Mater. Chem. A*, 2023, **11**, 24551–24565.
17 Y. Gao and T. W. Hamann, *Chem. Commun.*, 2017, **53**, 1285–1288.
18 D. Peeters, O. M. Reyes, L. Mai, A. Sadlo, S. Cwik, D. Rogalla, H.-W. Becker, H. M. Schütz, J. Hirst, S. Müller, D. Friedrich, D. Mitoraj, M. Nagli, M. C. Toroker, R. Eichberger, R. Beranek and A. Devi, *J. Mater. Chem. A*, 2018, **6**, 10206–10216.
19 F. F. Abdi, L. Han, A. H. M. Smets, M. Zeman, B. Dam and R. van de Krol, *Nat. Commun.*, 2013, **4**, 2195.
20 T. W. Kim and K.-S. Choi, *Science*, 2014, **343**, 990–994.
21 F. F. Abdi, T. J. Savenije, M. M. May, B. Dam and R. van de Krol, *J. Phys. Chem. Lett.*, 2013, **4**, 2752–2757.
22 J. H. Kim and J. S. Lee, *Adv. Mater.*, 2019, **31**, 1806938.
23 M. B. Vishlaghi, A. Kahraman, N. Österbacka, E. Usman, E. Erdem, A. Sennaroğlu, J. Wiktor and S. Kaya, *J. Mater. Chem. A*, 2023, **11**, 16648–16658.
24 R.-T. Gao, N. T. Nguyen, T. Nakajima, J. He, X. Liu, X. Zhang, L. Wang and L. Wu, *Sci. Adv.*, 2023, **9**, eade4589.

25 R.-T. Gao and L. Wang, *Angew. Chem., Int. Ed.*, 2020, **59**, 23094–23099.
26 T. Zhou, S. Chen, J. Wang, Y. Zhang, J. Li, J. Bai and B. Zhou, *Chem. Eng. J.*, 2021, **403**, 126350.
27 T. Zhou, J. Wang, Y. Zhang, C. Zhou, J. Bai, J. Li and B. Zhou, *Chem. Eng. J.*, 2022, **431**, 133414.
28 A. Polo, M. V. Dozzi, I. Grigioni, C. Lhermitte, N. Plainpan, L. Moretti, G. Cerullo, K. Sivula and E. Selli, *Sol. RRL*, 2022, **6**, 2200349.
29 S. Wang, P. Chen, J.-H. Yun, Y. Hu and L. Wang, *Angew. Chem., Int. Ed.*, 2017, **56**, 8500–8504.
30 W. Luo, Z. Yang, Z. Li, J. Zhang, J. Liu, Z. Zhao, Z. Wang, S. Yan, T. Yu and Z. Zou, *Energy Environ. Sci.*, 2011, **4**, 4046–4051.
31 Y. Park, D. Kang and K.-S. Choi, *Phys. Chem. Chem. Phys.*, 2014, **16**, 1238–1246.
32 H. W. Jeong, T. H. Jeon, J. S. Jang, W. Choi and H. Park, *J. Phys. Chem. C*, 2013, **117**, 9104–9112.
33 M. Rohloff, B. Anke, S. Zhang, U. Gernert, C. Scheu, M. Lerch and A. Fischer, *Sustainable Energy Fuels*, 2017, **1**, 1830–1846.
34 K.-H. Ye, H. Li, D. Huang, S. Xiao, W. Qiu, M. Li, Y. Hu, W. Mai, H. Ji and S. Yang, *Nat. Commun.*, 2019, **10**, 3687.
35 A. J. E. Rettie, H. C. Lee, L. G. Marshall, J.-F. Lin, C. Capan, J. Lindemuth, J. S. McCloy, J. Zhou, A. J. Bard and C. B. Mullins, *J. Am. Chem. Soc.*, 2013, **135**, 11389–11396.
36 B. Pattengale and J. Huang, *Phys. Chem. Chem. Phys.*, 2016, **18**, 32820–32825.
37 A. Polo, I. Grigioni, M. Magni, A. Facibeni, M. V. Dozzi and E. Selli, *Appl. Surf. Sci.*, 2021, **556**, 149759.
38 B. Liu, X. Wang, Y. Zhang, L. Xu, T. Wang, X. Xiao, S. Wang, L. Wang and W. Huang, *Angew. Chem., Int. Ed.*, 2023, **62**, e202217346.
39 R.-T. Gao, D. He, L. Wu, K. Hu, X. Liu, Y. Su and L. Wang, *Angew. Chem., Int. Ed.*, 2020, **59**, 6213–6218.
40 S. K. Pilli, T. E. Furtak, L. D. Brown, T. G. Deutsch, J. A. Turner and A. M. Herring, *Energy Environ. Sci.*, 2011, **4**, 5028–5034.
41 F. F. Abdi and R. van de Krol, *J. Phys. Chem. C*, 2012, **116**, 9398–9404.
42 B. Moss, F. S. Hegner, S. Corby, S. Selim, L. Francàs, N. López, S. Giménez, J.-R. Galán-Mascarós and J. R. Durrant, *ACS Energy Lett.*, 2019, **4**, 337–342.
43 Y. Yang, S. Wan, S. Li, R. Wang, M. Ou, B. Liu and Q. Zhong, *J. Mater. Chem. A*, 2023, **11**, 1756–1765.
44 H. Yin, Y. Guo, N. Zhang, Y. Wang, S. Zhang and R. Jiang, *J. Mater. Chem. A*, 2023, **11**, 24239–24247.
45 Y. Lu, J. Su, J. Shi and D. Zhou, *ACS Appl. Energy Mater.*, 2020, **3**, 9089–9097.
46 Y. Ma, A. Kafizas, S. R. Pendlebury, F. L. Formal and J. R. Durrant, *Adv. Funct. Mater.*, 2016, **26**, 4951–4960.
47 Y. Ma, F. L. Formal, A. Kafizas, S. R. Pendlebury and J. R. Durrant, *J. Mater. Chem. A*, 2015, **3**, 20649–20657.
48 C. Zachäus, F. F. Abdi, L. M. Peter and R. van de Krol, *Chem. Sci.*, 2017, **8**, 3712–3719.
49 F. S. Hegner, I. Herraiz-Cardona, D. Cardenas-Morcoso, N. López, J.-R. Galán-Mascarós and S. Gimenez, *ACS Appl. Mater. Interfaces*, 2017, **9**, 37671–37681.
50 L. Francàs, S. Selim, S. Corby, D. Lee, C. A. Mesa, E. Pastor, K.-S. Choi and J. R. Durrant, *Chem. Sci.*, 2021, **12**, 7442–7452.
51 C. Streb, K. Kastner and J. Tucher, *Phys. Sci. Rev.*, 2019, **4**, 20170177.
52 B. Schwarz, J. Förster, M. K. Goetz, D. Yücel, C. Berger, T. Jacob and C. Streb, *Angew. Chem., Int. Ed.*, 2016, **55**, 6329–6333.
53 H. Park and W. Choi, *J. Phys. Chem. B*, 2003, **107**, 3885–3890.
54 Q. Yin, J. M. Tan, C. Besson, Y. V. Geletii, D. G. Musaev, A. E. Kuznetsov, Z. Luo, K. I. Hardcastle and C. L. Hill, *Science*, 2010, **328**, 342–345.
55 J. J. Stracke and R. G. Finke, *ACS Catal.*, 2013, **3**, 1209–1219.
56 J. W. Vickers, H. Lv, J. M. Sumliner, G. Zhu, Z. Luo, D. G. Musaev, Y. V. Geletii and C. L. Hill, *J. Am. Chem. Soc.*, 2013, **135**, 14110–14118.
57 S. J. Folkman, J. Soriano-Lopez, J. R. Galán-Mascarós and R. G. Finke, *J. Am. Chem. Soc.*, 2018, **140**, 12040–12055.
58 J. J. Stracke and R. G. Finke, *J. Am. Chem. Soc.*, 2011, **133**, 14872–14875.
59 D. Jeon, H. Kim, C. Lee, Y. Han, M. Gu, B.-S. Kim and J. Ryu, *ACS Appl. Mater. Interfaces*, 2017, **9**, 40151–40161.
60 R. Gong, D. Mitoraj, D. Gao, M. Mundszinger, D. Sorsche, U. Kaiser, C. Streb, R. Beranek and S. Rau, *Adv. Sustainable Syst.*, 2022, **6**, 2100473.
61 K. Fan, H. Chen, B. He and J. Yu, *Chem. Eng. J.*, 2020, **392**, 123744.
62 J. Jian, Y. Xu, X. Yang, W. Liu, M. Fu, H. Yu, F. Xu, F. Feng, L. Jia, D. Friedrich, R. van de Krol and H. Wang, *Nat. Commun.*, 2019, **10**, 2609.
63 C. Li, F. Feng, J. Jian, Y. Xu, F. Li, H. Wang and L. Jia, *J. Mater. Sci. Tech.*, 2021, **79**, 21–28.
64 R. P. Antony, P. S. Bassi, F. F. Abdi, S. Y. Chiam, Y. Ren, J. Barber, J. S. C. Loo and L. H. Wong, *Electro. Acta*, 2016, **211**, 173–182.
65 G. Talasila, S. Sachdev, U. Srivastva, D. Saxena and S. S. V. Ramakumar, *Energy Rep.*, 2020, **6**, 1963–1972.
66 Y. Liu, P. Deng, R. Wu, R. A. Geioushy, Y. Li, Y. Liu, F. Zhou, H. Li and C. Sun, *Front. Phys.*, 2021, **16**, 53503.
67 G. Silversmit, D. Depla, H. Poelman, G. B. Marin and R. D. Gryse, *J. Electron Spectrosc. Relat. Phenom.*, 2004, **135**, 167–175.
68 S. S. Mali, G. Ryeol Park, H. Kim, H. H. Kim, J. V. Patil and C. K. Hong, *Nanoscale Adv.*, 2019, **1**, 799–806.
69 L. Chen, E. Alarcón-Lladó, M. Hettick, I. D. Sharp, Y. Lin, A. Javey and J. W. Ager, *J. Phys. Chem. C*, 2013, **117**, 21635–21642.
70 M. C. Biesinger, B. P. Payne, A. P. Grosvenor, L. W. M. Lau, A. R. Gerson and R. S. Smart, *Appl. Surf. Sci.*, 2011, **257**, 2717–2730.
71 R. Chong, Y. Du, Z. Chang, Y. Jia, Y. qiao, S. Liu, Y. Liu, Y. Zhou and D. Li, *Appl. Catal., B*, 2019, **250**, 224–233.

72 S. Yi, B. Wulan, J. Yan and Q. Jiang, *Adv. Funct. Mater.*, 2019, **29**, 1801902.
73 U. Prasad, J. Prakash, S. K. Gupta, J. Zuniga, Y. Mao, B. Azeredo and A. N. M. Kannan, *ACS Appl. Mater. Interfaces*, 2019, **11**, 19029–19039.
74 A. Walsh, Y. Yan, M. N. Huda, M. M. Al-Jassim and S.-H. Wei, *Chem. Mater.*, 2009, **21**, 547–551.
75 J. K. Cooper, S. Gul, F. M. Toma, L. Chen, Y.-S. Liu, J. Guo, J. W. Ager, J. Yano and I. D. Sharp, *J. Phys. Chem. C*, 2015, **119**, 2969–2974.
76 C. Lohaus, A. Klein and W. Jaegermann, *Nat. Commun.*, 2018, **9**, 4309.
77 E. Pastor, M. Sachs, S. Selim, J. R. Durrant, A. A. Bakulin and A. Walsh, *Nat. Rev. Mater.*, 2022, **7**, 503–521.
78 V. Jovic, J. Laverock, A. J. E. Rettie, J.-S. Zhou, C. B. Mullins, V. R. Singh, B. Lamoureux, D. Wilson, T.-Y. Su, B. Jovic, H. Bluhm, T. Söhnel and K. E. Smith, *J. Mater. Chem. A*, 2015, **3**, 23743–23753.
79 K. E. Kweon, G. S. Hwang, J. Kim, S. Kim and S. Kim, *Phys. Chem. Chem. Phys.*, 2015, **17**, 256–260.
80 J. Wiktor, F. Ambrosio and A. Pasquarello, *ACS Energy Lett.*, 2018, **3**, 1693–1697.
81 F. Wu and Y. Ping, *J. Mater. Chem. A*, 2018, **6**, 20025–20036.
82 L. M. Peter, *Chem. Rev.*, 1990, **90**, 753–769.
83 Y. Surendranath, M. Dincă and D. G. Nocera, *J. Am. Chem. Soc.*, 2009, **131**, 2615–2620.
84 M. Antuch, P. Millet, A. Iwase and A. Kudo, *Appl. Catal., B*, 2018, **237**, 401–408.
85 K. Szaciłowski and W. Macyk, *C. R. Chim*, 2006, **9**, 315–324.
86 R. Beranek and H. Kisch, *Angew. Chem., Int. Ed.*, 2008, **47**, 1320–1322.
87 M. Long, R. Beranek, W. Cai and H. Kisch, *Electro. Acta*, 2008, **53**, 4621–4626.
88 S. Gawęda, A. Podborska, W. Macyk and K. Szaciłowski, *Nanoscale*, 2009, **1**, 299–316.
89 A. Podborska, M. Suchecki, K. Mech, M. Marzec, K. Pilarczyk and K. Szaciłowski, *Nat. Commun.*, 2020, **11**, 854.
90 H. Dotan, K. Sivula, M. Grätzel, A. Rothschild and S. C. Warren, *Energy Environ. Sci.*, 2011, **4**, 958–964.
91 S. Zhang, I. Ahmet, S.-H. Kim, O. Kasian, A. M. Mingers, P. Schnell, M. Kölbach, J. Lim, A. Fischer, K. J. J. Mayrhofer, S. Cherevko, B. Gault, R. van de Krol and C. Scheu, *ACS Appl. Energy Mater.*, 2020, **3**, 9523–9527.

3.2 (FF-2) "Double-Use" Strategy for Improving the Photoelectrochemical Performance of $BiVO_4$ Photoanodes using a Cobalt-Functionalized Polyoxotungstate

Fan Feng, Dariusz Mitoraj, Ekemena Oseghe, Carsten Streb*, Radim Beranek*

* Corresponding authors

Published in ACS Applied Materials & Interfaces, **2025**.

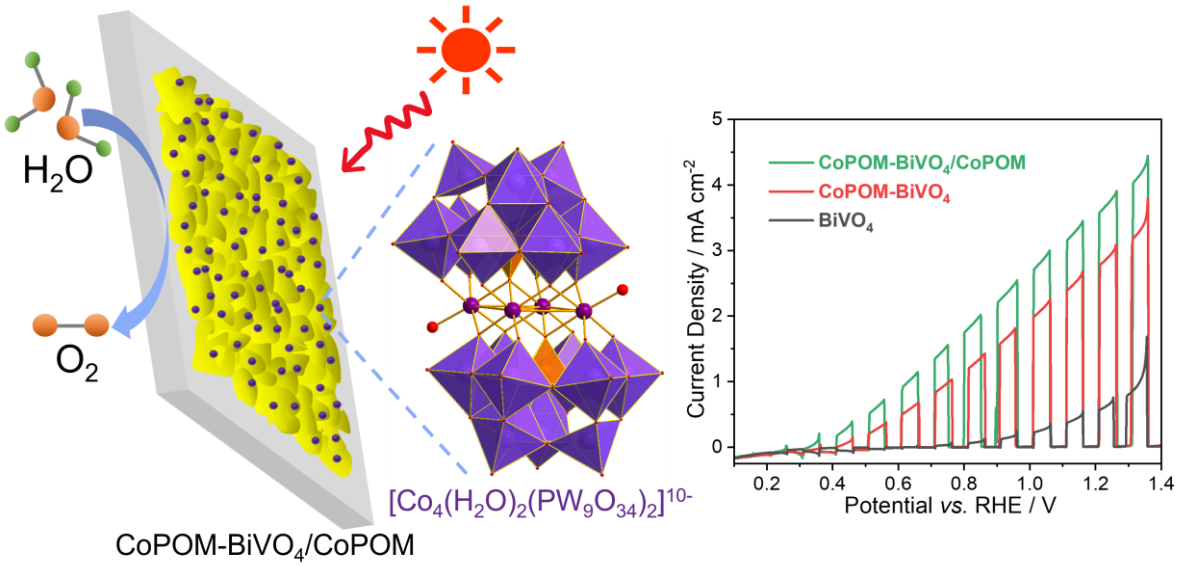

This publication reports on the synthesis and characterization a molecular cobalt-phosphotungstate (CoPOM = $Na_{10}[Co_4(H_2O)_2(PW_9O_{34})_2]$) is used both as a bulk doping agent as well as a surface-deposited water oxidation co-catalyst on $BiVO_4$ photoanodes for high-performance solar water splitting. The use of CoPOM for bulk doping of $BiVO_4$ is shown to enhance the electrical conductivity and improve the charge separation efficiency, resulting in the enhancement of the maximum applied-bias photoconversion efficiency (ABPE). The ratio of W/Co on the surface of photoanode is related to the activity and stability. In addition, modification of CoPOM-doped $BiVO_4$ with CoPOM as a surface co-catalyst enhances the hole extraction and improves the water oxidation kinetics, resulting in the overall enhancement of the ABPE.

Applied Materials & Interfaces, **2025**, 17, 3665−3675. **DOI:** 10.1021/acsami.4c21125.

Supporting Information can be found in chapter 6.2.

Author contributions:

Fan Feng:	Conceiving the idea for the project, fabrication of all electrodes and characterizations, photoelectrochemical and photophysical studies, data analyses and writing and revision of the manuscript.
Dariusz Mitoraj:	Analyzed data and provided discussions.
Ekemena Oseghe:	Analyzed data and provided discussions.
Carsten Streb:	Conceiving the research and finalizing the article.
Radim Beranek:	Conceiving the research and finalizing the article.

ACS APPLIED MATERIALS & INTERFACES

www.acsami.org Research Article

"Double-Use" Strategy for Improving the Photoelectrochemical Performance of $BiVO_4$ Photoanodes Using a Cobalt-Functionalized Polyoxotungstate

Fan Feng, Dariusz Mitoraj, Ekemena Oseghe, Carsten Streb,* and Radim Beranek*

Cite This: https://doi.org/10.1021/acsami.4c21125 Read Online

ACCESS | Metrics & More | Article Recommendations | Supporting Information

ABSTRACT: Doping and surface-modification are well-established strategies for the performance enhancement of bismuth vanadate ($BiVO_4$) photoanodes in photoelectrochemical (PEC) water splitting devices. Herein, a "double-use" strategy for the development of high-performance $BiVO_4$ photoanodes for solar water splitting is reported, where a molecular cobalt−phosphotungstate (CoPOM = $Na_{10}[Co_4(H_2O)_2(PW_9O_{34})_2]$) is used both as a bulk doping agent as well as a surface-deposited water oxidation cocatalyst. The use of CoPOM for bulk doping of $BiVO_4$ is shown to enhance the electrical conductivity and improve the charge separation efficiency, resulting in the enhancement of the maximum applied-bias photoconversion efficiency (ABPE) by a factor of ~18 to 0.54% at 0.87 V vs. RHE, as compared to pristine $BiVO_4$ (0.03% at 1.04 V vs. RHE). The ratio of W/Co on the surface of the photoanode is related to the activity and stability. In addition, modification of CoPOM-doped $BiVO_4$ with CoPOM as a surface cocatalyst enhances the hole extraction and improves the water oxidation kinetics, resulting in the overall enhancement of the ABPE to 0.79% (at 0.82 V vs. RHE), i.e., by a factor of ~26 with respect to pristine $BiVO_4$. This study establishes the "double-use" strategy involving CoPOMs as an effective, straightforward, and easily scalable approach for the development of high-quality photoanodes for solar water splitting and highlights the future potential of utilizing well-designed polyoxometalates as precursors for the synthesis of energy materials.

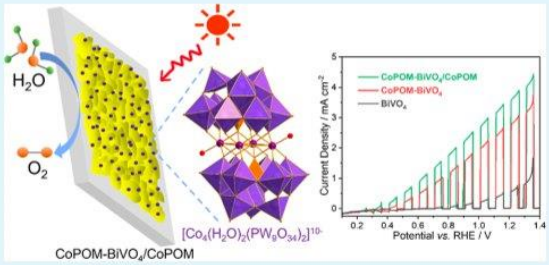

KEYWORDS: *$BiVO_4$, polyoxometalate, oxygen evolution, photoelectrode, photoelectrocatalysis*

1. INTRODUCTION

Photoelectrochemical (PEC) water splitting using semiconductor photoelectrodes is regarded as a promising and sustainable strategy to address the future supply of energy in a sustainable way.[1,2] However, the search for robust and efficient photoanode materials for water oxidation remains one of the biggest challenges for practical applications.[3,4] Bismuth vanadate ($BiVO_4$) is one of the most promising photoanode materials as it combines a suitable bandgap (ca. 2.4−2.6 eV) and good stability under typical operating conditions in aqueous solutions.[5,6] When compared with other metal oxides, such as α-Fe_2O_3, $BiVO_4$ exhibits charge carrier lifetimes that are 4 orders of magnitude higher and hole diffusion length 1 order of magnitude longer.[7−9] Nevertheless, pristine $BiVO_4$ still suffers from poor bulk electronic conductivity, ineffective hole extraction, and a slow rate of water oxidation.[7,10] As a result, the reported photocurrent densities at nonmodified $BiVO_4$ are typically much lower than the maximum theoretical value of 6.4−8.9 mA cm^{-2} under AM 1.5G illumination, corresponding to maximum solar-to-H_2 conversion efficiencies of 8−11%.[11,12] Thus, designing straightforward, scalable strategies to overcome these drawbacks of $BiVO_4$ materials represents an important research agenda, whereby the best-performing $BiVO_4$-based photoanodes reported so far typically employed doping by molybdenum or tungsten combined with surface functionalization by Ni/Fe-(oxy)hydroxides as cocatalysts.[13−16]

One recent approach to modify $BiVO_4$ photoelectrodes is the incorporation of polyoxometalates (POMs) as single-source molecular precursors. POMs are molecular metal oxide clusters formed by self-assembly in solution.[17−19] Of specific interest in this context is the cobalt-functionalized polyoxometalate $[Co_4(H_2O)_2(PW_9O_{34})_2]^{10-}$ (CoPOM), where a $\{Co_4O_4\}$ core is stabilized by two oxidatively resistant polyoxotungstate ligands.[20−22] The compound has been reported as an active water oxidation catalyst (WOC) as well

Received: December 2, 2024
Revised: December 18, 2024
Accepted: December 18, 2024

as precursor to highly reactive cobalt oxyhydroxides, so that operation under homogeneous or heterogenized conditions is possible.[19,23] This in turn has attracted major interest for surface-deposition as cocatalyst on $BiVO_4$ photoanodes. For example, Ryu et al. successfully designed a photoanode by depositing a thin film of cationic polyelectrolytes and anionic CoPOM-WOCs on the surface of various photoelectrode materials (e.g., Fe_2O_3, $BiVO_4$, and TiO_2) for improving the PEC performance as well as stability.[24] Fan et al. reported CoPOM as a novel molecular cocatalyst deposited on N-doped carbon (N/C) to boost the charge separation and injection of $BiVO_4$ photoanodes for PEC water oxidation.[25] Some of us have recently reported direct linking of CoPOMs to the surface of Mo-doped $BiVO_4$ photoanodes. The system showed significantly enhanced PEC performance, featuring lower photocurrent onset potentials and higher charge transfer efficiency.[26] These initial studies suggest that CoPOM is a promising cocatalyst for PEC water oxidation at $BiVO_4$ photoanodes as it improves the photogenerated hole extraction and enhances the oxygen evolution reaction kinetics. This inspired the present study to explore how a "double-use" of bulk and surface deposition of CoPOM can be used to optimize the performance.

Notably, transition metal doping is an established strategy to improve the conductivity of $BiVO_4$ and promote PEC performance. For example, He et al. developed $BiVO_4$ nanoflake array films codoped with Mo and W to increase the conductivity of $BiVO_4$ and to slightly to enhance the water oxidation kinetics.[27] Fang et al. reported that cobalt ion-doped $BiVO_4$ photoanodes exhibit an improved PEC performance, rationalized by the fact that a part of Co ions are doped into the $BiVO_4$ lattice to increase its electronic conductivity, whereby excess Co ions form a Co_3O_4 cocatalyst on the $BiVO_4$ surface.[28] Shi et al. reported that W-doped $BiVO_4$ shows a higher donor density and a higher concentration of surface states that can act as reaction sites, leading thus to improvements of both conductivity and surface catalytic activity.[29] To date, using POMs as a doping agent has been reported, for example, in the fields of gas sensing application,[30,31] dye-sensitized[32] or perovskite[33,34] solar cells, thiol detection,[35] and photocatalysis.[36] Due to the abundancy of transition metals involved in typical POMs, they also hold potential as doping agents in PEC water splitting systems. In view of enhancing the electron extraction and transport from $BiVO_4$ to the underlying FTO conductive glass substrate, Xi et al. fabricated composite photoanodes consisting of $BiVO_4$ and selected POMs, such as $[H_3PW_{12}O_{40}]$ (PW_{12}) and $K_6[CoW_{12}O_{40}]$ (CoW_{12}).[37] However, CoPOMs have rarely been used as doping agent to manipulate the electronic structure of $BiVO_4$ film photoanodes in a PEC water splitting system, and—to the best of our knowledge—CoPOM has not been used both as a dopant as well as a cocatalyst for $BiVO_4$ photoanodes.

Herein, we report a "double-use" strategy to modify $BiVO_4$ photoanodes using CoPOM simultaneously as both a doping agent and a cocatalyst in $BiVO_4$ photoanodes. We show that the combination of both modification routes results in significantly increased photocurrent densities compared with pristine (nonmodified) $BiVO_4$ and discuss in detail the mechanistic aspects of the improved activity and stability. These results establish the "double-use" strategy involving CoPOMs as a facile and scalable approach for the development of photoanodes for PEC water splitting.

2. EXPERIMENTAL SECTION

2.1. Materials. Fluorine-doped tin oxide (FTO) Pilkington TEC glass was purchased from XOP (XOP Glass, Castellón, Spain). Ethylene glycol ($C_2H_6O_2$, ≥99%) and boric acid (H_3BO_3, 99.5%) were provided by Carl Roth Gmbh & Co. KG. Sodium hydroxide (NaOH, 98.7%) was obtained from Fisher Scientific. Cobalt (II) nitrate hexahydrate ($Co(NO_3)_2{\cdot}6H_2O$, 98%), bismuth (III) nitrate pentahydrate ($Bi(NO_3)_3{\cdot}5H_2O$, ≥98.0%), triblock copolymer F-108, sodium sulfite (Na_2SO_3, 98%), and sodium phosphate (Na_2HPO_4, 99 + %) were supplied by Sigma-Aldrich. Sodium tungstate dihydrate ($NaWO_4{\cdot}2H_2O$) was provided by Merck. Vanadyl (IV) acetylacetonate ($C_{10}H_{14}O_5V$, 99%) was obtained from Acros Organics. Hydrochloric acid (HCl_{aq}, 37%), glacial acetic acid (CH_3COOH, 100%), and sodium chloride (NaCl, 99.7%) were purchased from VWR.

2.2. Synthesis of CoPOM. The CoPOM complex was synthesized using a slightly modified literature route.[19] Briefly, $NaWO_4{\cdot}2H_2O$ (35.62 g, 0.108 mol), $Na_2HPO_4{\cdot}7H_2O$ (1.70 g, 0.012 mol), and $Co(NO_3)_2{\cdot}6H_2O$ (6.98 g, 0.024 mol) were dissolved in 100 mL of deionized water in a 200 mL round-bottom flask. After the pH was adjusted to 7 using 9 M aqueous HCl solution under magnetic stirring, the purple suspension was stirred and refluxed at 105 °C bath temperature for 2 h. After reflux, the solution was saturated with 36 g of NaCl and allowed to cool to room temperature. The resulting purple crystals were collected, quickly washed with approximately 30 mL of water, and recrystallized from hot water. The purity of CoPOM was confirmed by Fourier transform infrared spectroscopy (FT-IR).

2.3. Preparation of CoPOM-Doped-$BiVO_4$ (Labeled Composite 1). In a typical synthetic procedure, a solution of 0.15 M $Bi(NO_3)_3{\cdot}5H_2O$ (0.2910 g, 0.6 mmol) was prepared in a solvent mixture of 1.5 mL of ethylene glycol, 2 mL of glacial acetic acid, 100 μL of 5 mM CoPOM aqueous solution (0.0027 g, 5×10^{-7} mol), and 400 μL of deionized water for **Composite 1**. (For the pure $BiVO_4$ reference, a similar synthetic mixture solvent was used containing 1.5 mL of ethylene glycol, 2 mL of glacial acetic acid, and 500 μL of deionized water. Other processes are the same as those for **Composite 1** samples.) After the mixture was stirred for 15 min, $VO(acac)_2$ (0.3182 g, 1.2 mmol) was added into the above solution, and the resulting solution was stirred at room temperature for 1 h. Then, 0.35 g triblock copolymer (F-108) as structure-directing agent was added in this solution, and the resulting solution was stirred at room temperature for 2 h. The resulting precursor solution was deposited on cleaned FTO glasses (2 × 2 cm) by spin-coating.[38] Spin-coating was performed for the ink precursor solution (75 μL per run) at 50 rps for 30 s, followed by baking at 250 °C for 5 min using a hot plate and then cooling down to room temperature naturally; the above coating and baking process was repeated five times. Finally, samples were annealed in a muffle oven with a heating rate of 3 °C/min and kept at 450 °C for 1 h, cooling down to room temperature naturally. After sintering, the sample was immersed in 1 M aqueous NaOH solution for 40 min to remove the excess V_2O_5, rinsed with deionized water, and dried with air flow. Different CoPOM-doping amount thin films were synthesized via the same procedure, except added amounts (50 μL, 150 μL, and 200 μL) of CoPOM aqueous solution (5 mM) in the solvent mixture were used instead of 100 μL. Deionized water and CoPOM aqueous solution in the solvent mixture make up a total of 500 μL, for example, 50 μL of CoPOM aqueous solution and 450 μL of deionized water in the mixture solvent for the CoPOM-$BiVO_4$ (50 μL) sample.

2.4. Preparation of CoPOM-Doped-$BiVO_4$/CoPOM (Labeled Composite 2). The **Composite 1** electrode was immersed in 50 mL 5 mM aqueous CoPOM solution (1.35 g, 2.5×10^{-4} mol) for 30 min, rinsed with distilled water, and dried in air flow. Different immersing time thin films were synthesized via the same procedure, except different immersing times (10 min and 60 min) were used instead of 30 min.

2.5. Preparation of Co/W/P-$BiVO_4$ (Labeled Composite 3). As a reference sample, a $BiVO_4$ photoanode containing the CoPOM components Co(II), W(VI), and P(V) was prepared as follows. A

https://doi.org/10.1021/acsami.4c21125
ACS Appl. Mater. Interfaces XXXX, XXX, XXX−XXX

solvent mixture was prepared containing 1.5 mL ethylene glycol, 2 mL glacial acetic acid, 100 μL 20 mM $Co(NO_3)_2{\cdot}6H_2O$ (0.58 mg, 2×10^{-6} mol) aqueous solution, 100 μL 90 mM $NaWO_4{\cdot}2H_2O$ (2.97 mg, 9×10^{-6} mol) aqueous solution, 100 μL 10 mM $Na_2HPO_4{\cdot}7H_2O$ (0.14 mg, 1×10^{-6} mol) aqueous solution, and 200 μL deionized water at room temperature. Other processes are the same as for **Composite 1** samples.

2.6. Preparation of Co/W-BiVO$_4$. A solvent mixture was prepared containing 1.5 mL ethylene glycol, 2 mL glacial acetic acid, 100 μL 20 mM $Co(NO_3)_2{\cdot}6H_2O$ (0.58 mg, 2×10^{-6} mol) aqueous solution, 100 μL 90 mM $NaWO_4{\cdot}2H_2O$ (2.97 mg, 9×10^{-6} mol) aqueous solution, and 300 μL deionized water at room temperature. Other processes are the same as for **Composite 1** samples.

2.7. Preparation of Co/P-BiVO$_4$. A solvent mixture was prepared containing 1.5 mL ethylene glycol, 2 mL glacial acetic acid, 100 μL 20 mM $Co(NO_3)_2$ $6H_2O$ (0.58 mg, 2×10^{-6} mol) aqueous solution, 100 μL 10 mM Na_2HPO_4 $7H_2O$ (0.14 mg, 1×10^{-6} mol) aqueous solution, and 300 μL deionized water at room temperature. Other processes are the same as for **Composite 1** samples.

2.8. Preparation of W/P-BiVO$_4$. A solvent mixture was prepared containing 1.5 mL of ethylene glycol, 2 mL of glacial acetic acid, 100 μL of 90 mM $NaWO_4{\cdot}2H_2O$ (2.97 mg, 9×10^{-6} mol) aqueous solution, 100 μL of10 mM $Na_2HPO_4{\cdot}7H_2O$ (0.14 mg, 1×10^{-6} mol) aqueous solution, and 300 μL of deionized water at room temperature. Other processes are the same as for **Composite 1** samples.

2.9. Preparation of Co-BiVO$_4$. A solvent mixture was prepared containing 1.5 mL of ethylene glycol, 2 mL of glacial acetic acid, 100 μL of 20 mM $Co(NO_3)_2$ $6H_2O$ (0.58 mg, 2×10^{-6} mol) aqueous solution, and 400 μL of deionized water at room temperature. Other processes are the same as for **Composite 1** samples.

2.10. Preparation of W-BiVO$_4$. A solvent mixture was prepared containing 1.5 mL of ethylene glycol, 2 mL of glacial acetic acid, 100 μL of 90 mM $NaWO_4{\cdot}2H_2O$ (2.97 mg, 9×10^{-6} mol) aqueous solution, and 400 μL of deionized water at room temperature. Other processes are the same as for **Composite 1** samples.

2.11. Preparation of P-BiVO$_4$. A solvent mixture was prepared containing 1.5 mL of ethylene glycol, 2 mL of glacial acetic acid, 100 μL of 10 mM $Na_2HPO_4{\cdot}7H_2O$ (0.14 mg, 1×10^{-6} mol) aqueous solution, and 400 μL of deionized water at room temperature. Other processes are the same as for **Composite 1** samples.

2.12. Characterization. The UV−vis absorption spectra were determined with a UV−vis spectrophotometer (UV-2600, Shimadzu, Japan) equipped with an integrating sphere. The absorbance (Abs) was calculated as follows

$$\text{absorptance (\%)} = 100\% - \text{reflectance (\%)} - \text{transmittance (\%)} \quad (1)$$

The baselines were recorded using an FTO glass and a $BaSO_4$ plate as references for transmittance and reflectance, respectively. Solid-state photoluminescence (PL) spectra were recorded under an excitation wavelength of 400 nm using a Shimadzu RF-6000 spectrometer. Scanning electron microscopy (SEM) was performed using a LEO Gemini 1530 scanning electron microscope operating at an acceleration voltage of 3 kV. The cross-section images of SEM were taken 75° pretilt for all photoanodes. Transmission electron microscopy (TEM) and energy-dispersive X-ray spectroscopy (EDX) elemental mapping were performed with FEI. FT-IR was performed on a Bruker Tensor 27 equipped with a PIKE Miracle Diamond ATR unit. X-ray photoelectron spectroscopy (XPS) measurements were performed with monochromatized Al Kα radiation (250 W, 15 kV) by using a PHI 5800 ESCA system. The binding energies were calibrated based on the C 1s peak of adventitious carbon (284.8 eV). X-ray diffraction (XRD) patterns were recorded on a Rigaku XRD-6000 diffractometer under the following conditions: 40 kV, 40 mA, and Cu Kα radiation (λ = 0.154 nm).

2.13. Photoelectrochemical Measurements. The PEC measurements were conducted using a CHI 760E electrochemical workstation or an SP-300 BioLogic potentiostat in a typical 3-electrode system with a Pt wire as the counter electrode, an Ag/AgCl (1.0 M KCl, 0.222 V vs. SHE) as the reference electrode, and film photoanodes as the working electrodes with a geometric irradiation area of 0.5 cm^2. A 150 W Xe lamp (L.O.T.-Oriel) equipped with a KG-3 (LOT-Quantum Design) heat-absorbing filter and an AM 1.5G filter was employed as the light source (light power intensity 100 mW cm^{-2}). The electrolyte was 0.5 M aqueous sodium borate, pH = 9.0. All electrodes were illuminated from the backside (through the FTO glass) unless noted otherwise.

All electrode potentials reported were converted to the RHE following the equation[39]

$$E_{RHE} = E_{Ag/AgCl} + 0.222 + 0.059 \times pH \quad (2)$$

where E_{RHE} is the pH-independent potential referenced against RHE, and $E_{Ag/AgCl}$ is the experimentally determined electrode potential referenced against an Ag/AgCl reference electrode.

The charge separation efficiency (η_{sep}) and the hole transfer efficiency (η_{tr}) were calculated using the approach reported by Dotan et al.[40] and Hamann et al.[41] The hole transfer efficiency (η_{tr}) was calculated using the equation

$$\eta_{tr} = J_{H_2O}/J_{Na_2SO_3} \quad (3)$$

where J_{H_2O} is the photocurrent measured in the absence of a hole scavenger, and $J_{Na_2SO_3}$ is the photocurrent in the presence of a hole scavenger (Na_2SO_3, 0.1 M).

The charge separation efficiency (η_{sep}) is calculated using the equation

$$\eta_{sep} = J_{Na_2SO_3}/J_{max} \quad (4)$$

where J_{max} is the maximal photocurrent density obtained by integrating the absorption spectrum of the photoanode (Figure S8, Supporting Information) between 300 and 560 nm over the reference AM 1.5G photon flux spectra (https://www.nrel.gov/grid/solar-resource/spectra-am1.5.html).

The incident photon-to-current conversion efficiency (IPCE) was recorded using a photoelectric spectrometer (Instytut Fotonowy Sp. z o.o.) with a 150 W xenon light source equipped with a monochromator, according to the equation[38]

$$\text{IPCE (\%)} = 1240 J_{ph}/(\lambda P) \times 100\% \quad (5)$$

where J_{ph} is the photocurrent density under monochromatic light, P is the monochromatic light power density, and λ is the irradiation wavelength.

The applied bias photoconversion efficiency (ABPE) was calculated using the equation[42]

$$\text{ABPE(\%)} = J_{ph} \times (1.23 - V_{app})/P \times 100\% \quad (6)$$

where J_{ph} is the photocurrent density, V_{app} is the applied bias (V vs. RHE), and P is the incident light intensity (100 mW cm^{-2}).

The transient decay time can be calculated from a logarithmic plot of parameter D, given by the equation[43]

$$D = (I_t - I_s)/(I_m - I_s) \quad (7)$$

where I_m is the photocurrent spike, I_t is the photocurrent at time t, and I_s is the steady-state photocurrent. I_s is achieved as the recombination and charge generation reach equilibrium. The transient decay time is defined as the time at which ln $D = -1$.

Oxygen evolution was detected using a FireSting optical fiber oxygen meter (PyroScience, GmbH) in a homemade airtight two-compartment cell. The oxygen collection efficiency of approximately 42.6% ± 1.6% was determined electrochemically using a Pt working electrode in a 3-electrode system and assuming a standard faradaic efficiency (FE, based only on dissolved O_2) of 100.0% ± 3.8%. The applied potential was 0.80 V vs RHE, and the electrolyte was bubbled with argon before the measurement.

https://doi.org/10.1021/acsami.4c21125
ACS Appl. Mater. Interfaces XXXX, XXX, XXX−XXX

ACS Applied Materials & Interfaces www.acsami.org Research Article

Scheme 1. "Double-Use" Strategy Utilizing CoPOM for Improved $BiVO_4$ Photoanodes: CoPOM Is Added to a Precursor Solution that Is Spin-Coated onto FTO-Glass Substrate and Annealed to Yield Doped $BiVO_4$ (= Composite 1); Further Impregnation by CoPOM Yields Doped $BiVO_4$ Surface-Modified with CoPOM (= Composite 2)

3. RESULTS AND DISCUSSION

After sample preparation as described in Scheme 1 and the Experimental Section, the phase purity and crystallinity of the $BiVO_4$ photoanodes were analyzed by powder X-ray diffraction (pXRD) (Figure S1, Supporting Information). All diffraction peaks can be indexed to monoclinic scheelite $BiVO_4$ (JCPDS card number 14-0688)[38] and to the FTO support. No crystalline impurities (such as V_2O_5) were detected. Moreover, no diffraction peaks associated with the CoPOM compound were observed. These observations highlight that the reported synthetic approach leads to thin-film $BiVO_4$ photoanodes, whereby the doping and surface-modification with CoPOM do not significantly alter the crystal lattice of the resulting system.

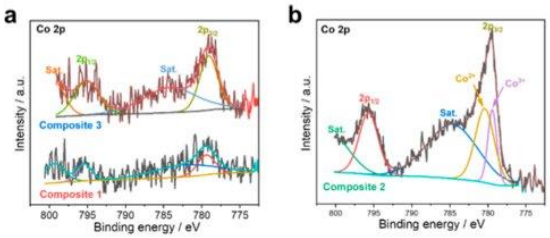

Figure 1. Co 2p XP spectra for (a) **Composite 1** and **Composite 3** and (b) **Composite 2** photoanodes.

XPS was used to assess the chemical environment and oxidation states of the relevant elements. XPS survey analysis indicates the presence of Bi, V, O, Co, W, and Sn signals on the surface of **Composite 2** photoanodes (Figure S2a, Supporting Information). The Sn signal is due to the use of FTO as a conductive transparent support.[44,45] The deconvoluted Bi 4f and V 2p spectra show the characteristic peaks for Bi^{3+} (at 164.9 and 159.6 eV for Bi $4f_{5/2}$ and Bi $4f_{7/2}$, respectively) and V^{5+} (at 522.7 eV for V $2p_{1/2}$ and 515.2 eV for V $2p_{3/2}$) expected for $BiVO_4$ (Figure S2b,c, Supporting Information).[46,47] In the O 1s spectrum, the two characteristic peaks located at 528.3 and 529.5 eV (Figure S2d, Supporting Information) are assigned to lattice oxygen in bismuth

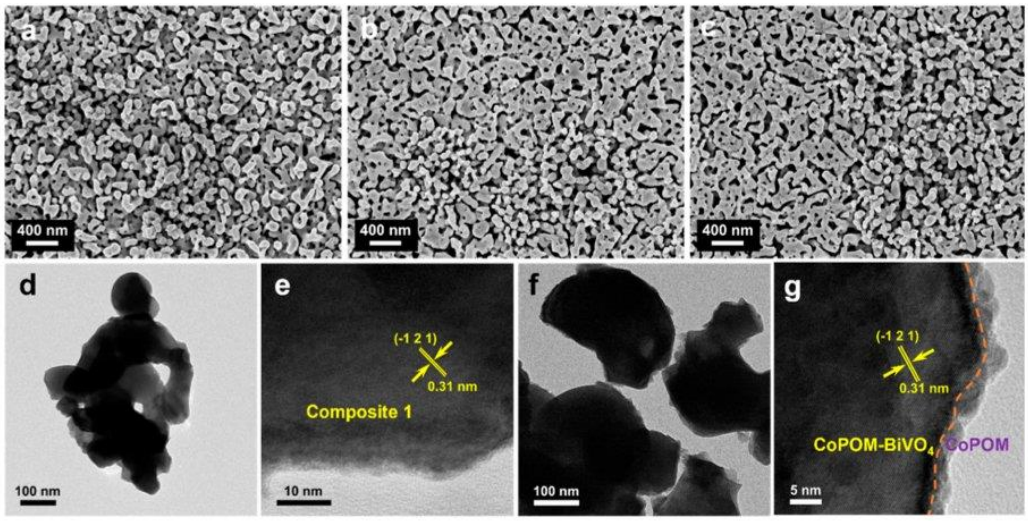

Figure 2. SEM images of (a) $BiVO_4$, (b) **Composite 1**, and (c) **Composite 2**. TEM and high-resolution TEM images for (d,e) **Composite 1** and (f,g) **Composite 2**.

https://doi.org/10.1021/acsami.4c21125
ACS Appl. Mater. Interfaces XXXX, XXX, XXX−XXX

ACS Applied Materials & Interfaces www.acsami.org Research Article

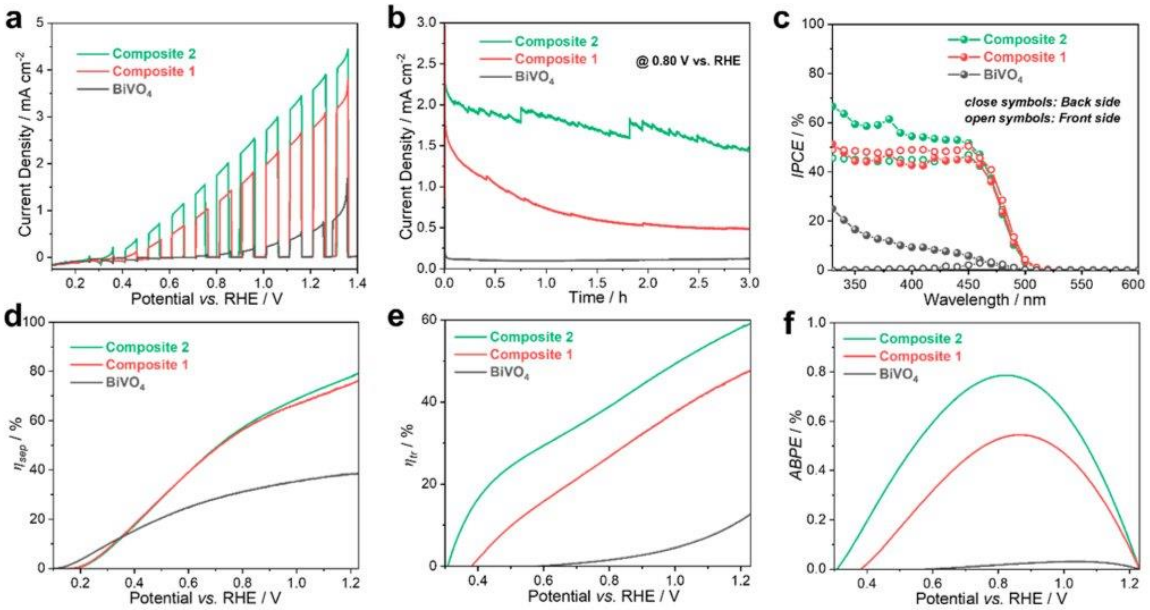

Figure 3. (a) Photocurrents recorded under AM 1.5G illumination in borate electrolyte at anodic sweep of 10 mV s^{-1}; (b) chronoamperometry curves under AM 1.5G illumination at 0.80 V vs. RHE; (c) IPCE spectra under intermittent monochromatic irradiation; (d) charge separation efficiency (η_{sep}), (e) hole transfer efficiency (η_{tr}), (f) ABPE plots for $BiVO_4$ and **Composite 1** and **Composite 2** photoanodes.

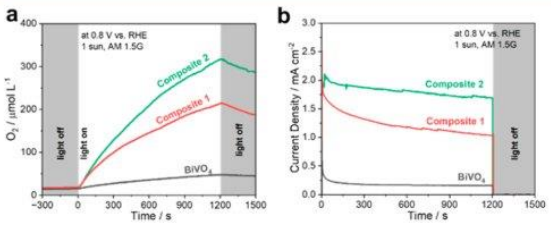

Figure 4. (a) Oxygen evolution and (b) corresponding photocurrent transients recorded under AM 1.5G at 0.80 V vs. RHE in a borate buffer for $BiVO_4$ and **Composite 1** and **Composite 2** photoanodes.

vanadate and surface hydroxyl oxygen, respectively.[48,49] Compared with pristine $BiVO_4$, the Bi 4f, V 2p, and O 1s peaks of **Composite 1** are shifted to higher binding energies by 0.1, 0.4, and 0.4 eV, respectively (Figure S2b–d, Supporting Information). This can be explained by interactions of dopant elements (Co^{3+}, W^{6+}, see below XPS analysis) from CoPOM with Bi, V, and O atoms. The slight shifts are expected due to the higher charge-densities of the dopants ($W^{6+} > V^{5+}$, $Co^{3+} > Bi^{3+}$).[50−52] These data support the successful incorporation of the CoPOM components (W^{6+}, Co^{3+}) into the $BiVO_4$ lattice. Note that similar shifts in binding energies are observed for the **Composite 3** reference photoanode (Figure S2b–d, Supporting Information).

To discriminate between the chemical states of elements originating from CoPOM and present either as a dopant or a cocatalyst, XPS analysis has been carried out, and the Co 2p and W 4f XP spectra are shown in Figures 1 and S3 (Supporting Information). As a reference, XPS analysis of the pristine CoPOM powder shows, as expected, the presence of Co^{2+} species at the binding energies of 797.0 and 781.1 eV for the Co $2p_{1/2}$ and Co $2p_{3/2}$ spin−orbit coupling peaks, respectively (Figure S4a, Supporting Information).[26] In contrast, the low-intensity Co 2p XPS data of the doped **Composite 1** sample (Figure 1a) show the Co $2p_{1/2}$ and Co $2p_{3/2}$ peaks located at 795.2 and 779.1 eV, which indicates the presence of Co^{3+}.[39,53] This suggests that Co^{2+} from the CoPOM dopant is oxidized to Co^{3+} during the photoanode annealing process. After additional surface modification with CoPOM, the resulting **Composite 2** photoanode exhibits signals characteristic of both Co^{2+} and Co^{3+} (Figure 1b). Taken together, these data indicate that while the Co dopant within the $BiVO_4$ bulk is present as Co^{3+}, the surface-deposited CoPOM retains its original Co^{2+} oxidation state, which is also in line with our previous study on CoPOM as cocatalyst.[26] In addition, the oxidation state of tungsten in all samples determined from the high-resolution XP spectra of W 4f was W^{6+} (Figure S3, Supporting Information), as expected for CoPOM derivatives.[25,54]

The morphology and film thickness of as-prepared $BiVO_4$ and **Composite 1** and **Composite 2** photoanodes were investigated by field emission scanning electron microscopy (FESEM). As shown in Figure 2a−c, all of the films are composed of worm-like nanoparticles forming a three-dimensional mesoporous structure. After the CoPOM doping and surface modification with CoPOM, the worm-like particle shape does not change significantly, as shown in Figure 2b,c, retaining the typical porous structure. However, after the CoPOM doping of $BiVO_4$, the average length of worm-like particles increases from 160 to 277 nm (see Figure S5d,e, Supporting Information) and the particles become more interconnected. The cross-sectional views (Figure S6, Supporting Information) show that the $BiVO_4$ layers have a comparable thickness of 520 ± 40 nm in all photoanodes. High-resolution transmission electron microscopy (HR-TEM) of **Composite 1** and **Composite 2** shows the presence of

https://doi.org/10.1021/acsami.4c21125
ACS Appl. Mater. Interfaces XXXX, XXX, XXX−XXX

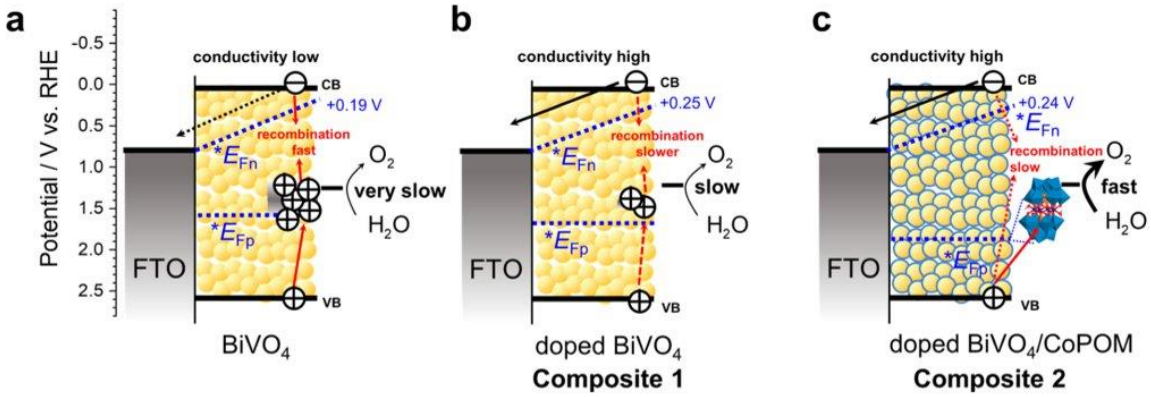

Figure 5. Simplified scheme summarizing the effect of the "double-use" strategy employing CoPOM on photoanodes at a moderate electrode bias of +0.80 V vs. RHE: (a) pristine $BiVO_4$ suffers both from ineffective electron transport through the mesoporous film and the accumulation of holes in surface states, resulting in enhanced recombination and very low photocurrents (compare with Figure 3a); (b) doped $BiVO_4$ (**Composite 1**) exhibits slower recombination due to higher conductivity and less pronounced hole accumulation; and (c) doped $BiVO_4$ surface-modified with CoPOM (**Composite 2**) exhibits the highest photocurrents due to both the high conductivity and the effective hole extraction and enhanced water oxidation by the CoPOM-derived surface cocatalyst. Note that the band bending is assumed to be negligible due to the mesoporous nature of the $BiVO_4$ film. CB and VB stand for the conduction band edge and valence band edge, respectively; $*E_{Fn}$ and $*E_{Fp}$ stand for the quasi-Fermi level of electrons and holes in the mesoporous film, respectively. The maximum values of $*E_{Fn}$ were taken as the maximum open-circuit photopotentials from the Figure S18a in the Supporting Information.

crystalline regions with a lattice d-spacing of 0.31 nm, which can be assigned to the (−121) plane of $BiVO_4$ (JCPDS 14-0688) (Figure 2e,g). As compared to **Composite 1** photoanodes (Figure 2e), additional surface modification with CoPOM leads to the presence of homogeneously distributed nanospheres with a size of ∼5 nm, as indicated by the orange dotted lines in Figure 2g. This suggests the formation of a CoPOM-derived surface layer on the **Composite 1** photoanodes, in line with our previous results.[21] To investigate the distribution of CoPOM, EDX elemental mapping was carried out. This analysis (Figure S7, Supporting Information) indicates the presence of Co and W elements, which is in line with the homogeneous distribution of CoPOM within the $BiVO_4$ bulk and on the $BiVO_4$ surface since the structure of the **Composite 1** material is porous and the CoPOM was deposited via impregnation.

The UV−vis electronic absorption spectra of all four samples displayed in Figure S8, Supporting Information, indicate that all samples exhibit nearly identical electronic absorption properties with an optical absorption edge at ∼530 nm. Therefore, we conclude that there is a negligible influence of either CoPOM-doping or Co/W/P-doping or the deposition of the CoPOM cocatalyst on the fundamental optical properties of our photoanodes, and all differences in photoelectrocatalytic behavior should be rather ascribed to changes in the electronic conductivity and surface catalytic properties.

To evaluate the performance of our photoanodes in water photooxidation, PEC measurements were conducted in a three-electrode setup under AM 1.5G (1 sun) illumination with a 0.5 M aqueous sodium borate solution (pH 9.0) as electrolyte. The photoanodes were optimized for the best PEC performance with respect to the amount of CoPOM used either as a bulk dopant and/or surface cocatalyst, as shown in Figure S9a,b, Supporting Information. As shown in Figure 3a, the pristine $BiVO_4$ photoanodes exhibit a relatively low photocurrent density (0.62 mA cm^{-2} at 1.23 V vs. RHE), which is mainly attributed to the poor electronic conductivity and sluggish oxygen evolution kinetics at the photoanode/electrolyte interfaces.[7,10] After CoPOM-doping, for **Composite 1**, a significantly improved photocurrent density (5-fold increase compared with pristine $BiVO_4$) is observed, reaching 2.86 mA cm^{-2} at 1.23 V vs. RHE. When the surface of the sample is further loaded with CoPOM as cocatalyst, the photocurrent density is further increased by a factor of ∼1.3 to 3.67 mA cm^{-2} at 1.23 V vs. RHE. Importantly, we observe a cathodic shift of the photocurrent onset potential by ∼0.3 V for **Composite 2** and ∼0.2 V for **Composite 1** compared with the nonmodified $BiVO_4$ photoanode (Figure 3a, see also Figure S10, Supporting Information). In other words, both CoPOM-doping and surface modification by CoPOM result in a significant increase of the photovoltage available for driving the water splitting reaction.[20] The reasons for this performance enhancement are discussed below. The dark current densities are similar for **Composite 1**, **Composite 2**, **Composite 3**, and $BiVO_4$ (Figure S10, Supporting Information) below the equilibrium potential of water oxidation (1.23 V vs. RHE), and the beneficial effects of CoPOM on electrocatalytic water oxidation reaction activity in the dark become apparent at bias potentials of >1.40 V vs. RHE.[55]

First, in order to gain insight into the role of the individual doping elements (Co, W, and P) present in CoPOM, we prepared also doped $BiVO_4$ samples where $NaWO_4{\cdot}2H_2O$, $Na_2HPO_4{\cdot}7H_2O$, and $Co(NO_3)_2{\cdot}6H_2O$ were used as sources of the respective elements, and identical molar amounts were incorporated as in the case of **Composite 1** photoanodes (see Figures 3a and S9c, Supporting Information). Notably, Co-doping of $BiVO_4$ exerts a positive influence on the photocurrent density also at lower electrode potentials (leading to the significant cathodic shift of the onset potential), while W-doping of $BiVO_4$ enhances photocurrents significantly only at higher bias potentials (>0.7 V vs. RHE). Interestingly, there is a clear beneficial synergistic effect when both Co- and W-doping of $BiVO_4$ are used. Furthermore, the photocurrent at

https://doi.org/10.1021/acsami.4c21125
ACS Appl. Mater. Interfaces XXXX, XXX, XXX−XXX

the **Composite 1** photoanode is slightly higher than that of the **Composite 3** photoanode in the full potential range. The possible reason is that the ratio of W/Co on the surface of $BiVO_4$ detected by XPS is different (2.29 for the **Composite 1** photoanode and 1.08 for the **Composite 3** photoanode), as shown in Table S1 (Supporting Information). We hypothesize that this difference in the W/Co ratio on the surface of the **Composite 1** and **Composite 3** photoanodes might be due to the different forms of the doping substances. For example, the structure of CoPOM is expected to be partially disintegrated but will still retain its core structure in the acid precursor solution, while the doping solution used for preparation of the reference **Composite 3** photoanode is fully homogeneous. Apparently, such small differences in the precursor chemistry can influence the W/Co ratio on the surface and impact the photocurrent generation.

Next, the photocurrent generation was tested at a constant potential of 0.80 V vs. RHE under prolonged (3 h) AM 1.5G (1 sun) illumination. As shown in Figure 3b, CoPOM-doped $BiVO_4$ showed a relatively fast and continuous decrease of photocurrent. To explore the reasons for the instability of **Composite 1** under PEC operation, we analyzed in detail the elemental composition of the surface for CoPOM-doped $BiVO_4$ before and after the PEC experiments, as shown in Figure S11 and Table S2, Supporting Information. Interestingly, the XPS analysis revealed that the signal related to the presence of Co is significantly stronger after PEC operation (Figure S11a, Supporting Information), while the signal of W practically did not change at all after PEC operation (Figure S11c, Supporting Information). Notably, the ratio of W/Co for the **Composite 1** photoanode significantly decreased after the PEC operation, from 2.29 for before PEC operation to 0.59 for after PEC operation (Table S2, Supporting Information). In other words, we see a similar trend as discussed above for the case of the **Composite 1** photoanode (higher ratio) and the **Composite 3** photoanode (lower ratio). We conclude that the PEC performance is related to the ratio of W/Co on the surface of photoanode, whereby a higher ratio of W/Co will result in better PEC performance. The underlying reasons are still under study. Previous reports indicated that W^{6+} sites can act as structure stabilizers to the OER active Co sites.[56] Therefore, a possible reason for this trend might be that at the lower ratios of W/Co, the low amount of W cannot prevent the pronounced leaching of Co from the $BiVO_4$ surface into the borate buffer electrolyte, leading eventually to the formation of cobalt borate (CoBi),[28] which is known to exhibit operational instability in $BiVO_4$/CoBi systems.[57]

Notably, employing CoPOM as a surface cocatalyst to modify the **Composite 1** photoanode turned out be highly beneficial as higher and much more stable photocurrents were observed (the green line in Figure 3b). The small jumps in the photocurrent were most probably due to the bubble release from the testing area, as observed visually during the PEC operation. We used XPS to analyze the elemental composition of the surface for **Composite 2** before and after the PEC experiments, as shown in Figure S11 and Table S3, Supporting Information. In contrast to **Composite 1**, the signals related to the presence of Co and W were significantly weaker after the PEC operation (Figure S11b,d, Supporting Information) with a slightly decreased ratio of W/Co for the **Composite 2** photoanode than before the PEC operation (Table S3, Supporting Information). In particular, the changes in signal intensities and ratio of W/Co indicate that a partial dissolution of the CoPOM cocatalyst and/or its conversion to cobalt and tungsten oxides can occur during the PEC operation, which is consistent with the findings discussed in detail in our previous study.[26] As shown in Figure S12a of the Supporting Information, the **Composite 3** shows a slightly lower photocurrent density during a 3 h stability measurement compared with **Composite 1**, which is also consistent with the lower W/Co ratio on the surface of **Composite 3** photoanodes (Table S1, Supporting Information).

Furthermore, the transient photocurrent measurements of pristine $BiVO_4$ and **Composite 1** and **Composite 2** photoanodes were investigated to assess the charge recombination dynamics at +0.80 V vs. RHE under chopped AM 1.5G (1 sun) illumination (Figure S12b, Supporting Information). The strong spike-like behavior of the photocurrent transients at pristine $BiVO_4$, a typical fingerprint of intense surface recombination due to slowly reacting holes accumulating in the surface states,[58] is clearly diminished to a large extent at the **Composite 1** and **Composite 2** samples, indicating reduced charge carrier recombination for these samples. In more quantitative terms, the diminished surface recombination is also reflected in the corresponding characteristic transient decay times[43] (see Figure S12d, Supporting Information), which increase from 1.1 s ($BiVO_4$) to 1.5 s (**Composite 3**) to 1.7 s (**Composite 1**) up to 3.5 s for **Composite 2**. These data demonstrate the importance of surface modification by CoPOM for reducing the surface recombination kinetics and highlight the improved surface catalysis as one of the key beneficial effects of the "double-use" strategy on the overall photoanode performance.

The performance of all three photoanodes was also examined by repeated linear sweep voltammetry (LSV) under chopped illumination in an aqueous borate electrolyte at pH 9.0 (Figure S13, Supporting Information). For the modified **Composite 1** and **Composite 2** electrodes, we noticed slightly increasing photocurrents between the first and second LSV scan. We suggest that this might be due to the oxidation of the Co from Co^{2+} to Co^{3+} in the surface layer, accompanied by partial conversion of CoPOM into cobalt oxide.[26] This was verified by performing the identical experiment with the individual Co-, W- or P-doped $BiVO_4$ (Figure S14, Supporting Information), where a similar initial photocurrent increase was only observed for the Co-doped $BiVO_4$ sample, while samples doped only with W or P did not show this initial increase of photocurrents. Notably, after the initial increase, photocurrents of the Co-doped $BiVO_4$ then dropped (Figure S14a, Supporting Information), suggesting that this sample is not stable under the operational conditions during repeated LSV measurements. Note that in the presence of both dopants, Co and W (Figure S14e,g, Supporting Information), we observe the characteristic behavior observed for the CoPOM-doped sample, i.e. initial increase of the photocurrent between the LSV runs 1 and 2, and stable photocurrents afterward in the repeated LSV measurements. These data again corroborate our hypothesis of a combined beneficial synergistic effect of doping with both Co and W on the $BiVO_4$ photoanode performance.

The wavelength-resolved IPCE was measured at E = 0.80 V vs. RHE both under irradiation from the back-side (BS, substrate side) and the front-side (FS, electrolyte side) (Figure 3c). The photoconversion efficiencies show a photoconversion onset at ca. 530 nm, which is in line with the optical absorption edge of all samples (Figure S8 in the Supporting Information).

https://doi.org/10.1021/acsami.4c21125
ACS Appl. Mater. Interfaces XXXX, XXX, XXX−XXX

Under the BS illumination, which is typically beneficial for mesoporous photoanodes such as ours since the performance-limiting process is the transport of electrons through the porous network into the underlying FTO substrate, the IPCE values of both the doped and surface-modified **Composite 2** photoanode are the highest in the whole wavelength range, as shown in Figure 3c. Notably, at the doped **Composite 1** photoanode the IPCE values under the FS illumination are nearly the same as under the BS illumination (Figure 3c). This implies that the CoPOM-doping has a notable enhancing effect on the electron transport properties of $BiVO_4$, and the electron transport no longer limits the photocurrents, even if the electrons have to be transported across longer pathways to the FTO support under the FS illumination.[59] This positive effect of the CoPOM doping is further apparent from the fact that at **Composite 3** the IPCE values under the FS illumination are still slightly lower compared to the BS illumination (Figure S15a, Supporting Information). On the other hand, in the case of the **Composite 2**, the expectedly higher IPCE values under the BS illumination as compared to the FS illumination are observed, which is most probably due to a more efficient hole extraction by the cocatalyst, rendering the electron transport through the electrode limiting again.[26]

Solid-state PL spectra recorded under the 400 nm excitation wavelength (Figure S16, Supporting Information) exhibit broad bands at ca. 480−510 nm (2.4−2.6 eV) that can be attributed to band-to-band recombination, typical for monoclinic $BiVO_4$ (bandgap of ca. 2.4 eV). The relative intensities for all samples are similar and do not show any definite trend, whereby the lowest intensity for **Composite 2** might suggest that the surface modification by CoPOM might have a positive effect on charge separation, as is apparent from slightly diminished radiative recombination.

To gain further insights into the factors limiting the performance of our photoanodes, the charge separation efficiency (η_{sep}) and the hole transfer efficiency (η_{tr}) were calculated by employing the methodology developed by Dotan et al.[40] and Hamann et al.[41] (see Experimental Section). According to the electronic absorption properties shown in Figure S8, Supporting Information, the J_{max} was calculated as 8.12 mA cm^{-2} ($BiVO_4$), 7.96 mA cm^{-2} (**Composite 1**), 8.11 mA cm^{-2} (**Composite 3**) and 8.09 mA cm^{-2} (**Composite 2**). In the presence of Na_2SO_3 as an effective hole scavenger, the photocurrent densities reach 3.22 mA cm^{-2} ($BiVO_4$), 6.32 mA cm^{-2} (**Composite 1**), 6.10 mA cm^{-2} (**Composite 3**), and 6.55 mA cm^{-2} (**Composite 2**) at 1.23 V vs. RHE, as shown in Figure S17, Supporting Information. As a result (Figure 3d), the η_{sep} for **Composite 1** and **Composite 2** photoanodes show much higher values than that for pristine $BiVO_4$ in the potential ranging from +0.35 to 1.23 V vs. RHE. The η_{sep} of **Composite 1** photoanode reaches 76.5% at 1.23 V vs. RHE, which is two times higher compared to the 38.3% of the nonmodified photoanode. This indicates that CoPOM-doping effectively improves the conductivity and facilitates charge transport through the photoanode. The increase in conductivity upon CoPOM doping is also further corroborated by electrochemical impedance spectroscopy (EIS) results (for details, see Figure S19 and Table S4, Supporting Information). Interestingly, at very low bias potentials (<0.35 V vs. RHE) the detrimental effects of doping are apparent as the η_{sep} decreases as compared to pristine $BiVO_4$. In our previous study on Mo-doped $BiVO_4$,[26] we discussed in detail these detrimental effects of doping as related to the higher concentration of electron polaronic states due to the presence of the dopant.[60] The electron trapping in these polaronic states limits the maximum achievable photovoltage and enhances the charge recombination, unless a sufficiently high bias is applied. Indeed, the negative effect of the CoPOM-doping is clearly corroborated by the reduced quasi-Fermi level of electrons after the photodoping, as apparent from reduced open-circuit photopotentials at **Composite 1** and **Composite 2** as compared to pristine $BiVO_4$ (see Figure S18a, Supporting Information). Furthermore, the hole transfer efficiency η_{tr} (Figure 3e) is significantly enhanced over the whole potential range and shifted to cathodic potentials for both modified photoanodes. Specifically, the η_{tr} increased from 12.7% for $BiVO_4$ to 47.8% for **Composite 1** and 59.2% for **Composite 2** photoanodes at 1.23 V vs. RHE. Notably, the beneficial effects of the CoPOM cocatalyst become particularly significant at very low bias potentials (<0.45 V vs. RHE), where it can partially compensate the detrimental effects of the electron polaronic states from doping. Interestingly, the η_{sep} for **Composite 1** and **Composite 3** photoanodes show a similar value over the whole potential range, while the value of η_{tr} is higher for **Composite 1** than that of **Composite 3** (Figure S15b,c, Supporting Information). This hints that hole transfer efficiency η_{tr} plays an important role in PEC performance and is in line with the difference of ratio of W/Co on the surface (see Table S1, Supporting Information). Taken together, all these findings indicate that the "double-use" of CoPOM as both a dopant and a surface cocatalyst can effectively promote the charge separation and hole transfer carrier dynamics at $BiVO_4$ photoanodes, respectively, in line with the established knowledge on the effects of doping and cocatalysts in the literature.[25,38]

To confirm the actual oxygen evolution performance of the photoanodes, we performed photoelectrocatalytic OER measurements (Figure 4a) in an aqueous borate solution (pH 9.0) under AM 1.5G (1 sun) illumination at E = 0.80 V vs. RHE. Under these conditions, we observed O_2 evolution rates of 104.1 ± 18.5 μmol L^{-1} h^{-1} ($BiVO_4$), 504.7 ± 26.7 μmol L^{-1} h^{-1} (**Composite 1**), and 856.9 ± 33.3 μmol L^{-1} h^{-1} (**Composite 2**) during a 20 min illumination experiment. The corresponding faradaic efficiencies are comparable for the three systems ($BiVO_4$:102.7% ± 13.2%; **Composite 1**: 97.5% ± 9.5%, **Composite 2**: 102.3% ± 12.2%), indicating the nearly quantitative oxygen evolution at all $BiVO_4$ photoanodes.

Finally, the ABPE was also determined. As shown in Figures 3f and S15d, the Supporting Information, the maximum photoconversion efficiencies are 0.03% (at 1.04 V vs. RHE) for $BiVO_4$, 0.39% (at 0.94 V vs. RHE) for **Composite 3**, 0.54% (at 0.87 V vs. RHE) for **Composite 1** and 0.79% (at 0.82 V vs. RHE) for **Composite 2**. Two points are noteworthy. First, the fact that the maximum power point is shifted to more negative bias potentials after doping and surface modification with CoPOM is highly beneficial in view of the potential construction of tandem solar-driven water-splitting systems in which photoanodes for O_2 evolution are combined with photocathodes for H_2 evolution. Second, the maximum ABPE is 0.79% (at 0.82 V vs. RHE) for the **Composite 2** is not only higher by a factor of ~26 as compared to pristine $BiVO_4$, but even slightly higher than the best performing Mo-doped $BiVO_4$ photoanode modified with CoPOM cocatalyst (ABPE of 0.73% at 0.86 V vs. RHE) we investigated recently.[26] This highlights the beneficial effect of the "double-use" strategy employing CoPOM on the fabrication of $BiVO_4$ photoanodes

https://doi.org/10.1021/acsami.4c21125
ACS Appl. Mater. Interfaces XXXX, XXX, XXX−XXX

with improved performance for a comprehensive comparative overview of key PEC performance factors of all photoanodes (see Table S5, Supporting Information). The key factors influencing the PEC performance of all electrodes at a moderate electrode bias of 0.80 V vs. RHE are summarized in Figure 5.

4. CONCLUSIONS

In conclusion, we have demonstrated a novel "double-use" strategy for the fabrication of high-performance $BiVO_4$ photoanodes for solar water splitting in which a single precursor, a molecular cobalt polyoxometalate (CoPOM), is used both as a doping agent and as a cocatalyst for water oxidation. Doping $BiVO_4$ by CoPOM significantly enhances the conductivity and improves the charge separation efficiency, resulting in the enhancement of the maximum ABPE by a factor of ~18 as compared to that of pristine $BiVO_4$. Further surface modification of CoPOM-doped $BiVO_4$ with CoPOM as a cocatalyst enhances the hole extraction and improves the water oxidation kinetics, yielding the overall enhancement of the ABPE as high as by a factor of ~26 with respect to pristine $BiVO_4$. Interestingly, with respect to the doped $BiVO_4$ photoanodes, we found systematic differences in the surface composition and PEC performance of samples doped with CoPOM compared to samples with identical elemental composition but doped with metal salts. While these differences are not fully understood yet, they point to possible advantages of using molecularly well-defined precursors, such as CoPOM, in the fabrication of high-performance photoelectrodes. Taken together, our results establish the "double-use" strategy involving CoPOMs as a remarkably effective, straightforward, and easily scalable approach for the development of high-quality photoanodes for solar water splitting and highlight the future potential of utilizing well-designed POMs as precursors for the synthesis of energy materials.

■ ASSOCIATED CONTENT

Supporting Information

The Supporting Information is available free of charge at https://pubs.acs.org/doi/10.1021/acsami.4c21125.

Additional analytical, characterization, and electrochemical data (PDF)

■ AUTHOR INFORMATION

Corresponding Authors

Carsten Streb − *Department of Chemistry, Johannes Gutenberg University Mainz, Mainz 55128, Germany;* orcid.org/0000-0002-5846-1905; Email: carsten.streb@uni-mainz.de

Radim Beranek − *Institute of Electrochemistry, Ulm University, Ulm 89081, Germany;* orcid.org/0000-0002-7926-0774; Email: radim.beranek@uni-ulm.de

Authors

Fan Feng − *Department of Chemistry, Johannes Gutenberg University Mainz, Mainz 55128, Germany*

Dariusz Mitoraj − *Institute of Electrochemistry, Ulm University, Ulm 89081, Germany*

Ekemena Oseghe − *Department of Chemistry, Johannes Gutenberg University Mainz, Mainz 55128, Germany*

Complete contact information is available at: https://pubs.acs.org/10.1021/acsami.4c21125

Author Contributions

F. F., C. S., and R. B. conceived the idea for the project. C. S. and R. B. supervised the study and acquired funding. F. F. designed the experiments, performed catalyst synthesis and photoelectrochemical measurements, acquired and analyzed data, and wrote the manuscript. D. M. and E. O. analyzed data and provided discussions. All coauthors wrote and reviewed the manuscript.

Notes

The authors declare no competing financial interest.

All data sets shown in this study are available from zenodo.org under the link 10.5281/zenodo.13882299.

■ ACKNOWLEDGMENTS

The authors gratefully acknowledge financial support by the Deutsche Forschungsgemeinschaft DFG (TRR 234 "CataLight, projects A4/B3/B6/C4, project no. 364549901). F. F. gratefully acknowledges the China Scholarship Council CSC for a PhD fellowship. R. B. and D. M. acknowledge funding from the European Union's Horizon Europe programme for research and innovation under grant agreement no. 101122061 (SUNGATE). C. S. acknowledges funding from the Top Level Research Area SusInnoScience of the federal state of Rheinland-Pfalz. The authors thank Gunnar Glaßer (SEM measurement) and Leon Prädel (XPS measurement) for their help.

■ REFERENCES

(1) Kim, J. H.; Lee, J. S. Elaborately Modified $BiVO_4$ Photoanodes for Solar Water Splitting. *Adv. Mater.* **2019**, *31*, 1806938.

(2) Roger, I.; Shipman, M. A.; Symes, M. D. Earth-abundant Catalysts for Electrochemical and Photoelectrochemical Water Splitting. *Nat. Rev. Chem* **2017**, *1*, 0003.

(3) Fujishima, A.; Honda, K. Electrochemical Photolysis of Water at a Semiconductor Electrode. *Nature* **1972**, *238*, 37−38.

(4) Jin, S.; Ma, X.; Pan, J.; Zhu, C.; Saji, S. E.; Hu, J.; Xu, X.; Sun, L.; Yin, Z. Oxygen Vacancies Activating Surface Reactivity to Favor Charge Separation and Transfer in Nanoporous $BiVO_4$ Photoanodes. *Appl. Cata. B: Environ.* **2021**, *281*, 119477.

(5) Zhang, Z.; Huang, X.; Zhang, B.; Bi, Y. High-performance and Stable $BiVO_4$ Photoanodes for Solar Water Splitting via Phosphorus−oxygen Bonded FeNi Catalysts. *Energy Environ. Sci.* **2022**, *15*, 2867−2873.

(6) Chi, J.; Jiang, Z.; Yan, J.; Larimi, A.; Wang, Z.; Wang, L.; Shangguan, W. Recent Advancements in Bismuth Vanadate Photoanodes for Photoelectrochemical Water Splitting. *Mater. Today Chem.* **2022**, *26*, 101060.

(7) Abdi, F. F.; Savenije, T. J.; May, M. M.; Dam, B.; van de Krol, R. The Origin of Slow Carrier Transport in $BiVO_4$ Thin Film Photoanodes: A Time-Resolved Microwave Conductivity Study. *J. Phys. Chem. Lett.* **2013**, *4*, 2752−2757.

(8) Wheeler, D. A.; Wang, G.; Ling, Y.; Li, Y.; Zhang, J. Z. Nanostructured Hematite: Synthesis, Characterization, Charge Carrier Dynamics, and Photoelectrochemical Properties. *Energy Environ. Sci.* **2012**, *5*, 6682−6702.

(9) Peerakiatkhajohn, P.; Yun, J. H.; Chen, H.; Lyu, M.; Butburee, T.; Wang, L. Stable Hematite Nanosheet Photoanodes for Enhanced Photoelectrochemical Water Splitting. *Adv. Mater.* **2016**, *28*, 6405−6410.

(10) Kim, C. W.; Son, Y. S.; Kang, M. J.; Kim, D. Y.; Kang, Y. S. 040-Crystal Facet Engineering of $BiVO_4$ Plate Photoanodes for Solar Fuel Production. *Adv. Energy Mater.* **2016**, *6*, 1501754.

(11) Park, Y.; McDonald, K. J.; Choi, K. S. Progress in Bismuth Vanadate Photoanodes for Use in Solar Water Oxidation. *Chem. Soc. Rev.* **2013**, *42*, 2321−2337.

(12) Wang, S.; Chen, P.; Yun, J.; Hu, Y.; Wang, L. An Electrochemically Treated $BiVO_4$ Photoanode for Efficient Photoelectrochemical Water Splitting. *Angew. Chem., Int. Ed.* **2017**, *56*, 8500−8504.
(13) Yang, J.; Deng, C.; Lei, Y.; Duan, M.; Yang, Y.; Chen, X.; Yang, S.; Li, J.; Sheng, H.; Shi, W.; Chen, C.; Zhao, J. Fe-N Co-Doped $BiVO_4$ Photoanode with Record Photocurrent for Water Oxidation. *Angew. Chem., Int. Ed.* **2024**, No. e202416340.
(14) Pan, J.; Wang, B.; Wang, J.; Ding, H.; Zhou, W.; Liu, X.; Zhang, J.; Shen, S.; Guo, J.; Chen, L.; Au, C.; Jiang, L.; Yin, S. Activity and Stability Boosting of an Oxygen-Vacancy-Rich $BiVO_4$ Photoanode by NiFe-MOFs Thin Layer for Water Oxidation. *Angew. Chem., Int. Ed.* **2021**, *60*, 1433−1440.
(15) Liu, B.; Wang, X.; Zhang, Y.; Xu, L.; Wang, T.; Xiao, X.; Wang, S.; Wang, L.; Huang, W. A $BiVO_4$ Photoanode with a VO_x Layer Bearing Oxygen Vacancies Offers Improved Charge Transfer and Oxygen Evolution Kinetics in Photoelectrochemical Water Splitting. *Angew. Chem., Int. Ed.* **2023**, *62*, No. e202217346.
(16) Lee, D. K.; Choi, K.-S. Enhancing Long-Term Photostability of $BiVO_4$ Photoanodes for Solar Water Splitting by Tuning Electrolyte Composition. *Nat. Energy* **2018**, *3*, 53−60.
(17) Long, D. L.; Tsunashima, R.; Cronin, L. Polyoxometalates: Building Blocks for Functional Nanoscale Systems. *Angew. Chem., Int. Ed.* **2010**, *49*, 1736−1758.
(18) Streb, C.; Kastner, K.; Tucher, J. Polyoxometalates in Photocatalysis. *Phys. Sci. Rev.* **2019**, *4*, 20170177.
(19) Yin, Q.; Tan, J. M.; Besson, C.; Geletii, Y. V.; Musaev, D. G.; Kuznetsov, A. E.; Luo, Z.; Hardcastle, K. I.; Hill, C. L. A Fast Soluble Carbon-Free Molecular Water Oxidation Catalyst Based on Abundant Metals. *Science* **2010**, *328*, 342−345.
(20) Lv, H.; Geletii, Y. V.; Zhao, C.; Vickers, J. W.; Zhu, G.; Luo, Z.; Song, J.; Lian, T.; Musaev, D. G.; Hill, C. L. Polyoxometalate Water Oxidation Catalysts and the Production of Green Fuel. *Chem. Soc. Rev.* **2012**, *41*, 7572−7589.
(21) Sartorel, A.; Bonchio, M.; Campagna, S.; Scandola, F. Tetrametallic Molecular Catalysts for Photochemical Water Oxidation. *Chem. Soc. Rev.* **2013**, *42*, 2262−2280.
(22) Gao, D.; Trentin, I.; Schwiedrzik, L.; González, L.; Streb, C. The Reactivity and Stability of Polyoxometalate Water Oxidation Electrocatalysts. *Molecules* **2020**, *25*, 157.
(23) Kund, J.; Kruse, J.-H.; Gruber, A.; Trentin, I.; Langer, M.; Read, C.; Neusser, G.; Blaimer, D.; Rupp, U.; Streb, C.; Leopold, K.; Schacher, F. H.; Kranz, C. Multimodal Analysis of Light-Driven Water Oxidation in Nanoporous Block Copolymer Membranes. *Angew. Chem., Int. Ed.* **2023**, *62*, No. e202217196.
(24) Jeon, D.; Kim, H.; Lee, C.; Han, Y.; Gu, M.; Kim, B.; Ryu, J. Layer-by-Layer Assembly of Polyoxometalates for Photoelectrochemical (PEC) Water Splitting: Toward Modular PEC Devices. *ACS Appl. Mater. Interfaces* **2017**, *9*, 40151−40161.
(25) Fan, K.; Chen, H.; He, B.; Yu, J. Cobalt Polyoxometalate on N-Doped Carbon Layer to Boost Photoelectrochemical Water Oxidation of $BiVO_4$. *Chem. Eng. J.* **2020**, *392*, 123744.
(26) Feng, F.; Mitoraj, D.; Gong, R.; Gao, D.; Elnagar, M.; Liu, R.; Beranek, R.; Streb, C. High-performance $BiVO_4$ Photoanodes: Elucidating the Combined Effects of Mo-doping and Modification with Cobalt Polyoxometalate. *Mater. Adv.* **2024**, *5*, 4932−4944.
(27) He, H.; Berglund, S. P.; Rettie, A. J. E.; Chemelewski, W. D.; Xiao, P.; Zhang, Y.; Mullins, C. B. Synthesis of $BiVO_4$ Nanoflake Array Films for Photoelectrochemical Water Oxidation. *J. Mater. Chem. A* **2014**, *2*, 9371−9379.
(28) Fang, W.; Fu, L.; Qin, A.; Lin, Y.; Xv, R. Highly Active and Self-Healing Co-Doped $BiVO_4$ Photoanode in Borate Buffer to Enhance Charge Separation and Water Oxidation Kinetics during Photoelectrochemical Water Splitting. *ACS Appl. Energy Mater.* **2022**, *5*, 6313−6323.
(29) Shi, Q.; Murcia-López, S.; Tang, P.; Flox, C.; Morante, J. R.; Bian, Z.; Wang, H.; Andreu, T. Role of Tungsten Doping on the Surface States in $BiVO_4$ Photoanodes for Water Oxidation: Tuning the Electron Trapping Process. *ACS Catal.* **2018**, *8*, 3331−3342.
(30) Shi, H.; Li, N.; Sun, Z.; Wang, T.; Xu, L. Interface Modification of Titanium Dioxide Nanoparticles by Titaniumsubstituted Polyoxometalate Doping for Improvement of Photoconductivity and Gas sensing Applications. *J. Phys. & Chem. Solids* **2018**, *120*, 57−63.
(31) Tian, J.; Chen, X.; Wang, T.; Pei, W.; Li, F.; Li, D.; Yang, Y.; Dong, X. Modification of Indium Oxide Nanofibers by Polyoxometalate Electron Acceptor Doping for Enhancement of Gas Sensing at Room Temperature. *Sensors & Actuators: B. Chem.* **2021**, *344*, 130227.
(32) Yuan, C.; Guo, S.; Wang, S.; Liu, L.; Chen, W.; Wang, E. Electropolymerization Polyoxometalate (POM)-Doped PEDOT Film Electrodes with Mastoid Microstructure and Its Application in Dye-Sensitized Solar Cells (DSSCs). *Ind. Eng. Chem. Res.* **2013**, *52*, 6694−6703.
(33) Hu, B.; Zhang, J.; Yang, Y.; Wang, J.; Wang, W.; Li, J.; Liu, S.; Xia, D.; Lin, K.; Dong, Y.; Fan, R. Investigation on the Mechanism of Radical Intermediate Formation and Moderate Oxidation of Spiro-OMeTAD by the Synergistic Effect of Multisubstituted Polyoxometalates in Perovskite Solar Cells. *ACS Appl. Mater. Interfaces* **2022**, *14*, 17610−17620.
(34) Fan, X.; Zhang, J.; Yang, Y.; Xia, D.; Dong, Y.; Qiu, L.; Wang, J.; Cao, W.; Wang, W.; Hu, B.; Fan, R. New Insight into the Grafted Transition Metal Ions in Trilacunary Keggin Polyoxometalates Dopants for Efficient and Stable Perovskite Solar Cells. *J. Power Sources* **2021**, *504*, 230073.
(35) Xu, M.; Li, X.; Sha, J.-Q.; Tong, Z.; Li, Q.; Liu, C. Hollow POM@MOF-derived Porous $NiMo_6@Co_3O_4$ for Biothiol Colorimetric Detection. *Chem.—Eur. J.* **2021**, *27*, 9141−9151.
(36) Lan, J.; Zhu, Q.; Gu, X.; Ma, M.; Li, D.; Huang, K.; Fu, X.; Zhu, Y.; Zhang, Y. Understanding the Mechanism of Saturated and Mono-/tri-lacunary Keggin SiWx Doped in Bi_2WO_6 and BiOBr for Efficient Photocatalytic CO_2 Reduction. *Sep. Purif. Technol.* **2023**, *321*, 124228.
(37) Xi, L.; Jin, Z.; Sun, Z.; Liu, R.; Xu, L. Enhanced Photoelectrocatalytic Performance for Water Oxidation by Polyoxometalate Molecular Doping in $BiVO_4$ Photoanodes. *Appl. Cata. A: General* **2017**, *536*, 67−74.
(38) Jian, J.; Xu, Y.; Yang, X.; Liu, W.; Fu, M.; Yu, H.; Xu, F.; Feng, F.; Jia, L.; Friedrich, D.; van de Krol, R.; Wang, H. Embedding Laser Generated Nanocrystals in $BiVO_4$ Photoanode for Efficient Photoelectrochemical Water Splitting. *Nat. Commun.* **2019**, *10*, 2609.
(39) Cao, X.; Wang, Y.; Lin, J.; Ding, Y. Ultrathin CoOx Nanolayers Derived from Polyoxometalate for Enhanced Photoelectrochemical Performance of Hematite Photoanodes. *J. Mater. Chem. A* **2019**, *7*, 6294−6303.
(40) Dotan, H.; Sivula, K.; Grätzel, M.; Rothschild, A.; Warren, S. C. Probing the Photoelectrochemical Properties of Hematite (α-Fe_2O_3) Electrodes Using Hydrogen Peroxide as a Hole Scavenger. *Energy Environ. Sci.* **2011**, *4*, 958−964.
(41) Gao, Y.; Hamann, T. W. Quantitative Hole Collection for Photoelectrochemical Water Oxidation with $CuWO_4$. *Chem. Commun.* **2017**, *53*, 1285−1288.
(42) Kim, T. W.; Choi, K. Nanoporous $BiVO_4$ Photoanodes with Dual-Layer Oxygen Evolution Catalysts for Solar Water Splitting. *Science* **2014**, *343*, 990−994.
(43) Wang, Y.; Chen, Y.; Yun, Y.; Hong, X.; Huang, Y.; Ji, H. CoMoP Hole Transfer Layer Functionally Enhances Efficiency and Stability of $BiVO_4$ Based Photoanode for Solar Water Splitting. *Appl. Cata. B: Environ. & Energy* **2024**, *358*, 124375.
(44) Chen, B.; Li, D.; Yang, Z.; Li, Q.; Chen, X.; Li, L.; Shi, W. Ultra-Efficient Post-treatment Flame Method to Introduce Abundant Oxygen Vacancies in $BiVO_4$ Photoanode toward Solar Water Splitting. *Chem. Eng. Sci.* **2022**, *251*, 117433.
(45) Lamers, M.; Fiechter, S.; Friedrich, D.; Abdi, F. F.; van de Krol, R. Formation and Suppression of Defects during Heat Treatment of $BiVO_4$ Photoanodes for Solar Water Splitting. *J. Mater. Chem. A* **2018**, *6*, 18694−18700.
(46) Chen, L.; Alarcón-Lladó, E.; Hettick, M.; Sharp, I. D.; Lin, Y.; Javey, A.; Ager, J. W. Reactive Sputtering of Bismuth Vanadate

https://doi.org/10.1021/acsami.4c21125
ACS Appl. Mater. Interfaces XXXX, XXX, XXX−XXX

Photoanodes for Solar Water Splitting. *J. Phys. Chem. C* **2013**, *117*, 21635−21642.
(47) Silversmit, G.; Depla, D.; Poelman, H.; Marin, G. B.; De Gryse, R. Determination of the V 2p XPS Binding Energies for Different Vanadium Oxidation States (V^{5+} to V^{0+}). *J. Electron Spectro. & Related Phenomena* **2004**, *135*, 167−175.
(48) Liu, Y.; Deng, P.; Wu, R.; Geioushy, R. A.; Li, Y.; Liu, Y.; Zhou, F.; Li, H.; Sun, C. $BiVO_4/TiO_2$ Heterojunction with Rich Oxygen Vacancies for Enhanced Electrocatalytic Nitrogen Reduction Reaction. *Front. Phys.* **2021**, *16*, 53503.
(49) Jian, J.; Wang, S.; Ye, Q.; Li, F.; Su, G.; Liu, W.; Qu, C.; Liu, F.; Li, C.; Jia, L.; Novikov, A. A.; Vinokurov, V. A.; Harvey, D. H. S.; Shchukin, D.; Friedrich, D.; van de Krol, R.; Wang, H. Activating a Semiconductor−Liquid Junction via Laser-Derived Dual Interfacial Layers for Boosted Photoelectrochemical Water Splitting. *Adv. Mater.* **2022**, *34*, 2201140.
(50) Jiang, Z.; Liu, Y.; Jing, T.; Huang, B.; Zhang, X.; Qin, X.; Dai, Y.; Whangbo, M.-H. Enhancing the Photocatalytic Activity of $BiVO_4$ for Oxygen Evolution by Ce Doping: Ce^{3+} Ions as Hole Traps. *J. Phys. Chem. C* **2016**, *120*, 2058−2063.
(51) Thalluri, S. M.; Hernández, S.; Bensaid, S.; Saracco, G.; Russo, N. Green-synthesized W- and Mo-doped $BiVO_4$ Oriented along the {040} Facet with Enhanced Activity for the Sun-driven Water Oxidation. *Appl. Cata. B: Environ.* **2016**, *180*, 630−636.
(52) Zhang, B.; Zhang, H.; Wang, Z.; Zhang, X.; Qin, X.; Dai, Y.; Liu, Y.; Wang, P.; Li, Y.; Huang, B. Doping Strategy to Promote the Charge Separation in $BiVO_4$ Photoanodes. *Appl. Cata. B: Environ.* **2017**, *211*, 258−265.
(53) Gong, R.; Gao, D.; Liu, R.; Sorsche, D.; Biskupek, J.; Kaiser, U.; Rau, S.; Streb, C. Self-Activation of a Polyoxometalate-Derived Composite Electrocatalyst for the Oxygen Evolution Reaction. *ACS Appl. Energy Mater.* **2021**, *4*, 12671−12676.
(54) Prasad, U.; Prakash, J.; Gupta, S. K.; Zuniga, J.; Mao, Y.; Azeredo, B.; Kannan, A. N. M. Enhanced Photoelectrochemical Water Splitting with Er- and W-Codoped Bismuth Vanadate with WO_3 Heterojunction-Based Two-Dimensional Photoelectrode. *ACS Appl. Mater. Interfaces* **2019**, *11*, 19029−19039.
(55) Yang, X.; Cui, J.; Lin, L.; Bian, A.; Dai, J.; Du, W.; Guo, S.; Hu, J.; Xu, X. Enhanced Charge Separation in Nanoporous $BiVO_4$ by External Electron Transport Layer Boosts Solar Water Splitting. *Adv. Sci.* **2024**, *11*, 2305567.
(56) Gupta, N.; Segre, C.; Nickel, C.; Streb, C.; Gao, D.; Glusac, K. D. Catalytic Water Electrolysis by Co−Cu−W Mixed Metal Oxides: Insights from X-ray Absorption Spectroelectrochemistry. *ACS Appl. Mater. Interfaces* **2024**, *16*, 35793−35804.
(57) Ding, C.; Shi, J.; Wang, D.; Wang, Z.; Wang, N.; Liu, G.; Xiong, F.; Li, C. Visible Light Driven Overall Water Splitting Using Co-catalyst/$BiVO_4$ Photoanode with Minimized Bias. *Phys. Chem. Chem. Phys.* **2013**, *15*, 4589−4595.
(58) Peter, L. M. Dynamic Aspects of Semiconductor Photoelectrochemistry. *Chem. Rev.* **1990**, *90*, 753−769.
(59) Surendranath, Y.; Dinca, M.; Nocera, D. G. Electrolyte-Dependent Electrosynthesis and Activity of Cobalt-Based Water Oxidation Catalysts. *J. Am. Chem. Soc.* **2009**, *131*, 2615−2620.
(60) Pastor, E.; Sachs, M.; Selim, S.; Durrant, J. R.; Bakulin, A. A.; Walsh, A. Electronic Defects in Metal Oxide Photocatalysts. *Nat. Rev. Mater.* **2022**, *7*, 503−521.

https://doi.org/10.1021/acsami.4c21125
ACS Appl. Mater. Interfaces XXXX, XXX, XXX−XXX

3.3 (FF-3) Atomically Engineered Defect-Rich Palladium Metallene for High-Performance Alkaline Oxygen Reduction Electrocatalysis

Yupeng Zhao, Zhengfan Chen, Nana Ma, Weiyi Cheng, Dong Zhang, Kecheng Cao, Fan Feng, Dandan Gao, Rongji Liu,* Shujun Li,* and Carsten Streb*

* Corresponding authors

Published in Adv. Sci., **2024**.

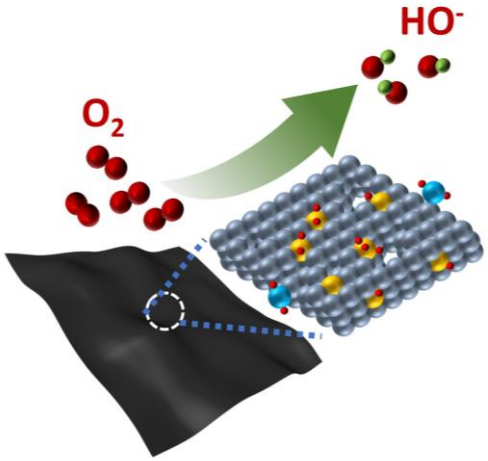

This publication reports a defect-rich WO_x and MoO_x modified Pd metallene (denoted: D-Pd M) synthesized by a facile wet-chemical approach. Detailed structural analyses reveal the presence of three distinct atomic-level defects, that are pores, concave surfaces, and surface-anchored individual WO_x and MoO_x sites, resulting in a highly active catalyst for the alkaline oxygen reduction reaction (ORR). When integrated into a custom-built Zn-air battery at low D-Pd M loading for the practical usage of the compound, the system achieves high specific capacity and excellent discharge potential stability.

Supporting Information can be found in chapter 6.3.

Author contributions:

Yupeng Zhao:	Conceptualization, methodology, data analyses, investigation, writing and revision of the manuscript.
Zhengfan Chen:	Investigation, data analyses, writing original draft.
Nana Ma:	Data analyses, writing original draft.
Weiyi Cheng:	Data analyses, writing original draft.
Dong Zhang:	Investigation, Data analyses, writing original draft.
Kecheng Cao:	Investigation, Data analyses, writing original draft.
Fan Feng:	Investigation, Data analyses, writing original draft.
Dandan Gao:	Investigation, Data analyses, writing original draft.
Rongji Liu:	Conceptualization, supervision, Data analyses, methodology, finalizing the article.
Shujun Li:	Conceptualization, supervision, Data analyses, methodology, finalizing the article.
Carsten Streb:	Project administration, funding acquisition, conceptualization, supervision, Data analyses, methodology, finalizing the article.

RESEARCH ARTICLE

ADVANCED SCIENCE Open Access

www.advancedscience.com

Atomically Engineered Defect-Rich Palladium Metallene for High-Performance Alkaline Oxygen Reduction Electrocatalysis

Yupeng Zhao, Zhengfan Chen, Nana Ma, Weiyi Cheng, Dong Zhang, Kecheng Cao, Fan Feng, Dandan Gao, Rongji Liu, Shujun Li,* and Carsten Streb**

Defect engineering is a key chemical tool to modulate the electronic structure and reactivity of nanostructured catalysts. Here, it is reported how targeted introduction of defect sites in a 2D palladium metallene nanostructure results in a highly active catalyst for the alkaline oxygen reduction reaction (ORR). A defect-rich WO_x and MoO_x modified Pd metallene (denoted: D-Pd M) is synthesized by a facile and scalable approach. Detailed structural analyses reveal the presence of three distinct atomic-level defects, that are pores, concave surfaces, and surface-anchored individual WO_x and MoO_x sites. Mechanistic studies reveal that these defects result in excellent catalytic ORR activity (half-wave potential 0.93 V vs. RHE, mass activity 1.3 A $mgPd^{-1}$ at 0.9 V vs. RHE), outperforming the commercial references Pt/C and Pd/C by factors of ≈7 and ≈4, respectively. The practical usage of the compound is demonstrated by integration into a custom-built Zn-air battery. At low D-Pd M loading (26 µgPd cm^{-2}), the system achieves high specific capacity (809 mAh g_{Zn}^{-1}) and shows excellent discharge potential stability. This study therefore provides a blueprint for the molecular design of defect sites in 2D metallene nanostructures for advanced energy technology applications.

1. Introduction

The oxygen reduction reaction (ORR) is one of the most important catalytic processes for energy conversion and storage technologies including fuel cells, metal-air batteries, and electrochemical H_2O_2 production.[1–3] The ORR is a challenging reaction, due to the high O_2 bond dissociation energy (498 KJ mol^{-1}) and the sluggish kinetics of O_2-related proton-coupled multi-electron processes.[2,4] These factors significantly impede the practical application of the ORR. To overcome these challenges, numerous electrocatalysts have been developed, including those based on platinum group metals (PGMs),[5] noble metal-free materials,[6,7] and even metal-free catalysts.[8] Currently, both the intrinsic activity and the long-term stability of noble metal-free and metal-free catalysts are significantly inferior to those of PGM-based electrocatalysts.[4]

Owing to their unique electronic structure and optimum oxygen molecule adsorption energy, electrocatalysts based on PGMs have received widespread attention and are still a focal point for advanced ORR catalyst development.[9] However, challenges remain, particularly in the case of platinum-based catalysts. While these materials demonstrate excellent catalytic performance, they often suffer from poor long-term stability.[10–12] Importantly, highly dispersed Pt nanoparticles show a notable tendency to aggregate

Y. Zhao, Z. Chen, F. Feng, D. Gao, R. Liu, C. Streb
Department of Chemistry
Johannes Gutenberg University Mainz
Duesbergweg 10–14, 55128 Mainz, Germany
E-mail: rongji.liu@uni-mainz.de; carsten.streb@uni-mainz.de

Y. Zhao, Z. Chen, F. Feng, D. Gao, R. Liu, C. Streb
Institute of Inorganic Chemistry I
Ulm University
Albert-Einstein-Allee 11, 89081 Ulm, Germany

N. Ma, W. Cheng, S. Li
Henan Key Laboratory of Boron Chemistry and Advanced Materials
School of Chemistry and Chemical Engineering
Henan Normal University
Xinxiang 453007, China
E-mail: lisj@htu.edu.cn

D. Zhang, K. Cao
School of Physical Science and Technology
ShanghaiTech University
Shanghai 201210, China

R. Liu, C. Streb
Helmholtz-Institute Ulm
Electrochemical Energy Conversion
Helmholtzstr. 11, 89081 Ulm, Germany

The ORCID identification number(s) for the author(s) of this article can be found under https://doi.org/10.1002/advs.202405187

DOI: 10.1002/advs.202405187

during catalysis, resulting in the formation of larger particles with reduced reactivity.[13] Furthermore, the high binding energy of Pt and Pd to oxygen molecules limits the generation and conversion of intermediates (such as *OH and *OOH) into H_2O/OH^-, indicating potential opportunities for enhancing the catalytic properties by modification in their electronic structure.[14,15] Moreover, the substantial cost associated with Pt and Pd is major impediment to their broad industrial use.[16] Thus, chemical strategies are urgently required which optimize electronic structure and reactivity of PGMs while at the same time making optimum use of all metal centers available in the catalyst.[17–19]

These challenges have recently been targeted by the development of two-dimensional (2D) metal nanosheets, so-called metallenes, which have shown unique electronic structure and high reactivity and durability.[20–22] Metallenes are metal or alloy materials featuring individual layers of atomic thickness.[23,24] Metallenes offer optimum utilization of the individual metal atoms due to their high specific accessible surface area and abundance of low-coordinated reactive metal sites.[25–27] A significant breakthrough in this realm was achieved by Guo and colleagues, who successfully synthesized PdMo bimetallene.[28] The group discovered that strain and quantum effects within the ultrathin structure of the metallene lead to a downward shift of the d-band center, thereby lowering the oxygen molecule binding energy and enhancing electrocatalytic performance. Moreover, the electronic structure can be further modulated by doping with Mo atoms. As a result, PdMo bimetallene exhibits a lower d-band center and superior ORR catalytic activity compared to pure Pd metallene. Building on this advancement, Jin and co-workers further demonstrated that the durability of PdMo bimetallene can be significantly improved by interstitial doping with carbon. This modification results in stabilization of the Mo sites within the bimetallene structure.[29] In addition, defect engineering has proven to be a critical tool in the advancement of Pd metallene. Wang and colleagues successfully developed a defect rich Pd metallene characterized by abundant pores, which created a multitude of highly active sites. This innovation resulted in a significant enhancement in ORR activity.[30] Concurrently, research by Guo and coworkers revealed that the concave surfaces on Pd metallene lead to a modest downward shift in the d-band center and allow fine-tuning of oxygen molecule binding energies. This structural modification contributes to improved ORR performance, showcasing the impact of the surface geometry on catalytic efficiency.[31]

Here, we build on these pioneering studies and report a novel ultrathin Pd metallene doped with atomic WO_x/MoO_x (referred to as **D-Pd M**) featuring by a curved defect-rich structure. Key for the synthetic access to this new compound is the use of molecular metal oxides (polyoxometalates, POMs), here reduced $[H_3PMo_{12}O_{40}] \bullet x\ H_2O$ (= PMo_{12}), N, N-dimethylformamide (DMF), and tungsten hexacarbonyl ($W(CO)_6$) as reducing agents. Meawhile, $W(CO)_6$ was used as a structure-directing agent. PMo_{12} and $W(CO)_6$ also acted as molecular precursors to deposit MoO_x and WO_x into the Pd metallene. The resulting **D-Pd M** showed excellent ORR activity, with a high half-wave potential ($E_{1/2}$ = 0.93 V vs. RHE), high mass activity (1.3 A mg_{Pd}^{-1} at 0.9 V vs. RHE) and superior stability over 10,000 test cycles. Practical applicability of **D-Pd M** was demonstrated by integration into an operational Zn-air battery at ultra-low Pd loading (26 $\mu g_{Pd}\ cm^{-2}$), showing high specific capacity (809 mAh g_{Zn}^{-1}), exceptional discharge performance and ultra-long cycling stability (continuous operation for 300 h over 300 charge/discharge cycles).

2. Results and Discussion

Figure 1 illustrates the synthetic procedure to access **D-Pd M**. Initially, a solution of PMo_{12} in DMF was irradiated with ultraviolet (UV) light (l_{max} = 254 nm) to reduce the POM cluster. The solution undergoes a clear transition from its initial yellow to dark blue color, and a new broad peak at 760 nm appeared in the reduced solution (Figure S1, Supporting Information), all of which suggests that the POM cluster was reduced to heteropoly blue.[32,33] The solution containing the reduced PMo_{12} was then combined with a DMF solution containing the metal precursors palladium (II) acetylacetonate ($Pd(acac)_2$) and $W(CO)_6$, resulting in reduction of Pd^{2+} to Pd (0) and formation of the palladene sheets.[30] During the reaction, carbon monoxide was gradually released by thermal decomposition of $W(CO)_6$. CO is known to strongly adsorb on Pd (111) facet, which in turn facilitates the anisotropic lateral growth and formation of 2D ultrathin metallene.[23,31,34] For comparison, conventional Pd metallene (**Pd M**) weas prepared using a modified literature method, see Supporting Information (SI),[34] where citric acid was used as the reducing agent instead of PMo_{12}.

The morphology and structural properties of the as-synthesized **D-Pd M** and Pd M were characterized by transmission electron microscopy (TEM) and high-resolution transmission electron microscopy (HRTEM). As shown in **Figure 2a**, D-**Pd M** exhibits an ultrathin 2D nanosheet structure with a lateral diameter of ≈1 µm. In contrast, Pd M exhibits a hexagonal nanosheet structure with an average diameter of 70 nm (Figure S2, Supporting Information). Selected area electron diffraction (Figure S3, Supporting Information) confirms the presence of a face-centered cubic (fcc) structure, and atomic force microscopy measurements (Figure S4, Supporting Information) give an average thickness of ≈0.9 nm, suggesting the presence of 3 to 5 Pd atom layers.[28] TEM energy-dispersive X-ray spectroscopy (TEM-EDX; Figure S5, Supporting Information) shows the homogenous distribution of Pd, W, and Mo throughout the metallene. The atomic ratio of Pd:W:Mo was determined by inductively coupled plasma optical emission spectroscopy (ICP-OES) to be 93.8: 5.2: 1. Detailed morphological analysis of the TEM data reveals curved surface with abundant defects, including pores and concave structures (Figure S6, Supporting Information), which could be due to the oxidative etching of O_2 and PMo_{12} in the highly acidic environment provided by PMo_{12}.[26,31] The defects were further probed by HR-STEM. Figure 2b shows the presence of pores (red circle, **area 1**) and concave areas (dark blue circle, **area 2**), also see Figure S7 (Supporting Information).[15] The brighter contrast observed in Figure 2b is indicative of the lower thickness in these areas compared to their surroundings. Notably, in the higher magnification of **area 1** (Figure 2c), step atoms at the inner edge can be observed. Meanwhile, in Figure 2d, the clear atom distribution and brighter contrast indicate the presence of a concave structure.[15] Numerous concave structures with various diameters, typically less than 10 nm, are observed in Figure 2e (dark blue circles).

ADVANCED SCIENCE NEWS
www.advancedsciencenews.com

ADVANCED SCIENCE Open Access
www.advancedscience.com

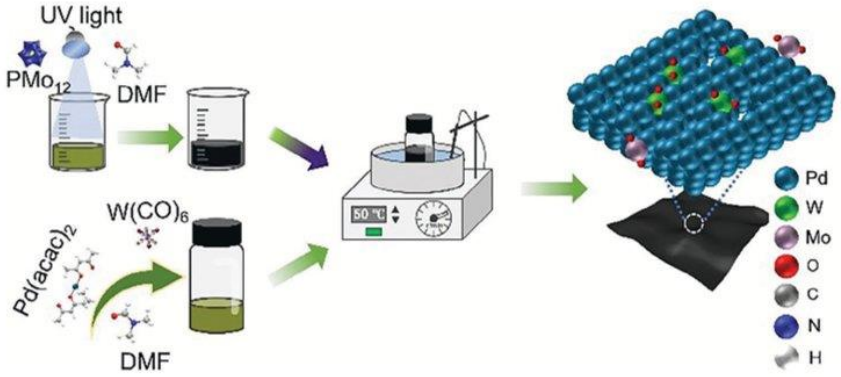

Figure 1. Schematic illustration for the fabrication of **D-Pd M**.

We also use a false-color mode to illustrate the thickness contrast more clearly (Figure S8a–d, Supporting Information). Additionally, curved structures are also observed in HRTEM (green rectangles in Figure 2e; Figure S8e, Supporting Information), which leads to lattice distortion. The fast Fourier transformation (FFT) pattern (Figure S8f, Supporting Information) exhibits a sixfold symmetric fcc structure, implying that the metallene is stacked dominantly along the (111) facets.[15] TEM analyses give a lattice spacing of 0.23 nm (Figure 2f), which exceeds that of bulk Pd, suggesting the presence of intrinsic tensile strain due to its atomically thin structure.

The results are consistent with powder X-ray diffraction (pXRD) analyses shown in Figure 2g, where the peak at 39.4° is attributed to the (111) plane of the fcc structure of Pd metallene. Additionally, smaller peaks corresponding to the (200) plane at 46.7° and the (220) plane at 68.1° in **D-Pd M** compared to Pd M and Pd/C indicate the predominance of the (111)-exposed feature. Furthermore, the shifts to lower 2θ angles observed in **D-Pd M** compared to Pd M and Pd/C are attributed to strain effects and lattice distortions caused by the defect structure. Next, the oxidation states of **D-Pd M** were investigated by X-ray photoelectron spectroscopy (XPS). The deconvoluted spectrum of Pd 3d shows the distinct characteristic peaks centered at 335.4 and 340.7 eV, which are assigned to Pd (0) $3d_{5/2}$ and Pd (0) $3d_{3/2}$, respectively (Figure 2h). The small peaks at 336.7 and 342 eV are assigned to PdO, assigned to surface oxidation of Pd.[25,26] The results indicate that **D-Pd M** is dominated by metallic Pd. The deconvoluted W 4f spectrum (Figure 2i) shows the existence of W^{5+} species.[35] In contrast, the oxidation state of Mo cannot be assigned reliably by XPS due the low concentration of Mo species in **D-Pd M**.

X-ray absorption spectroscopy (XAS) characterization was performed to further investigate the chemical states and local coordination environments of **D-Pd M**. The normalized Pd K-edge X-ray absorption near-edge structure (XANES) spectrum (**Figure** 3a) of **D-Pd M** is similar to the Pd foil reference, indicating its dominant metallic state,[25,26] which coincides with the XPS result. Fourier transform extended X-ray absorption fine structures (FT-EXAFS) analysis was employed to investigate the local environment of the Pd atoms (Figure 3b). The strong peak in the **D-Pd M** EXAFS spectrum at 2.57 Å is assigned to the Pd-Pd pairs.[28] The average coordination number (CN) of elements is proportional to the intensity of FT-χ(k) peak and the corresponding fitting results of Pd K-edge FT-EXAFS (Figure S9 and Table S1, Supporting Information) give an average CN of 10.7 ± 1.0, which is lower than that in Pd foil ($CN_{Pd\ foil} = 12$), indicating the existence of unsaturated Pd sites. This is in agreement with the proposed thin-layered structure and the presence of multiple defects in the **D-Pd M**.[31] The W species in **D-Pd M** was further investigated by analyzing its L_3-edge XANES and FT-EXAFS spectra. As shown in Figure 3c, the white-line peak intensity is between WO_2 and WO_3, which gives an approximate oxidation state of +5.[35,36] This finding is consistent with the results obtained from XPS analysis. In addition, the peaks in the FT-EXAFS spectrum (Figure 3d) at 1.38 and 2.43 Å can be assigned to W-O and W-Pd environments.[36,37] The corresponding fitting results of W L_3-edge FT-EXAFS show the CN of W-Pd is 6.3 ± 0.8. Based on these results, we propose that WO_x ($x = 2.5$) is doped on the surface of metallene. Additionally, W substitutes the position of Pd, as illustrated in Figure S12 (Supporting Information).[38] Notably, while W-W pairs are present in bulk WO_2 and WO_3, they are not observed in **D-Pd M** according to the FT-EXAFS spectrum and wavelet transform analysis (Figure 3g), which can better resolve features in K-space and radial distance. The results indicate that atomic WO_x species are doped on the surface of the metallene. Furthermore, we also investigated the chemical states and local coordination environments of Mo in **D-Pd M** by employing MoO_2, MoO_3, and Mo foil as reference materials. In Figure 3e, MoO_3 exhibits a distinct pre-edge feature at ≈19,995 eV, which is not observed in MoO_2 and Mo foil. Additionally, a weak pre-edge is observed in **D-Pd M**, suggesting that the oxidation state of Mo in **D-Pd M** falls between that of MoO_2 and MoO_3.[39] Furthermore, the near-edge structure XANES spectra also support this conclusion. The FT-EXAFS spectrum in Figure 3f indicates the presence of Mo-O and Mo-Pd pairs, with no Mo-Mo species observed (Figure 3h), suggesting atomic dispersion of MoO_x. The fitting results of Mo K-edge FT-EXAFS for Mo-Pd give a CN of 0.9 ± 0.2, indicating that the MoO_x are located on the surface of the Pd sheets rather than being embedded in the Pd lattice, as illustrated in Figure S12 (Supporting Information).[39] More detailed peak assignments for FT-EXAFS of Pd, W, and Mo can be found in Table S1 (Supporting Information). The comparison of

ADVANCED SCIENCE NEWS
www.advancedsciencenews.com

ADVANCED SCIENCE Open Access
www.advancedscience.com

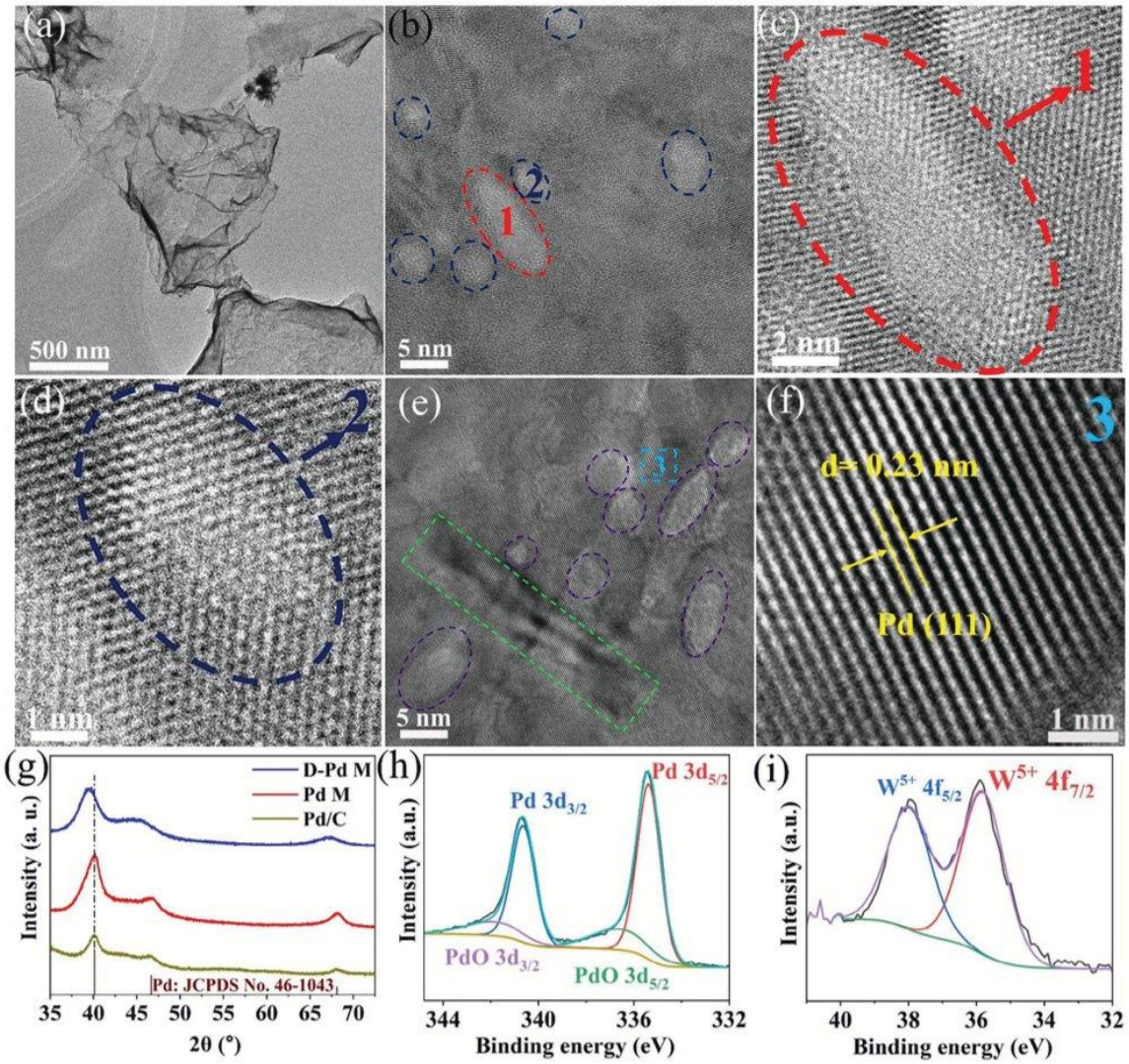

Figure 2. a) TEM image and b,e) HRTEM images of **D-Pd M**, with corresponding enlarged crystal details shown in c,d,f) for selected areas (area 1, area 2, and area 3, respectively). g) XRD patterns of **D-Pd M**, Pd M, and Pd/C. h) Deconvoluted XPS spectra of Pd 3d and i) W 4f of **D-Pd M**.

corresponding fitting results and the raw data can be found in Figures S9–S11 (Supporting Information).

In the next step, we evaluated the electrocatalytic performance of the **D-Pd M** for ORR in 0.1 M aqueous KOH using a typical three-electrode electrochemical setup. Here, the saturated calomel electrode was used as the reference electrode, and a graphite rod was employed as the counter electrode. All potentials in this study have been converted to reversible hydrogen electrode potentials (RHE, see details in the Supporting Information). Prior to the measurement, freshly prepared **D-Pd M** and Pd M were deposited on a VULCAN® XC-72 carbon support (See details in Supporting Information). In addition, commercial 10% Pd/C and 20% Pt/C were also used as ORR catalyst references. The respective catalysts ink was drop-cast onto the glassy carbon rotating disk electrode, which acted as the working electrode. The metal loading on the electrode for **D-Pd M**/C and Pd M/C was controlled to be 10 μg cm^{-2}, while that of commercial Pd/C and Pt/C was controlled to be 15 μg cm^{-2} to reach the well-defined limiting current densities. The typical cyclic voltammetry (CV) curves of all the catalysts were recorded in N_2-saturated 0.1 M KOH at a scan rate of 50 mV s^{-1}. As shown in **Figure** 4a and Figure S13 (Supporting Information), the peak located at 0.74 V of **D-Pd M**/C is assigned to Pd oxide reduction.[28] Notably, the reduction potential is a descriptor of the Pd-O binding energy. Compared to Pd/C (0.69 V) and Pd M/C (0.73 V), the peak of **D-Pd M**/C shifts positively, revealing its weaker

ADVANCED SCIENCE NEWS
www.advancedsciencenews.com

ADVANCED SCIENCE Open Access
www.advancedscience.com

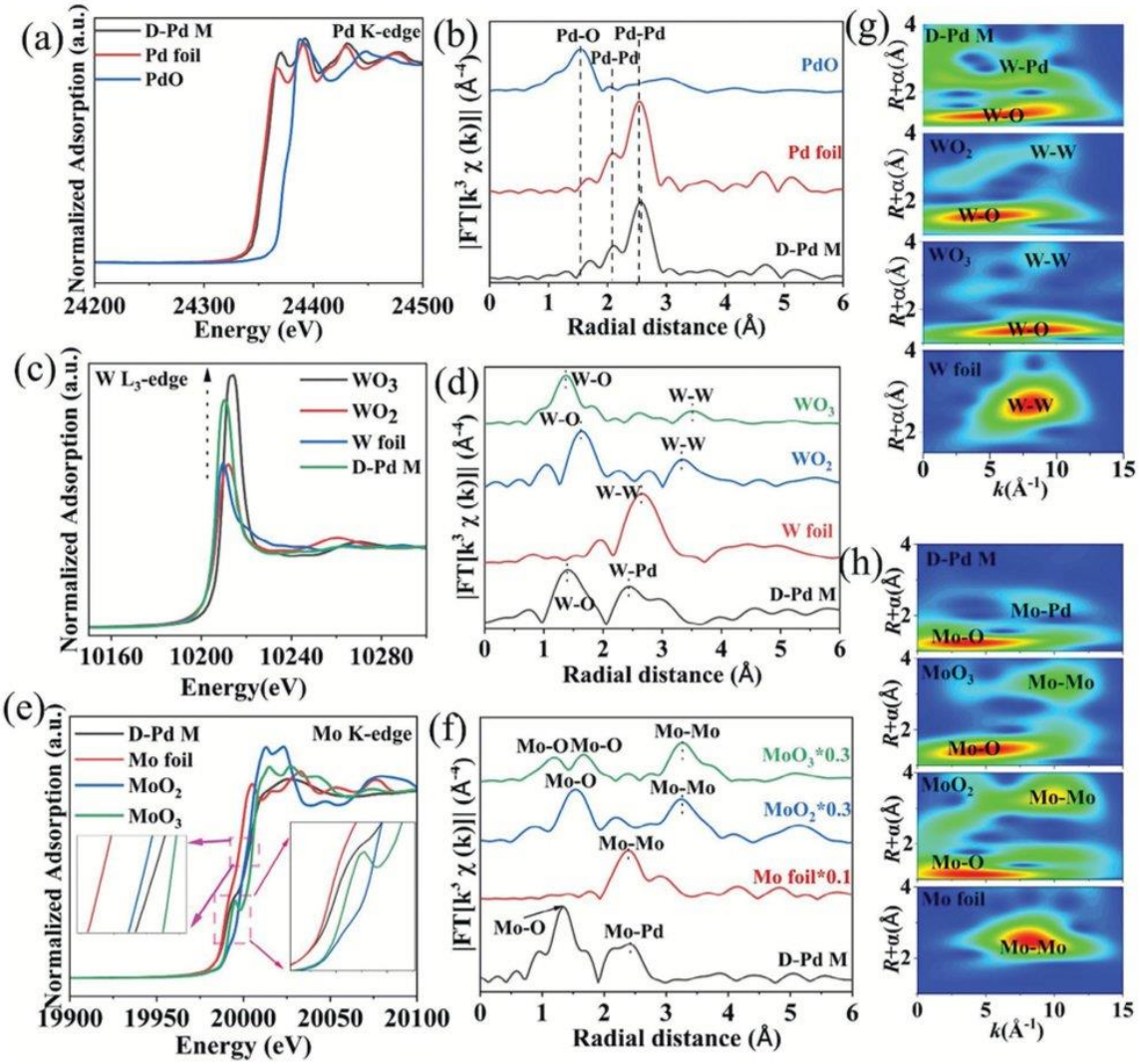

Figure 3. XAS characterizations of **D-Pd M**. Experimental XANES spectra a,c,e) and EXAFS spectra b,d,f) of Pd, W, and Mo, respectively. Wavelet transform profiles of W g) and Mo h).

oxygen affinity.[27,40] Next, we determined the electrochemically active surface areas (ECSAs) of **D-Pd M**/C and reference catalysts by underpotentially deposited hydrogen (H_{upd}) and underpotentially depositing copper (Cu_{upd}) methods (See method details in Supporting Information). The ECSAs determined from the Cu_{upd} method were used for further analysis. The ECSA values are estimated by Cu_{upd} to be 79 m^2 g_{Pd}^{-1} for **D-Pd M**/C, 70.5 m^2 g_{Pd}^{-1} for Pd M/C, 40.4 m^2 g_{Pd}^{-1} for Pd/C, and 51.8 m^2 g_{Pt}^{-1} for Pt/C, respectively (Figure S14, Supporting Information). The increased active areas of **D-Pd M** can be attributed to its porous and curved structure. This structural characteristic ensures that more active sites are exposed to the electrolyte during the catalytic process.

The linear sweep voltammetry (LSV) curves of all the samples were determined in an O_2-saturated 0.1 M KOH electrolyte at a scan rate of 20 mV s^{-1} to assess their ORR performance. As shown in Figure 4b, **D-Pd M**/C shows the most positive half-wave potential ($E_{1/2}$, 0.93 V) and onset potential (E_{onset}, 1.02 V), as compared with those of Pd M/C (0.87 and 0.99 V), Pd/C (0.87 and 1.02 V), and Pt/C (0.88 and 1.01 V), revealing that **D-Pd M**/C exhibited the best catalytic performance for ORR among all the catalysts. The diffusion-limiting current density (j_L) of **D-Pd M**/C (5.7 mA cm^{-2}) is also higher than that of Pd M/C (5.4 mA cm^{-2}), Pd/C (5.5 mA cm^{-2}), and Pt/C (5.6 mA cm^{-2}). Such high limiting current density is a benefit to the high-power densities of Zn-air batteries. Besides, **D-Pd M**/C has the smallest Tafel slope

ADVANCED SCIENCE NEWS
www.advancedsciencenews.com

ADVANCED SCIENCE Open Access
www.advancedscience.com

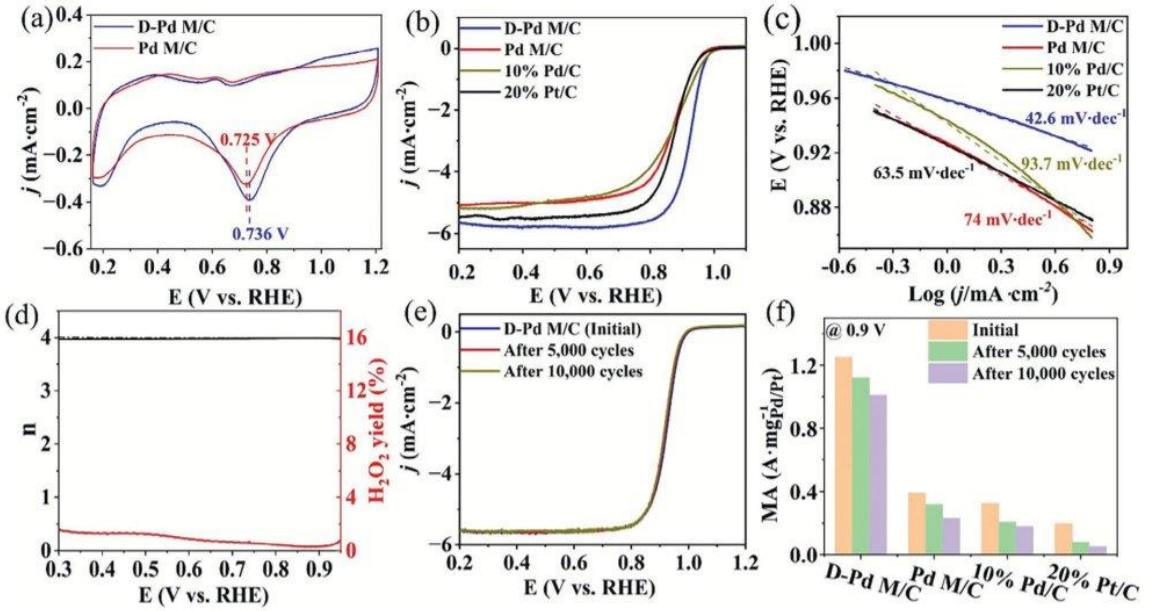

Figure 4. a) CVs of **D-Pd M**/C and Pd M/C, b) LSVs, and c) Tafel slopes of **D-Pd M**/C, Pd M/C, Pd/C, and Pt/C, d) electron transfer number and H_2O_2 yield of **D-Pd M**, e) LSVs of **D-Pd M**, and f) mass activities of **D-Pd M**/C, Pd M/C, Pd/C, and Pt/C at 0.9 V before and after 5,000 and 10,000 cycles.

value (Figure 4c) of 42.6 mV dec^{-1}, compared with that of Pd M/C (74 mV dec^{-1}), Pd/C (93.7 mV dec^{-1}), and Pt/C (63.5 mV dec^{-1}), which indicates faster ORR reaction kinetics on the surface of **D-Pd M**. To further quantify the intrinsic ORR activity, kinetic currents were calculated for all catalysts using the Koutecký-Levich (K-L) equation (see details in Supporting Information). These were then normalized based on the metal mass loading of the catalysts and the ECSA to determine the mass avtivity (MA) and specific activity (SA). As shown in Figure S15 (Supporting Information), **D-Pd M**/C achieves an MA of 1.3 A mg_{Pd}^{-1} at the generally chosen potential of 0.9 V, which is 3.3, 3.9, and 6.5 times higher than that of Pd M/C, commercial Pd/C, and commercial Pt/C. Additionally, **D-Pd M**/C delivers an MA of 5.2 A mg_{Pd}^{-1} at 0.85 V. This value is also apparently higher than that of Pd M/C (1.4 A mg_{Pd}^{-1}), commercial Pd/C (0.88 A mg_{Pd}^{-1}), and commercial Pt/C (0.88 A mg_{Pt}^{-1}). Likewise, **D-Pd M**/C also has specific activities of 6.13 and 1.5 mA cm^{-2} at 0.85 and 0.9 V, respectively, which significantly outperform Pd M/C (1.86 and 0.52 mA cm^{-2}), commercial Pd/C (2.46 and 0.91 mA cm^{-2}), and commercial Pt/C (1.31 and 0.3 mA cm^{-2}). The excellent ORR catalytic performance of **D-Pd M**/C can be attributed to the lower Pd-O binding energy, which facilitates the generation of intermediates (*OH and *OOH) and their transformation to H_2O. Furthermore, to understand the catalytic process of **D-Pd M**, rotating ring-disk electrode measurements were used to determine the electron transfer number (n) and hydrogen peroxide yield, see details in Supporting Information. As shown in Figure 4d and Figure S16a (Supporting Information), the electron transfer number is >3.9 between 0.3 to 0.95 V, revealing a four-electron transfer-dominated pathway, which agrees well with the results obtained from the K-L plot at rotation rates between 625 and 2025 rpm (Figure S16b,c, Supporting Information). The H_2O_2 yield is only 0–1.6% within the potential range from 0.8 to 0.3 V. Pd M/C, Pd/C, and Pt/C exhibit similar results, indicating a consistent four-electron transfer process (Figure S17, Supporting Information).

Apart from electrocatalytic activity, stability is another essential criterion for the comprehensive evaluation of the catalytic performance. Therefore, we employed accelerated durability tests by CV cycling between 0.6 and 1.0 V at a scan rate of 200 mV s^{-1} in an O_2-saturated 0.1 M KOH electrolyte. As shown in Figure 4e, after 5,000 and 10,000 cycles, the $E_{1/2}$ of **D-Pd M**/C shows only negligible decay (4 and 6 mV, respectively). In contrast, an apparent negative shift was observed for Pd M/C (10 and 23 mV), commercial Pd/C (19 and 23 mV), and commercial Pt/C (25 mV and 38 m), respectively (Figure S18, Supporting Information). In addition, the MA of **D-Pd M** /C at 0.9 V has decreased by 10.4% and 19.2% after 5,000 and 10,000 cycles (Figure 3f), which outperforms those of Pd M/C (18.7% and 41%), commercial Pd/C (36.6% and 44.6%), and commercial Pt/C (60.4% and 74.6%). The same scenario was also observed at 0.85 V vs. RHE in all the catalysts (Figure S19, Supporting Information). Additionally, the morphology and structure of **D-Pd M** have no obvious degradation after 10,000 cycles, compared to the pristine sample. In comparison, the apparent aggregation of Pt nanoparticles was observed in Pt/C (Figure S20, Supporting Information). The composition of D-Pd M was determined by ICP-OES, which shows the atomic ratio of Pd:W is 94.2:5.8. However, no Mo was determined, which indicates that MoO_x dissolved under the electrochemical tests and explained the slight catalytic degradation.

Based on the previous report from Norskov, the binding energy between catalysts and O_2 is linearly correlated with the

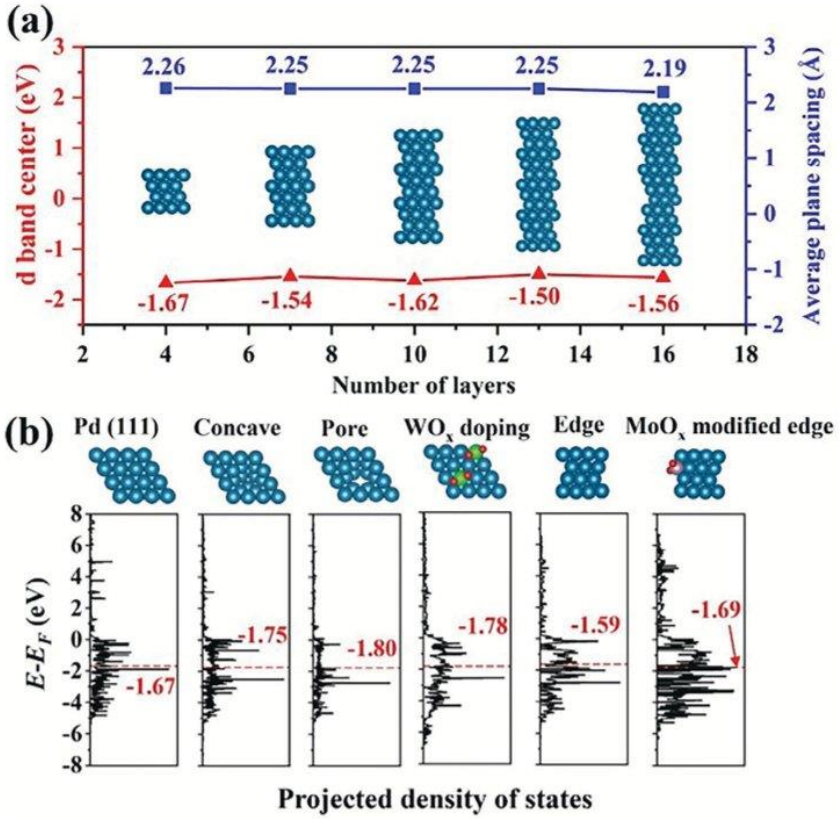

Figure 5. DFT calculations of *d*-band centers. a) The *d*-band center of surface atoms and average plane spacings of Pd nanosheets with 4, 7, 10, 13, and 16 layers. The side view of atomic models is inserted. b) From left to right, the d band centers of surface atoms in Pd (111), exposed sublayer atoms in concave defects, exposed sublayer atoms in pores defects, surface atoms in WO_x doping, edge atoms, and MoO_x modified edge atoms. The first four schematic illustrations are from the top view and the last two are from side view of atomic model. The navy, green, pink, and red balls represent Pd, W, Mo, and O, respectively.

energy center of the valence *d*-band density of states (*d*-band center), making it one of the most successful descriptors of ORR activity.[41] We therefore calculated the *d*-band centers of various defects in **D-Pd M** using density functional theory (DFT) to elucidate the reasons for the superior ORR activity of **D-Pd M**. We constructed a four-atom layer model for the **D-Pd M**, incorporating WO_x doping into the surface lattice of metallene and MoO_x attachment to the edge Pd atoms. The loading of W and Mo were set to 5% and 1%, respectively, to be in line with experimental results. As shown in **Figure** 5a, the *d*-band centers of surface Pd atoms in different layer Pd sheets were calculated. A downward shift (≈0.11 eV) in the *d*-band center of surface atoms is observed in the four-layer Pd sheet compared to the sixteen-layer Pd sheet, which results in less strongly bound O_2 on the surface Pd atoms.[28] We note that the average spacing between the planes in four-layer Pd metallene is 3.2% greater than in a 16-layered nanosheet, indicating a higher level of tensile strain in the four-layer structure compared to multilayer Pd sheets. The electronic structures tuned by defects were also investigated. As illustrated in Figure 5b, in a perfect four-layer Pd sheet, the *d*-band center of the surface atoms in the (111) plane is −1.67 eV. However, when subjected to concave defects and pore defects, the sublayer layer atoms feature substantially lower *d*-band centers (−1.75 and −1.8 eV, respectively) compared to the surface atoms. This indicates a weaker binding ability to O_2, thereby facilitating the formation and conversion of intermediates (*OH and *OOH) to H_2O/OH^-.[14,15] The findings confirm that concave and pore defects serve as effective means to introduce highly active sites, thereby enhancing the catalytic properties for ORR. Moreover, embedding WO_x into the surface Pd lattice also leads to a downshift of the *d*-band center by 0.11 eV. The average *d*-band center of edge Pd atoms was calculated to be −1.59 eV, significantly higher than that of surface atoms. This discrepancy reveals the less favorable catalytic features for ORR exhibited by edge atoms. After attaching MoO_x to the edge Pd atoms, the *d*-band center of these atoms shifted downward to −1.69 eV, a value similar to the *d*-band center of surface atoms in Pd (111), indicating the improved catalytic properties. These computational results suggest that size effects, pore defects, concave defects, WO_x doping, and MoO_x modification can effectively enhance the ORR activity of

ADVANCED SCIENCE NEWS
www.advancedsciencenews.com

ADVANCED SCIENCE Open Access
www.advancedscience.com

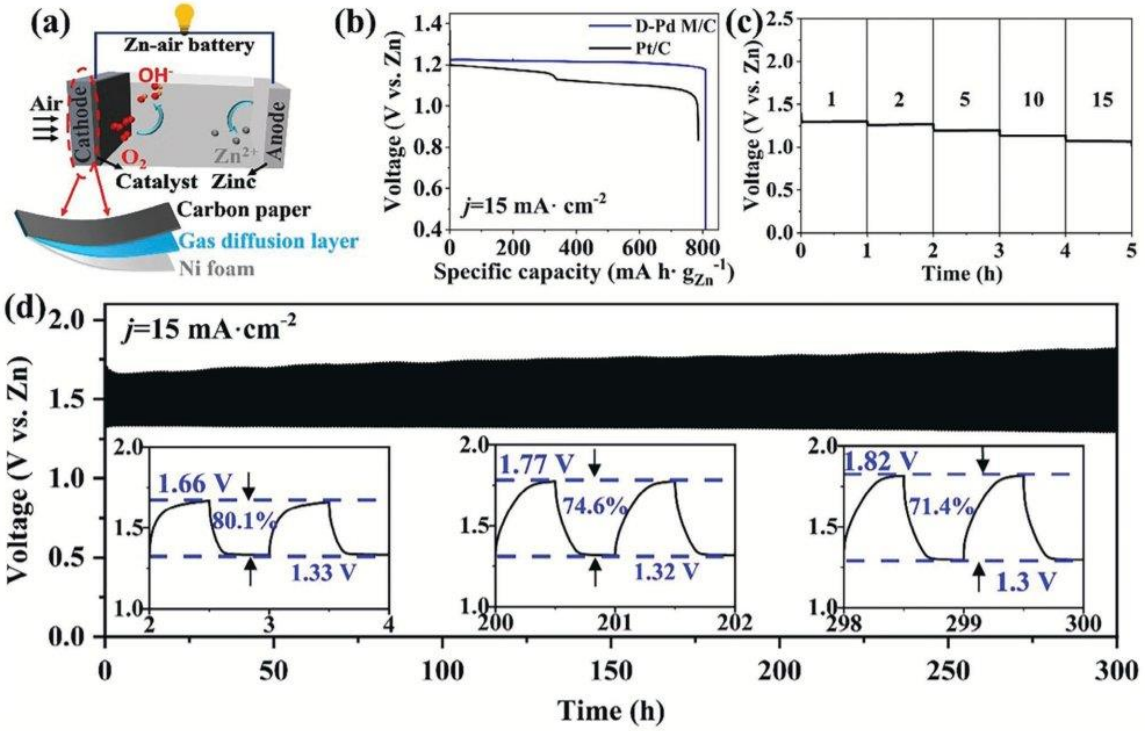

Figure 6. a) Scheme of the aqueous Zn-air battery, b) full discharge profile (voltage versus specific capacity of discharge) for a Zn-air battery using **D-Pd M**/C as the air cathode at a current density of 15 mA cm^{-2}, c) the discharge curves of Zn-air batteries at current densities of 1, 2, 5, 10, and 15 mA cm^{-2}, and d) the charge–discharge profiles of two Zn-air batteries worked at a current density of 15 mA cm^{-2} with each cycle lasting 60 min.

D-Pd M. We note that these calculations do not consider the leaching of MoO_x species during long-term electrochemical operation (see above).

Next, the practical utility of the **D-Pd M** catalyst was tested by integration into an aqueous custom-built Zn-air battery (Figure S21, Supporting Information). Given the economic expense of Pd metal, we opted to test the system at an extremely low Pd loading at the cathode (26 μg_{Pd} cm^{-2}). The principal structure of the Zn-air battery is shown in **Figure 6a**; briefly, the battery is based on a carbon paper-supported **D-Pd M**/C as the air cathode, a Zn plate as the anode, and 6 M aqueous KOH solution containing 0.2 M $Zn(CH_3COO)_2$ as the electrolyte. Initial tests show that the Zn-air battery achieves a high open-circuit potential (OCP) of 1.4 V (Figure S21, Supporting Information). The specific capacities of the **D-Pd M**/C- battery at 15 mA cm^{-2} is illustrated in Figure 6b. For comparison, a reference Zn-air battery using commercial Pt/C coated carbon paper (26 μg_{Pt} cm^{-2}) as air cathode was tested under the same conditions. After normalizing for the weight loss of Zn, the **D-Pd M**/C-based battery exhibits a discharge specific capacity of 809 mAh g_{Zn}^{-1}, corresponding to an energy density of 982 Wh kg_{Zn}^{-1}, which outperforms the Pt/C-based battery (785 mAh g_{Zn}^{-1} and 890 Wh kg_{Zn}^{-1}). In addition, during the long-term discharge test, the potential of the **D-Pd M**/C-based cell remained remarkably stable and only a slight potential decrease of 0.05 V was observed. In contrast, a notable potential drop (>0.2 V) was observed for the Pt/C-based battery. The stability of the **D-Pd M**/C-based battery is further shown by the discharge curves at various current densities (Figure 6c). Also, the **D-Pd M**/C-based battery achieves a high power density (55 mW cm^{-2}) compared with the Pt/C-based battery (37 mW cm^{-2}), see Figure S22a (Supporting Information). The power density of the **D-Pd M**/C-based battery can be increased by at higher **D-Pd M** loadings, see Figure S22b (Supporting Information).

To assess the cycling durability, the **D-Pd M**/C-based Zn-air battery was further tested at a charging and discharging rate of 15 mA cm^{-2} for 60 min per cycle. As illustrated in Figure 6d, **D-Pd M**/C-based battery exhibits a significantly longer cycling lifetime over 300 cycles (≈300 h) with a small charge/discharge voltage gap. Initially, the charge/discharge voltage efficiency reached 80.1% with a potential gap of 0.33 V. During cycling, the voltage efficiency decreased slowly, while the discharging potential remained exceptionally stable throughout the measurement. The gradual increase in charging potential resulted in a decrease in round-trip voltage efficiency, possibly attributed to imperfect oxygen evolution activity under conditions of very low palladium loading (Figure S22c, Supporting Information).

3. Conclusion

In summary, we demonstrate how molecular-level tuning of 2D metallene structures becomes possible using bottom-up materials design routes. The study shows how introduction of various defect sites impacts the oxygen reduction reaction reactivity of a 2D palladene nanostructure catalyst, leading to high reactivity and stability under harsh conditions. Combined experimental and theoretical analyses reveal the correlation between defects, change in electronic structure, and resulting reactivity. Integration of the catalyst into as cathode in a Zn-air battery demonstrated outstanding performance at very low Pd loading. This study offers valuable insights into the design of efficient ORR catalysts with reduced precious metal consumption, which can open new paths for larger-scale deployment of non-earth-abundant elements.

4. Experimental Section

The authors have cited additional references within the Supporting Information.[31,33,42–46] A preprint of this manuscript has been deposited at https://doi.org/10.26434/chemrxiv-2024-fkr00.

Supporting Information

Supporting Information is available from the Wiley Online Library or from the author.

Acknowledgements

Y.Z. and Z.C. contributed equally to this work. The authors gratefully acknowledge financial support by the Deutsche Forschungsgemeinschaft DFG (Cluster of Excellence EXC2154, POLiS, project number: 390874152 and TRR 234 CataLight, project no. 364549901 and project no. 389183496). R.L. gratefully acknowledges financial support by the Alexander von Humboldt Foundation. S.L. and N.M. gratefully acknowledge financial support by National Natural Science Foundation of China (22171073) and the Program for Innovation Talents in Universities of Henan Province (23HASTIT005). D.G. acknowledges the Deutsche Forschungsgemeinschaft (DFG) for a Walter Benjamin Fellowship (project no. 510966757). Financial support by the Carl Zeiss Foundation (Halocycles, project no P2021-10-007) is gratefully acknowledged by D.G. and C.S.. Z.C. and F. F. gratefully acknowledge the China Scholarship Council CSC for a Ph.D. fellowship. R.L., D.G., and C.S. gratefully acknowledge financial support by Johannes Gutenberg University Mainz, the Top-Level Research Initiative SusInnoScience and the Gutenberg Research College.

Open access funding enabled and organized by Projekt DEAL.

Conflict of Interest

The authors declare no conflict of interest.

Data Availability Statement

The data that support the findings of this study are openly available in Zenodo.org at https://doi.org/10.5281/zenodo.10984539, reference number 10984539.

Keywords

defect engineering, electrocatalysis, metallene, oxygen reduction reaction, zn-air battery

Received: June 1, 2024
Revised: July 24, 2024
Published online: August 19, 2024

[1] S. Chu, A. Majumdar, *Nature* **2012**, *488*, 294.
[2] A. Han, X. Wang, K. Tang, Z. Zhang, C. Ye, K. Kong, H. Hu, L. Zheng, P. Jiang, C. Zhao, Q. Zhang, D. Wang, Y. Li, *Angew. Chem., Int. Ed.* **2021**, *60*, 19262.
[3] C. Lim, A. R. Fairhurst, B. J. Ransom, D. Haering, V. R. Stamenkovic, *ACS Catal.* **2023**, *13*, 14874.
[4] Z. Ma, Z. P. Cano, A. Yu, Z. Chen, G. Jiang, X. Fu, L. Yang, T. Wu, Z. Bai, J. Lu, *Angew. Chem., Int. Ed.* **2020**, *59*, 18334.
[5] Z. Lyu, X.-G. Zhang, Y. Wang, K. Liu, C. Qiu, X. Liao, W. Yang, Z. Xie, S. Xie, *Angew. Chem., Int. Ed.* **2021**, *60*, 16093.
[6] Q. Yang, Y. Jia, F. Wei, L. Zhuang, D. Yang, J. Liu, X. Wang, S. Lin, P. Yuan, X. Yao, *Angew. Chem., Int. Ed.* **2023**, *62*, 202315752.
[7] M. A. de Araújo, A. A. Koverga, A. M. P. Sakita, F. B. Ometto, L. G. daTrindade, E. A. Ticianelli, *ChemCatChem* **2023**, *15*, 202201594.
[8] J. Zhang, L. iangti Qu, G. Shi, J. Liu, J. Chen, L. Dai, D. Zhang, J. Liu, L. Dai, L. Qu, G. Shi, J. Chen, *Angew. Chem., Int. Ed.* **2016**, *55*, 2230.
[9] Z. Zhao, C. Chen, Z. Liu, J. Huang, M. Wu, H. Liu, Y. Li, Y. Huang, *Adv. Mater.* **2019**, *31*, 1808115.
[10] K. J. Sawant, Z. Zeng, J. P. Greeley, *Angew. Chem., Int. Ed.* **2024**, *63*, 202312747.
[11] E. Hornberger, V. Mastronardi, R. Brescia, P. P. Pompa, M. Klingenhof, F. Dionigi, M. Moglianetti, P. Strasser, *ACS Appl. Energy Mater.* **2021**, *4*, 9542.
[12] T. Đukić, L. Pavko, P. Jovanovič, N. Maselj, M. Gatalo, N. Hodnik, *Chem. Commun.* **2022**, *58*, 13832.
[13] D. Y. Chung, J. M. Yoo, Y. E. Sung, *Adv. Mater.* **2018**, *30*, 1704123.
[14] S. Huang, S. Lu, S. Gong, Q. Zhang, F. Duan, H. Zhu, H. Gu, W. Dong, M. Du, *ACS Nano* **2022**, *16*, 522.
[15] F. Lin, F. Lv, Q. Zhang, H. Luo, K. Wang, J. Zhou, W. Zhang, W. Zhang, D. Wang, L. Gu, S. Guo, *Adv. Mater.* **2022**, *34*, 2202084.
[16] N. Zhang, Q. Shao, X. Xiao, X. Huang, *Adv. Funct. Mater.* **2019**, *29*, 1808161.
[17] L. Bu, N. Zhang, S. Guo, X. Zhang, J. Li, J. Yao, T. Wu, G. Lu, J. Y. Ma, D. Su, X. Huang, *Science* **2016**, *354*, 1410.
[18] X. Wang, Z. Li, Y. Qu, T. Yuan, W. Wang, Y. Wu, Y. Li, *Chem* **2019**, *5*, 1486.
[19] Y. Yang, W. Xiao, X. Feng, Y. Xiong, M. Gong, T. Shen, Y. Lu, H. D. Abruña, D. Wang, *ACS Nano* **2019**, *13*, 5968.
[20] L. Zhang, Z. Zhao, X. Fu, S. Zhu, Y. Min, Q. Xu, Q. Li, *ACS Appl. Mater. Interfaces* **2023**, *15*, 5198.
[21] Q. Yang, L. Shi, B. Yu, J. Xu, C. Wei, Y. Wang, H. Chen, *J. Mater. Chem. A* **2019**, *7*, 18846.
[22] B. R. Anne, S. Il Choi, *Curr. Opin. Electrochem.* **2023**, *39*, 101303.
[23] S. Huang, S. Lu, S. Gong, Q. Zhang, F. Duan, H. Zhu, H. Gu, W. Dong, M. Du, *ACS Nano* **2022**, *16*, 522.
[24] M. Xie, S. Tang, B. Zhang, G. Yu, *Mater. Horiz.* **2023**, *10*, 407.
[25] K. Chen, Z. Ma, X. Li, J. Kang, D. Ma, K. Chu, *Adv. Funct. Mater.* **2023**, *33*, 2209890.
[26] Y. Xiong, J. M. McLellan, J. Chen, Y. Yin, Z. Li, Y. Xia, *J. Am. Chem. Soc.* **2005**, *127*, 17118.
[27] J. Guo, L. Gao, X. Tan, Y. Yuan, J. Kim, Y. Wang, H. Wang, Y. J. Zeng, S. Il Choi, S. C. Smith, H. Huang, *Angew. Chem., Int. Ed.* **2021**, *60*, 10942.
[28] M. Luo, Z. Zhao, Y. Zhang, Y. Sun, Y. Xing, F. Lv, Y. Yang, X. Zhang, S. Hwang, Y. Qin, J. Y. Ma, F. Lin, D. Su, G. Lu, S. Guo, *NatureNature* **2019**, *574*, 81.
[29] K. Zhang, Y. He, R. Guo, W. Wang, Q. Zhan, R. Li, T. He, C. Wu, M. Jin, *ACS Energy Lett.* **2022**, *7*, 3329.

[30] H. Yu, T. Zhou, Z. Wang, Y. Xu, X. Li, L. Wang, H. Wang, *Angew. Chem., Int. Ed.* **2021**, *60*, 12027.
[31] J. Ge, P. Wei, G. Wu, Y. Liu, T. Yuan, Z. Li, Y. Qu, Y. Wu, H. Li, Z. Zhuang, X. Hong, Y. Li, *Angew. Chem., Int. Ed.* **2018**, *57*, 3435.
[32] E. A. Nagul, I. D. McKelvie, P. Worsfold, S. D. Kolev, *Anal. Chim. Acta* **2015**, *890*, 60.
[33] J. N. Barrows, G. B. Jameson, M. T. Pope, *J. Am. Chem. Soc.* **1985**, *107*, 1771.
[34] Y. Li, Y. Yan, Y. Li, H. Zhang, D. Li, D. Yang, *CrystEngComm* **2015**, *17*, 1833.
[35] P. Castillero, V. Rico-Gavira, C. López-Santos, A. Barranco, V. Pérez-Dieste, C. Escudero, J. P. Espinós, A. R. González-Elipe, *J. Phys. Chem. C* **2017**, *121*, 15719.
[36] H. Wang, H. Zheng, L. Ling, Q. Fang, L. Jiao, L. Zheng, Y. Qin, Z. Luo, W. Gu, W. Song, C. Zhu, *ACS Nano* **2022**, *16*, 21266.
[37] K. Chen, F. Wang, X. Lu, Y. Li, K. Chu, *ACS Catal* **2023**, *13*, 9550.
[38] K. Chen, Z. Ma, X. Li, J. Kang, D. Ma, K. Chu, *Adv. Funct. Mater.* **2023**, *33*, 2209890.
[39] J. Wu, J. Fan, X. Zhao, Y. Wang, D. Wang, H. Liu, L. Gu, Q. Zhang, L. Zheng, D. J. Singh, X. Cui, W. Zheng, *Angew. Chem., Int. Ed.* **2022**, *61*, 202207512.
[40] Y. Wang, D. Sun, M. Wang, Z. Feng, A. S. Hall, *J. Phys. Chem. C* **2020**, *124*, 5220.
[41] B. Hammer, J. K. Nørskov, *Surf. Sci.* **1995**, *343*, 211.
[42] G. Kresse, J. Furthmüller, *Comput. Mater. Sci.* **1996**, *6*, 15.
[43] G. Kresse, J. Hafner, *Phys. Rev. B* **1994**, *49*, 14251.
[44] G. Kresse, D. Joubert, *Phys. Rev. B* **1999**, *59*, 1758.
[45] K. Lee, É. D. Murray, L. Kong, B. I. Lundqvist, D. C. Langreth, *Phys. Rev. B* **2010**, *82*, 081101.
[46] V. Wang, N. Xu, J. C. Liu, G. Tang, W. T. Geng, *Comput. Phys. Commun.* **2021**, *267*, 108033.

4. Summary and outlook

This thesis aims to achieve superior OER performance in photoelectrochemical water splitting using CoPOM-based $BiVO_4$ photoanodes. The study includes thorough characterization of the materials' composition both before and after catalysis, as well as an analysis of the contributions from the doping agent and CoPOM cocatalysts modification. This leads to a detailed understanding of the role of CoPOM-based water oxidation catalysts and doping agents in the $BiVO_4$ system, promoting enhanced photo-electrocatalytic activities. The specific objectives corresponding to Chapter 2 are outlined and summarized in the document.

4.1 Mo-doping of $BiVO_4$ photoanodes combined with cobalt polyoxometalate water oxidation catalyst for PEC water oxidation

We use a facile two-in-one strategy to enhance the performance of $BiVO_4$ photoanodes for water oxidation by combining the bulk doping of $BiVO_4$ with molybdenum and its surface modification with a well-defined molecular cobalt polyoxometalate (CoPOM). The resulting modified photoanodes show significantly improved photocurrent densities compared to non-modified reference. Mechanistic investigations elucidate the contributions of Mo-doping and modification with CoPOM to the performance enhancement for water oxidation. Mo-doping leads to enhanced electronic conductivity and passivation of surface states. The deposition of CoPOM enhances photocurrents across the whole potential range, which results in enhanced water oxidation catalysis. Experimental evidence shows that under the PEC operating conditions the molecular CoPOM is, at least partially, disintegrated and converted to cobalt oxide, and is therefore considered as a pre-catalyst. In summary, this work establishes CoPOM-derived catalysts as effective water oxidation catalysts for $BiVO_4$ photoanodes and provides new insights into the combined effects of Mo doping and modification with molecular cobalt polyoxometalates on the PEC performance of $BiVO_4$. Furthermore, it suggests that further advancements in the development of $BiVO_4$ photoanodes critically depend on devising alternative doping strategies to mitigate the negative polaronic effects associated with bulk doping of $BiVO_4$, as these detrimental effects impose fundamental limits on the maximum achievable photovoltage and compromise overall photoconversion efficiency.

4.2 CoPOM-doping $BiVO_4$ with modification CoPOM on the surface for light-driven OER

We have demonstrated a novel ‘Double-Use’ strategy for fabrication of high-performance $BiVO_4$ photoanodes for solar water splitting in which a single precursor, a

molecular cobalt polyoxometalate (CoPOM), is used both as a doping agent and as a co-catalyst for water oxidation. Doping $BiVO_4$ by CoPOM significantly enhances the conductivity and improves the charge separation efficiency, resulting in the enhancement of the maximum applied-bias photoconversion efficiency (ABPE) by a factor of ~18 as compared to pristine $BiVO_4$. Further surface modification of CoPOM-doped $BiVO_4$ with CoPOM as a co-catalyst enhances the hole extraction and improves the water oxidation kinetics, yielding the overall enhancement of the ABPE as high as by a factor of ~26 with respect to pristine $BiVO_4$. Interestingly, with respect to the doped $BiVO_4$ photoanodes, we found systematic differences in the surface composition and PEC performance of samples doped with CoPOM as compared to samples with identical elemental composition but doped with metal salts. While these differences are not fully understood yet, they point to possible advantages of using molecularly well-defined precursors, such as CoPOM, in fabrication of high-performance photoelectrodes. Taken together, our results establish the 'Double-Use' strategy involving CoPOMs as a remarkably effective, straightforward and easily scalable approach for the development of high-quality photoanodes for solar water splitting and highlight the future potential of utilizing well-designed polyoxometalates as precursors for the synthesis of energy materials.

4.3 Defect rich Pt metallene for ORR

We demonstrate a defect-rich Pd metallene (D-Pd M) synthesized by a facile wet-chemical approach. Detailed structural analyses reveal the presence of three distinct atomic-level defects, including pores, concave surfaces, and atomic doping with tungsten and molybdenum oxides (WO_x and MoO_x). Density functional theory (DFT) calculations indicated that these defects resulted in a downward shift of the d-band center in Pd, which in turn led to a reduced binding energy with O_2. As a result, D-Pd M shows a high ORR reactivity and stability under harsh conditions. Integration of the catalyst into as cathode in a Zn-air battery demonstrated impressive specific capacity and outstanding stability in discharge potential at very low Pd loading. This study offers valuable insights into the design of efficient ORR catalysts with reduced precious metal consumption, which can open new paths for larger-scale deployment of non-earth-abundant elements.

5. References

1. *https://ourworldindata.org/energy-production-consumption?ref=ai-infra-link.com*
2. International Energy Outlook 2016 (US Energy Information Administration, **2016**). *https://www.eia.gov/outlooks/ieo/pdf/0484(2016).pdf*
3. S. Chu, Y. Cui, N. Liu. The Path Towards Sustainable Energy. *Nat. Mater.*, **2017**, 16, 16−22.
4. L. Chen, Y. Hu, R. Wang, X. Li, Z. Chen, J. Hua, A. I. Osman, M. Farghali, L. Huang, J. Li, L. Dong, D. W. Rooney, P.-S. Yap. Green Building Practices to Integrate Renewable Energy in the Construction Sector: A Review. *Environ. Chem. L.*, **2024**, 22, 751–784.
5. S. Chu, A. Majumdar. Opportunities and Challenges for A Sustainable Energy Future. *Nature*, **2012**, 488, 294–303.
6. J.P. Holdren. Energy and Sustainability. *Science*, **2007**, 315, 737.
7. H. Meschede, P. Bertheau, S. Khalili, C. Breyer. A review of 100% Renewable Energy Scenarios on Islands. *WIREs Energy Environ.*, **2022**, 11, e450.
8. R. Avtar, N. Sahu, A. K. Aggarwal, S. Chakraborty, A. Kharrazi, A. P. Yunus, J. Dou, T. A. Kurniawan. Exploring Renewable Energy Resources Using Remote Sensing and GIS—A Review. *Resources*, **2019**, 8, 149.
9. *https://energy.ec.europa.eu/topics/renewable-energy/solar-energy_en*
10. X. Lv, W. Tian, Z. Yuan. Recent Advances in High-Efficiency Electrocatalytic Water Splitting Systems. *Electron. Energy Rev.*, **2023**, 6, 23.
11. T. Nann, S. K. Ibrahim, P.-M. Woi, S. Xu, J. Ziegler, C. J. Pickett. Water Splitting by Visible Light: A Nanophotocathode for Hydrogen Production. *Angew. Chem. Int. Ed.*, **2010**, 49, 1574–1577.
12. B. Zhang, Z. Wu, W. Shao, Y. Gao, W. Wang, T. Ma, L. Ma, S. Li, C. Cheng, C. Zhao. Interfacial Atom-Substitution Engineered Transition-Metal Hydroxide Nanofibers with High-Valence Fe for Efficient Electrochemical Water Oxidation. *Angew. Chem., Int. Ed.*, **2022**, 61, e202115331.
13. P. Zhou, I. A. Navid, Y. Ma, Y. Xiao, P. Wang, Z. Ye, B. Zhou, K. Sun, Z. Mi. Solar-to-Hydrogen Efficiency of more than 9% in Photocatalytic Water Splitting. *Nature*, **2023**, 613, 66−70.
14. A. Vasileff, Y. Zheng, S. Z. Qiao. Carbon Solving Carbon's Problems: Recent Progress of Nanostructured Carbon-Based Catalysts for the Electrochemical Reduction of CO_2. *Adv. Energy Mater.*, **2017**, 7,1700759.
15. M. Aresta, A. Dibenedetto, A. Angelini. Catalysis for the Valorization of Exhaust Carbon: from CO_2 to Chemicals, Materials, and Fuels. Technological Use of CO_2. *Chem. Rev.*, **2014**, 114, 1709−1742.

16. I. E. Khalil, C. Xue, W. Liu, X. Li, Y. Shen, S. Li, W. Zhang, F. Huo. The Role of Defects in Metal–Organic Frameworks for Nitrogen Reduction Reaction: When Defects Switch to Features. *Adv. Funct. Mater.*, **2021**, 31, 2010052.

17. D. Liu, M. Chen, X. Du, H. Ai, K. H. Lo, S. Wang, S. Chen, G. Xing, X. Wang, H. Pan. Development of Electrocatalysts for Efficient Nitrogen Reduction Reaction under Ambient Condition. *Adv. Funct. Mater.*, **2021**, 31, 2008983.

18. D. Liu, L. Qiao, S. Peng, H. Bai, C. Liu, W. F. Ip, K. H. Lo, H. Liu, K. W. Ng, S. Wang, X. Yang, H. Pan. Recent Advances in Electrocatalysts for Efficient Nitrate Reduction to Ammonia. *Adv. Funct. Mater.*, **2023**, 33, 2303480.

19. V. Kyriakou, I. Garagounis, A. Vourros, E. Vasileiou, M. Stoukides. An Electrochemical Haber-Bosch Process. *Joule*, **2020**, 4, 142–158.

20. C. Li, Z. Luo, T. Wang, J. Gong. Surface, Bulk, and Interface: Rational Design of Hematite Architecture toward Efficient Photo-Electrochemical Water Splitting. *Adv. Mater.*, **2018**, 30, 1707502.

21. Z. Chen, H. N. Dinh, E. Miller. Photoelectrochemical Water Splitting: Standards, Experimental Methods, and Protocols. *New York: Springer*, **2013**. https://link.springer.com/book/10.1007/978-1-4614-8298-7

22. A. Fujishima, K. Honda. Electrochemical Photolysis of Water at a Semiconductor Electrode. *Nature*, **1972**, 238, 37–38.

23. J. H. Kim, J. S. Lee. Elaborately Modified $BiVO_4$ Photoanodes for Solar Water Splitting. *Adv. Mater.*, **2019**, 31, 1806938.

24. I. Roger, M. A. Shipman, M. D. Symes. Earth-abundant Catalysts for Electrochemical and Photoelectrochemical Water Splitting. *Nat. Rev. Chem.*, **2017**, 1, 0003.

25. J. Song, C. Wei, Z. Huang, C. Liu, L. Zeng, X. Wang, Z. J. Xu. A Review on Fundamentals for Designing Oxygen Evolution Electrocatalysts. *Chem. Soc. Rev.*, **2020**, 49, 2196–2214.

26. M. T. Pope, A. Miiller. Polyoxometalate Chemistry: An Old Field with New Dimensions in Several Disciplines. *Angew. Chem. Int. Ed. Engl.*, **1991**, 30, 34−48.

27. L. Guo, L. He, Q. Zhuang, B. Li, C. Wang, Y. Lv, J. Chu, Y. Song. Recent Advances in Confining Polyoxometalates and the Applications. *Small*, **2023**, 19, 2207315.

28. F. M. B. Gusmão, D. Mladenović, K. Radinović, D. M. F. Santos, B. Šljukić. Polyoxometalates as Electrocatalysts for Electrochemical Energy Conversion and Storage. *Energies*, **2022**, 15, 9021.

29. L. Zhang, Z. Chen. Polyoxometalates: Tailoring Metal Oxides in Molecular Dimension Toward Energy Applications. *Int. J. Energy Res.*, **2020**, 44, 3316−3346.

30. R. van de Krol, M. Grätzel. Photoelectrochemical Hydrogen Production. *New York: Springer*, **2012**. https://link.springer.com/book/10.1007/978-1-4614-1380-6

31. M. A. Gaikwad, U. P. Suryawanshi, U. V. Ghorpade, J. S. Jang, M. P. Suryawanshi, J. H. Kim. Emerging Surface, Bulk, and Interface Engineering Strategies on $BiVO_4$ for Photoelectrochemical Water Splitting. *Small*, **2022**, 18, 2105084.

32. S. Yi, J. Yan, Q. Jiang. Carbon Quantum Dot Sensitized Integrated Fe_2O_3@g-C_3N_4 Core–shell Nanoarray Photoanode Towards Highly Efficient Water Oxidation. *J. Mater. Chem. A*, **2018**, 6, 9839–9845.

33. J. Jian, Y. Xu, X. Yang, W. Liu, M. Fu, H. Yu, F. Xu, F. Feng, L. Jia, D. Friedrich, R. van de Krol, H. Wang. Embedding Laser Generated Nanocrystals in $BiVO_4$ Photoanode for Efficient Photoelectrochemical Water Splitting. *Nat. Commun.*, **2019**, 10, 2609.

34. J. Jian, S. Wang, Q. Ye, F. Li, G. Su, W. Liu, C. Qu, F. Liu, C. Li, L. Jia, A. A. Novikov, V. A. Vinokurov, D. H. S. Harvey, D. Shchukin, D. Friedrich, R. van de Krol, H. Wang. Activating Semiconductor-Liquid Junction via Laser Derived Dual Interfacial Layers for Boosted Photoelectrochemical Water Splitting. *Adv. Mater.*, **2022**, 34, 2201140.

35. J. R. Bolton, S. J. Stricklert, J. S. Connolly. Limiting and Realizable Efficiencies of Solar Photolysis of Water. *Nature*, **1985**, 316, 495–500.

36. K. Zhang, M. Ma, P. Li, D. H. Wang, J. H. Park. Water Splitting Progress in Tandem Devices: Moving Photolysis beyond Electrolysis. *Adv. Energy Mater.*, **2016**, 6, 1600602.

37. Z. Yu, H. Liu, M. Zhu, Y. Li, W. Li. Interfacial Charge Transport in 1D TiO_2 Based Photoelectrodes for Photoelectrochemical Water Splitting. *Small*, **2021**, 17, 1903378.

38. T. Butburee, Y. Bai, H. Wang, H. Chen, Z. Wang, G. Liu, J. Zou, P. Khemthong, G. Q. M. Lu, L. Wang. 2D Porous TiO_2 Single-Crystalline Nanostructure Demonstrating High Photo-Electrochemical Water Splitting Performance. *Adv. Mater.*, **2018**, 30, 1705666.

39. I. S. Cho, C. H. Lee, Y. Feng, M. Logar, P. M. Rao, L. Cai, D. R. Kim, R. Sinclair, X. Zheng. Codoping Titanium Dioxide Nanowires with Tungsten and Carbon for Enhanced Photoelectrochemical Performance. *Nat. Commun.*, **2013**, 4, 1723.

40. F. Feng, C. Li, J. Jian, X. Qiao, H. Wang, L. Jia. Boosting Hematite Photoelectrochemical Water Splitting by Decoration of TiO_2 at the Grain Boundaries. *Chem. Eng. J.*, **2019**, 368, 959–967.

41. M. Sarnowska, K. Bienkowski, P. J. Barczuk, R. Solarska, J. Augustynski. Highly Efficient and Stable Solar Water Splitting at (Na)WO_3 Photoanodes in Acidic Electrolyte Assisted by Non-Noble Metal Oxygen Evolution Catalyst. *Adv. Energy Mater.*, **2016**, 6, 1600526.

42. Y. Zhao, S. Balasubramanyam, R. Sinha, R. Lavrijsen, M. A. Verheijen, A. A. Bol, A. Bieberle-Hütter. Physical and Chemical Defects in WO_3 Thin Films and Their Impact on Photoelectrochemical Water Splitting. *ACS Appl. Energy Mater.*, **2018**, 1, 5887−5895.

43. M. Zhong, T. Hisatomi, Y. Kuang, J. Zhao, M. Liu, A. Iwase, Q. Jia, H. Nishiyama, T. Minegishi, M. Nakabayashi, N. Shibata, R. Niishiro, C. Katayama, H. Shibano, M. Katayama, A. Kudo, T. Yamada, K. Domen. Surface Modification of CoO_x Loaded $BiVO_4$ Photoanodes with Ultrathin p-Type NiO Layers for Improved Solar Water Oxidation. *J. Am. Chem. Soc.*, **2015**, 137, 5053−5060.

44. J. Pan, S. Shen, L. Chen, C. Au, S. Yin. Core–Shell Photoanodes for Photoelectrochemical Water Oxidation. *Adv. Funct. Mater.*, **2021**, 31, 2104269.

45. G. Liu, S. Ye, P. Yan, F. Xiong, P. Fu, Z. Wang, Z. Chen, J. Shi, C. Li. Enabling an Integrated Tantalum Nitride Photoanode to Approach the Theoretical Photocurrent Limit for Solar Water Splitting. *Energy Environ. Sci.*, **2016**, 9, 1327−1334.

46. L. Wang, X. Zhou, N. T. Nguyen, I. Hwang, P. Schmuki. Strongly Enhanced Water Splitting Performance of Ta_3N_5 Nanotube Photoanodes with Subnitrides. *Adv. Mater.*, **2016**, 28, 2432–2438.

47. L. Zhang, D. Bahnemann. Synthesis of Nanovoid Bi_2WO_6 2D Ordered Arrays as Photoanodes for Photoelectrochemical Water Splitting. *ChemSusChem*, **2013**, 6, 283–290.

48. S. Wang, P. Chen, J. Yun, Y. Hu, L. Wang. An Electrochemically Treated $BiVO_4$ Photoanode for Efficient Photoelectrochemical Water Splitting. *Angew. Chem. Int. Ed.*, **2017**, 56, 8500–8504.

49. H. Yin, Y. Guo, N. Zhang, Y. Wang, S. Zhang, R. Jiang. Boosting Photoelectrochemical Water Oxidation by Sandwiching Gold Nanoparticles Between $BiVO_4$ and NiFeOOH. *J. Mater. Chem. A*, **2023**, 11, 24239–24247.

50. S. Wang, G. Liu, L. Wang. Crystal Facet Engineering of Photoelectrodes for Photoelectrochemical Water Splitting. *Chem. Rev.*, **2019**, 119, 5192−5247.

51. D. Zhou, L. Pang, D. Wang, I. M. Reaney. $BiVO_4$ Based High k Microwave Dielectric Materials: A Review. *J. Mater. Chem. C*, **2018**, 6, 9290−9313.

52. L. Gao, F. Li, H. Hu, X. Long, N. Xu, Y. Hu, S. Wei, C. Wang, J. Ma, J. Jin. Dual Modification of a $BiVO_4$ Photoanode for Enhanced Photoelectrochemical Performance. *ChemSusChem*, **2018**, 11, 2502–2509.

53. Z. Zhang, X. Huang, B. Zhang, Y. Bi. High-Performance and Stable $BiVO_4$ Photoanodes for Solar Water Splitting via Phosphorus–oxygen Bonded FeNi Catalysts. *Energy Environ. Sci.*, **2022**, 15, 2867–2873.

54. J. Wiktor, F. Ambrosio, A. Pasquarello. Role of Polarons in Water Splitting: The Case of $BiVO_4$. *ACS Energy Lett.*, **2018**, 3, 1693−1697.

55. Y. Uemura, D. Kido, A. Koide, Y. Wakisaka, Y. Niwa, S. Nozawa, K. Ichiyanagi, R. Fukaya, S. Adachi, T. Katayama, T. Togashi, S. Owada, M. Yabashi, K. Hatada, A. Iwase, A. Kudo, S. Takakusagi, T. Yokoyama, K. Asakura. Capturing Local Structure Modulations of Photoexcited $BiVO_4$ by Ultrafast Transient XAFS. *Chem. Commun.*, **2017**, 53, 7314−7317.

56. F. F. Abdi, T. J. Savenije, M. M. May, B. Dam, R. van de Krol. The Origin of Slow Carrier Transport in $BiVO_4$ Thin Film Photoanodes: A Time-Resolved Microwave Conductivity Study. *J. Phys. Chem. Lett.*, **2013**, 4, 2752−2757.

57. F. M. Toma, J. K. Cooper, V. Kunzelmann, M. T. McDowell, J. Yu, D. M. Larson, N. J. Borys, C. Abelyan, J. W. Beeman, K. M. Yu, J. Yang, L. Chen, M. R. Shaner, J. Spurgeon, F. A. Houle, K. A. Persson, I. D. Sharp. Mechanistic Insights into Chemical and Photochemical Transformations of Bismuth Vanadate Photoanodes. *Nat. Commun.*, **2016**, 7, 12012.

58. K. Sayama, A. Nomura, T. Arai, T. Sugita, R. Abe, M. Yanagida, T. Oi, Y. Iwasaki, Y. Abe, H. Sugihara. Photoelectrochemical Decomposition of Water into H_2 and O_2 on Porous $BiVO_4$ Thin-Film Electrodes under Visible Light and Significant Effect of Ag Ion Treatment. *J. Phys. Chem. B*, **2006**, 110, 11352−11360.

59. Y. Park, K. J. McDonald, K.-S. Choi. Progress in Bismuth Vanadate Photoanodes for Use in Solar Water Oxidation. *Chem. Soc. Rev.*, **2013**, 42, 2321–2337.

60. I. Grigioni, K. G. Stamplecoskie, D. H. Jara, M. V. Dozzi, A. Oriana, G. Cerullo, P. V. Kamat, E. Selli. Wavelength-Dependent Ultrafast Charge Carrier Separation in the WO_3/$BiVO_4$ Coupled System. *ACS Energy Lett.*, **2017**, 2, 1362−1367.

61. J. Song, J. Cha, M. G. Lee, H. W. Jeong, S. Seo, J. A. Yoo, T. L. Kim, J. Lee, H. No, D. H. Kim, S. Y. Jeong, H. An, B. H. Lee, C. W. Bark, H. Park, H. W. Jang, S. Lee. Template-Engineered Epitaxial $BiVO_4$ Photoanodes for Efficient Solar Water Splitting. *J. Mater. Chem. A*, **2017**, 5, 18831–18838.

62. A. Kubacka, M. Fernández-García, G. Colón. Advanced Nanoarchitectures for Solar Photocatalytic Applications. *Chem. Rev.*, **2012**, 112, 1555–1614.

63. S. Wang, D. Cui, W. Hao, Y. Du. Roles of Cocatalysts on $BiVO_4$ Photoanodes for Photoelectrochemical Water Oxidation: A Minireview. *Energy Fuels*, **2022**, 36, 11394–11403.

64. G. Dong, L. Yan, Y. Bi. Advanced Oxygen Evolution Reaction Catalysts for Solar-driven Photoelectrochemical Water Splitting. *J. Mater. Chem. A*, **2023**, 11, 3888–3903.

65. J. H. Kim, J. W. Jang, H. J. Kang, G. Magesh, J. Y. Kim, J. H. Kim, J. Lee, J. S. Lee. Palladium Oxide as a Novel Oxygen Evolution Catalyst on $BiVO_4$ Photoanode for Photoelectrochemical Water Splitting. *J. Catal.*, **2014**, 317, 126–134.

66. J. H. Kim, S. Han, Y. H. Jo, Y. Bak, J. S. Lee. A Precious Metal-free Solar Water Splitting Cell with a Bifunctional Cobalt Phosphide Electrocatalyst and Doubly Promoted Bismuth Vanadate Photoanode. *J. Mater. Chem. A*, **2018**, 6, 1266–1274.

67. F. F. Abdi, R. van de Krol. Nature and Light Dependence of Bulk Recombination in Co-Pi-Catalyzed $BiVO_4$ Photoanodes. *J. Phys. Chem. C*, **2012**, 116, 9398−9404.

68. M. R. Nellist, J. Qiu, F. A. L. Laskowski, F. M. Toma, S. W. Boettcher. Potential-Sensing Electrochemical AFM Shows CoPi as a Hole Collector and Oxygen Evolution Catalyst on $BiVO_4$ Water-Splitting Photoanodes. *ACS Energy Lett.*, **2018**, 3, 2286−2291.

69. M. Zhou, J. Bao, W. Bi, Y. Zeng, R. Zhu, M. Tao, Y. Xie. Efficient Water Splitting via a Heteroepitaxial $BiVO_4$ Photoelectrode Decorated with Co-Pi Catalysts. *ChemSusChem*, **2012**, 5, 1420–1425.

70. F. F. Abdi, N. Firet, R. van de Krol. Efficient $BiVO_4$ Thin Film Photoanodes Modified with Cobalt Phosphate Catalyst and W-doping. *ChemCatChem*, **2013**, 5, 490–496.

71. S. K. Pilli, T. E. Furtak, L. D. Brown, T. G. Deutsch, J. A. Turner, A. M. Herring. Cobalt-Phosphate (Co-Pi) Catalyst Modified Mo-doped $BiVO_4$ Photoelectrodes for Solar Water Oxidation. *Energy Environ. Sci.*, **2011**, 4, 5028–5034.

72. J. Huang, Y. Tian, Y. Wang, T. Liu. Load CoO_x Cocatalyst on Photoanode by Spin Coating and Calcination for Enhanced Photoelectrochemical Water Oxidation: A Case Study on $BiVO_4$. *J. Solid State Chem.*, **2021**, 299, 122154.

73. L. Zhang, M. Yang, Z. Luo, J. Zhang, Y. Hou. Photodeposited CoO_x as Highly Active Phases to Boost Water Oxidation on $BiVO_4/WO_3$ Photoanode. *Int. J. Hydro. Energy*, **2019**, 44, 25652–25661.

74. S. Wang, T. He, J.-H. Yun, Y. Hu, M. Xiao, A. Du, L. Wang. New Iron-Cobalt Oxide Catalysts Promoting $BiVO_4$ Films for Photoelectrochemical Water Splitting. *Adv. Funct. Mater.*, **2018**, 28, 1802685.

75. F. Tang, W. Cheng, H. Su, X. Zhao, Q. Liu. Smoothing Surface Trapping States in 3D Coral-Like CoOOH-Wrapped-$BiVO_4$ for Efficient Photoelectrochemical Water Oxidation. *ACS Appl. Mater. Interfaces*, **2018**, 10, 6228−6234.

76. B. Zhang, X. Huang, H. Hu, L. Chou, Y. Bi. Defect-rich and Ultrathin CoOOH Nanolayers as Highly Efficient Oxygen Evolution Catalysts for Photoelectrochemical Water Splitting. *J. Mater. Chem. A*, **2019**, 7, 4415–4419.

77. M. W. Kanan, D. G. Nocera. In Situ Formation of an Oxygen-Evolving Catalyst in Neutral Water Containing Phosphate and Co^{2+}. *Science*, **2008**, 321, 1072–1075.

78. D. K. Zhong, S. Choi, D. R. Gamelin. Near-Complete Suppression of Surface Recombination in Solar Photoelectrolysis by "Co-Pi" Catalyst-Modified W: $BiVO_4$. *J. Am. Chem. Soc.*, **2011**, 133, 18370–18377.

79. Y. Ma, A. Kafizas, S. R. Pendlebury, F. Le Formal, J. R. Durrant. Photoinduced Absorption Spectroscopy of CoPi on $BiVO_4$: The Function of CoPi during Water Oxidation. *Adv. Funct. Mater.*, **2016**, 26, 4951–4960.

80. C. Zachäus, F. F. Abdi, L. M. Peter, R. van de Krol. Photocurrent of $BiVO_4$ is Limited by Surface Recombination, Not Surface Catalysis. *Chem. Sci.*, **2017**, 8, 3712–3719.

81. J. H. Kim, Y. Jo, J. H. Kim, J. W. Jang, H. J. Kang, Y. H. Lee, D. S. Kim, Y. Jun, J. S. Lee. Wireless Solar Water Splitting Device with Robust Cobalt-Catalyzed, Dual-Doped $BiVO_4$ Photoanode and Perovskite Solar Cell in Tandem: A Dual Absorber Artificial Leaf. *ASC Nano*, **2015**, 9, 11820–11829.

82. C. Ding, J. Shi, D. Wang, Z. Wang, N. Wang, G. Liu, F. Xiong, C. Li. Visible Light Driven Overall Water Splitting Using Cocatalyst/$BiVO_4$ Photoanode with Minimized Bias. *Phys. Chem. Chem. Phys.*, **2013**, 15, 4589–4595.

83. J. A. Seabold, K.-S. Choi. Efficient and Stable Photo-Oxidation of Water by a Bismuth Vanadate Photoanode Coupled with an Iron Oxyhydroxide Oxygen Evolution Catalyst. *J. Am. Chem. Soc.*, **2012**, 134, 2186−2192.

84. R. Gao, D. He, L. Wu, K. Hu, X. Liu, Y. Su, L. Wang. Towards Long-Term Photostability of Nickel Hydroxide/$BiVO_4$ Photoanodes for Oxygen Evolution Catalysts via In Situ Catalyst Tuning. *Angew. Chem.*, **2020**, 132, 6272–6277.

85. T. W. Kim, K.-S. Choi. Nanoporous $BiVO_4$ Photoanodes with Dual-Layer Oxygen Evolution Catalysts for Solar Water Splitting. *Science*, **2014**, 343, 990–994.

86. B. Zhang, S. Yu, Y. Dai, X. Huang, L. Chou, G. Lu, G. Dong, Y. Bi. Nitrogen-Incorporation Activates $NiFeO_x$ Catalysts for Efficiently Boosting Oxygen Evolution Activity and Stability of $BiVO_4$ Photoanodes. *Nat. Commun.*, **2021**, 12, 6969.

87. B. Liu, X. Wang, Y. Zhang, L. Xu, T. Wang, X. Xiao, S. Wang, L. Wang, W. Huang. A $BiVO_4$ Photoanode with a VO_x Layer Bearing Oxygen Vacancies Offers Improved Charge Transfer and Oxygen Evolution Kinetics in Photoelectrochemical Water Splitting. *Angew. Chem.*, **2023**, 135, e202217346.

88. Y. Lu, J. Su, J. Shi, D. Zhou. Surface Recombination Passivation of the $BiVO_4$ Photoanode by the Synergistic Effect of the Cobalt/Nickel Sulfide Cocatalyst. *ACS Appl. Energy Mater.*, **2020**, 3, 9089–9097.

89. Y. Guo, T. Park, J. W. Yi, J. Henzie, J. Kim, Z. Wang, B. Jiang, Y. Bando, Y. Sugahara, J. Tang, Y. Yamauchi. Nanoarchitectonics for Transition-Metal-Sulfide-Based Electrocatalysts for Water Splitting. *Adv. Mater.*, **2019**, 31, 1807134.

90. Y. Liang, J. Messinger. Improving $BiVO_4$ Photoanodes for Solar Water Splitting Through Surface Passivation. *Phys. Chem. Chem. Phys.*, **2014**, 16, 12014–12020.

91. G. Chang, D. Wang, Y. Zhang, A. Aldalbahi, L. Wang, Q. Li, K. Wang. ALD-coated Ultrathin Al_2O_3 Film on $BiVO_4$ Nanoparticles for Efficient PEC Water Splitting. *Nucl. Sci. Tech.*, **2016**, 27, 108.

92. A. Sharma, S. Manna, A. K. Satpati. Enhancement in Photoelectrochemical Efficiency and Modulation of Surface States in $BiVO_4$ through the TiO_2 Outer Layer Using the Atomic Layer Deposition Technique. *J. Phys. Chem. C*, **2023**, 127, 4395–4406.

93. L. Xia, J. Li, J. Bai, L. Li, Q. Zeng, Q. Xu, B. Zhou. Preparation of a $BiVO_4$ Nanoporous Photoanode Based on Peroxovanadate Reduction and Conversion for Efficient Photoelectrochemical Performance. *Nanoscale*, **2018**, 10, 2848–2855.

94. X. Yuan, X. Sun, H. Zhou, S. Zeng, B. Liu, X. Li, D. Liu. Free-Standing Electrospun W-Doped $BiVO_4$ Porous Nanotubes for the Efficient Photoelectrochemical Water Oxidation. *Front. Chem.*, **2020**, 8, 311.

95. C. Liu, J. Su, J. Zhou, L. Guo. A Multistep Ion Exchange Approach for Fabrication of Porous $BiVO_4$ Nanorod Arrays on Transparent Conductive Substrate. *ACS Sustainable Chem. Eng.*, **2016**, 4, 4492–4497.

96. H. He, S. P. Berglund, A. J. E. Rettie, W. D. Chemelewski, P. Xiao, Y. Zhang, C. B. Mullins. Synthesis of $BiVO_4$ Nanoflake Array Films for Photoelectrochemical Water Oxidation. *J. Mater. Chem. A*, **2014**, 2, 9371–9379.

97. Y. Kuang, Q. Jia, H. Nishiyama, T. Yamada, A. Kudo, K. Domen. A Front-Illuminated Nanostructured Transparent $BiVO_4$ Photoanode for >2% Efficient Water Splitting. *Adv. Energy Mater.*, **2016**, 6, 1501645.

98. M Zhou, J. Bao, Y. Xu, J. Zhang, J. Xie, M. Guan, C. Wang, L. Wen, Y. Lei, Y. Xie. Photoelectrodes Based upon Mo:$BiVO_4$ Inverse Opals for Photoelectrochemical Water Splitting. *ACS Nano*, **2014**, 8, 7088–7098.

99. S. Ju, H. Kang, J. Jun, S. Son, J. Park, W. Kim, H. Lee. Periodic Micropillar-Patterned FTO/$BiVO_4$ with Superior Light Absorption and Separation Efficiency for Efficient PEC Performance. *Small*, **2021**, 17, 2006558.

100. A. Polo, M. V. Dozzi, I. Grigioni, C. Lhermitte, N. Plainpan, L. Moretti, G. Cerullo, K. Sivula, E. Selli. Multiple Effects Induced by Mo^{6+} Doping in $BiVO_4$ Photoanodes. *Sol. RRL*, **2022**, 6, 2200349.

101. Q. Shi, S. Murcia-López, P. Tang, C. Flox, J. R. Morante, Z. Bian, H. Wang, Teresa Andreu. Role of Tungsten Doping on the Surface States in $BiVO_4$ Photoanodes for Water Oxidation: Tuning the Electron Trapping Process. *ACS Catal.*, **2018**, 8, 3331–3342.

102. W. Fang, L. Fu, A. Qin, Y. Lin, R. Xv. Highly Active and Self-Healing Co-Doped $BiVO_4$ Photoanode in Borate Buffer to Enhance Charge Separation and Water Oxidation Kinetics during Photoelectrochemical Water Splitting. *ACS Appl. Energy Mater.*, **2022**, 5, 6313–6323.

103. K. P. S. Parmar, H. J. Kang, A. Bist, P. Dua, J. S. Jang, J. S. Lee. Photocatalytic and Photoelectrochemical Water Oxidation over Metal-Doped Monoclinic $BiVO_4$ Photoanodes. *ChemSusChem*, **2012**, 5, 1926–1934.

104. B. Zhang, H. Zhang, Z. Wang, X. Zhang, X. Qin, Y. Dai, Y. Liu, P. Wang, Y. Li, B. Huang. Doping Strategy to Promote the Charge Separation in $BiVO_4$ Photoanodes. *Appl. Catal. B: Environ.*, **2017**, 211, 258–265.

105. F. F. Abdi, L. Han, A. H. M. Smets, M. Zeman, B. Dam, R. van de Krol. Efficient Solar Water Splitting by Enhanced Charge Separation in A Bismuth Vanadate-silicon Tandem Photoelectrode. *Nat. Commun.*, **2013**, 4, 2195.

106. M. Lamers, W. Li, M. Favaro, D. E. Starr, D. Friedrich, S. Lardhi, L. Cavallo, M. Harb, R. van de Krol, L. H. Wong, F. F. Abdi. Enhanced Carrier Transport and Bandgap Reduction in Sulfur-Modified $BiVO_4$ Photoanodes. *Chem. Mater.*, **2018**, 30, 8630–8638.

107. W. J. Jo, J.-W. Jang, K. Kong, H. J. Kang, J. Y. Kim, H. Jun, K. P. S. Parmar, J. S. Lee. Phosphate Doping into Monoclinic $BiVO_4$ for Enhanced Photoelectrochemical Water Oxidation Activity. *Angew. Chem. Int. Ed.*, **2012**, 51, 1–6.

108. R. Gao, L. Wang. Stable Cocatalyst-Free $BiVO_4$ Photoanodes with Passivated Surface States for Photocorrosion Inhibition. *Angew. Chem. Int. Ed.*, **2020**, 59, 23094–23099.

109. G. Wang, Y. Ling, X. Lu, F. Qian, Y. Tong, J. Z. Zhang, V. Lordi, C. R. Leao, Y. Li. Computational and Photoelectrochemical Study of Hydrogenated Bismuth Vanadate. *J. Phys. Chem. C*, **2013**, 117, 10957–10964.

110. B. J. Trześniewski, I. A. Digdaya, T. Nagaki, S. Ravishankar, I. Herraiz-Cardona, D. A. Vermaas, A. Longo, S. Gimenez, W. A. Smith. Near-complete Suppression of Surface

Losses and Total Internal Quantum Efficiency in $BiVO_4$ Photoanodes. *Energy Environ. Sci.*, **2017**, 10, 1517–1529.

111. T. W. Kim, Y. Ping, G. A. Galli, K.-S. Choi. Simultaneous Enhancements in Photon Absorption and Charge Transport of Bismuth Vanadate Photoanodes for Solar Water Splitting. *Nat. Commun.*, **2015**, 6, 8769.

112. W. Fang, Y. Lin, R. Xv, L. Fu. Boosting Photoelectrochemical Performance of $BiVO_4$ Photoanode by Synergistic Effect of $WO_3/BiVO_4$ Heterojunction Construction and NiOOH Water Oxidation Cocatalyst Modification. *ACS Appl. Energy Mater.*, **2022**, 5, 11402–11412.

113. H. Jung, S. Y. Chae, C. Shin, B. K. Min, O.-S. Joo, Y. J. Hwang. Effect of the $Si/TiO_2/BiVO_4$ Heterojunction on the Onset Potential of Photocurrents for Solar Water Oxidation. *ACS Appl. Mater. Interfaces*, **2015**, 7, 5788–5796.

114. S. Byun, B. Kim, S. Jeon, B. Shin. Effects of A SnO_2 Hole Blocking Layer in A $BiVO_4$-Based Photoanode on Photoelectrocatalytic Water Oxidation. *J. Mater. Chem. A*, **2017**, 5, 6905–6913.

115. T. Ma, R. Yan, X. Wu, M. Wang, B. Yin, S. Li, C. Cheng, A. Thomas. Polyoxometalate-Structured Materials: Molecular Fundamentals and Electrocatalytic Roles in Energy Conversion. *Adv. Mater.*, **2024**, 36, 2310283.

116. D. Gao, I. Trentin, L. Schwiedrzik, L. González, C. Streb. The Reactivity and Stability of Polyoxometalate Water Oxidation Electrocatalysts. *Molecules*, **2020**, 25, 157.

117. M. T. Pope, A. Müller. Polyoxometalate Chemistry from Topology via Self-Assembly to Applications. *Dordrecht:* Springer, **2001**. https://link.springer.com/book/10.1007/0-306-47625-8

118. M. Samaniyan, M. Mirzaei, R. Khajavian, H. Eshtiagh-Hosseini, C. Streb. Heterogeneous Catalysis by Polyoxometalates in Metal−Organic Frameworks. *ACS Catal.*, **2019**, 9, 10174−10191.

119. I. A. Weinstock, R. E. Schreiber, R. Neumann. Dioxygen in Polyoxometalate Mediated Reactions. *Chem. Rev.*, **2018**, 118, 2680−2717.

120. S. Repp. Self-assembly and Supramolecular Functionalization of Hybrid Organic-inorganic Molecular Vanadium Oxides. *Universität Ulm*, **2023**. https://oparu.uni-ulm.de/items/4d1e0d41-7250-48b2-a2d4-c62ea6d6833f

121. D.-L. Long, L. Cronin. Towards Polyoxometalate-Integrated Nanosystems. *Chem. Eur. J.*, **2006**, 12, 3698–3706.

122. A. Müller, E. Krickemeyer, J. Meyer, H. Bögge, F. Peters, W. Plass, E. Diemann, S. Dillinger, F. Nonnenbruch, M. Randerath, C. Menke. $[Mo_{154}(NO)_{14}O_{420}(OH)_{28}(H_2O)_{70}]^{(25\pm5)-}$: A Water-Soluble Big Wheel with More than 700 Atoms and a Relative Molecular Mass of About 24000. *Angew Chem. Int. Ed. Engl.*, **1995,** 34(19), 2122−2124.

123. A. Müller, E. Krickemeyer, H. Bögge, M. Schmidtmann, F. Peters. Organizational Forms of Matter: An Inorganic Super Fullerene and Keplerate Based on Molybdenum Oxide. *Angew. Chem. Int. Ed.*, **1998**, 37(24), 3360−3363.

124. H. N. Miras, L. Vilà-Nadal, L. Cronin. Polyoxometalate Based Open-frameworks (POM-OFs). *Chem. Soc. Rev.*, **2014**, 43, 5679−5699.

125. L. Chen, W. Chen, X. Wang, Y. Li, Z. Su, E. Wang. Polyoxometalates in Dye-Sensitized Solar Cells. *Chem. Soc. Rev.*, **2019**, 48, 260−284.

126. S. Lentink, D. E. S. Marcano, M. A. Moussawi, T. N. Parac-Vogt. Exploiting Interactions between Polyoxometalates and Proteins for Applications in (Bio)chemistry and Medicine. *Angew. Chem. Int. Ed.*, **2023**, 62, e202303817.

127. N. Li, J. Liu, B. Dong, Y. Lan. Polyoxometalate-Based Compounds for Photo- and Electrocatalytic Applications. *Angew. Chem. Int. Ed.*, **2020**, 59, 20779–20793.

128. J. W. Vickers, H. Lv, J. M. Sumliner, G. Zhu, Z. Luo, D. G. Musaev, Y. V. Geletii, C. L. Hill. Differentiating Homogeneous and Heterogeneous Water Oxidation Catalysis: Confirmation that $[Co_4(H_2O)_2(\alpha\text{-}PW_9O_{34})_2]^{10-}$ Is a Molecular Water Oxidation Catalyst. *J. Am. Chem. Soc.*, **2015**, 137, 5486−5493.

129. Q. Yin, J. M. Tan, C. Besson, Y. V. Geletii, D G. Musaev, A. E. Kuznetsov, Z. Luo, K. I. Hardcastle, C. L. Hill. A Fast Soluble Carbon-Free Molecular Water Oxidation Catalyst Based on Abundant Metals. *Science*, **2010**, 328, 342−345.

130. V. K. Abdelkader-Fernández, D. M. Fernandes, S. S. Balula, L. Cunha-Silva, C. Freire. Oxygen Evolution Reaction Electrocatalytic Improvement in POM@ZIF Nanocomposites: A Bidirectional Synergistic Effect. *ACS Appl. Energy Mater.*, **2020**, 3, 2925−2934.

131. Y. Zhang, Y. Liu, D. Wang, J. Liu, J. Zhao, L. Chen. State-of-the-art Advances in the Syntheses, Structures, and Applications of Polyoxometalate-based Metal–organic Frameworks. *Polyoxometalates*, **2023**, 2, 9140017.

132. W. Luo, J. Hu, H. Diao, B. Schwarz, C. Streb, Y. Song. Robust Polyoxometalate/Nickel Foam Composite Electrodes for Sustained Electrochemical Oxygen Evolution at High pH. *Angew. Chem. Int. Ed.*, **2017**, 56, 4941–4944.

133. D. Gao, R. Liu, J. Biskupek, U. Kaiser, Y. Song, C. Streb. Modular Design of Noble-Metal-Free Mixed Metal Oxide Electrocatalysts for Complete Water Splitting. *Angew. Chem. Int. Ed.*, **2019**, 58, 4644–4648.

134. S. M. Lauinger, J. M. Sumliner, Q. Yin, Z. Xu, G. Liang, E. N. Glass, T. Lian, C. L. Hill. High Stability of Immobilized Polyoxometalates on TiO_2 Nanoparticles and Nanoporous Films for Robust, Light-Induced Water Oxidation. *Chem. Mater.*, **2015**, 27, 5886−5891.

135. R. Solarska, K. Bienkowski, S. Zoladek, A. Majcher, T. Stefaniuk, P. J. Kulesza, J. Augustynski. Enhanced Water Splitting at Thin Film Tungsten Trioxide Photoanodes Bearing Plasmonic Gold–Polyoxometalate Particles. *Angew. Chem. Int. Ed.*, **2014**, 53, 14196–14200.

136. D. Jeon, H. Kim, C. Lee, Y. Han, M. Gu, B.-S. Kim, J. Ryu. Layer-by-Layer Assembly of Polyoxometalates for Photoelectrochemical (PEC) Water Splitting: Toward Modular PEC Devices. *ACS Appl. Mater. Interfaces*, **2017**, 9, 40151–40161.

137. Y. Zhang, Y. Zhao, F. Li, Z. Sun, L. Xu, X. Guo. Photovoltaic Performance Enhancement of Cu_2O Photocathodes by Electrostatic Adsorption of Polyoxometalate on Cu_2O Crystal Faces. *RSC Adv.*, **2014**, 4, 1362–1365.

138. W. Fang, D. Liu, Y. Zhang, H. Feng, Q. Li. Improved Photoelectrochemical Performance by Polyoxometalate–Modified $CuBi_2O_4$/Mg-$CuBi_2O_4$ Homojunction Photocathode. *Acta Phys. -Chim. Sin.*, **2024**, 40 (2), 2304006.

139. D. Jeon, N. Kim, S. Bae, Y. Han, J. Ryu. WO_3/Conducting Polymer Heterojunction Photoanodes for Efficient and Stable Photoelectrochemical Water Splitting. *ACS Appl. Mater. Interfaces*, **2018**, 10, 8036−8044.

140. F. Zhao, T. Cheng, X. Lu, N. Ghorai, Y. Yang, Y. V. Geletii, D. G. Musaev, C. L. Hill, T. Lian. Charge Transfer Mechanism on a Cobalt-Polyoxometalate-TiO_2 Photoanode for Water Oxidation in Acid. *J. Am. Chem. Soc.*, **2024**, 146, 14600−14609.

141. R. Gong, D. Mitoraj, D. Gao, M. Mundszinger, D. Sorsche, U. Kaiser, C. Streb, R. Beranek, S. Rau. A Triad Photoanode for Visible Light-Driven Water Oxidation via Immobilization of Molecular Polyoxometalate on Polymeric Carbon Nitride. *Adv. Sustainable Syst.*, **2022**, 6, 2100473.

142. J. J. Stracke, R. G. Finke. Water Oxidation Catalysis Beginning with 2.5 μM $[Co_4(H_2O)_2(PW_9O_{34})_2]^{10-}$: Investigation of the True Electrochemically Driven Catalyst at ⩾600 mV Overpotential at a Glassy Carbon Electrode. *ACS Catal.*, **2013**, 3, 1209–1219.

143. J. J. Stracke, R. G. Finke. Electrocatalytic Water Oxidation Beginning with the Cobalt Polyoxometalate $[Co_4(H_2O)_2(PW_9O_{34})_2]^{10-}$: Identification of Heterogeneous CoOx as the Dominant Catalyst. *J. Am. Chem. Soc.*, **2011**, 133, 14872–14875.

144. S. J. Folkman, J. Soriano-Lopez, J. R. Galán-Mascarós, R. G. Finke, Electrochemically Driven Water-Oxidation Catalysis Beginning with Six Exemplary Cobalt Polyoxometalates: Is It Molecular, Homogeneous Catalysis or Electrode-Bound, Heterogeneous CoO_x Catalysis? *J. Am. Chem. Soc.*, **2018**, 140, 12040–12055.

145. R. Gong, D. Gao, R. Liu, D. Sorsche, J. Biskupek, U. Kaiser, S. Rau, C. Streb. Self-Activation of a Polyoxometalate-Derived Composite Electrocatalyst for the Oxygen Evolution Reaction. *ACS Appl. Energy Mater.*, **2021**, 4, 12671–12676.

146. X. Han, Z. Zhang, T. Zhang, Y. Li, W. Lin, W. You, Z. Su, E. Wang. Polyoxometalate-Based Cobalt−Phosphate Molecular Catalysts for Visible Light-Driven Water Oxidation. *J. Am. Chem. Soc.*, **2014**, 136, 5359–5366.

147. X. Cao, Y. Wang, J. Lin, Y. Ding. Ultrathin CoO_x Nanolayers Derived from Polyoxometalate for Enhanced Photoelectrochemical Performance of Hematite Photoanodes. *J. Mater. Chem. A*, **2019**, 7, 6294–6303.

148. M. Zheng, X. Cao, Y. Ding, T. Tian, J. Lin. Boosting Photocatalytic Water Oxidation Achieved by $BiVO_4$ Coupled with Iron-containing Polyoxometalate: Analysis the True Catalyst. *J. Catal.*, **2018,** 363, 109–116.

149. S. M. Lauinger, B. D. Piercy, W. Li, Q. Yin, D. L. Collins-Wildman, E. N. Glass, M. D. Losego, D. Wang, Y. V. Geletii, C. L. Hill. Stabilization of Polyoxometalate Water Oxidation Catalysts on Hematite by Atomic Layer Deposition. *ACS Appl. Mater. Interfaces*, **2017**, 9, 35048−35056.

150. Y. Han, K. Choi, H. Oh, C. Kim, D. Jeon, C. Lee, J. H. Lee, J. Ryu. Cobalt Polyoxometalate-Derived $CoWO_4$ Oxygen-Evolving Catalysts for Efficient Electrochemical and Photoelectrochemical Water Oxidation. *J. Catal.*, **2018**, 367, 212–220.

151. W. Fang, R. Tao, Z. Jin, Z. Sun, F. Li, L. Xu. Sandwich-Type Cobalt-Polyoxometalate as an Effective Hole Extraction Layer for Enhancing $BiVO_4$-based Photoelectrochemical Oxidation. *J. Alloys & Compounds*, **2019**, 797, 140-147.

152. S. Bae, H. Kim, D. Jeon, J. Ryu. Catalytic Multilayers for Efficient Solar Water Oxidation through Catalyst Loading and Surface-State Passivation of $BiVO_4$ Photoanodes. *ACS Appl. Mater. Interfaces*, **2019**, 11, 7990–7999.

153. C. Hu, C. Xu, X. Li, B. Li, X. Ma, J. Zhu, C. Dong, Y. Ding. Coupling Ni_3POM with FeOOH on $BiVO_4$ Photoanodes for Efficient Photoelectrochemical Water Splitting. *ACS Sustainable Chem. Eng.*, **2023**, 11, 7367–7377.

154. K. Fan, H. Chen, B. He, J. Yu. Cobalt Polyoxometalate on N-Doped Carbon Layer to Boost Photoelectrochemical Water Oxidation of $BiVO_4$. *Chem. Eng. J.*, **2020**, 392, 123744.

155. H. Kim, S. Bae, D. Jeon, J. Ryu. Fully Solution-Processable Cu_2O–$BiVO_4$ Photoelectrochemical Cells for Bias-Free Solar Water Splitting. *Green Chem.*, **2018**, 20, 3732–3742.

156. D. Xiao, G. Cheng, H. She, X. Chen, J. Huang, L. Wang, Q. Wang. Enhanced Photoelectrochemical Water Splitting Performance of $BiVO_4$ Photoanode by Integrating Electron-Rich Polyoxometalate into Metal−Organic Framework. *J. Phys. Chem. C*, **2024**, 128, 15266−15276.

157. Z. Tao, J. Yang, Y. Wu, Q. Zhao, J. Li, G. Liu. Coupling Polyoxometalate with CoOOH on $BiVO_4$ Photoanodes Towards Efficient Photoelectrochemical Water Oxidation. *Int. J. Hydrogen Energy*, **2024**, 61, 851–858.

158. Y. Wu, L. Bi. Research Progress on Catalytic Water Splitting Based on Polyoxometalate/Semiconductor Composites. *Catal.*, **2021**, 11, 524.

159. H. Park, W. Choi. Photoelectrochemical Investigation on Electron Transfer Mediating Behaviors of Polyoxometalate in UV-Illuminated Suspensions of TiO_2 and Pt/TiO_2. *J. Phys. Chem. B*, **2003**, 107, 3885–3890.

160. C. Streb, K. Kastner, J. Tucher. Polyoxometalates in Photocatalysis. *Phys. Sci. Rev.*, **2019**, 20170177.

161. L. Xi, Z. Jin, Z. Sun, R. Liu, L. Xu. Enhanced Photoelectrocatalytic Performance for Water Oxidation by Polyoxometalate Molecular Doping in $BiVO_4$ photoanodes. *Appl. Catal. A: General*, **2017**, 536, 67–74.

162. S. Dai, L. Jiang, C. Zhao, F. Chen, R. Chen, R. Qin, W. Zhang, W. Zhang, B. Wu, N. Zheng. Intimate Interfacial Interaction Between Amino-Modified Ti_5 Clusters and $BiVO_4$ Towards Efficient Photoelectrochemical Water Splitting. *ChemNanoMat*, **2019**, 5, 1110–1114.

163. E. O. Najafabadi, F. R. Astaraei, M. Tayebi, Z. Masoumi, O. Moradlou, M. M. Momeni, H.-G. Kim, F. K. Bahnamiri, M. Khalili, B.-K. Lee. Embedding Cobalt Polyoxometalate in Polypyrrole Shell for Improved Photoelectrochemical Performance of $BiVO_4$ Core. *Mater. Chem. Phy.*, **2023**, 309, 128430.

164. L. Xi, Q. Zhang, Z. Sun, C. Song, L. Xu. Rational Design of Ternary Composite Photoanode $BiVO_4/PW_{12}$/NiTsPc for Improved Photoelectrochemical Water Oxidation. *ChemElectroChem*, **2018**, 5, 2534–2541.

165. J. Tian, X. Chen, T. Wang, W. Pei, F. Li, D. Li, Y. Yang, X. Dong. Modification of Indium Oxide Nanofibers by Polyoxometalate Electron Acceptor Doping for Enhancement of Gas Sensing at Room Temperature. *Sensors & Actuators: B. Chem.*, **2021**, 344, 130227.

166. C. Yuan, S. Guo, S. Wang, L. Liu, W. Chen, E. Wang. Electropolymerization Polyoxometalate (POM)-Doped PEDOT Film Electrodes with Mastoid Microstructure and Its Application in Dye-Sensitized Solar Cells (DSSCs). *Ind. Eng. Chem. Res.*, **2013**, 52, 6694−6703.

167. R. Tao, Y. Zhang, Z. Jin, Z. Sun, L. Xu. Polyoxometalate Doped Tin Oxide as Electron Transport Layer for Low Cost, Hole-transport-material-free Perovskite Solar Cells. *Electrochimica Acta*, **2018**, 284, 10–17.

168. M. Xu, X. Li, J. Sha, Z. Tong, Q. Li, C. Liu. Hollow POM@MOF-derived Porous $NiMo_6@Co_3O_4$ for Biothiol Colorimetric Detection. *Chem. Eur. J.*, 2021, 27, 9141–9151.

169. H. Shi, H. Zhu, T. Jin, L. Chen, J. Zhang, K. Qiao, Z. Chen. Construction of Bi/Polyoxometalate Doped TiO_2 Composite with Efficient Visible-light Photocatalytic Performance: Mechanism Insight, Degradation Pathway and Toxicity Evaluation. *Appl. Surface Sci.*, **2023**, 615, 156310.

170. Y. Zhao, X. Qin, X. Zhao, X. Wang, H. Tan, H. Sun, G. Yan, H. Li, W. Ho, S. Lee. Polyoxometalates-Doped Bi_2O_3–x/Bi Photocatalyst for Highly Efficient Visible-light Photodegradation of Tetrabromobisphenol A and Removal of NO. *Chinese J. Catal.*, **2022**, 43, 771–781.

6. Appendix

6.1 (FF-1) Supporting Information: High-Performance $BiVO_4$ Photoanodes: Elucidating the Combined Effects of Mo-Doping and Modification with Cobalt Polyoxometalate

Electronic Supplementary Material (ESI) for Materials Advances.

Supporting Information

High-Performance $BiVO_4$ Photoanodes: Elucidating the Combined Effects of Mo-Doping and Modification with Cobalt Polyoxometalate

Fan Feng,[a] Dariusz Mitoraj,[b] Ruihao Gong,[c] Dandan Gao,[a] Mohamed M. Elnagar,[b] Rongji Liu,[a] Radim Beranek,[b,*] Carsten Streb[a,*]

[a] Department of Chemistry, Johannes Gutenberg University Mainz, Duesbergweg 10-14, 55128 Mainz, Germany

[b] Institute of Electrochemistry, Ulm University, Albert-Einstein-Allee 47, 89081 Ulm, Germany

[c] Institute of Inorganic Chemistry I, Ulm University, Albert-Einstein-Allee 11, 89081 Ulm, Germany

* Corresponding authors: radim.beranek@uni-ulm.de, carsten.streb@uni-mainz.de

1. Experimental Section

Materials: Fluorine-doped tin oxide (FTO) Pilkington TEC glass was purchased from XOP company (XOP Glass, Castellón Spain). Sodium hydroxide (NaOH, ≥99%) was provided by Carl Roth Gmbh & Co. KG. Boric acid (H_3BO_3, 99.5%), cobalt (II) nitrate hexahydrate ($Co(NO_3)_2 \cdot 6H_2O$, 98%), bismuth (III) nitrate pentahydrate ($Bi(NO_3)_3 \cdot 5H_2O$, ≥98.0%), ethylene glycol ($C_2H_6O_2$, ≥99%), polyethyleneimine (PEI, 50 wt%, dissolved in water), tri-block copolymer F-108 and bis(acetylacetonate) dioxomolybdenum (VI) ($MoO_2(acac)_2$) were all supplied by Sigma-Aldrich. Sodium tungstate dihydrate ($NaWO_4 \cdot 2H_2O$) and hydrochloric acid (HCl, 37%) were provided by Merck. Sodium sulfite (Na_2SO_3, 98%) and ammonia solution (NH_4OH, 25%) were purchased from J.T. Baker. Potassium dihydrogen phosphate (KH_2PO_4, 99.0%) was purchased from Applichem GmbH. Sodium chloride (NaCl, 99%) was provided by abcr Gmbh & Co. KG. Potassium phosphate (K_2HPO_4, 99+%), glacial acetic acid (CH_3COOH, 99.5%), sodium phosphate (Na_2HPO_4, 99+%) and vanadyl (IV) acetylacetonate ($C_{10}H_{14}O_5V$, 99%) were obtained from Acros Organics.

Preparation of Mo-$BiVO_4$ substrates: Mo-$BiVO_4$ photoanodes were deposited on cleaned FTO by a spin-coating process.[1] In a typical synthesis procedure, 0.15 M $Bi(NO_3)_3 \cdot 5H_2O$ as Bi precursor was dissolved in the solvent containing 1.5 mL ethylene glycol, 2 mL glacial acetic acid and 0.5 mL deionized water at room temperature. After stirring for 15 min, 0.3 M $VO(acac)_2$ as V precursor was added subsequently to the above solution, stirred for another 1 h. Then 240 µL of 50 mM $MoO_2(acac)_2$ ethylene glycol solution as a doping element was added to the above solution. The 0.35 g F-108 as a structural agent was then added in and stirred for 2 h to make a porous structure. After that, a uniform viscous ink for spin coating was obtained. Mo-$BiVO_4$ photoanodes were deposited on cleaned FTO-coated glass substrates at 50 rps for 30 s followed by drying at 250 °C for 5 min and the above coating and drying process was repeated five times. Finally, samples were calcined in a muffle oven at 450 °C for 1 hour with a heating rate of 3 °C/min. After sintering, 1 M NaOH was used to remove the excess V_2O_5. Pristine $BiVO_4$ was obtained by the same procedure omitting the addition of the Mo-precursor. Mo-$BiVO_4$(500 °C) and Mo-

$BiVO_4$(400 °C) was obtained by the same procedure except calcined temperature. Mo(400 μL)-$BiVO_4$ and Mo(80 μL)-$BiVO_4$ was obtained by the same procedure except adding 400 μL and 80 μL of $MoO_2(acac)_2$ ethylene glycol solution into precursor solution, respectively.

Synthesis of CoPOM: The CoPOM complex was synthesized according to literature.[2] Briefly, $NaWO_4 \cdot 2H_2O$ (35.62 g, 0.108 mol), $Na_2HPO_4 \cdot 7H_2O$ (1.70 g, 0.012 mol) and $Co(NO_3)_2 \cdot 6H_2O$ (6.98 g, 0.024 mol) were dissolved in 100 mL deionized water in a 200 mL round-bottom flask. After adjusting the pH to 7 by 9 M HCl under magnetic stirring, this purple suspension was then stirred and refluxed at 105°C for 2 hours. After reflux, the solution was saturated with 36 g NaCl and allowed to cool to room temperature. The resulting purple crystals were collected, quickly washed with approximately 30 mL of water, and recrystallized from hot water. The identity of the CoPOM is confirmed by Fourier transform infrared spectroscopy (FT-IR).

Preparation of Mo-$BiVO_4$/CoPOM: The Mo-$BiVO_4$ electrode was dipped into the aqueous CoPOM (5 mM) solution for 5 min, then rinsed with distilled water and dried in air. Then this process was repeated 5 times to acquire the desired amount of CoPOM and the sample was named as Mo-$BiVO_4$/CoPOM. Repeating 3 times (Mo-$BiVO_4$/CoPOM 3L), 5 times (Mo-$BiVO_4$/CoPOM 5L) and 8 times (Mo-$BiVO_4$/CoPOM 8L) were obtained by choosing different times of impregnation.

Preparation of Mo-$BiVO_4$/PEI+CoPOM: The Mo-$BiVO_4$ modified with PEI and CoPOM was prepared by dipping the Mo-$BiVO_4$ electrode into an aqueous PEI (6 mM) solutions of sodium phosphate (10 mM, pH = 5.4~5.7) and NaCl (137 mM) for 5 min, then rinsed with distilled water and dried in air, followed by dipping in CoPOM solution (5 mM) for another 5 min. The dipping processes in PEI and CoPOM solution were repeated 5 times and named as Mo-$BiVO_4$/PEI+CoPOM.[3]

Preparation of Mo-$BiVO_4$/CoPi: CoPi was loaded on Mo-$BiVO_4$ via the photo-assisted electrodeposition method previously reported.[4] Briefly, the electrolyte is 0.5 mM $Co(NO_3)_2$ dissolved in 0.1 M sodium phosphate buffer solution with pH value of 7.0. The prepared Mo-$BiVO_4$ photoanode was taken as the working electrode, Pt as the counter electrode and Ag/AgCl as the reference electrode (3.5 M KCl),

respectively. The photo-assisted electrodeposition was conducted at a bias of 0.4 V vs. Ag/AgCl (1.0 V *vs*. RHE) for 1 min under simulated sunlight (AM1.5G at 100 mW cm^{-2}).

Preparation of Mo-$BiVO_4$/$CoO(OH)_x$: Loading with $CoO(OH)_x$ nanoparticles in Mo-$BiVO_4$ photoanodes was using a two-step impregnation process.[5] First, the prepared Mo-$BiVO_4$ photoanodes were immersed into an aqueous solution of 0.1 M $Co(NO_3)_2$ for 10 minutes at room temperature. Subsequently, the electrodes were dried in air, quickly dipped into NH_4OH solution and dried again in air.

Characterization: The *UV-vis absorption spectra* were determined by a UV-Vis spectrophotometer (UV-2600, Shimadzu, Japan) equipped with the integrating sphere. The absorptance (Abs.) was calculated by the equation:

$$Absorptance\ (\%) = 100\% - Reflectance\ (\%) - Transmittance\ (\%)$$

The baselines were recorded using an FTO glass and a $BaSO_4$ plate as references for transmittance and reflectance, respectively (Fig. S5a). Scanning Electron Microscopy (SEM) and energy-dispersive X-ray spectroscopy (EDX) elemental mapping of samples before the PEC operation were performed using a ZEISS LEO 1550 VP scanning electron microscope operating at an acceleration voltage of 15 kV and coupled with energy dispersive spectroscopy (EDS, Ametek, USA). To improve the conductivity and achieve higher resolution SEM imaging and EDS analysis for the cross-sectional view, a 10 nm thick layer of C was deposited onto the sample surface. The EDX mappings of samples after the PEC operation were recorded with an AMETEK EDAX Octane Elite detector (the used software was APEX in version 2.5.1001.0001), and a 15nm thick carbon layer was deposited for better conductivity. For the focused ion beam (FIB) cross sections, a Zeiss NVision 40 Ar was used. For better-cut quality, the region of interest was treated with a felt tip pen (Pilot Super Color Marker). The at% of C is subtracted for the presented values in the EDS analysis of the cross-sectional view. Transmission electron microscopy (TEM) and energy-dispersive X-ray spectroscopy (EDX) elemental mapping were recorded with FEI Tecnai G2 Spirit. *Fourier transform infrared spectroscopy (FT-IR)* was performed on a Bruker Tensor 27 equipped with a PIKE Miracle Diamond ATR unit. *X-ray photoelectron spectroscopy (XPS)* measurements were performed with monochromatized Al Kα radiation (250 W, 15 kV) using a PHI 5800 ESCA system.

The binding energies were calibrated based on C 1s peak of adventitious carbon (284.8 eV). *X-ray diffraction (XRD)* patterns were recorded on a Rigaku XRD-6000 diffractometer under the following conditions: 40 kV, 40 mA, CuKα radiation (λ = 0.154 nm). Inductively coupled plasma atomic emission spectrometry (ICP-AES) was performed on a Perkin Elmer Plasma 400 spectrometer.

Photoelectrochemical measurements: The photoelectrochemical measurements were conducted using a SP-300 BioLogic potentiostat in a typical 3-electrode system with a Pt wire as counter electrode, an Ag/AgCl (3.5 M KCl, 0.205 V *vs*. SHE) as reference electrode and film photoanodes as working electrodes with geometric irradiation area of 0.5 cm^2. A 150 W Xe lamp (L.O.T.-Oriel) was employed as the light source with a light power density of 100 mW cm^{-2}, equipped with a KG-3 (LOT-Quantum Design) heat-absorbing filter and an AM 1.5G filter. All electrodes were illuminated from back-side (through FTO glass).

All potentials of photoelectrodes in this paper are reported against RHE:[6]

$$E_{RHE} = E_{Ag/AgCl} + 0.205 + 0.059 \times pH$$

where E_{RHE} is the converted potential referred to the RHE and $E_{Ag/AgCl}$ is the experimentally measured potential against the Ag/AgCl reference electrode.

The charge separation efficiency (η_{sep}) and the hole transfer efficiency (η_{tr}) were calculated for the prepared photoanodes using the approach reported by Donat et al.[7]

The hole transfer efficiency (η_{tr}) was determined using the equation:

$$\eta_{tr} = \frac{J_{H_2O}}{J_{Na_2SO_3}}$$

where J_{H_2O} and $J_{Na_2SO_3}$ are the photocurrents measured in the absence and presence of an additional hole scavenger (Na_2SO_3, 0.1 M) which is a readily oxidizable reducing agent.

The charge separation efficiency (η_{sep}) is estimated by the equation:

$$\eta_{sep} = \frac{J_{Na_2SO_3}}{J_{max}}$$

where J_{max} is the maximal photocurrent density obtained by integrating the absorptance spectrum (Fig. S5b) over the AM 1.5G solar spectrum from 300 nm to 560 nm with absorptance.

The incident photon-to-current conversion efficiency (IPCE) was recorded using a photoelectric spectrometer (Instytut Fotonowy Sp. z o.o.) equipped with a 150 W Xenon lamp and a monochromator, according to the equation:[1]

$$IPCE(\%) = \frac{1240 J_{ph}}{\lambda P} 100\%$$

where J_{ph} is the photocurrent density under monochromatic light, P is the monochromatic light power density, λ is the irradiation wavelength.

The applied bias photoconversion efficiency (ABPE) was also used to quantify the photoanode performance following the below equation:[8]

$$ABPE(\%) = \frac{J_{ph}(1.23 - V_{app})}{P} 100\%$$

in which J_{ph} is the photocurrent density, V_{app} is the applied bias (V *vs*. RHE), and P is the incident light density (100 mW cm^{-2}).

The oxygen evolution was recorded by the FireSting optical fiber oxygen meter (PyroScience, GmbH) in a home-made air-tight two-compartment cell using a Pt working electrode with the oxygen collection efficiency as approximately 50.2% ± 3.8%, which is value as a standard faradaic efficiency (FE, only based on dissolved O_2), 100.0% ± 7.6%. The volume of the photoanode compartment was 4.6 mL. The electrolyte was bubbled with argon before the electrodes were illuminated under an applied potential of 0.74 V *vs*. RHE. The electrolyte was 0.5 M aqueous sodium borate buffer electrolyte with a pH value of 9.0.

2. Analytical section

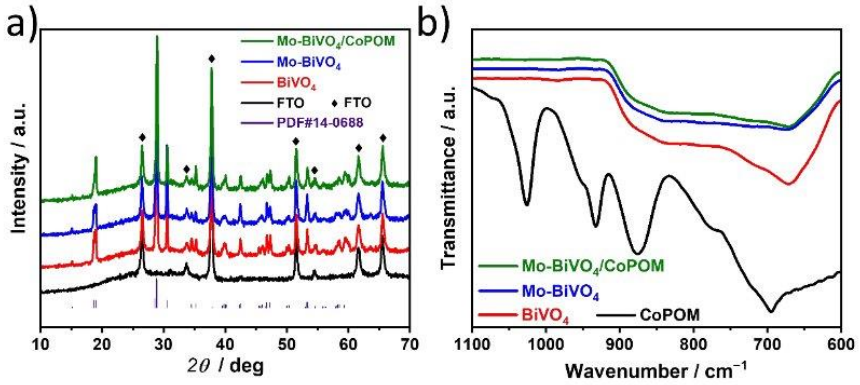

Fig. S1 (a) XRD patterns of $BiVO_4$, Mo-$BiVO_4$, Mo-$BiVO_4$/CoPOM and FTO substrate. Asterisk denotes reflections of the FTO substrate. Vertical lines represent the literature[9] pattern of bismuth vanadate (PDF # 14-0688) and (b) ATR-FTIR spectra of all $BiVO_4$-containing photoanodes and CoPOM powder.

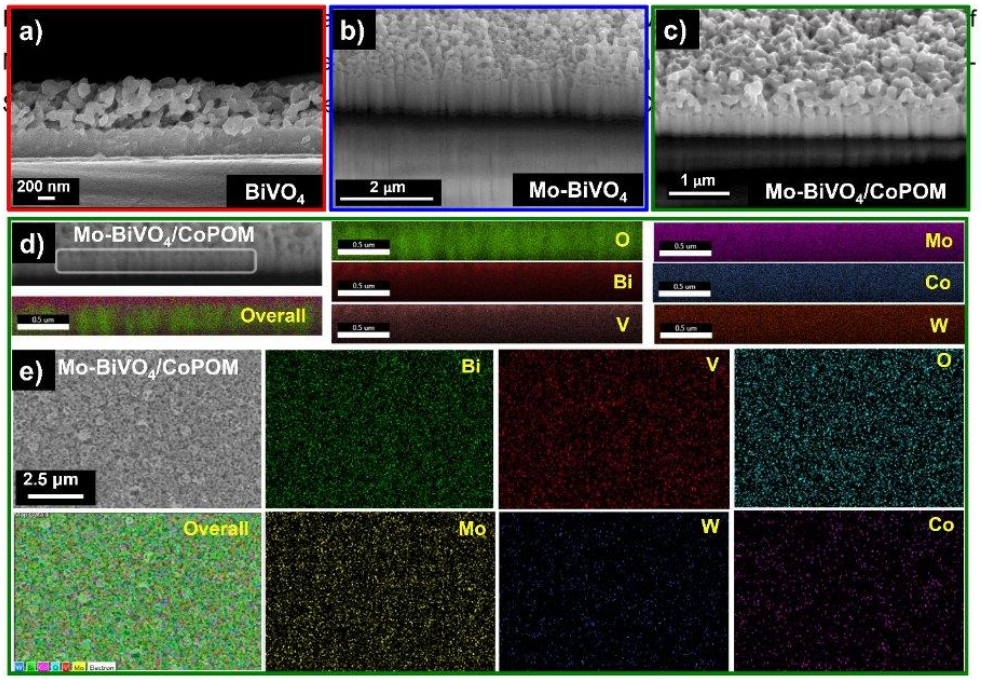
a)
200 nm
BiVO4
b)
2 µm
Mo-BiVO4
c)
1 µm
Mo-BiVO4/CoPOM
d)
Mo-BiVO4/CoPOM
Overall
O
Bi
V
Mo
Co
W
e)
Mo-BiVO4/CoPOM
2.5 µm
Bi
V
O
Overall
Mo
W
Co

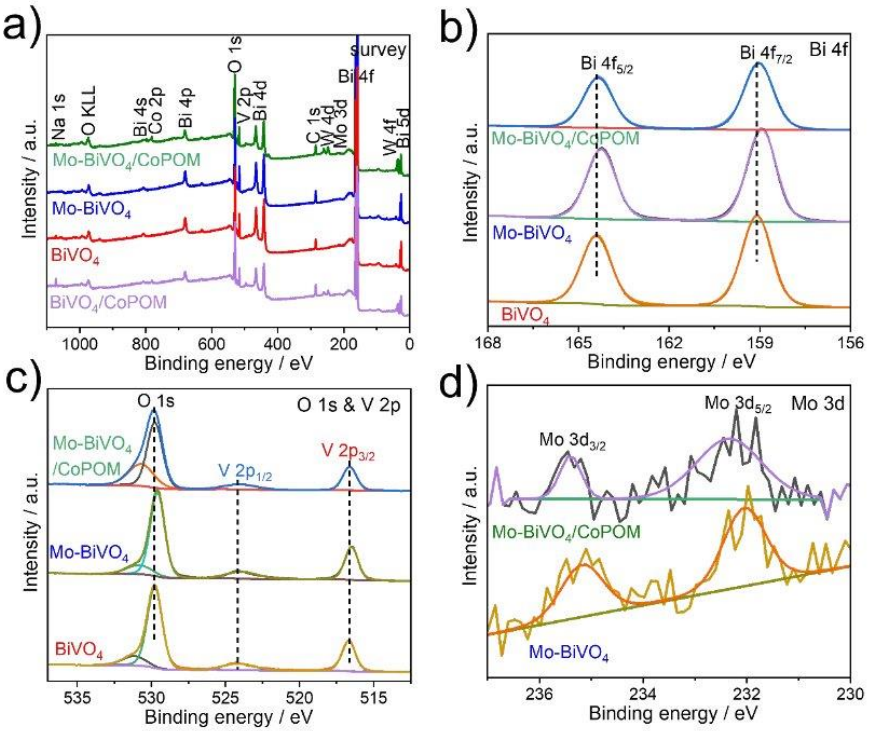

Fig. S3 (a) XPS survey spectra of $BiVO_4$, Mo-$BiVO_4$, Mo-$BiVO_4$/CoPOM and $BiVO_4$/CoPOM. (b) Bi 4f and (c) O1s and V 2p XPS spectra of $BiVO_4$, Mo-$BiVO_4$ and Mo-$BiVO_4$/CoPOM photoanodes. (d) Mo 3d XPS spectra of Mo-$BiVO_4$, Mo-$BiVO_4$/CoPOM photoanodes.

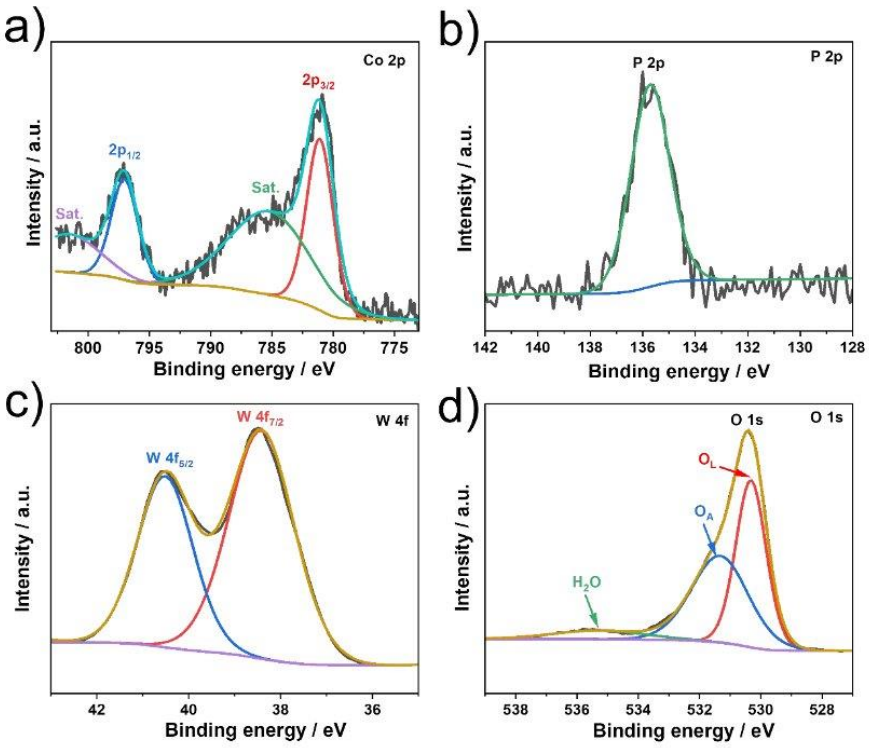

Fig. S4 XPS spectra of **CoPOM powder** (a) Co 2p, (b) P 2p, (c) W 4f and (d) O 1s.

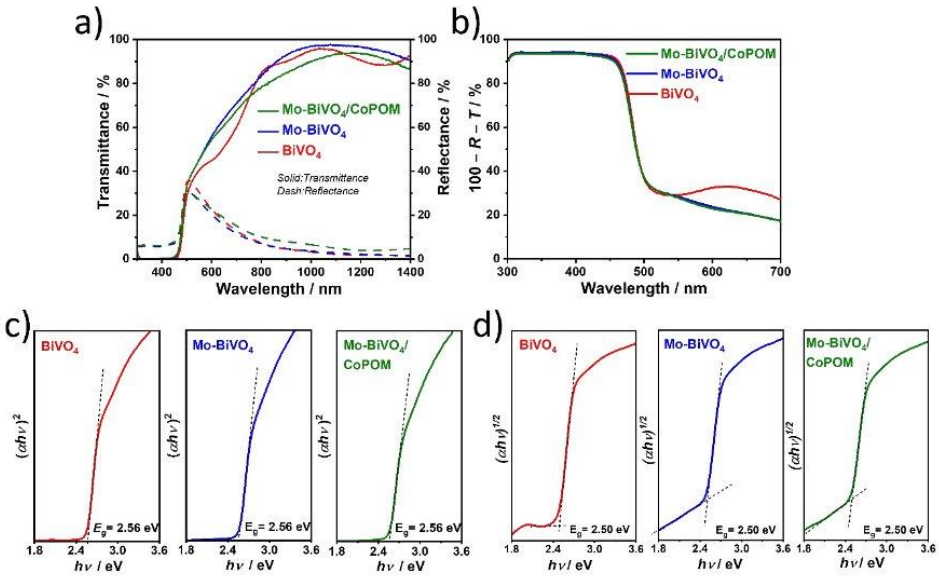

Fig. S5 (a, b) UV-Vis electronic absorption spectra of the photoanodes. $Absorptance$ (%) = 100% − $Reflectance$ (%) − $Transmittance$ (%). The nonzero baseline can be ascribed to the differences in internal reflection and scattering at the FTO/$BiVO_4$ interface in the transmittance and reflectance measurement modes.[10] Determination of the fundamental optical absorption edge using the Tauc approach for direct (c) and indirect (d) bandgaps.

Tab. S1 Concentrations (in at.%) of elements detected by SEM-EDX.

Samples	Bi	V	Mo	W	Co	O
Mo-$BiVO_4$/CoPOM	15.27	13.51	0.79	1.92	0.95	67.59
Mo-$BiVO_4$	15.22	15.14	1.16	-	-	68.49
$BiVO_4$	16.27	16.23	-	-	-	67.50

Tab. S2 Concentrations (in at.%) of elements detected by XPS.

Samples	C	Na	Bi	V	Mo	W	Co	O
$BiVO_4$	18.9	1.6	18.4	8.1	-	-	-	53.1
Mo-$BiVO_4$	21.0	-	17.7	8.3	0.1	-	-	52.9
Mo-$BiVO_4$/CoPOM	19.6	0.9	12.3	6.0	0.1	3.1	2.3	55.8

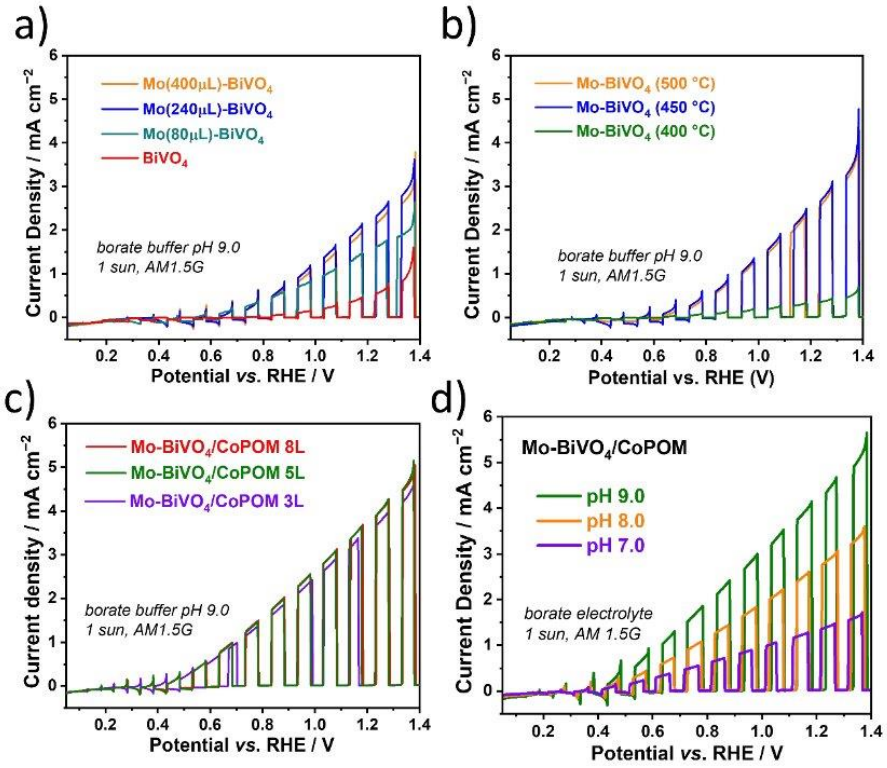

Fig. S6 *J-V* curves of (a) different amounts for Mo doping on $BiVO_4$ photoanodes, (b) different temperatures for calcination of Mo-$BiVO_4$ photoanodes, (c) different amounts for CoPOM on Mo-$BiVO_4$ photoanodes measured in sodium borate buffer electrolyte (pH = 9.0) under AM 1.5G one sun and (d) different pH for sodium borate electrolyte for Mo-$BiVO_4$/CoPOM photoanodes measured under AM 1.5G (1 sun).

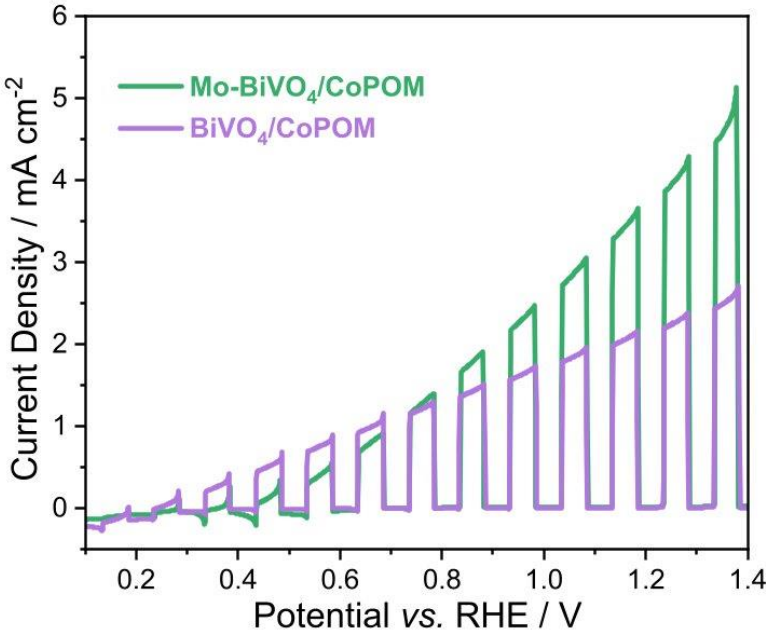

Fig. S7 Photocurrents recorded under AM 1.5G (1 sun) illumination in a borate electrolyte (0.5 M, pH 9.0) for Mo-$BiVO_4$/CoPOM and $BiVO_4$/CoPOM.

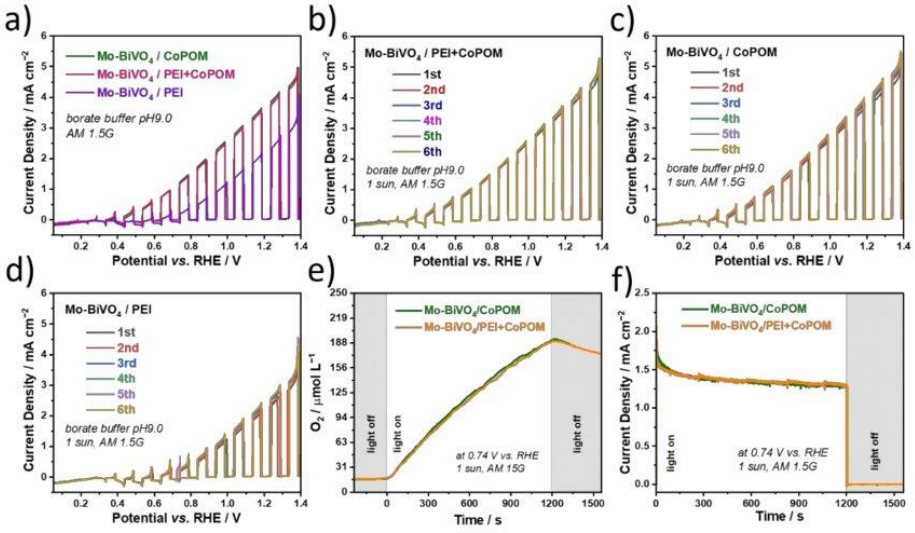

Fig. S8 *J-V* curves of (a) Mo-$BiVO_4$ with CoPOM, PEI or PEI+CoPOM; Photocurrent stability test recorded under AM 1.5G illumination at cathodic sweep of 10 mV s^{-1} for (b) Mo-$BiVO_4$/PEI+CoPOM, (c) Mo-$BiVO_4$/CoPOM and (d) Mo-$BiVO_4$/PEI. (e) Dioxygen evolution and (f) corresponding photocurrent transients.

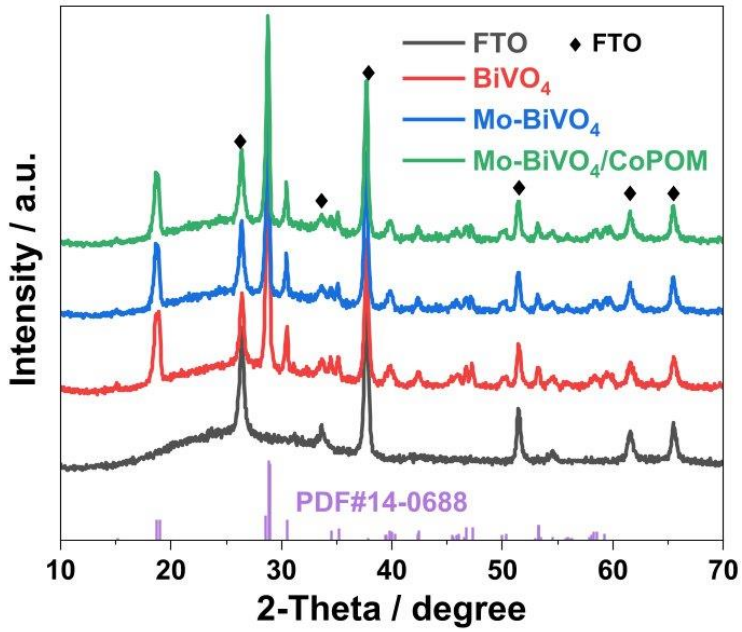

Fig. S9 XRD patterns of $BiVO_4$, Mo-$BiVO_4$, Mo-$BiVO_4$/CoPOM *after PEC* for 4 h in borate buffer electrolyte (0.5 M, pH 9.0) at 0.74 V *vs*. RHE and FTO substrate.

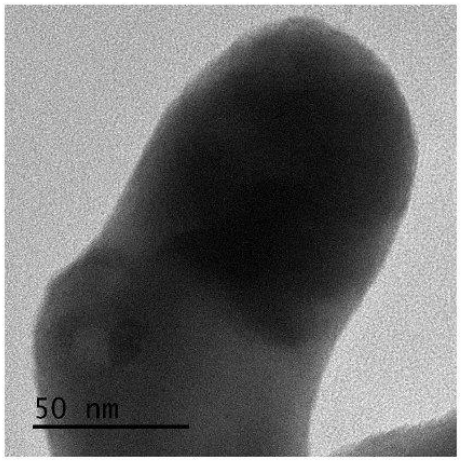

Fig. S10 High-resolution TEM image of Mo-$BiVO_4$/CoPOM after PEC operation for 4 h in borate buffer electrolyte (0.5 M, pH 9.0) at 0.74 V *vs*. RHE.

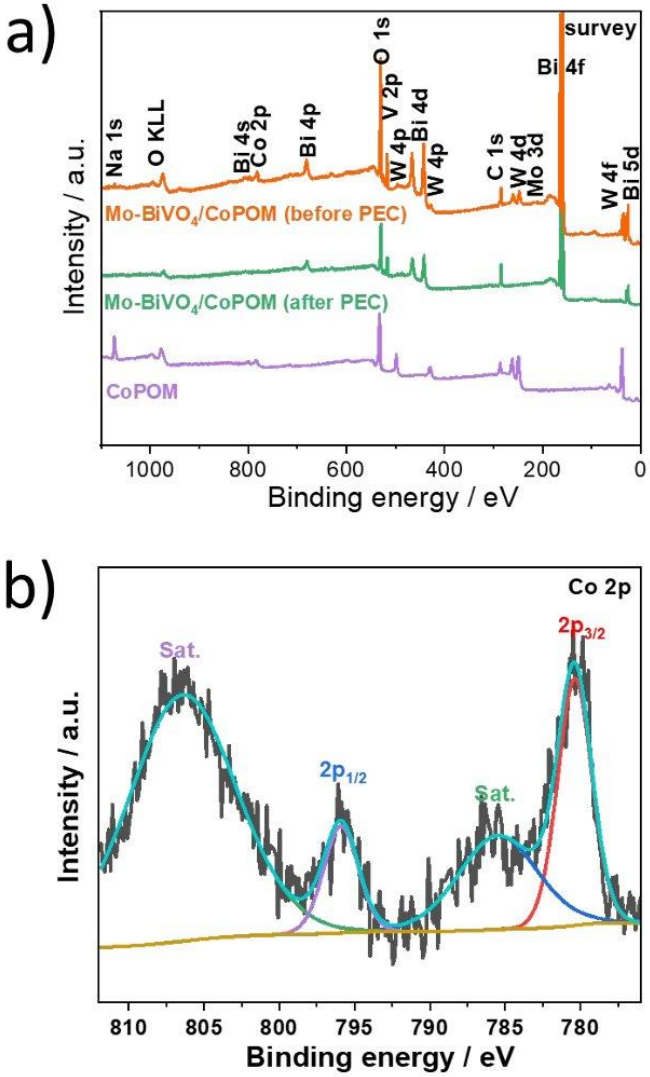

Fig. S11 (a) XP survey spectra of CoPOM powder, Mo-$BiVO_4$/CoPOM photoanodes *before* and *after PEC* for 4 h in borate buffer electrolyte (0.5 M, pH 9.0) at 0.74 V *vs.* RHE. (b) High resolution XP spectra of Co 2p for Mo-$BiVO_4$/CoPOM photoanodes *after PEC* for 4 h in borate buffer electrolyte (0.5 M, pH 9.0) at 0.74 V *vs.* RHE.

Tab. S3 Concentrations (in at.%) of elements detected by XPS for Mo-$BiVO_4$/CoPOM measured before and after the PEC experiment for 4 h in borate buffer electrolyte (0.5 M, pH 9.0) at 0.74 V *vs.* RHE.

Samples	C	Na	Bi	V	Mo	W	Co	O	Ratio (W/Co)
Before	19.6	0.9	12.3	6.0	0.1	3.1	2.3	55.8	1.3
After	38.4	0.0	12.2	6.8	0.0	0.4	0.2	42.0	2.0

Tab. S4 Concentration (in at.%) of the detected elements in SEM-EDX (from the top-view) for Mo-$BiVO_4$/CoPOM measured before and after PEC experiment for 4 h in borate buffer electrolyte (0.5 M, pH 9.0) at 0.74 V *vs.* RHE.

Samples	Bi	V	Mo	W	Co	O	Ratio (W/Co)
Before	15.27	13.51	0.79	1.92	0.95	67.59	2.1
After	10.45	9.41	0.91	3.79	0.25	75.19	15.2

Tab. S5 Concentration (in at.%) of the detected W and Co by SEM-EDX (from the cross-sectional view) for Mo-$BiVO_4$/CoPOM measured before and after PEC experiment for 4 h in borate buffer electrolyte (0.5 M, pH 9.0) at 0.74 V *vs.* RHE.

Samples	W	Co	Ratio (W/Co)
Before	0.64	0.41	1.56
After	0.80	0.21	3.81

Tab. S6 ICP-AES of cobalt measured in the electrolyte before and after chronoamperometry at 0.74 V *vs*. RHE under AM 1.5G one sun illumination for a Mo-$BiVO_4$/CoPOM electrode.

Probe	Element	Result	Unit	Stand. deviation	Unit
1 – Pristine borate buffer solution	Co	not detected			
	K	1,5422	mg/L	0,3600	%
	Na	3351,3333	mg/L	3,8156	%
	P	not detected			
	W	0,0956	mg/L	0,0378	%
	B	3458,0000	mg/L	2,5699	%
2 – Borate buffer solution after PEC expertiment	Co	not detected			
	K	7,8625	mg/L	0,3625	%
	Na	3076,5000	mg/L	2,6358	%
	P	0,6363	mg/L	0,0038	%
	W	0,0688	mg/L	0,0063	%
	B	3196,5000	mg/L	3,5699	%
3 – Pristine phosphate buffer solution	Co	not detected			
	K	38146,0000	mg/L	4,5699	%
	Na	83,6600	mg/L	0,7500	%
	P	15634,0000	mg/L	3,6330	%
	W	0,2550	mg/L	0,1025	%
	B	5,2790	mg/L	0,4138	%
4 – Phosphate buffer solution after PEC expertiment	Co	not detected			
	K	38620,0000	mg/L	3,2319	%
	Na	85,8600	mg/L	4,8500	%
	P	16122,0000	mg/L	3,1255	%
	W	0,1250	mg/L	0,0125	%
	B	3,8528	mg/L	0,3625	%

Tab. S7. Photoelectrochemical performance (photocurrent density at 1.23 V vs. RHE and maximum ABPE) of selected $BiVO_4$-based photoanodes from the literature.

References	Photoanodes	Electrolyte	Photocurrent ($1.23\ V_{RHE}$)	ABPE (maximum)
3[ref]	$FeNiPO_x/BiVO_4$	0.5 M K_3BO_3	6.73 mA cm^{-2}	~2.3%
20[ref]	Gradient W:$BiVO_4$/CoPi	0.1 M KPi	3.6 mA cm^{-2}	Not reported
21[ref]	$BiVO_4$/FeOOH/NiOOH	0.5 M KPi	4.2 mA cm^{-2}	1.75%
24[ref]	$BiVO_4$-85/Co-Pi	0.5 M KPi	2.94 mA cm^{-2}	Not reported
27[ref]	CoBi/E-$BiVO_4$	1 M KBi	3.2 mA cm^{-2}	1.1%
29[ref]	$BiV_{0.97}Mo_{0.03}O_4$/FeOOH	0.1 M KPi	3.0 mA cm^{-2}	Not reported
30[ref]	WO_3/Mo-$BiVO_4$/Co-Pi	0.1 M KPi	2.4 mA cm^{-2}	Not reported
35[ref]	Mo:$BiVO_4$-$NiFeO_x$	0.5 M Na_2SO_4	~1.2 mA cm^{-2}	Not reported
37[ref]	Co-Pi/$BiV_{0.98}Mo_{0.02}O_4$	0.5 M Na_2SO_4	~1 mA cm^{-2}	Not reported
38[ref]	$BiVO_4$/CoPi	0.5 M K_2SO_4 + 0.09 M KH_2PO_4 + 0.01 M K_2HPO_4	1.7 mA cm^{-2}	Not reported
40[ref]	N-$BiVO_4$/$NiFeO_x$	0.5 M K_3BO_3	5.40 mA cm^{-2}	1.79%
41[ref]	$BiVO_4$/Au/NiFeOOH	0.5 M K_3BO_3	5.3 mA cm^{-2}	1.56%
42[ref]	$BiVO_4$/$NiCo_2S_4$	0.5 M Na_2SO_4	1.4 mA cm^{-2}	Not reported
56[ref]	$BiVO_4$-$(b\text{-}PEI/POM)_{10}$	80 mM KPi	~2.8 mA cm^{-2}	Not reported
58[ref]	$BiVO_4$-N/C-CoPOM	0.5 M KPi	3.30 mA cm^{-2}	1.22%
59[ref]	La:$BaSnO_3$-Mo:$BiVO_4$	1 M KPi	3.23 mA cm^{-2}	Not reported
S11[11]	$BiVO_4$/$ZnFe_2O_4$/Bi NPs	0.5 M Na_2SO_4	2.72 mA cm^{-2}	0.51%
S12[12]	Ni:FeOOH/$BiVO_4$	0.5 M Na_2SO_4	4.21 mA cm^{-2}	0.80%
S13[13]	−0.8 V reduced-$BiVO_4$/FeOOH	0.2 M Na_2SO_4	2.02 mA cm^{-2}	0.51%
S14[14]	NiFeV/B-$BiVO_4$	1 M KBi	4.6 mA cm^{-2}	1.85%
This work	Mo-$BiVO_4$/CoPOM	0.5 M KBi	4.32 mA cm^{-2}	0.73%

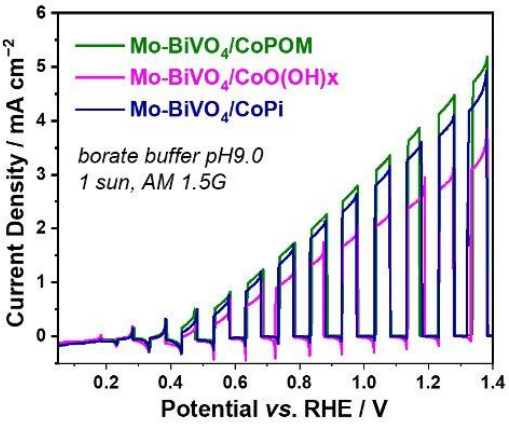

Fig. S12 Photocurrents recorded under AM 1.5G illumination in borate electrolyte (0.5 M, pH 9.0) for Mo-$BiVO_4$/CoPOM, Mo-$BiVO_4$/CoPi and Mo-$BiVO_4$/$CoO(OH)_x$.

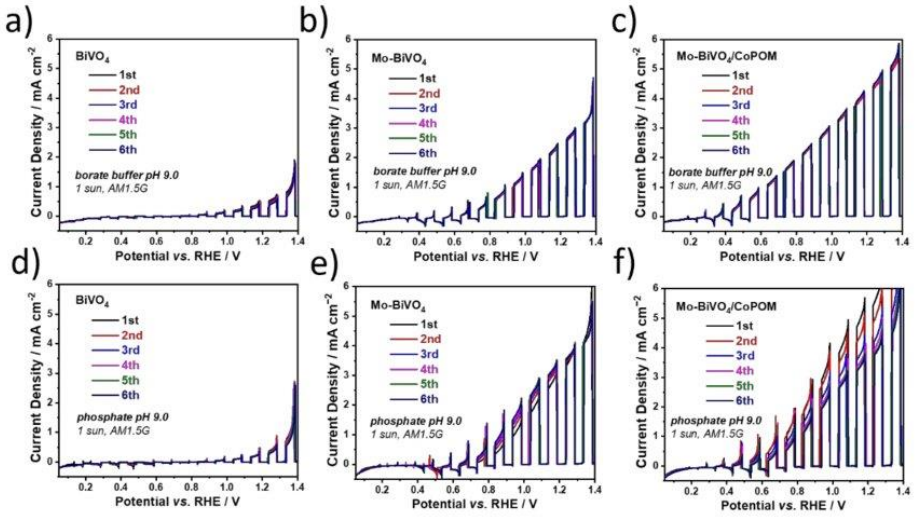

Fig. S13 Photocurrent stability test recorded under AM 1.5G one sun illumination at cathodic sweep of 10 mV s^{-1} for three photoanodes in (a-c) a borate buffer electrolyte of pH value 9.0 and (d-f) a phosphate electrolyte of pH value 9.0.

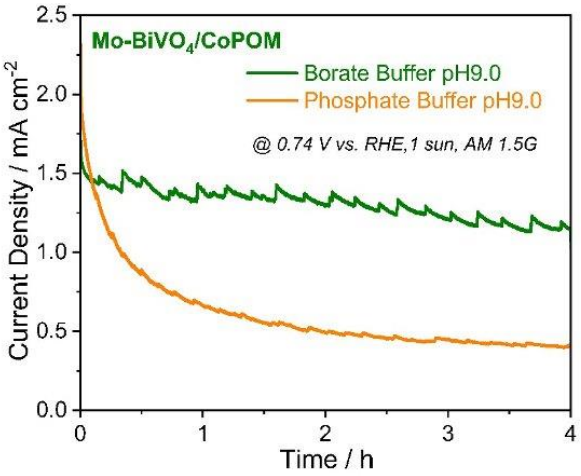

Fig. S14 Stability chronoamperometry curves for Mo-$BiVO_4$/CoPOM in borate buffer (0.5 M, pH 9.0) and phosphate electrolyte (0.5 M, pH 9.0) at 0.74 V *vs.* RHE under AM 1.5G (1 sun) illumination.

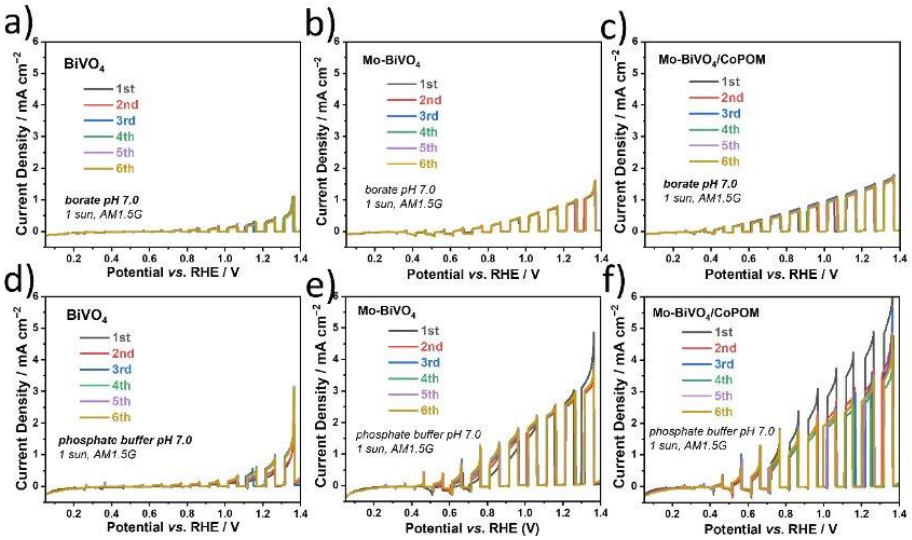

Fig. S15 Photocurrent stability test recorded under AM 1.5G illumination at cathodic sweep of 10 mV s^{-1} for three photoanodes in (a-c) a borate buffer electrolyte of pH value 7.0 and (d-f) a phosphate buffer electrolyte of pH value 7.0.

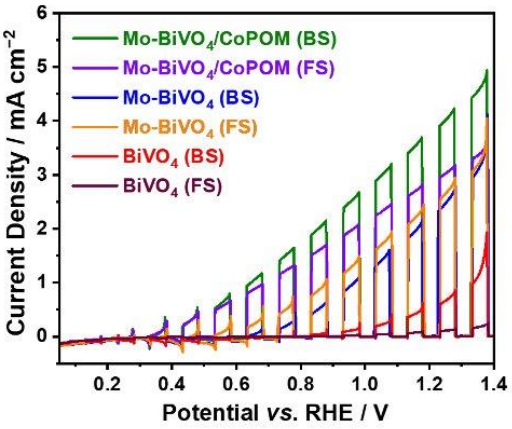

Fig. S16 *J-V* curves under AM 1.5G one sun illumination for all three photoanodes under back-side illumination from the FTO-glass side or under front-side illumination from the active layer material side.

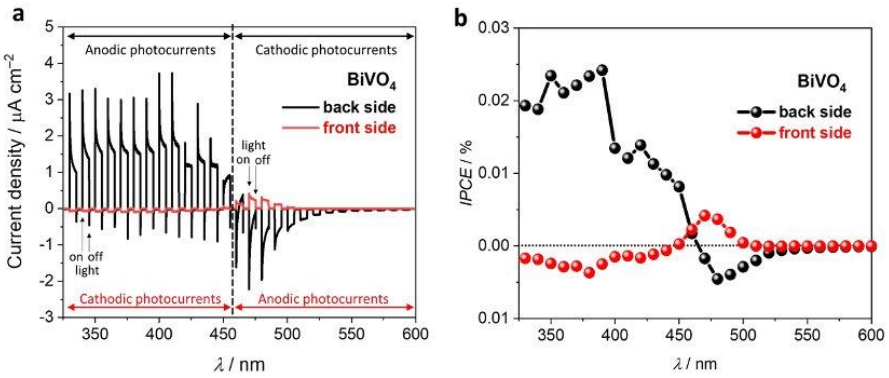

Fig. S17 Photocurrent transients (a) and the corresponding IPCE spectra (b) measured at a pristine $BiVO_4$ photoanode under the front-side and back-side chopped irradiation with monochromatic light of different wavelengths in borate electrolyte (pH 9.0) at 0.74 V *vs*. RHE.

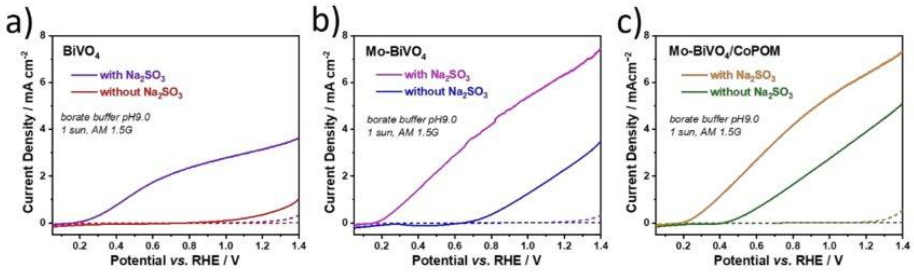

Fig. S18 *J-V* plots of (a) $BiVO_4$, (b) Mo-$BiVO_4$ and (c) Mo-$BiVO_4$/CoPOM in 0.5 M borate buffer electrolyte pH 9.0 with and without 0.1 M Na_2SO_3 under AM 1.5G one sun illumination. Dotted curves represent measurements in dark.

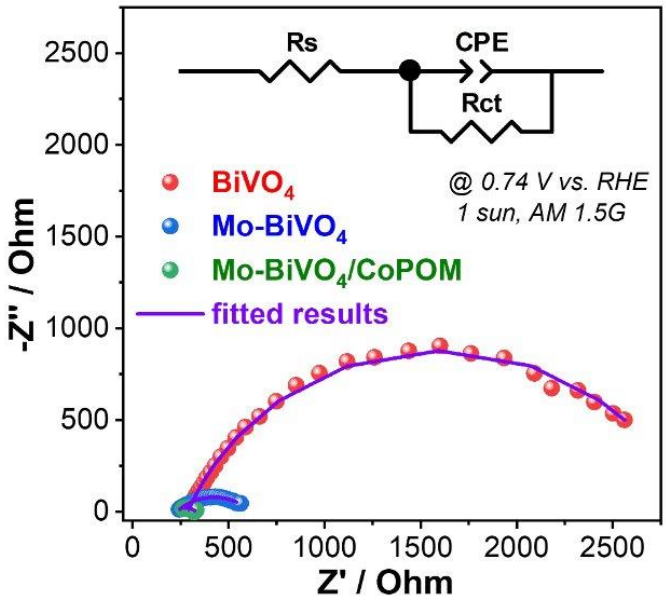

Fig. S19 EIS curves (inset: equivalent circuit used for fitting) of $BiVO_4$, Mo-$BiVO_4$ and Mo-$BiVO_4$/CoPOM in 0.5 M borate buffer electrolyte pH 9.0 under AM 1.5G one sun illumination. Solid curves represent the fitted results.

Tab. S8 The fitted results of EIS data using the equivalent circuit in Fig. S19.

Samples	R_s (Ω)	R_{ct} (Ω)
Mo-$BiVO_4$/CoPOM	217.3 ± 11.6	113.4 ± 13.4
Mo-$BiVO_4$	231.3 ± 1.5	385.3 ± 6.9
$BiVO_4$	288.0 ± 1.9	2620.0 ± 36.5

References

1. J. Jian, Y. Xu, X. Yang, W. Liu, M. Fu, H. Yu, F. Xu, F. Feng, L. Jia, D. Friedrich, R. van de Krol and H. Wang, *Nat. Commun.*, 2019, **10**, 2609.
2. Q. Yin, J. M. Tan, C. Besson, Y. V. Geletii, D. G. Musaev, A. E. Kuznetsov, Z. Luo, K. I. Hardcastle and C. L. Hill, *Science*, 2010, **328,** 342–345.
3. R. Gong, D. Mitoraj, D. Gao, M. Mundszinger, D. Sorsche, U. Kaiser, C. Streb, R. Beranek and S. Rau, *Adv. Sustainable Syst.*, 2022, **6**, 2100473.
4. Z. Luo, C. Li, S. Liu, T. Wang and J. Gong, *Chem. Sci.*, 2017, **8**, 91–100.
5. L. Wang, D. Mitoraj, S. Turner, O. V. Khavryuchenko, T. Jacob, R. K. Hocking and R. Beranek, *ACS Catal.*, 2017, **7**, 4759–4767.
6. X. Cao, Y. Wang, J. Lin and Y. Ding, *J. Mater. Chem. A*, 2019, **7**, 6294–6303.
7. H. Dotan, K. Sivula, M. Grätzel, A. Rothschild and S. C. Warren, *Energy Environ. Sci.*, 2011, **4**, 958–964.
8. T. W. Kim and K. Choi, *Science*, 2014, **343**, 990–994.
9. A. W. Sleight, H. Chen and A. Ferretti, *Mat. Res. Bull.*, 1979, **14**, 1571–1581.
10. I. S. Cho, Z. Chen, A. J. Forman, D. R. Kim, P. M. Rao, T. F. Jaramillo and X. Zheng, *Nano Lett.*, 2011, **11**, 4978–4984.
11. S. Bai, S. Jia, S. Yan, Y. Zhao, P. Tang, R. Luo, Y. Feng, D. Li and A. Chen, *Inter. J. Hydrogen Energy*, 2024, **54**, 1008–1016.
12. J. Wang, Y. Zhang, J. Bai, J. Li, C. Zhou, L. Li, C. Xie, T. Zhou, H. Zhu and B. Zhou, *J. Colloid & Interface Sci.,* 2023, **644**, 509–518.
13. P. Yang, H. Shi, H. Wu, D. Yu, L Huang, Y. Wu, X. Gong, P. Xiao and Y, Zhang, *Nanoscale*, 2023, **15**, 4536–4545.
14. Q. Meng, B. Zhang, H. Yang, C. Liu, Y. Li, A. Kravchenko, X. Sheng, L. Fan, F. Li and L. Sun, *Mater. Adv.,* 2021, **2**, 4323–4332.

6.2 (FF-2) Supporting Information: "Double-Use" Strategy for Improving the Photoelectrochemical Performance of $BiVO_4$ Photoanodes using a Cobalt-Functionalized Polyoxotungstate

SUPPORTING INFORMATION

"Double-Use" Strategy for Improving the Photoelectrochemical Performance of $BiVO_4$ Photoanodes using a Cobalt-Functionalized Polyoxotungstate

Fan Feng,[†] Dariusz Mitoraj,[‡] Ekemena Oseghe,[†] Carsten Streb,*[,†] Radim Beranek*[,‡]

[†] Department of Chemistry, Johannes Gutenberg University Mainz, Duesbergweg 10-14, 55128 Mainz, Germany
[‡] Institute of Electrochemistry, Ulm University, Albert-Einstein-Allee 47, 89081 Ulm, Germany
* Corresponding authors: radim.beranek@uni-ulm.de, carsten.streb@uni-mainz.de

Analytical section:

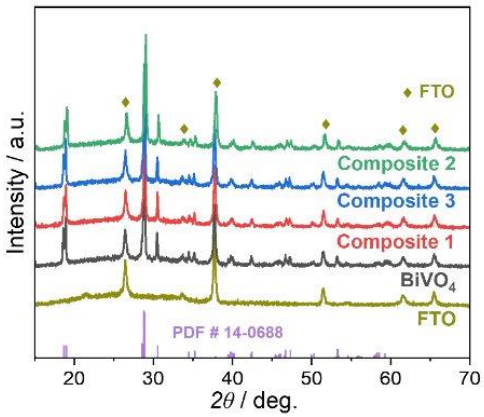

Figure S1: XRD patterns of $BiVO_4$, **Composite 1**, **Composite 3**, **Composite 2** and FTO substrate.

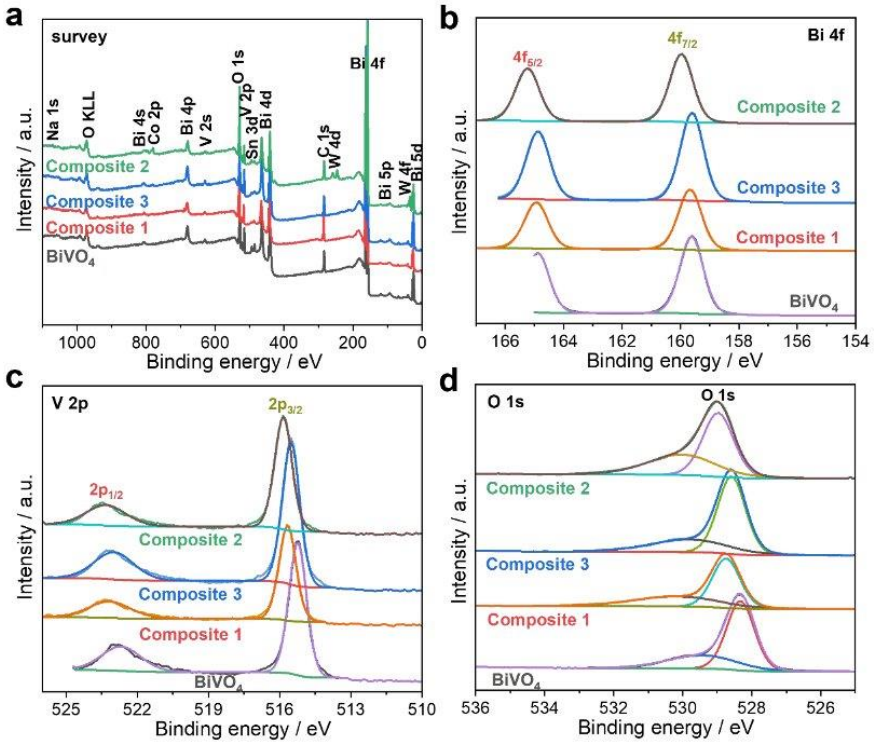

Figure S2: XPS spectroscopic analysis of all photoanodes reported: (a) survey spectra, (b) deconvoluted Bi 4f region, (c) deconvoluted V 2p region, (d) deconvoluted O 1s region.

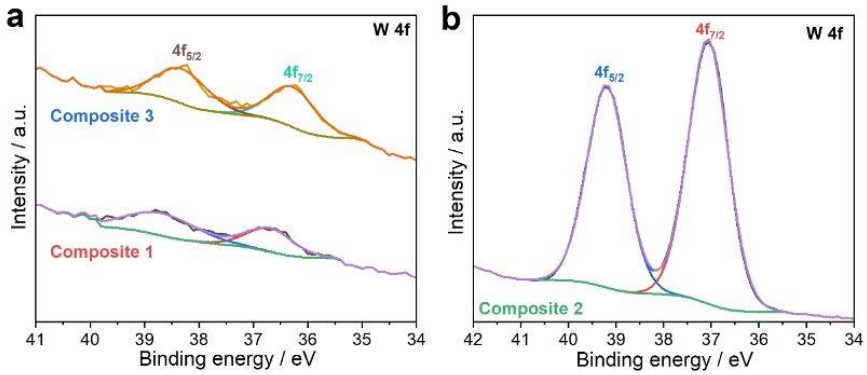

Figure S3: W 4f XP spectra for (a) **Composite 1** and **Composite 3**, (b) **Composite 2** photoanodes.

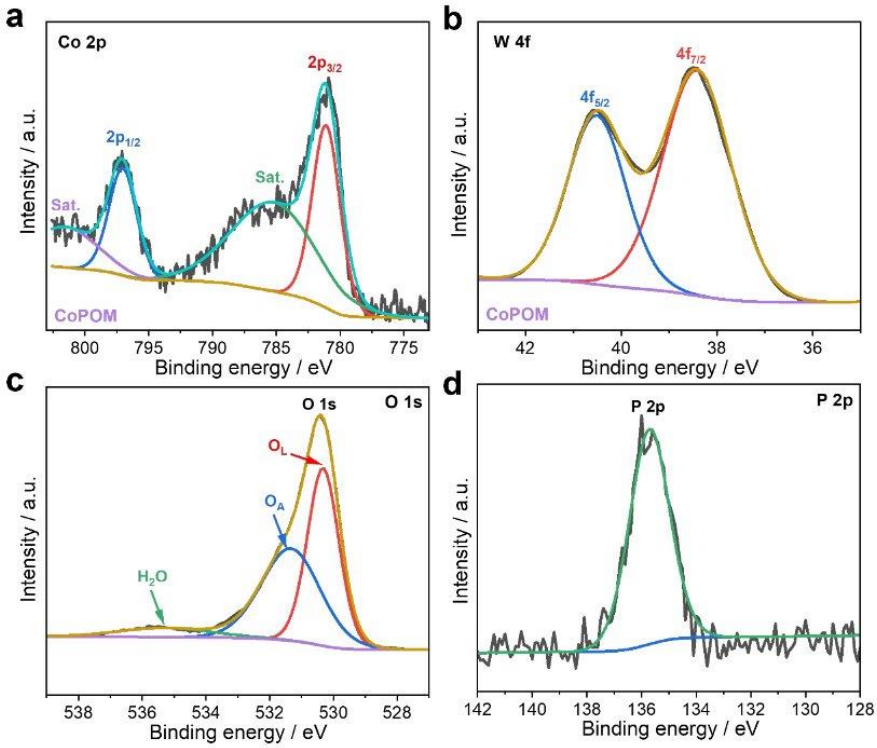

Figure S4: XP spectra of CoPOM powder (a) Co 2p, (b) W 4f, (c) O 1s and (d) P 2p.

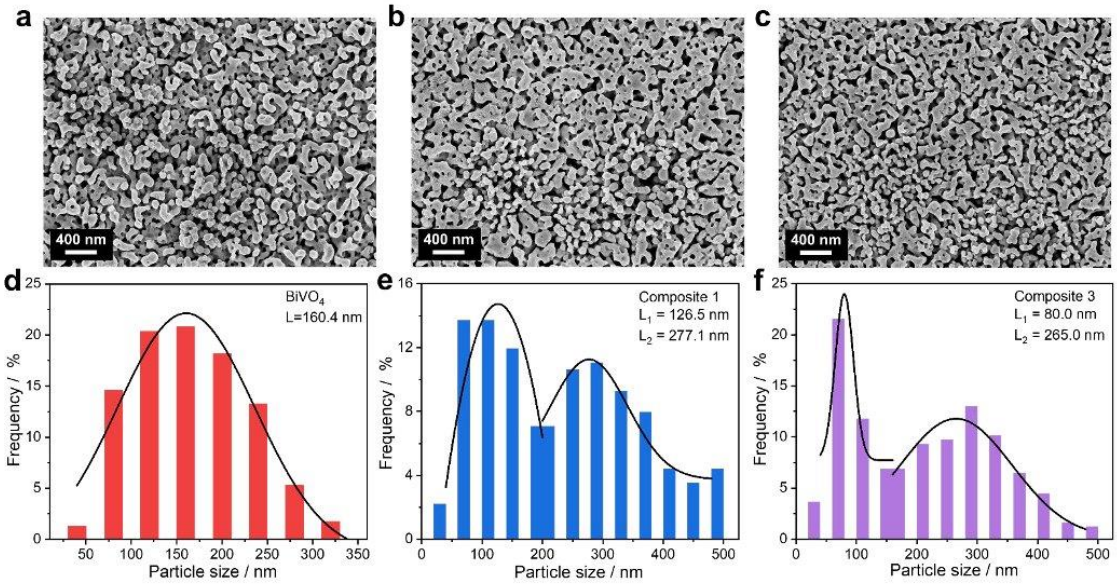

Figure S5: SEM images of (a) $BiVO_4$, (b) **Composite 1** and (c) **Composite 3**. Diagrams of particle size distribution statistics of (d) $BiVO_4$, (e) **Composite 1** and (f) **Composite 3**.

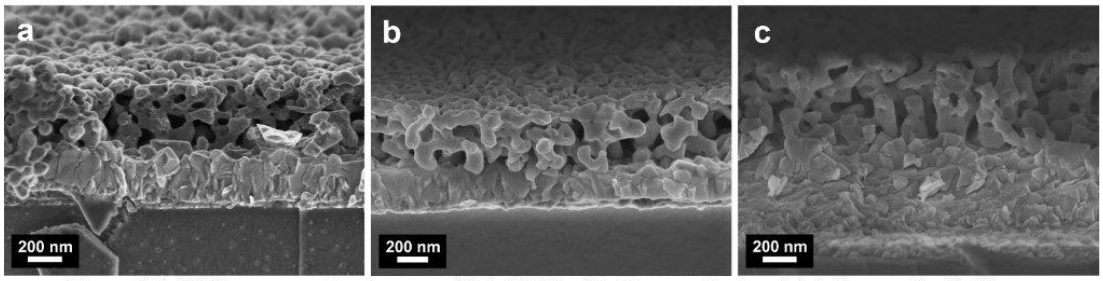

Figure S6: SEM cross-section images of (a) $BiVO_4$, (b) **Composite 1** and (c) **Composite 2**. The x-section images were taken 75° pre-tilt for all photoanodes.

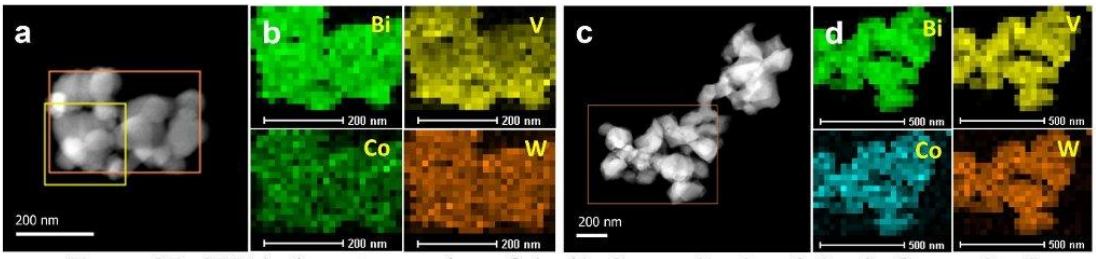

Figure S7: STEM elements mapping of (a, b) **Composite 1** and (c, d) **Composite 2** photoanodes.

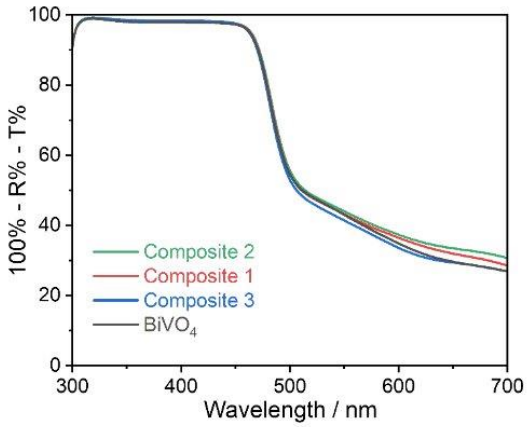

Figure S8: UV-Vis electronic absorption spectra of the photoanodes. $Absorptance\ (\%) = 100\% - Reflectance\ (\%) - Transmittance\ (\%)$.

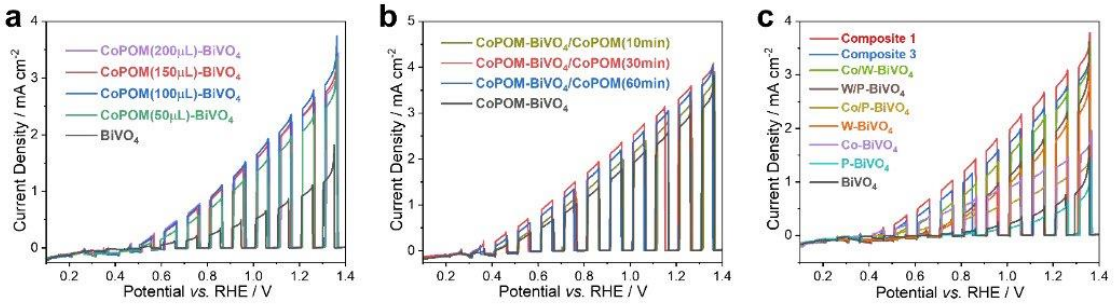

Figure S9: J-V curves of (a) different amount for CoPOM doping on $BiVO_4$ photoanodes; (b) different amount for CoPOM on CoPOM-$BiVO_4$ phtoanodes; (c) different element-doping with the same molar amount with CoPOM doping samples in sodium borate buffer electrolyte under AM 1.5G (1 sun).

The photocurrent density of P-$BiVO_4$ and Co/P-$BiVO_4$ are slightly decreased compared to the P-doped-free samples, while the photocurrent density of W/P-$BiVO_4$ shows a slight increase trend compared with W-$BiVO_4$ photoanodes, suggestion is that W-doped can be able to a stable factor for doped $BiVO_4$-based samples.

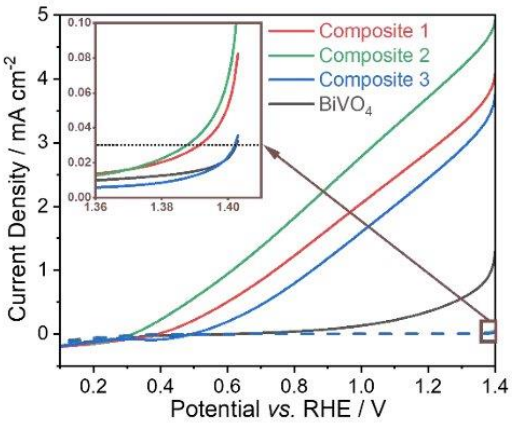

Figure S10: LSV curves of $BiVO_4$, **Composite 1, Composite 3** and **Composite 2** in borate buffer electrolyte pH 9.0 under AM 1.5G (1 sun) illumination. Dotted curves represent measurements carried out in the dark, and the inset shows an enlarged view of curves measured in the dark. The lowest overpotential of 158 mV (@ j = 0.03 mA cm^{-2}) is observed for **Composite 2** compared to that of **Composite 1** (161 mV), **Composite 3** (172 mV) and pure $BiVO_4$ (173 mV).

Table S1: concentration (in at.%) of the detected elements in XPS

Samples	Bi	V	O	C	Co	W	P	Na	Ratio (W/Co)
$BiVO_4$	14.35	7.14	49.14	29.13	-	-	-	0.24	-
Composite 1	10.00	5.44	36.43	47.90	0.07	0.16	0.00	0.01	2.29
Composite 3	13.76	7.33	48.90	29.52	0.24	0.26	0.00	0.00	1.08
Composite 2	11.23	5.86	53.75	25.99	1.28	1.42	0.00	0.48	1.11

Table S2: concentration (in at.%) of the detected elements in XPS for **Composite 1** before PEC and after PEC.

Samples	Bi	V	O	C	Co	W	P	Na	Ratio (W/Co)
Before	10.00	5.44	36.43	47.90	0.07	0.16	0.00	0.01	2.29
Normalized (Before)	19.19	10.44	69.92	-	0.13	0.30	0.00	0.02	2.31
After	13.76	5.98	46.17	32.82	0.68	0.40	0.00	0.18	0.59
Normalized (After)	20.48	8.90	68.73	-	1.02	0.60	0.00	0.27	0.59

Table S3: concentration (in at.%) of the detected elements in XPS for **Composite 2** before PEC and after PEC.

Samples	Bi	V	O	C	Co	W	P	Na	Ratio (W/Co)
Before	11.23	5.86	53.75	25.99	1.28	1.42	0.00	0.48	1.11
Normalized (Before)	15.17	7.92	72.62	-	1.73	1.92	0.00	0.65	1.11
After	10.46	5.72	46.50	34.65	1.53	1.10	0.00	0.04	0.72
Normalized (After)	16.01	8.75	71.16	-	2.34	1.68	0.00	0.06	0.72

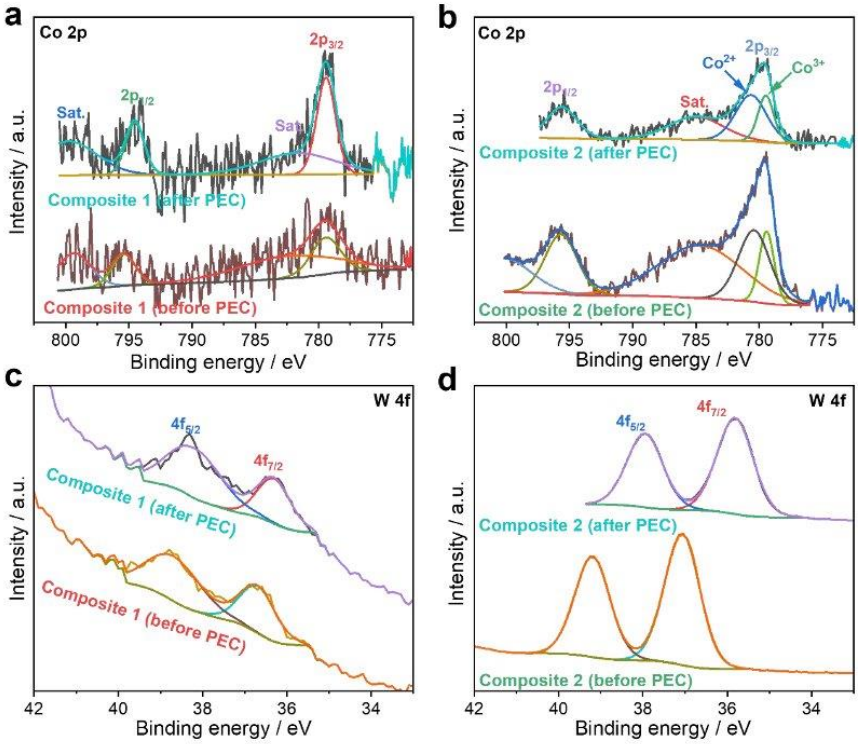

Figure S11: Co 2p XP spectra for (a) **Composite 1**, (b) **Composite 2** and W 4f XP spektra for (c) **Composite 1**, (d) **Composite 2** before and after PEC stability experiments (4 h).

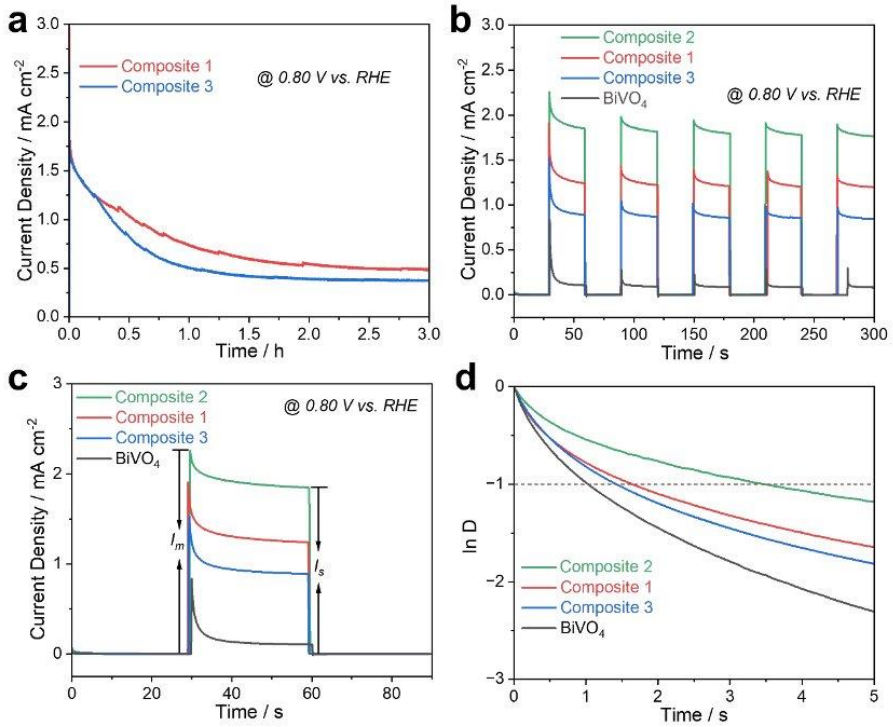

Figure S12: (a) Chronoamperometry curves under AM 1.5G illumination at 0.80 V *vs*. RHE for **Composite 1** and **Composite 3**. (b, c) Photocurrent transients under AM 1.5G (1 sun) illumination at +0.80 V *vs.* RHE, and (d) transient decay times (taken as time at ln D = –1) of $BiVO_4$, **Composite 1**, **Composite 2** and **Composite 3**.

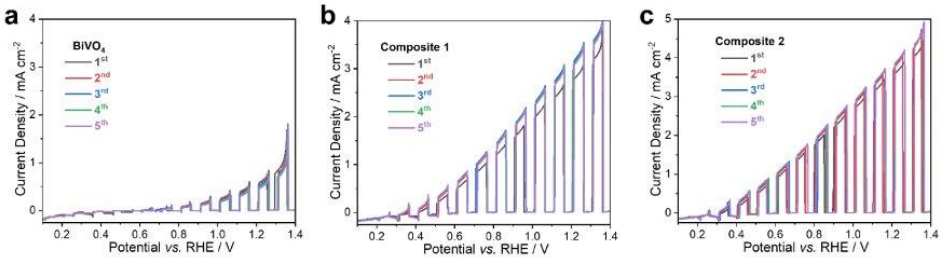

Figure S13: Photocurrent stability test recorded under AM 1.5G (1 sun) illumination at anodic sweep of 10 mV s^{-1} for (a) $BiVO_4$, (b) **Composite 1**, and (c) **Composite 2** samples.

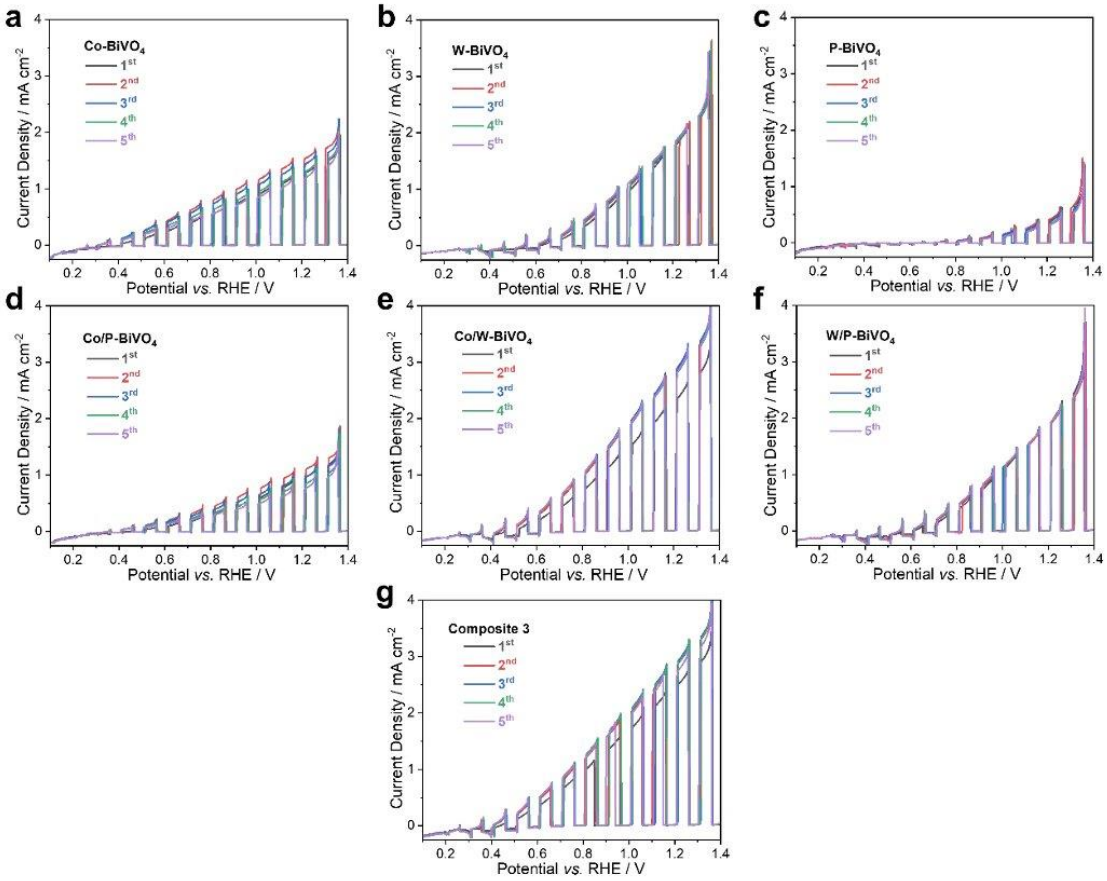

Figure S14: Photocurrent stability test recorded under AM 1.5G illumination at anodic sweep of 10 mV s^{-1} for (a) Co-$BiVO_4$, (b) W-$BiVO_4$, (c) P-$BiVO_4$, (d) Co/P-$BiVO_4$, (e) Co/W-$BiVO_4$, (f) W/P-$BiVO_4$ and (g) **Composite 3** samples.

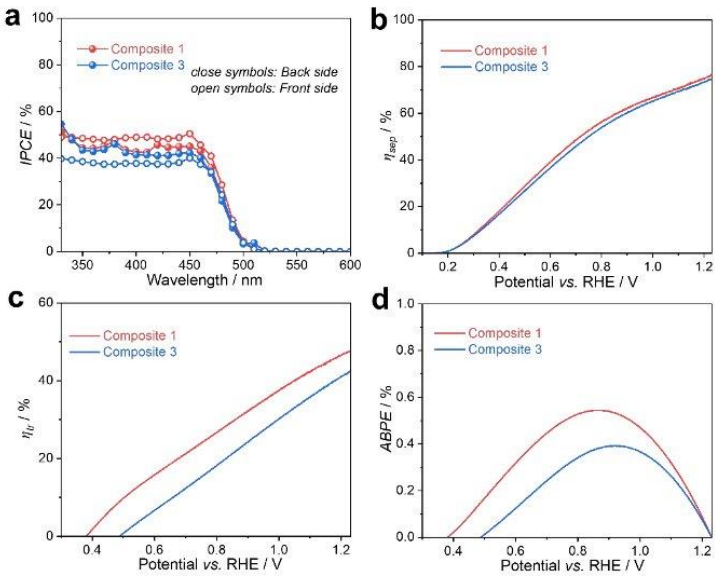

Figure S15: (a) IPCE spectra under intermittent monochromatic irradiation; (b) Charge separation efficiency (η_{sep}), (c) hole transfer efficiency (η_{tr}) and (d) applied bias photoconversion efficiency (ABPE) plots for **Composite 1** and **Composite 3** photoanodes.

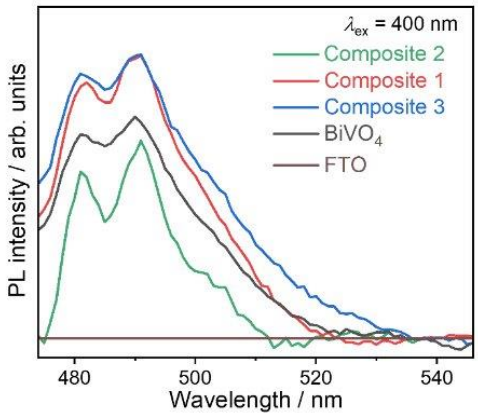

Figure S16: PL spectra (after abstraction of the baseline due to the FTO response) of FTO, $BiVO_4$, **Composite 1**, **Composite 2** and **Composite 3** photoanodes recorded at the excitation wavelength of 400 nm.

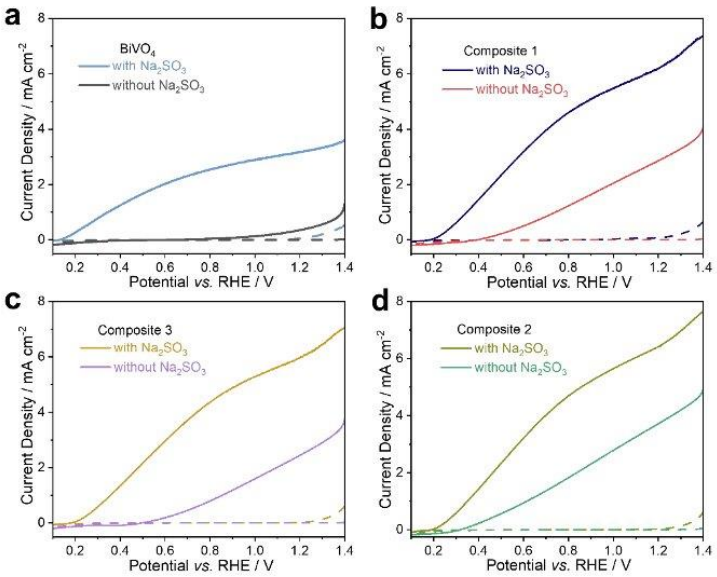

Figure S17: J-V curves of (a) $BiVO_4$, (b) **Composite 1,** (c) **Composite 3** and (d) **Composite 2** in borate buffer electrolyte pH 9.0 with and without 0.1 M Na_2SO_3 under AM 1.5G (1 sun) illumination. Dotted curves represent measurements in the dark.

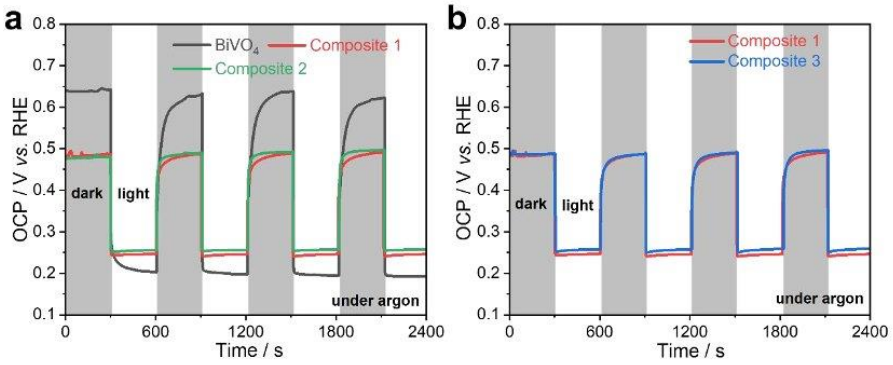

Figure S18: Open-circuit potential transients recorded under AM 1.5G in 0.5 M borate buffer under argon atmosphere for (a) $BiVO_4$, **Composite 1** and **Composite 2**, and (b) **Composite 1** and **Composite 3**. The electrodes were irradiated from the back-side.

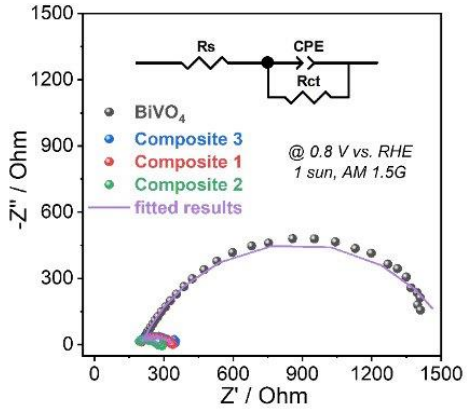

Figure S19: EIS curves (inset: equivalent circuit used for fitting) of $BiVO_4$, **Composite 1, Composite 2** and **Composite 3** in 0.5 M borate buffer electrolyte pH 9.0 under AM 1.5G 1 sun illumination. Solid curves represent the fitted results.

Table S4: The fitted results of EIS data using the equivalent circuit in Fig. S19.

Samples	R_s (Ω)	R_{ct} (Ω)
Composite 2	158.5 ± 16.1	130.4 ± 19.1
Composite 1	185.8 ± 2.8	153.7 ± 4.4
Composite 3	174.3 ±4.4	174.4 ± 6.5
$BiVO_4$	203.5 ± 1.9	1353.0 ± 18.4

For simplicity, we used a Randles-type equivalent circuit model, where R_s represents the uncompensated series resistance, R_{ct} in our case represents the combined charge transport and interfacial charge transfer resistance and CPE is the constant phase element for the electrode/electrolyte interface. The fitted values of R_s and R_{ct} are shown in Table S4. The similar Rs values of four films indicate that the effect of series resistance is negligible, while the values of R_{ct} of **Composite 1** (~154 Ω), **Composite 3** (~174 Ω) and **Composite 2** (~130 Ω) decrease significantly as compared to pristine $BiVO_4$ (~1353 Ω), indicating that 'Double-Use' of CoPOM greatly enhances both charge transport (i.e., conductivity) and the charge transfer, resulting in enhanced photocurrent density. Additionally, the value of R_{ct} of **Composite 1** is slightly smaller than that of **Composite 3**, which is also a factor to explain the slightly enhanced photocurrent density.

Table S5: The comparison of photoelectrochemical performance.

Samples	**Composite 2**	**Composite 1**	**Composite 3**	$BiVO_4$
Photocurrent density @ 1.23 V *vs.* RHE	3.67 mA cm^{-2}	2.86 mA cm^{-2}	2.57 mA cm^{-2}	0.62 mA cm^{-2}
Onset potential	~ 0.32 V *vs.* RHE	~ 0.39 V *vs.* RHE	~ 0.50 V *vs.* RHE	~ 0.61 V *vs.* RHE
η_{sep} @ 1.23 V vs. RHE	79.3%	76.5%	74.7%	38.3%
η_{tr} @ 1.23 V vs. RHE	59.2%	47.8%	42.5%	12.7%
ABPE (maximum value)	0.79% @ 0.82 V *vs*. RHE	0.54% @ 0.87 V *vs*. RHE	0.39% @ 0.94 V *vs*. RHE	0.03% @ 1.04 V *vs*. RHE
IPCE @ 450 nm	BS: 51.7% FS: 46.9%	BS: 45.1% FS: 50.5%	BS: 42.3% FS: 40.0%	BS: 5.9% FS: 2.1%

6.3 (FF-3) Supporting Information: Atomically Engineered Defect-Rich Palladium Metallene for High-Performance Alkaline Oxygen Reduction Electrocatalysis

ADVANCED SCIENCE
Open Access

Supporting Information

for *Adv. Sci.*, DOI 10.1002/advs.202405187

Atomically Engineered Defect-Rich Palladium Metallene for High-Performance Alkaline Oxygen Reduction Electrocatalysis

Yupeng Zhao, Zhengfan Chen, Nana Ma, Weiyi Cheng, Dong Zhang, Kecheng Cao, Fan Feng, Dandan Gao, Rongji Liu, Shujun Li* and Carsten Streb**

Atomically Engineered Defect-Rich Palladium Metallene for High-Performance Alkaline Oxygen Reduction Electrocatalysis

Yupeng Zhao, Zhengfan Chen, Nana Ma, Weiyi Cheng, Dong Zhang, Kecheng Cao, Fan Feng, Dandan Gao, Rongji Liu*, Shujun Li*, Carsten Streb*

Supporting Information

Table of contents

S1 Experimental procedures

Chemicals and Materials: Palladium (II) acetylacetonate ($Pd(acac)_2$, 99%), 12-Molybdophosphoric acid hydrate ($H_3PMo_{12}O_{40} \cdot xH_2O$, analysis), and cyclohexane (≥ 99.9%) were purchased from Merck. Tungsten hexacarbonyl ($W(CO)_6$, 97%) and Nafion solution (D-520 dispersion 5% w/w aq. and 1-propanol) were purchased from Alfa Aesar. Potassium hydroxide (KOH, ≥85%), ethanol (CH_3CH_2OH, absolute), commercial Pt/C (20 wt%), and commercial Pd/C (10 wt%), and N, N-Dimethylformamide (DMF, 99.5%) were purchased from Fisher Scientific. Acetic acid (CH_3COOH, 99.5%) was purchased from VWR. Cetyltrimethylammonium bromide (CTAB, $C_{19}H_{42}BrN$), citric acid (CA, $C_6H_8O_7$, ≥ 99.5 %), polyvinyl pyrrolidone (PVP, Mw = 55 000) were purchased from Sigma-Aldrich. Vulcan XC-72 carbon was purchased from BC Berlin Catalysts GmbH. All chemicals were used in this experiment without further purification.

Synthesis of D-Pd M and Pd M:

The defect-rich Pd metallene (**D-Pd M**) was synthesized by a simple wet-chemical method. Typically, 42 mg of $H_3PMo_{12}O_{40} \cdot xH_2O$ was dissolved in 10 mL of DMF solution followed by deaeration with Ar for 15 min. Then the solution was irradiated under UV light (Wavelength = 254 nm) for 30 min to get solution A. In addition, 10.0 mg of $Pd(acac)_2$ and 20 mg of $W(CO)_6$ were added into a 25 mL bottle containing 8 mL of DMF and then sonicated for half an hour to yield a homogeneous solution (B). Afterward, solution A was added to solution B and was placed in an oil bath at 50 °C for 6 h. After cooling to room temperature, the black colloidal product was collected by centrifugation and washed six times with a mixture of ethanol and cyclohexane ($v_{ethanol}$ /$v_{cyclohexane}$ = 1:1). The final product was dispersed in cyclohexane for further use.

The hexagonal Pd metallene (Pd M) for comparison were prepared according to a previous approach with slight modifications.[1,2] 16 mg of $Pd(acac)_2$, 90 mg of CA, 60 mg of CTAB, and 30 mg of PVP were added into 10 mL of DMF and stirred for 1 h to get a homogeneous orange-red solution. The obtained solution was then transferred into a 25 mL vial and 100 mg of $W(CO)_6$ was added to the vial under N_2 atmosphere. The vial was capped and heated at 80 °C for 1 h. After the reaction, Pd nanosheets were collected by centrifugation using enough acetone and then redispersed in acetone for further use.

S2 Characterizations

Powder X-ray diffraction (XRD): Bruker D2 Phaser equipment, with Cu Kα radiation (λ = 1.5406 Å).

Transmission electron microscopy (TEM): Tecnai G2 Spirit operated at 120 kV (Imaging).

High-resolution transmission electron microscopy (HRTEM) and energy-dispersive X-ray spectroscopy (EDX): Jeol F200 equipped with a SuperX EDX detector, operated at 200 kV (Imaging and diffraction pattern).

Inductively Coupled Plasma Optical Emission Spectroscopy (ICP-OES): Agilent 5800 VDV ICP-OES (optical emission spectrometer) with the automatic sampler SPS 4.

X-ray photoelectron spectroscopy (XPS): Monochromatized Al Kα exciting X-radiation using a PHI Quantera SXM system. The binding energies were calibrated based on C1s (284.8 eV).

Ultraviolet - visible spectroscopy (UV-vis): Cary 3500 UV-Vis Spectrophotometer equipped with a Xenon flash lamp (250 Hz). Measurements were performed in standard 1 cm cuvettes.

Atomic force microscopy (AFM): Bruker Dimension Icon.

X-ray absorption spectroscopy (XAS) experiment and data processing: Pd K-edge, W L_3-edge, and Mo L_3-edge X-ray absorption fine structure (XAFS) analyses were performed with Si (111) crystal monochromators at the BL14W Beam line at the Shanghai Synchrotron Radiation Facility (SSRF) (Shanghai, China). Before the analysis at the beamline, samples were placed into aluminum sample holders and sealed using Kapton tape film. The XAFS spectra were recorded at room temperature using a 4-channel Silicon Drift Detector (SDD) Bruker 5040. Pd K-edge and W L_3-edge extended X-ray absorption fine structure (EXAFS) spectra were recorded in transmission mode. Mo L_3-edge extended X-ray absorption fine structure (EXAFS) spectra were recorded in fluorescence mode. Negligible changes in the line shape and peak position of Pd K-edge, W L_3-edge, and Mo L_3-edge XANES spectra were observed between two scans taken for a specific sample. The spectra were processed and analyzed by the software code Athena.

S3 Electrochemical measurements:

The as-prepared **D-Pd M** and Pd M catalysts were loaded on carbon black (Vulcan XC-72) before electrochemical tests. Typically, the **D-Pd M** (2 mg) was mixed with carbon black (8 mg) in cyclohexane (10 mL) under ambient sonication for 1 h. After stirring for another 12 h, the product was collected by centrifugation and washed three times with ethanol. Afterward, the product was treated in pure acetic acid (10 mL) at 70 °C for 2 h to remove excess impurities and excess surfactants for further use. At the end, **D-Pd M**/C was collected by centrifugation, washed three times with ethanol, and dried at 60°C for 3 hours. Pd M/C was prepared by the same method.

To prepare the catalyst inks, the as-prepared **D-Pd M**/C (1 mg) was re-dispersed in a solution containing 15 μL DI water, 980 μL ethanol, and 5 μL Nafion solution by at least 30 min sonication in an ice-water bath to form a catalyst ink. Then the **D-Pd M**/C catalyst ink was dipped on the electrode with a controllable amount of **D-Pd M** catalyst being 10 $\mu g \cdot cm^{-2}$. Likewise, the Pd M/C was processed in the same way. The controllable amount of commercial Pd/C, and commercial Pt/C were 15 $\mu g \cdot cm^{-2}$ to reach the well-defined limited current density. The loading amount on the electrode of prepared catalysts was determined by ICP-OES.

Electrochemical tests were conducted using a three-electrode system on an Ametek electrochemical workstation (channel PMC 1000) equipped with an RRDE setup (Pine, USA). A glassy carbon rotating disk electrode (GC RDE, diameter: 5 mm, area: 0.196 cm^2), a saturated calomel electrode (SCE), and a graphite rod were used as the working electrode, reference electrode, and counter electrode, respectively. All potentials in this study were reported on a reversible hydrogen electrode (RHE) scale according to the Nernst equation ($E_{RHE} = E_{SCE} + E^0_{SCE} + 0.059\ V \times pH$). The cyclic voltammetry (CV) curves were recorded in N_2-saturated 0.1 M KOH at a scan rate of 50 $mV \cdot s^{-1}$. ORR linear sweep voltammetry (LSV) was recorded in O_2-saturated 0.1 M KOH at 20 $mV \cdot s^{-1}$ and a rotating rate of 1600 rpm. It is worth noting that the ORR LSV curves have been corrected in the N_2-saturated 0.1 M KOH to eliminate the interference of double-layer capacity. The current densities ($\boldsymbol{j}$) were normalized regarding the geometric area of the GC RDE. Notably, all ORR LSV curves were iR-corrected (95%) before applying the K-L equation: $\boldsymbol{I}_k = (\boldsymbol{I}_d \times \boldsymbol{I})/(\boldsymbol{I}_d - \boldsymbol{I})$, where $\boldsymbol{I}_k$, $\boldsymbol{I}_d$, and $\boldsymbol{I}$ represent the kinetic, diffusion limiting, and measured current, respectively.

The electrochemical active surface areas (ECSAs) of all the catalysts were calculated using the underpotentially deposited H (H_{upd}) and Cu stripping. The underpotentially deposited H (H_{upd})

data was obtained in the N_2-saturated 0.1 M $HClO_4$. The peaks of H_{upd} were recorded by cyclic voltammetry (CV) with a scan rate of 50 $mV \cdot s^{-1}$ to calculate the ECSAs. In the calculation, we used a charge density of 210 $\mu C \cdot cm^{-2}$ for one monolayer of hydrogen coverage on commercial Pt/C and Pd/C, and a charge density of 240 $\mu C \cdot cm^{-2}$ (a value for the (111) surface) for one monolayer of hydrogen coverage on D-Pd M/C and Pd M/C. For the Cu stripping experiments, an Ar-saturated solution containing 2 mM $CuSO_4$ and 0.05 M H_2SO_4 was used as the electrolyte. The potential was first held at 0.3 V versus RHE for 100 s to form a Cu_{upd} monolayer, and then CVs were obtained from 0.3 V to 1.0 V at 20 $mV \cdot s^{-1}$. The ECSAs were calculated by subtracting the background CVs that were collected in Ar-saturated 0.05 M H_2SO_4 at 20 $mV \cdot s^{-1}$, assuming a charge density of 470 $\mu C \cdot cm^{-2}$.

The electron transfer number (n) and the hydrogen peroxide yield ($\boldsymbol{H_2O_2}$%) were tested by a rotating Pt ring - GC disk electrode (RRDE) device (Pine, USA), where the surface area of the GC disk and Pt ring are 0.2475 cm^{-2} and 0.1866 cm^{-2}, respectively. The disk electrode was conducted LSV scan, and the ring electrode potential was set to 1.4 V vs. RHE. The $\boldsymbol{H_2O_2}$% and n were calculated by the following equations:

$$\boldsymbol{H_2O_2}\% = 200 \times \frac{\frac{I_r}{N}}{\frac{I_r}{N}+I_d}$$

$$n = 4 \times \frac{I_d}{\frac{I_r}{N}+I_d}$$

where $\boldsymbol{I}_d$ is the disk current, $\boldsymbol{I}_r$ is the ring current, and N is the ring collection efficiency (N=0.37). In addition, the electron transfer number during the ORR process of **D-Pd M** was also determined by applying different rotating rates to the Koutecky-Levich equation:

$$\frac{1}{j} = \frac{1}{j_K} + \frac{1}{j_L} = \frac{1}{B\omega^{1/2}} + \frac{1}{j_L}$$

$$B = 0.2nFC_0D_0^{2/3}\upsilon^{-1/6}$$

where j, j_k, and j_L represent measured current density, the kinetic and limiting current densities the kinetic, respectively. F is the Faraday constant (96485 C mol^{-1}), C_0 is the bulk concentration of O_2 (1.26×10^{-6} $mol \cdot cm^{-3}$), D_0 is the diffusion coefficient of O_2 in 0.1 M KOH (1.93×10^{-5} $cm^2 \cdot s^{-1}$), and υ is the kinetic viscosity (0.01 $cm^2 \cdot s^{-1}$). The rotation speed is expressed in rpm.

Accelerated durability tests (ADTs) were conducted by cycling between 0.6 V and 1.0 V vs. RHE at 200 mV/s for 5,000 cycles and 10,000 cycles in 0.1 M O_2-saturated KOH solution at 1600 rpm.

S4 Computational details

All DFT calculations in the present work were performed using the Vienna Ab initio Simulation Package (VASP)[3,4] with the Perdew-Burke-Ernzerhof (PBE)[3] functional. The ion-electron interactions were modeled using the projector-augmented wave (PAW) method[5]. The plane wave cutoff energy was set to 400 eV in all calculations. The convergence criteria were set to be 10-5 eV and 0.01 eV/Å for wavefunction and geometry optimization, respectively. A Γ-centred Monkhorst–Pack k-point mesh with a size of 3×3×1was applied for all supercells. The vacuum region was set to 15 Å. The DFT-D3 scheme of dispersion correction was employed to describe van der Waals interactions[6]. The electronic density of the structure was processed using VASPKIT[7].

S5 Zn-air battery meansurement

The zinc-air battery was measured in a labmade battery mode, consisting of an anode and a cathode. The anode is a polished Zn foil (with a thickness of 0.5 mm), the air cathode is the catalyst-loaded carbon paper (ThermoFisher Scientific), and the electrolyte is a 6 M KOH solution containing 0.2 M $Zn(CH_3COO)_2$. The catalyst inks were prepared with the same method we mentioned above but at a concentration of 10 $mg \cdot mL^{-1}$. The catalyst-loaded carbon paper was prepared by spreading as-prepared catalyst ink onto carbon paper and drying at room temperature. The mass loading of 20% **D-Pd M**/C and 20% Pt/C catalysts is 130 $\mu g \cdot cm^{-2}$, and the mass loading of Pd/Pt is 26 $\mu g \cdot cm^{-2}$. The polarization curves were performed at the CHI 760E electrochemistry station. Galvanostatic cycling tests were collected at the **LAND CT2003A** multi-channel battery testing system. When testing the specific capacity of zinc-air potential, the discharge current was set at 15 mA and the cut-off voltage was 0.5 V. The charge and discharge current density was set at 15 mA, the discharge cut-off voltage was set to 0.2 V, and the charge cut-off voltage was set to 1. 85 V.

S6 Supplementary figures

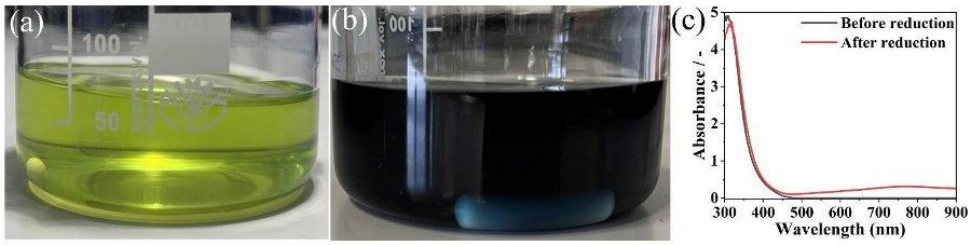

Figure S1. The optical photographs of PMo_{12} in DMF solution before (a) and after (b) reduction, and corresponding UV-visible spectra after being diluted to 1/10 of original concentration.

The color changes from bright yellow to dark blue and newly appeared broad in reduced solution indicate the reduction of PMo_{12} clusters to heteropoly blue. Approximately 5.2% of PMo_{12} underwent reduction to form heteropoly blue,[8,9] according to the Beer-Lambert law: $A = \varepsilon bc$; A is absorbance, ε is molar absorptivity (here: 2600 $M^{-1} \cdot cm^{-1}$), b is length of light path (here: 1 cm), and c is concentration, respectively.

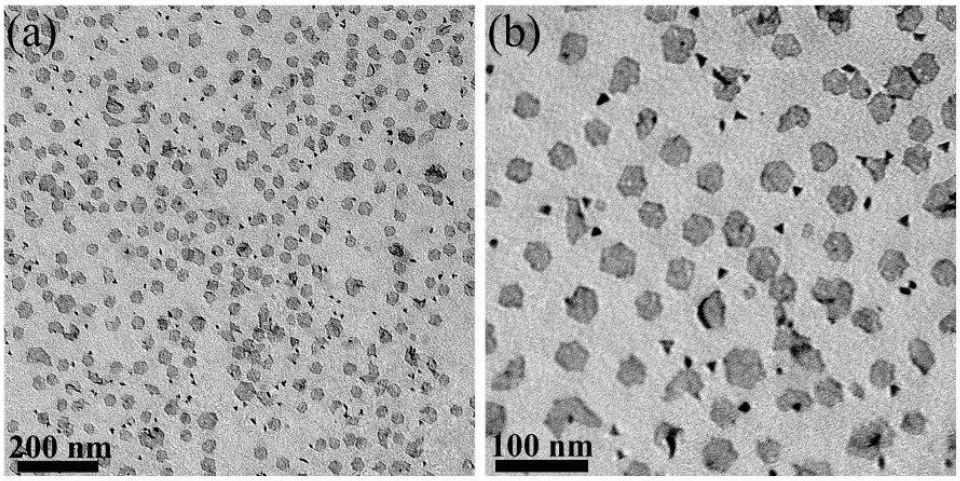

Figure S2. TEM images of Pd M at low (a) and (high) magnification.

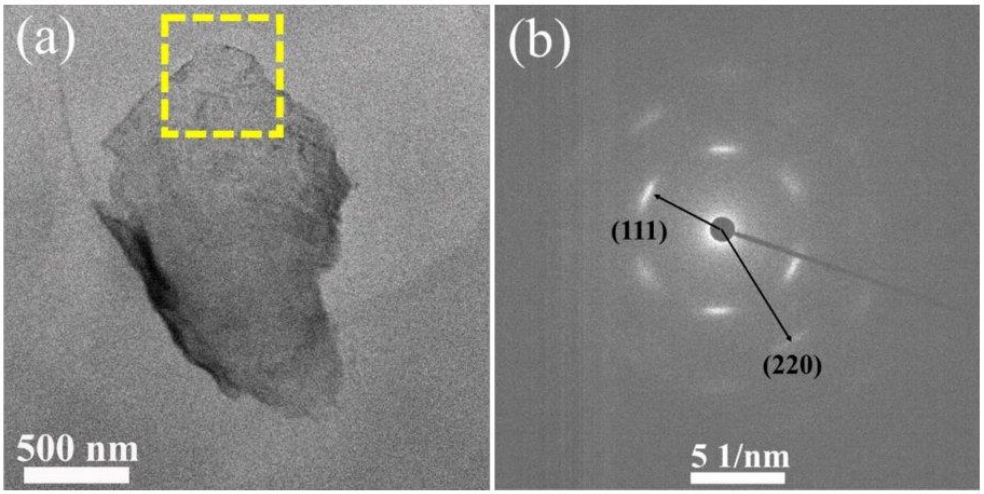

Figure S3. (a) TEM image and (b) the corresponding selected area electron diffraction (SAED) pattern in selected area in (a) of **D-Pd M**.

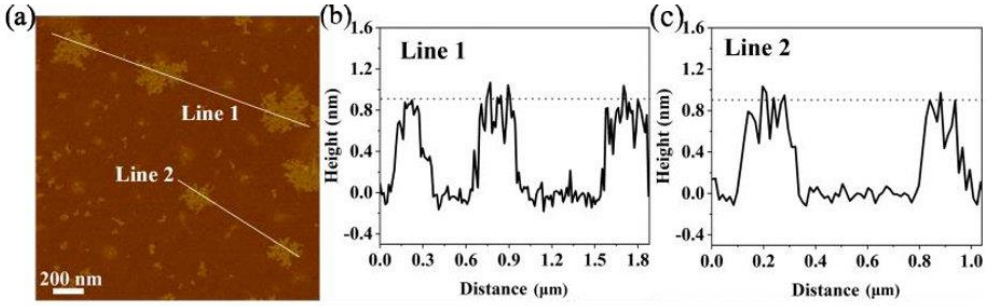

Figure S4. Atomic force microscopy (AFM) image (a) and corresponding height profiles (b and c) of **D-Pd M**.

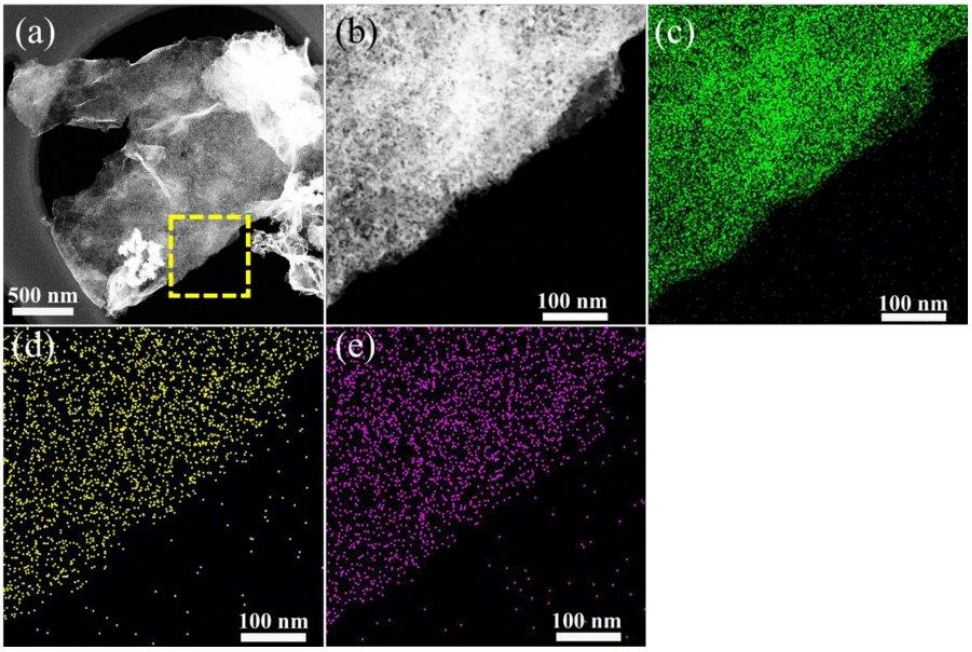

Figure S5. (a) HAADF-STEM image, (b) the magnification of selected area (in a, yellow square), (c-d) and the corresponding elemental mapping of Pd, Mo, and W elements of the **D-Pd M**.

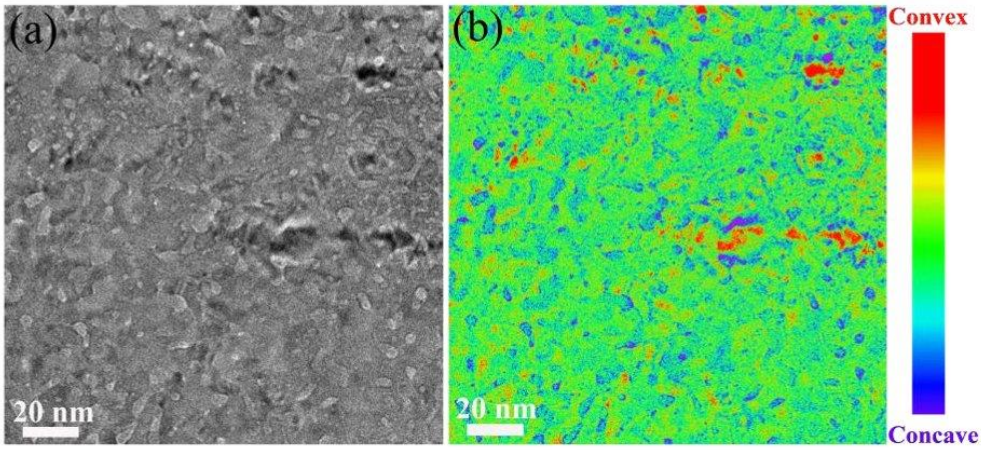

Figure S6. (a) TEM images and (b) corresponding false color mode of **D-Pd M**.

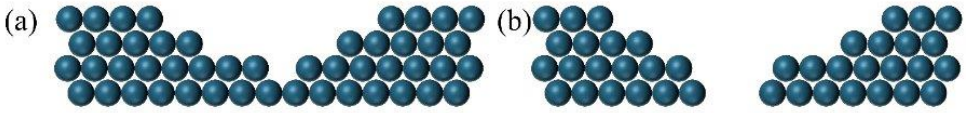

Figure S7. Schematic of pores (a) and concave (b) defects from side view.

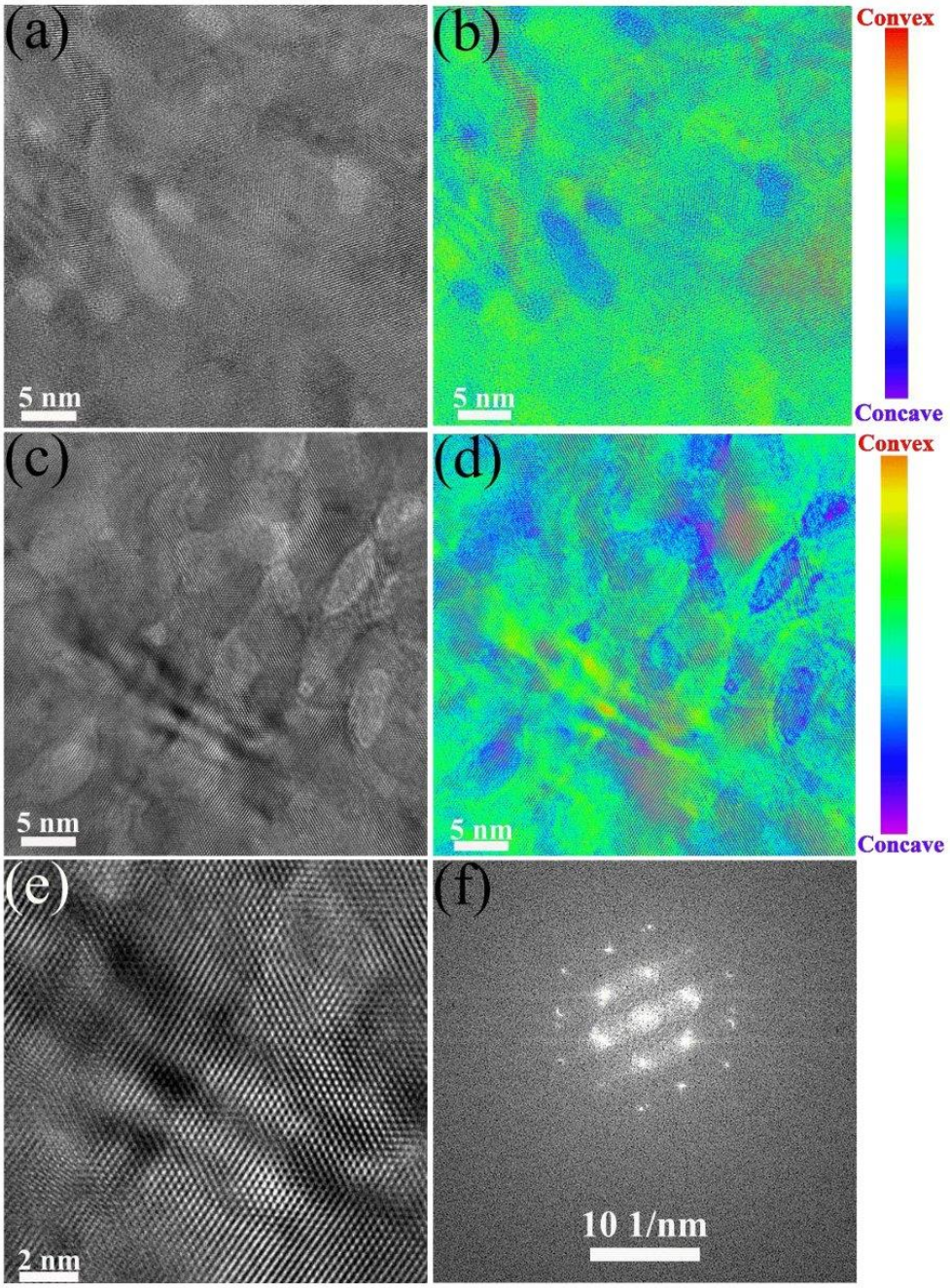

Figure S8. HRTEM images of **D-Pd M**. (a, c, and e) crude images, (b and d) temperature mode of corresponding images, in which dark blue represents concave sites and bright orange represents convex sites. (f) fast Fourier transform pattern of (e).

Table S1. EXAFS fitting parameters at the Mo&Pd *K*-edge and W L_3-edge for **D-Pd M**.

Sample	Shell	CN^a	R(Å)^b	σ^2(Å^2)^c	ΔE_0(eV)^d	R factor
Pd						
Pd foil	Pd-Pd	12*	2.737±0.002	0.0055±0.0002	3.4±0.2	0.0020
PdO	Pd-O	4.0±0.2	2.017±0.001	0.0023±0.0006	7.9±0.3	0.0042
	Pd-Pd	3.7±0.8	3.018±0.001	0.0089±0.0017	1.5±0.9	
	Pd-Pd	7.7±0.8	3.388±0.001	0.0124±0.0001	2.3±0.7	
D-Pd M	Pd-Pd/Mo/W	10.7±1.0	2.738±0.005	0.0060±0.0006	6.0±0.7	0.0062
W						
W-foil	W-W	8*	2.734±0.006	0.0037±0.0007	5.3±1.0	0.0049
	W-W	6*	3.160±0.012	0.0043±0.0010	8.4±1.7	
WO_2	W-O	4.0±0.7	2.013±0.001	0.0015±0.0021	11.4±1.0	0.0081
D-Pd M	W-O	1.4±0.3	1.779±0.001	0.0070±0.0014	-7.9±1.0	0.0062
	W-O	2.8±0.4	2.111±0.001			
	W-Pd	6.3±0.8	2.605±0.001	0.0189±0.0011	2.0±0.6	
	W-O	15.9±1.8	3.499±0.001			
Mo						
Mo foil	Mo-Mo	8*	2.724±0.003	0.0041±0.0003	4.9±0.5	0.0040
	Mo-Mo	6*	3.150±0.005	0.0040±0.0004	7.5±1.0	
MoO_2	Mo-O	6.0±0.3	1.999±0.001	0.0033±0.0006	2.8±0.3	0.0035
	Mo-Mo	3.1±0.6	2.569±0.001	0.0105±0.0017	8.8±0.8	
	Mo-Mo	1.9±0.2	3.087±0.001	0.0040±0.0001	-11.1±0.5	
	Mo-Mo	6.2±0.3	3.642±0.001			
	Mo-Mo	7.4±1.6	4.058±0.001	0.0130±0.0001	0.8±0.1	
MoO_3	Mo-O	2.0±0.2	1.685±0.001	0.0037±0.0006	4.5±0.9	0.0080
	Mo-O	2.7±0.3	1.975±0.001		14.0±0.1	
	Mo-O	3.1±0.4	2.286±0.001	0.0095±0.0001		
	Mo-Mo	6.3±1.1	3.430±0.001	0.0086±0.0006	-	
	Mo-Mo	15.4±1.9	3.625±0.001		12.0±0.4	
	Mo-Mo	2.5±0.4	4.062±0.001	0.0051±0.0001	13.3±1.3	
D-Pd M	Mo-O	1.4±0.2	1.745±0.001	0.0023±0.0009	8.5±0.8	0.0070
	Mo-O	0.4±0.2	2.044±0.001			
	Mo-O	0.5±0.2	2.429±0.001	0.0046±0.0014	-3.0±1.2	
	Mo-Pd	0.9±0.2	2.681±0.001			

^{a}*CN*, coordination number; ^{b}*R*, the distance to the neighboring atom; $^c\sigma^2$, Debye-Waller factor, the Mean Square Relative Displacement (MSRD); $^d\Delta E_0$, inner potential correction; *R* factor indicates the goodness of the fit. S_0^2 was fixed to 0.992, 0.812, and 0.958, according to the experimental EXAFS fit of Mo foil, Pd foil, and W foil by fixing *CN* as the known crystallographic value. * This value was fixed during EXAFS fitting, based on the known structure of Mo, Pd, and W. Fitting range: $3.0 \le k$ (/Å) ≤ 14.0 and $1.0 \le R$ (Å) ≤ 3.3 (Mo foil); $3.0 \le k$ (/Å) ≤ 12.0 and $1.1 \le R$ (Å) ≤ 3.9 (MoO2); $3.0 \le k$ (/Å) ≤ 13.0 and $1.0 \le R$ (Å) ≤ 4.1 (MoO_3); $3.0 \le k$ (/Å) ≤ 13.0 and $1.0 \le R$ (Å) ≤ 3.0 (D-Pd M_Mo); $3.0 \le k$ (/Å) ≤ 13.0 and $1.0 \le R$ (Å) ≤ 2.9 (Pd foil); $3.0 \le k$ (/Å) ≤ 12.0 and $1.0 \le R$ (Å) ≤ 3.6 (PdO); $3.0 \le k$ (/Å) ≤ 13.0 and $1.9 \le R$ (Å) ≤ 3.0 (D-Pd M_Pd); $3.0 \le k$ (/Å) ≤ 12.0 and $1.0 \le R$ (Å) ≤ 3.5 (W foil); $3.0 \le k$ (/Å) ≤ 11.0 and $1.2 \le R$ (Å) ≤ 2.0 (WO_2); $3.0 \le k$ (/Å) ≤ 10.0 and $1.0 \le R$ (Å) ≤ 3.8 (D-Pd M_W). A reasonable range of EXAFS fitting parameters: $0.700 < S_0^2 < 1.000$; $CN > 0$; $\sigma^2 > 0$ Å^2; $|\Delta E_0| < 15$ eV; *R* factor < 0.02.

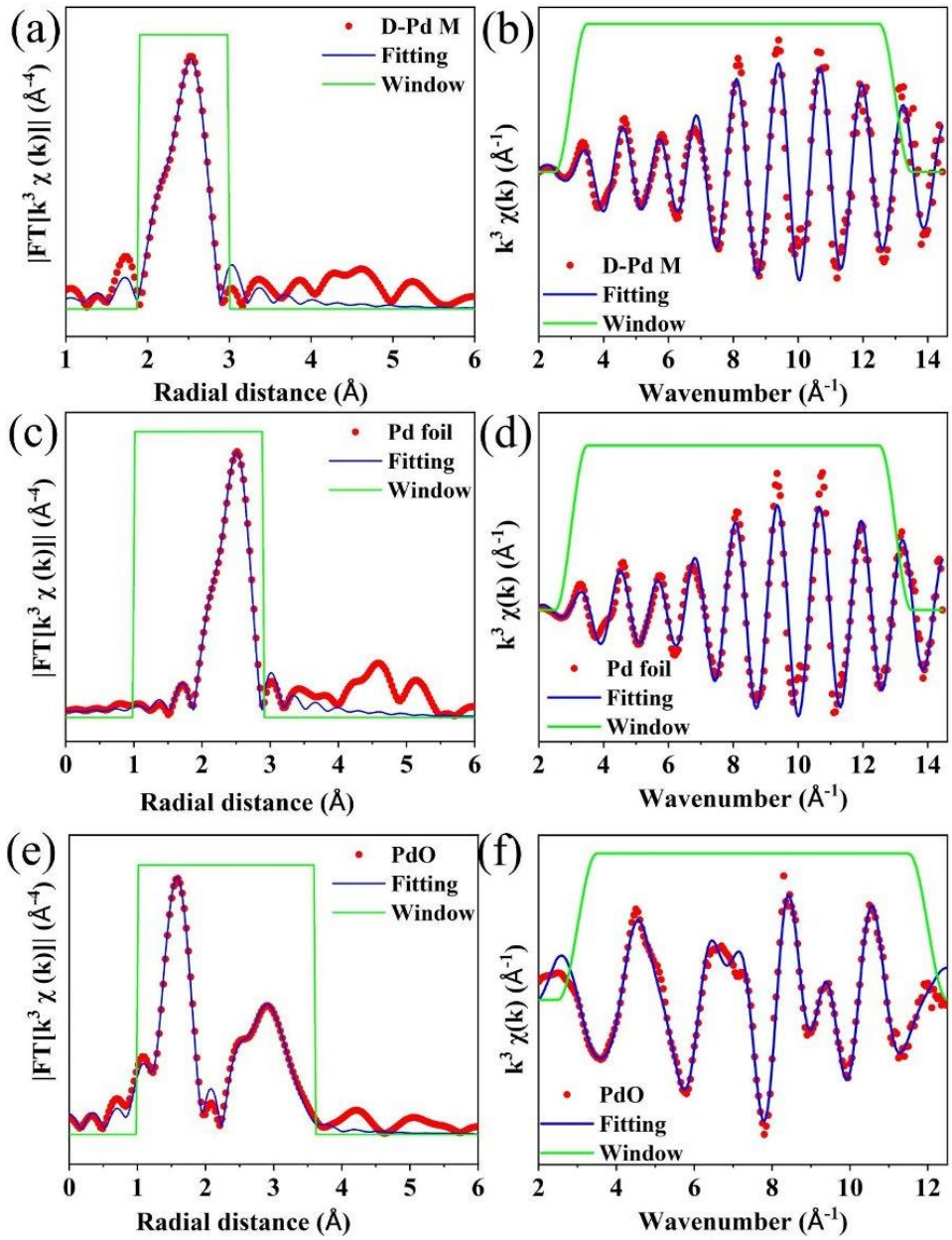

Fig. S9. R space and k space fitting results of Pd K-edge. (a and b) **D-Pd M**, (c and d) Pd foil, and (e and f) PdO. The dots or lines in red, blue, and green represent raw data, fitting results and FT fitting range windows.

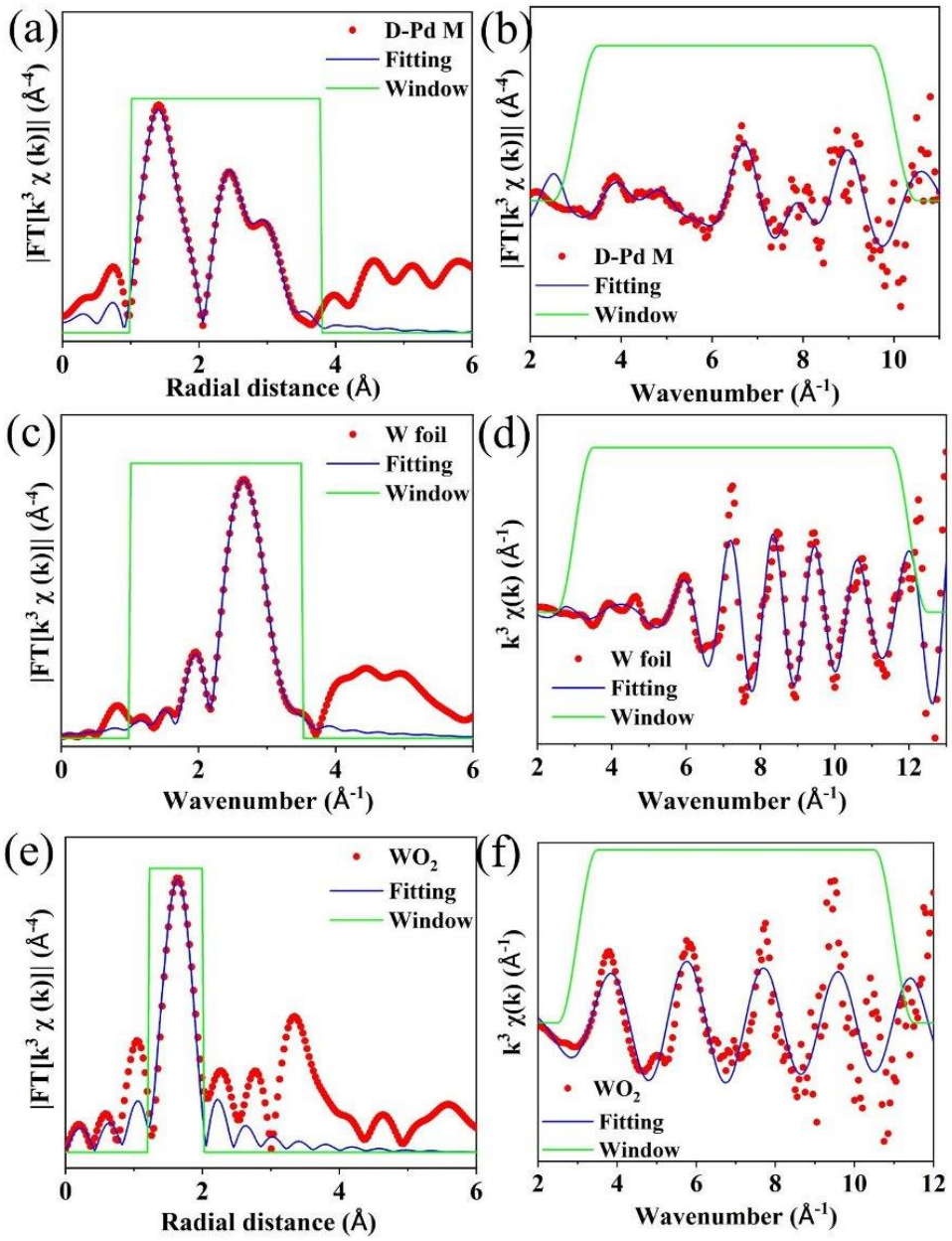

Fig. S10. R space and k space fitting results of W L-edge. (a and b) **D-Pd M**, (c and d) W foil, and (e and f) WO_2. The dots or lines in red, blue, and green represent raw data, fitting results and FT fitting range windows.

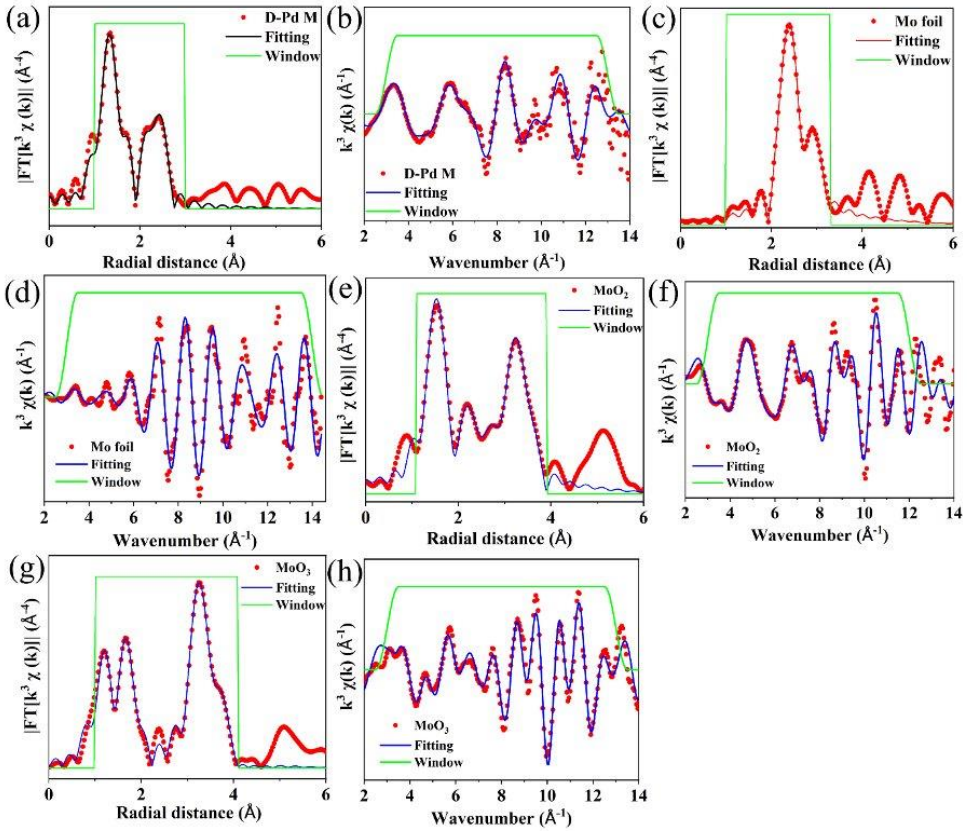

Fig. S11. R space and k space fitting results of Mo K-edge. (a and b) **D-Pd M**, (c and d) Mo foil, (e and f) MoO_2, and (g and h) MoO_3. The dots or lines in red, blue, and green represent raw data, fitting results and FT fitting range windows.

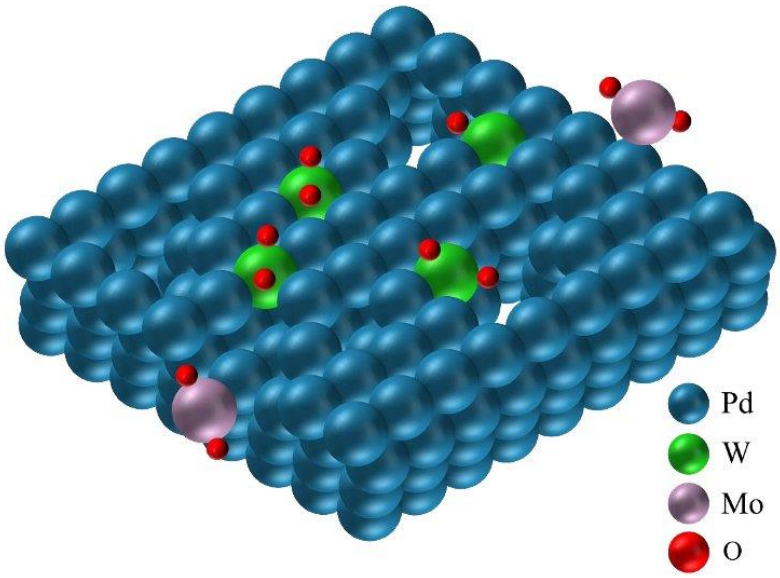

Figure S12. Schematic of MoO_x and WO_x doping. W atoms substitute the position of Pd, but Mo just dispersed on the edge of Pd.

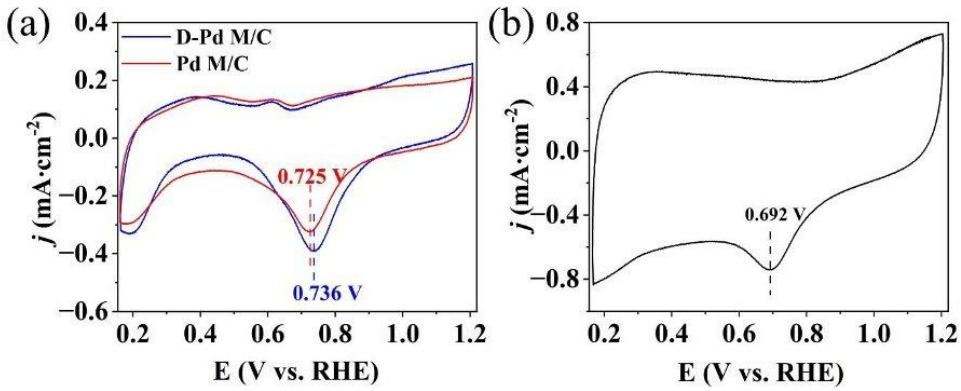

Figure S13. CV curves of (a) **D-Pd M**/C, Pd M/C, and (b) Pd/C in N_2-saturated 0.1 M KOH solution at a scan rate of 50 $mV \cdot s^{-1}$.

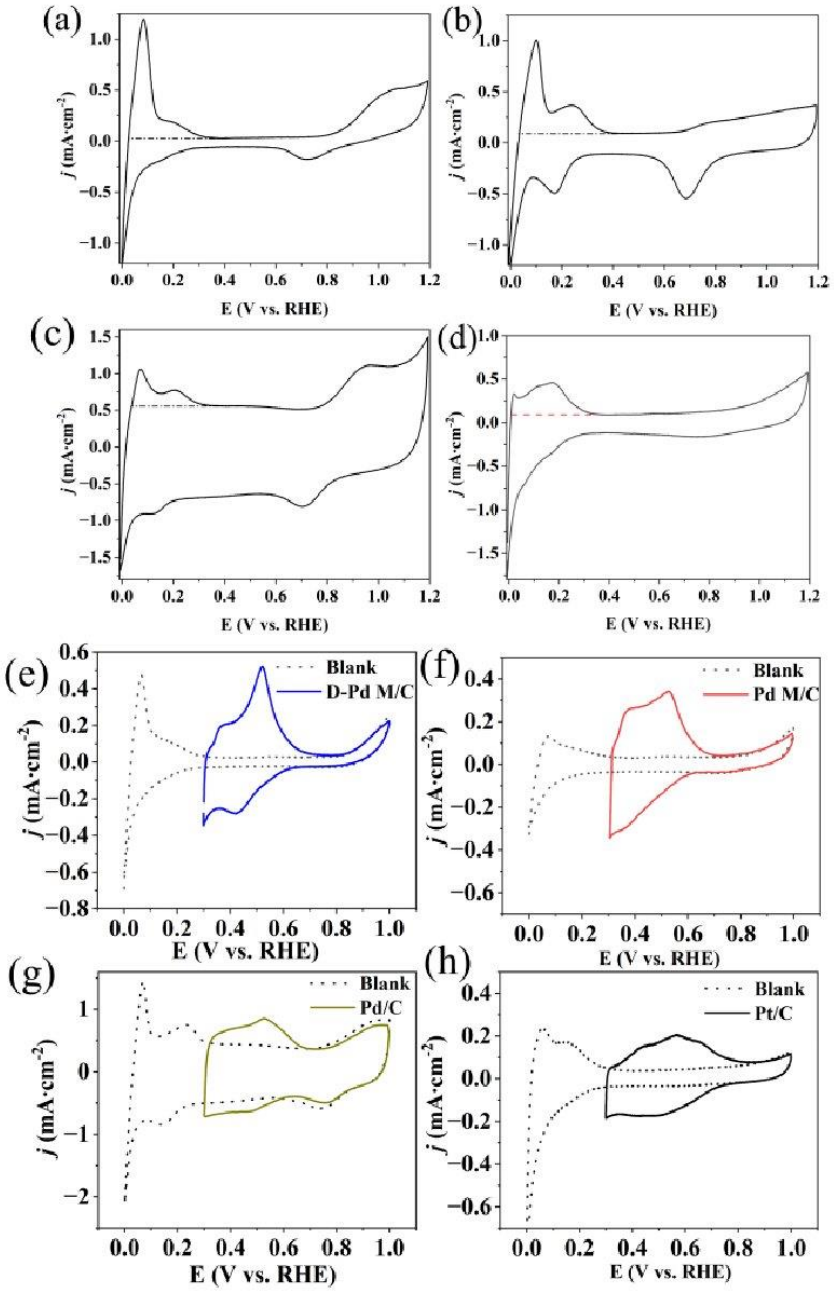

Figure S14. CVs of (a) **D-Pd M**/C, (b) Pd M/C, (c) Pd/C, and (d) Pt/C in N_2-saturated 0.1 M $HClO_4$ at a scan rate of 50 $mV \cdot s^{-1}$ (e-h) CVs and Cu stripping voltammograms of **D-Pd M**/C, Pd M/C, Pd/C, and Pt/C.

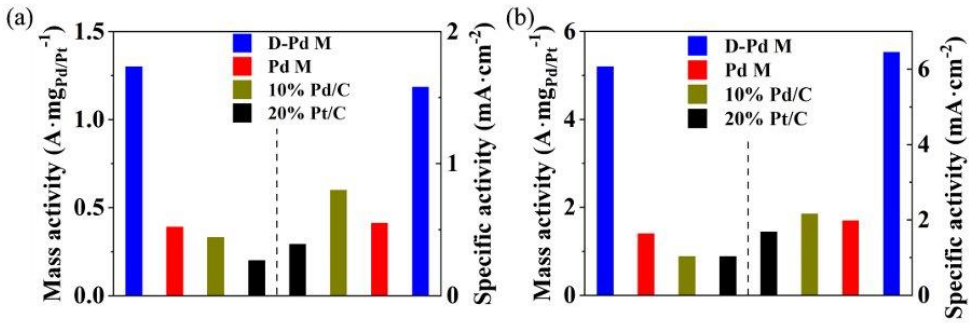

Figure S15. MAs and SAs of **D-Pd M**/C, Pd M/C, Pd/C, and Pt/C at (a) 0.9 V vs. RHE and (b) 0.85 V vs. RHE.

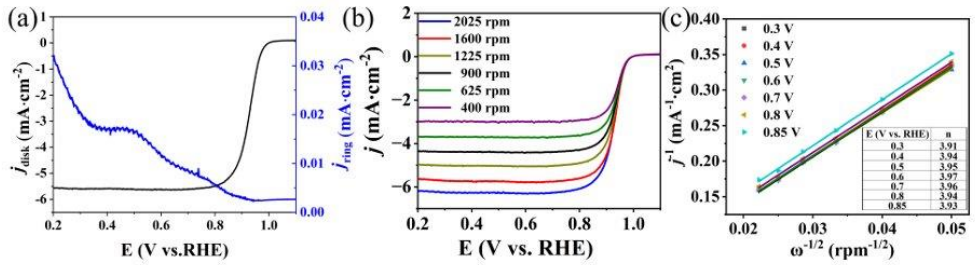

Figure S16. (a) Ring and disk current density of **D-Pd M** in O_2-saturated 0.1 M KOH solution, potential applied on ring was set 1.4 V vs. RHE, (b)LSV curves of **D-Pd M**/C at different scan rates and (c) corresponding K–L plot and electron transfer numbers (insert).

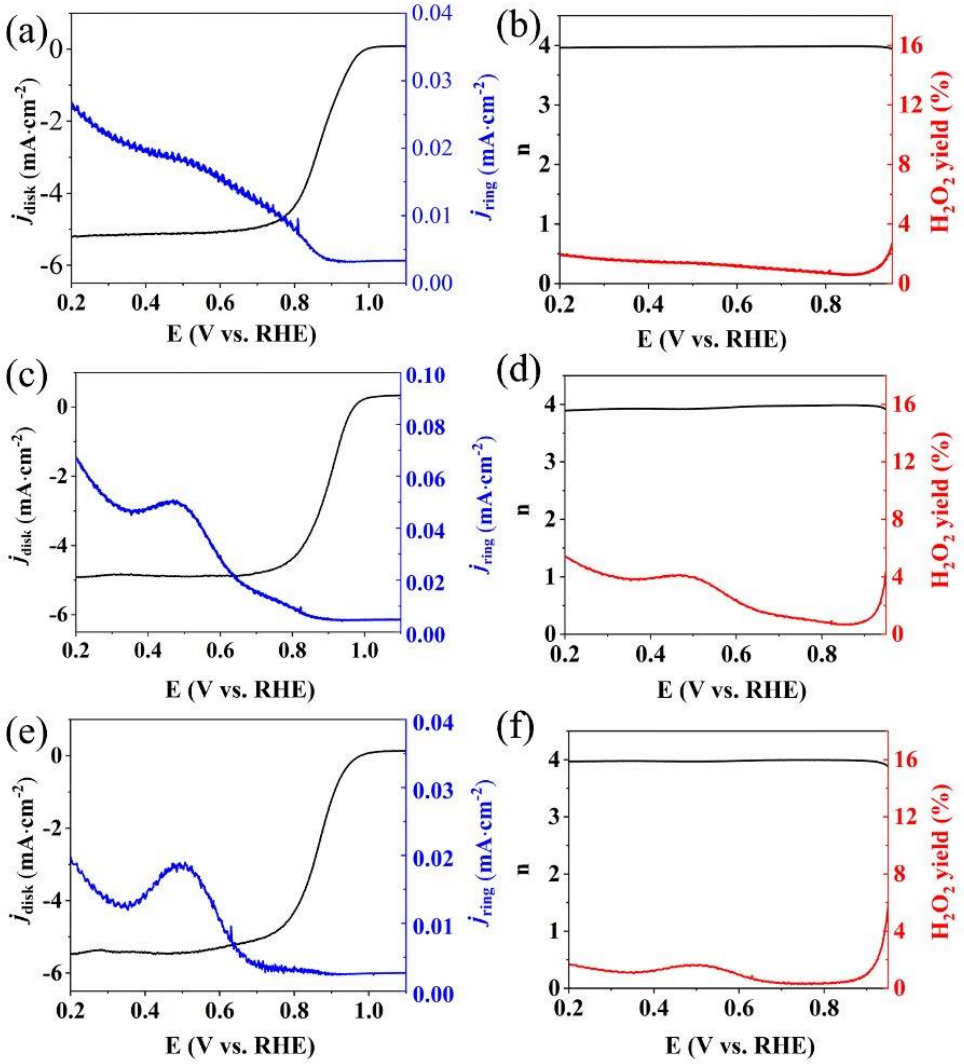

Figure S17. Ring and disk current density of (a) Pd M/C, (c) Pd/C, and (e) Pt/C in O_2-saturated 0.1 M KOH solution, potential applied on ring was set 1.4 V vs. RHE. The electron transfer number and H_2O_2 yield of (b) Pd M/C, (d) Pd/C, and (f) Pt/C.

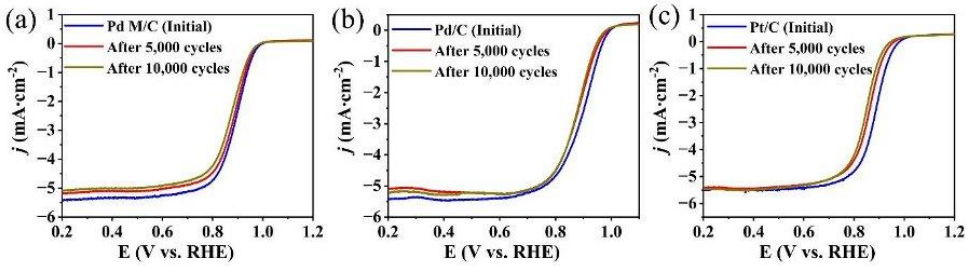

Figure S18. LSVs of (a) Pd M/C, (c) Pd/C, and (e) Pt/C in O_2-saturated 0.1 M KOH solution before and after 5,000 and 10,000 CV scans.

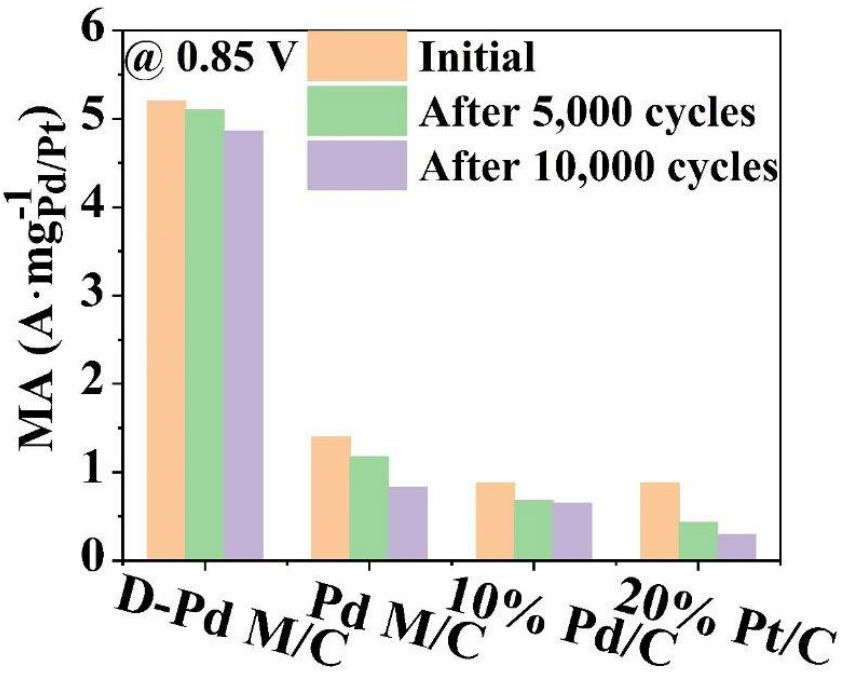

Figure S19. MAs of **D-Pd M**/C, Pd M/C, Pd/C, and Pt/C at 0.85 V vs. RHE before and after 5,000 and 10,000 cycles

Table S2. Comparison of electroactivity of recent reported representative Pd-based catalysts for alkaline ORR

Samples	Half-wave potential (V vs. RHE)	Specific activitiy ($mA \cdot cm^{-2}$ at 0.9 V)	Mass activitiy ($A \cdot mg_{Pd}^{-1}$ at 0.9 V)	Reference
D-Pd M	**0.93**	**6.13**	**1.3**	This work
Pd M	0.87	1.86	0.39	This work
PdCu Metallene	0.943	1.67	0.905	[10]
Defect-Rich Pd Metallene	0.90	1.336	0.892	[11]
$Pd_9Pt_1Ni_1$	0.928	1.22	0.29	[12]
Fe–Pd UPM	0.914	0.89	0.736	[13]
PdMo bimetallene	0.95	11.64	16.37	[14]
Pd_3Pb/PdTetragonal Nanosheets	0.9	1.31	0.57	[15]
Pd3Pb Nanosheet	0.91	0.989	0.697	[16]
Pd@PEI-EDA metallene	0.968	1.3	0.93	[17]
N–Pd MNRs	0.95	1.29	0.68	[18]

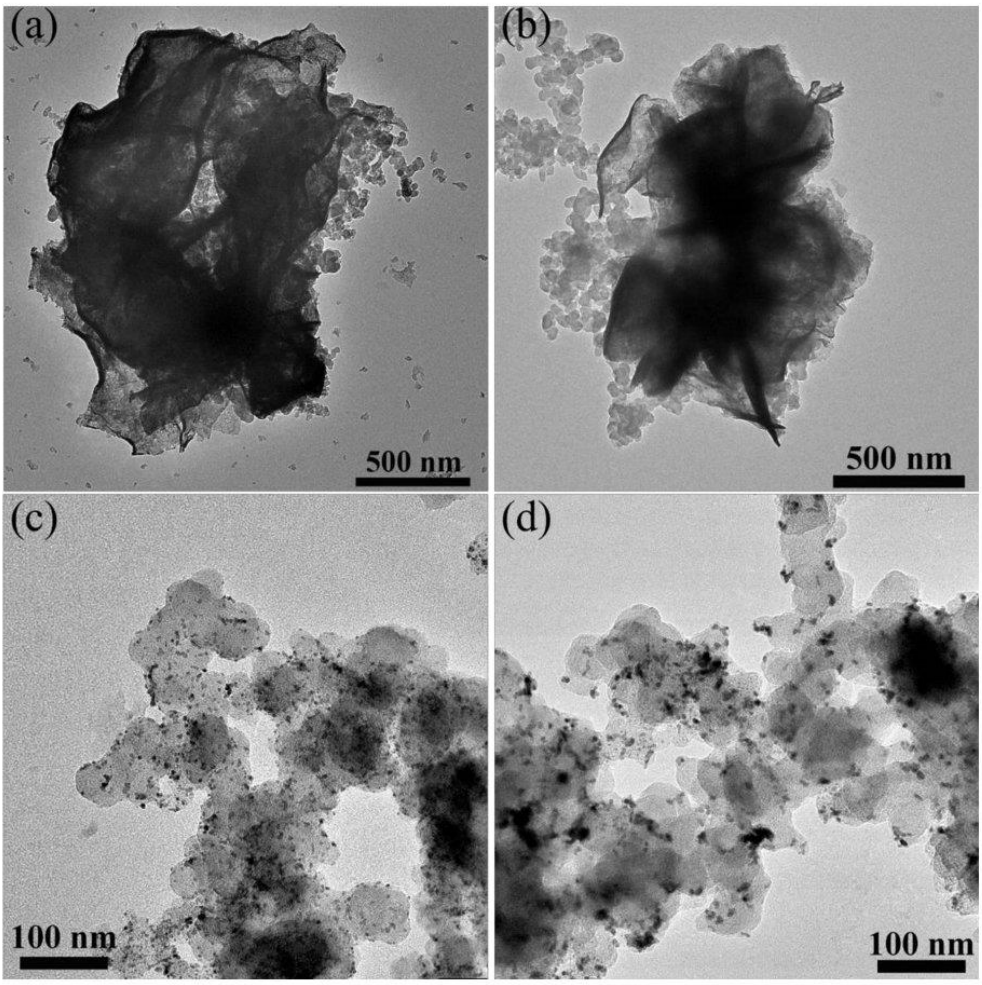

Figure S20. The morphologies of **D-Pd M** (a, b) and Pt/C (c, d) before and after ADT test.

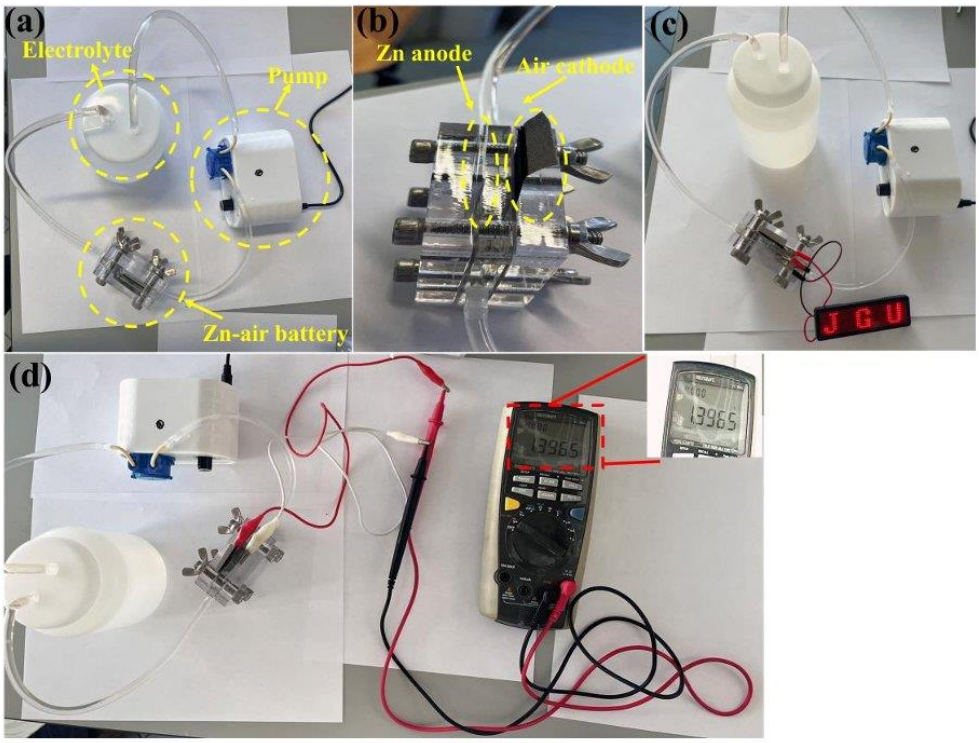

Figure S21. Photographs of the whole Zn-air battery system (a) and Zn-air battery (b), (c) red LED (the operating voltage only > **1** V) powered by **D-Pd M** based Zn-air battery, and (c) an open-circuit voltage of 1.397 V obtained with **D-Pd M** based Zn-air battery.

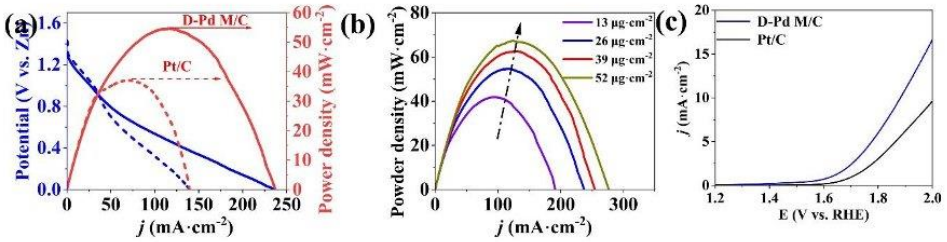

Figure S22. (a)Polarization and corresponding power density curves of **D-Pd M**/C (line) and Pt/C (dashes), (b) power density curves of **D-Pd M**/C at different loading, (c) OER polarization curves of **D-Pd M**/C and Pt/C in O_2-saturated 0.1 M KOH at a scan rate of 5 $mV \cdot s^{-1}$.

Table S3. Comparison of the performance of the Zn-air battery prepared in this work and representative literature.

Air cathode	Catalyst loading ($mg \cdot cm^{-2}$)	Open circuit Voltage (V)	Specific capacity ($mAh \cdot g_{Zn}^{-1}$)	Voltage (V)	Reference
D-Pd M	**0.026**	**1.4**	**809**	**1.25 V @ 15 $mA \cdot cm^{-2}$**	**This work**
PdMo bimetallene	0.2	1.48	798	1.35 V @ 10 $mA \cdot cm^{-2}$	[14]
Pd−Gd2O3/C+RuO2	NA	1.46	724	1.3 V @ 5 $mA \cdot cm^{-2}$	[19]
Pd/B4C	0.6	1.43	NA	1.2 V @ 5 $mA \cdot cm^{-2}$	[20]
Commercial Pt/C + IrO_2	1	1.36	499	1.21@ 10$mA \cdot cm^{-2}$	[14]
Pd/CoOx/d-NC	1	1.476	760	1.2@ 10$mA \cdot cm^{-2}$	[21]
Ni SAs-Pd@NC	10	1.44	719.2	1.3 @ 5 $mA \cdot cm^{-2}$	[22]
$Pd_{55}Au_{45}$	2	1.44	821.4	1.3 V @ 10 $mA \cdot cm^{-2}$	[23]
PdMoCrW Tetrametallene	1	1.48	895	1.21@ 10$mA \cdot cm^{-2}$	[24]

S7 Reference

[1] W. Zhu, L. Zhang, P. Yang, C. Hu, Z. Luo, X. Chang, Z.-J. Zhao, J. Gong,] W Zhu,] L Zhang,] P Yang, C. Hu, Z. Luo, X. Chang, Z. Zhao, J. Gong, *Angewandte Chemie International Edition* **2018**, *57*, 11544–11548.

[2] Y. Li, Y. Yan, Y. Li, H. Zhang, D. Li, D. Yang, *CrystEngComm* **2015**, *17*, 1833–1838.

[3] G. Kresse, J. Furthmüller, *Comput Mater Sci* **1996**, *6*, 15–50.

[4] G. Kresse, J. Hafner, *Phys Rev B* **1994**, *49*, 14251.

[5] G. Kresse, D. Joubert, *Phys Rev B* **1999**, *59*, 1758.

[6] K. Lee, É. D. Murray, L. Kong, B. I. Lundqvist, D. C. Langreth, *Phys Rev B Condens Matter Mater Phys* **2010**, *82*, 081101.

[7] V. Wang, N. Xu, J. C. Liu, G. Tang, W. T. Geng, *Comput Phys Commun* **2021**, *267*, 108033.

[8] E. A. Nagul, I. D. McKelvie, P. Worsfold, S. D. Kolev, *Anal Chim Acta* **2015**, *890*, 60–82.

[9] H. Zhou, Z. Ma, G. Yang, X. Jiang, S. Duan, Y. Wu, M. Wang, L. Ni, L. Feng, G. Diao, *Batter Supercaps* **2024**, e202300563.

[10] L. Zhang, Z. Zhao, X. Fu, S. Zhu, Y. Min, Q. Xu, Q. Li, *ACS Appl Mater Interfaces* **2023**, *15*, 5198–5208.

[11] H. Yu, T. Zhou, Z. Wang, Y. Xu, X. Li, L. Wang, H. Wang, *Angewandte Chemie International Edition* **2021**, *60*, 12027–12031.

[12] Q. Yang, L. Shi, B. Yu, J. Xu, C. Wei, Y. Wang, H. Chen, *J Mater Chem A Mater* **2019**, *7*, 18846–18851.

[13] S. Huang, S. Lu, S. Gong, Q. Zhang, F. Duan, H. Zhu, H. Gu, W. Dong, M. Du, *ACS Nano* **2022**, *16*, 522–532.

[14] M. Luo, Z. Zhao, Y. Zhang, Y. Sun, Y. Xing, F. Lv, Y. Yang, X. Zhang, S. Hwang, Y. Qin, J. Y. Ma, F. Lin, D. Su, G. Lu, S. Guo, *Nature 2019 574:7776* **2019**, *574*, 81–85.

[15] C. Tang, N. Zhang, Y. Ji, Q. Shao, Y. Li, X. Xiao, X. Huang, *Nano Lett* **2019**, *19*, 1336–1342.

[16] L. Bu, C. Tang, Q. Shao, X. Zhu, X. Huang, *ACS Catal* **2018**, *8*, 4569–4575.

[17] Z. Wang, S. Xu, Q. Mao, K. Deng, Y. Xu, H. Wang, H. Yu, L. Wang, *Inorg Chem* **2023**, *62*, 13537–13543.

[18] H. Wang, Y. Li, S. Liu, H. Yu, K. Deng, Z. Wang, Y. Xu, L. Wang, *Chemical Communications* **2023**, *59*, 11101–11104.

[19] S. Ning, M. Li, X. Wang, D. Zhang, B. Zhang, C. Wang, D. Sun, Y. Tang, H. Li, K. Sun, G. Fu, *Angewandte Chemie International Edition* **2023**, *62*, e202314565.

[20] Y. N. Chen, X. Zhang, H. Cui, X. Zhang, Z. Xie, X. G. Wang, M. Jiao, Z. Zhou, *Energy Storage Mater* **2018**, *15*, 226–233.

[21] T. Kang, D. Nam, J. Kim, *Appl Surf Sci* **2022**, *582*, 152442.

[22] S. Wang, Z. Lin, M. Li, Z. Yu, M. Zhang, M. Gong, Y. Tang, X. Qiu, *J Mater Chem A Mater* **2022**, *10*, 6086–6095.

[23] S. Qiao, H. Shou, W. Xu, Y. Cao, Y. Zhou, Z. Wang, X. Wu, Q. He, L. Song, *Energy Environ Sci* **2023**, *16*, 5842–5851.

[24] Z. Zheng, K. Dong, X. Yang, Q. Yuan, *Langmuir* **2024**, DOI:10.1021/ACS.LANGMUIR.4C01196.

S8 Author contributions

Y.Z., R.L., S. Li, and C.S. conceived the project. R.L., S. Li, and C.S. supervised the project. Y.Z. carried out the material fabrication. Y.Z., F. F, D. G, and R.L. designed and performed electrocatalytic studies. R.L. Y.Z., and C.S. performed data analysis. S. Li. and Y. Z. performed XAS analyses. Z.C. and Y. Z. performed battery tests. K.C. and D.Z. performed (S)TEM analyses. N. M. and W. C. performed computational calculations. All authors co-wrote the manuscript.

7. Curriculum Vitae

This page has been removed for data privacy protection reasons.

This page has been removed for data privacy protection reasons.

8. Acknowledgement

This page has been removed for data privacy protection reasons.

This page has been removed for data privacy protection reasons.